

Costa Rica nurtures a new
cadre of ecologists p. 1558

Y chromosome replacement in
Neanderthals pp. 1565 & 1653

Exploring nonlinear effects
with x-rays pp. 1568 & 1630

Science

\$15
25 SEPTEMBER 2020

AAAS

AVIAN AWARENESS

Carrion crows display sensory
consciousness pp. 1567 & 1626





★ *Devoted to Neuromodulation for more than 20 years !*

- In 2000, started to work on the DBS (Deep Brain Stimulation) initiative
- In 2012, set up the national research platform 'National Engineering Laboratory of Neuromodulation Technology'
- In 2016, established Science & PINS prize for Neuromodulation with Science
PINS DBS products got CE marked
- In 2017, Professor Alim-Louis Benabid, founder of DBS therapy and winner of Lasker Medical Research Awards, visited PINS
- In 2018, PINS 'Remote programming system of implantable medical devices' won the gold medal award of Geneva International Invention Exhibition
- In 2019, PINS DBS project won the first prize of 2018 National Science and Technology Progress Award (China's top Science and Technology Progress Award)

Beijing PINS Medical Co., Ltd. focuses on the development and innovation of neuromodulation technologies, aiming to provide more comprehensive and professional solutions for patients suffering from functional neurological disorder.

CONTENTS

25 SEPTEMBER 2020 • VOLUME 369 • ISSUE 6511

1558

Costa Rica's biodiversity has been a magnet for outside scientists.

NEWS

IN BRIEF

1548 News at a glance

IN DEPTH

1550 Flawed interferon response spurs severe illness

Antibodies or mutations that cripple key antiviral protein underlie 14% of severe cases
By M. Wadman

RESEARCH ARTICLE BY Q. ZHANG ET AL.
DX.DOI.ORG/10.1126/SCIENCE.ABD4570;
RESEARCH ARTICLE BY P. BASTARD ET AL.
DX.DOI.ORG/10.1126/SCIENCE.ABD4585

1551 Fighting to be counted

The pandemic has fueled Abigail Echo-Hawk's quest for health data on Indigenous people in the United States
By L. Wade

1553 Despite obstacles, WHO unveils plan to distribute vaccine

Nations with nearly two-thirds of world's population have joined, but not the United States, Russia, or China
By K. Kupferschmidt

1554 Turkey targets critics of its pandemic response

Researchers and physicians who question data or policies face lengthy investigations
By K. McTighe

1555 Curved scour marks trace the directions of ancient quakes

"Slickenlines" etched in rocks could help refine shaking hazard for cities near the ends of faults
By P. Voosen

1556 The short, strange life of quantum radar

In spite of military interest, quantum mechanics won't defeat stealth technologies
By A. Cho

1557 Sizing up a green carbon sink

Studies zero in on forests' potential to fight warming
By G. Popkin

FEATURES

1558 Seeking a niche

Costa Rica is producing a new generation of skilled tropical biologists. But many can't find jobs at home
By J. Kaiser

..... **1561** A tropical research treasure faces difficult times
By J. Kaiser

INSIGHTS

PERSPECTIVES

1562 Transformative tools for parasitic flatworms

Schistosome single-cell atlas and genome-wide functional dissection reveal druggable targets
By T. J. C. Anderson and M. T. Duraissingham
REPORTS pp. 1644 & 1649

1564 Preventing pores and inflammation

Metabolite-directed modification of pore-forming cell death protein limits inflammation
By R. J. Pickering and C. E. Bryant
REPORT p. 1633

1565 The last pieces of a puzzling early meeting

Y chromosomes transferred from *Homo sapiens* to Neanderthals between 350,000 to 150,000 years ago
By M. H. Schierup
REPORT p. 1653

1567 Birds do have a brain cortex—and think

Like mammals, birds have a pallium that sustains correlates of consciousness
By S. Herculano-Houzel
RESEARCH ARTICLE p. 1585; REPORT p. 1626

1568 Intense x-rays can be (slightly) exciting

Imaging of neutral "survivor" atoms excited by x-ray blasts fights radiation damage
By T. Pfeifer
REPORT p. 1630

POLICY FORUM

1570 Self-experimentation, ethics, and regulation of vaccines

DIY COVID-19 vaccines raise legal and ethical questions
By C. J. Guerrini et al.

BOOKS ET AL.

1573 Understanding quantum cause and effect

Correlations at a distance needn't necessarily be "spooky"
By A. Stairs

1574 The race to decipher Egyptian hieroglyphs

A pair of scholars recount the rivalry that defined efforts to interpret the Rosetta stone
By A. Robinson

NEVER STOP

ADVANCING BIOPHARMACEUTICALS

With over 80 years' experience in healthcare, Fujifilm is committed to enhancing patient care and addressing unmet medical needs. As a world-leading contract biopharmaceutical manufacturer (CDMO), we're helping accelerate the development of new drugs with a complete range of services. Our state-of-the-art facilities deliver precise control of process conditions and unmatched productivity. Utilizing our cell biology and bioprocessing expertise, we provide high-quality cell culture media to our biopharma partners for the production of many of the world's leading drugs. At Fujifilm, we'll NEVER STOP pushing scientific boundaries to help develop novel therapies and life-changing treatments that create a healthier world for all.

FUJIFILM
Value from Innovation


Follow [Fujifilm Life Sciences](#) on 

Image is an actual manufacturing facility of Fujifilm in Denmark.
FUJIFILM and Fujifilm Value from Innovation are trademarks of FUJIFILM Corporation.
©2020 FUJIFILM Corporation. All rights reserved.

1562, 1644, & 1649



LETTERS

1575 India needs an effective flood policy

By Y. Jameel et al.

1576 Traditional Knowledge underlies One Health

By J. Copper Jack et al.

1576 Swiss law would weaken wildlife protection

By R. Arlettaz and G. Chapron

RESEARCH

IN BRIEF

1579 From *Science* and other journals

REVIEW

1582 Immunology

The science and medicine of human immunology *B. Pulendran and M. M. Davis*

REVIEW SUMMARY; FOR FULL TEXT:
DX.DOI.ORG/10.1126/SCIENCE.AAY4014

RESEARCH ARTICLES

1583 Structural biology

The endoplasmic reticulum P5A-ATPase is a transmembrane helix dislocase *M. J. McKenna et al.*

RESEARCH ARTICLE SUMMARY; FOR FULL TEXT:
DX.DOI.ORG/10.1126/SCIENCE.ABC5809

1584 Prebiotic chemistry

Synthetic connectivity, emergence, and self-regeneration in the network of prebiotic chemistry *A. Wofos et al.*

RESEARCH ARTICLE SUMMARY; FOR FULL TEXT:
DX.DOI.ORG/10.1126/SCIENCE.AAW1955

1585 Neuroscience

A cortex-like canonical circuit in the avian forebrain *M. Stacho et al.*

RESEARCH ARTICLE SUMMARY; FOR FULL TEXT:
DX.DOI.ORG/10.1126/SCIENCE.ABC5534
PERSPECTIVE p. 1567

1586 Coronavirus

Distinct conformational states of SARS-CoV-2 spike protein *Y. Cai et al.*

1592 Chemical physics

Rotational resonances in the H₂CO roaming reaction are revealed by detailed correlations *M. S. Quinn et al.*

1597 Graphene

Inducing metallicity in graphene nanoribbons via zero-mode superlattices *D. J. Rizzo et al.*

1603 Coronavirus

Adaptation of SARS-CoV-2 in BALB/c mice for testing vaccine efficacy *H. Gu et al.*

1608 Immune systems

The immunogenetics of sexual parasitism *J. B. Swann et al.*

REPORTS

1615 Solar cells

Stable perovskite solar cells with efficiency exceeding 24.8% and 0.3-V voltage loss *M. Jeong et al.*

1621 Ocean temperature

High-impact marine heatwaves attributable to human-induced global warming *C. Laufkötter et al.*

1626 Consciousness

A neural correlate of sensory consciousness in a corvid bird *A. Nieder et al.*

PERSPECTIVE p. 1567

1630 Spectroscopy

Photon-recoil imaging: Expanding the view of nonlinear x-ray physics *U. Eichmann et al.*

PERSPECTIVE p. 1568

1633 Immunometabolism

Succination inactivates gasdermin D and blocks pyroptosis *F. Humphries et al.*

PERSPECTIVE p. 1564

1637 Protein design

Designed protein logic to target cells with precise combinations of surface antigens *M. J. Lajoie et al.*

Parasite genetics

1644 A single-cell RNA-seq atlas of *Schistosoma mansoni* identifies a key regulator of blood feeding *G. Wendt et al.*

1649 Large-scale RNAi screening uncovers therapeutic targets in the parasite *Schistosoma mansoni* *J. Wang et al.*

PERSPECTIVE p. 1562

1653 Y evolution

The evolutionary history of Neanderthal and Denisovan Y chromosomes *M. Petr et al.*

PERSPECTIVE p. 1565; PODCAST

DEPARTMENTS

1543 Editorial

Dark skies and bright satellites
By Anthony Tyson and Joel Parriott

1662 Working Life

Full disclosure
By Emily Ashkin and Michelle Atallah

ON THE COVER

The ancestors of the carrion crow diverged from the mammalian lineage as early as 320 million years ago. Carrion crow brain activity suggests that sensory consciousness developed either before the emergence



of mammals or independently in the avian lineage and may not require a cerebral cortex, as we know it. See pages 1567 and 1626. Photo: Tobias Machts, University of Tübingen

Science Staff 1542
AAAS News & Notes 1577
Science Careers 1657

SCIENCE (ISSN 0036-8075) is published weekly on Friday, except last week in December, by the American Association for the Advancement of Science, 1200 New York Avenue, NW, Washington, DC 20005. Periodicals mail postage (publication No. 484460) paid at Washington, DC, and additional mailing offices. Copyright © 2020 by the American Association for the Advancement of Science. The title SCIENCE is a registered trademark of the AAAS. Domestic individual membership, including subscription (12 months): \$165 (\$74 allocated to subscription). Domestic institutional subscription (51 issues): \$2148; Foreign postage extra: Air assist delivery: \$98. First class, airmail, student, and emeritus rates on request. Canadian rates with GST available upon request. GST #125488122. Publications Mail Agreement Number 1069624. Printed in the U.S.A.

Change of address: Allow 4 weeks, giving old and new addresses and 8-digit account number. **Postmaster:** Send change of address to AAAS, P.O. Box 96178, Washington, DC 20090-6178. **Single-copy sales:** \$15 each plus shipping and handling available from backissues.science.org; bulk rate on request. **Authorization to reproduce** material for internal or personal use under circumstances not falling within the fair use provisions of the Copyright Act can be obtained through the Copyright Clearance Center (CCC), www.copyright.com. The identification code for Science is 0036-8075. Science is indexed in the Reader's Guide to Periodical Literature and in several specialized indexes.

Editor-in-Chief Holden Thorp, hthorp@aaas.org

Executive Editor Monica M. Bradford

Editors, Research Valda Vinson, Jake S. Yeston Editor, Insights Lisa D. Chong

DEPUTY EDITORS Julia Fahrenkamp-Uppenbrink (UK), Stella M. Hurtley (UK), Phillip D. Szurmi, Sacha Vignieri **SR. EDITORIAL FELLOW** Andrew M. Sugden (UK) **SR. EDITORS** Gemma Alderton (UK), Caroline Ash (UK), Brent Grocholski, Pamela J. Hines, Di Jiang, Marc S. Lavine (Canada), Ian S. Osborne (UK), Beverly A. Purnell, L. Bryan Ray, H. Jesse Smith, Keith T. Smith (UK), Jelena Stajic, Peter Stern (UK), Valerie B. Thompson, Brad Wible, Laura M. Zahn **ASSOCIATE EDITORS** Michael A. Funk, Priscilla N. Kelly, Tage S. Rai, Seth Thomas Scanlon (UK), Yury V. Suleymanov **LETTERS EDITOR** Jennifer Sills **LEAD CONTENT PRODUCTION EDITORS** Harry Jach, Lauren Kmec **CONTENT PRODUCTION EDITORS** Amelia Beyna, Jeffrey E. Cook, Chris Filatreau, Julia Katris, Nida Masjulis, Suzanne M. White **SR. EDITORIAL COORDINATORS** Carolyn Kyle, Beverly Shields **EDITORIAL COORDINATORS** Aneera Dobbins, Joi S. Granger, Jeffrey Hearn, Lisa Johnson, Maryrose Madrid, Ope Martins, Shannon McMahon, Jerry Richardson, Hilary Stewart (UK), Alana Warnke, Alice Whaley (UK), Anita Wynn **PUBLICATIONS ASSISTANTS** Jeremy Dow, Alexander Kief, Ronnel Navas, Brian White **EXECUTIVE ASSISTANT** Jessica Slater **ASI DIRECTOR, OPERATIONS** Janet Clements (UK) **ASI SR. OFFICE ADMINISTRATOR** Jessica Waldoock (UK)

News Editor Tim Appenzeller

NEWS MANAGING EDITOR John Travis **INTERNATIONAL EDITOR** Martin Enserink **DEPUTY NEWS EDITORS** Elizabeth Culotta, Lila Guterman, David Grimm, Eric Hand (Europe), David Malakoff **SR. CORRESPONDENTS** Daniel Clery (UK), Jon Cohen, Jeffrey Mervis, Elizabeth Pennisi **ASSOCIATE EDITORS** Jeffrey Brainerd, Catherine Maticic **NEWS REPORTERS** Adrian Cho, Jennifer Couzin-Frankel, Jocelyn Kaiser, Kelly Servick, Robert F. Service, Erik Stokstad, Paul Voosen, Meredith Wadman **INTERNS** Eva Frederick, Rodrigo Perez Ortega **CONTRIBUTING CORRESPONDENTS** Warren Cornwall, Ann Gibbons, Mara Hvistendahl, Sam Kean, Eli Kintisch, Kai Kupferschmidt (Berlin), Andrew Lawler, Mitch Leslie, Eliot Marshall, Virginia Morell, Dennis Normile (Shanghai), Elisabeth Pain (Careers), Charles Pillar, Michael Price, Tania Rabesandratana (Barcelona), Emily Underwood, Gretchen Vogel (Berlin), Lizzie Wade (Mexico City) **CAREERS** Donisha Adams, Rachel Bernstein (Editor), Katie Langin (Acting Editor) **COPY EDITORS** Julia Cole (Senior Copy Editor), Cyra Master (Copy Chief) **ADMINISTRATIVE SUPPORT** Meagan Weiland

Creative Director Beth Rakouskas

DESIGN MANAGING EDITOR Marcy Atarod **GRAPHICS MANAGING EDITOR** Alberto Cuadra **PHOTOGRAPHY MANAGING EDITOR** William Douthitt **WEB CONTENT STRATEGY MANAGER** Kara Estelle-Powers **DESIGN EDITOR** Chrystal Smith **DESIGNER** Christina Aycock **GRAPHICS EDITOR** Nirja Desai **INTERACTIVE GRAPHICS EDITOR** Xing Liu **SENIOR SCIENTIFIC ILLUSTRATORS** Valerie Altounian, Chris Bickel **SCIENTIFIC ILLUSTRATOR** Alice Kitterman **SENIOR GRAPHICS SPECIALISTS** Holly Bishop, Nathalie Cary **SENIOR PHOTO EDITOR** Emily Petersen **PHOTO EDITOR** Kaitlyn Dolan **WEB DESIGNER** Jennie Pajewski

Chief Executive Officer and Executive Publisher Sudip Parikh

Publisher, Science Family of Journals Bill Moran

DIRECTOR, BUSINESS SYSTEMS AND FINANCIAL ANALYSIS Randy Yi **DIRECTOR, BUSINESS OPERATIONS & ANALYSIS** Eric Knott **DIRECTOR OF ANALYTICS** Enrique Gonzales **MANAGER, BUSINESS OPERATIONS** Jessica Tierney **SENIOR BUSINESS ANALYST** Cory Lipman, Meron Kebede **FINANCIAL ANALYST** Alexander Lee **ADVERTISING SYSTEM ADMINISTRATOR** Tina Burks **SENIOR SALES COORDINATOR** Shirley Young **DIGITAL/PRINT STRATEGY MANAGER** Jason Hillman **QUALITY TECHNICAL MANAGER** Marcus Spiegler **ASSISTANT MANAGER DIGITAL/PRINT** Rebecca Doshi **SENIOR CONTENT SPECIALISTS** Steve Forrester, Jacob Hedrick, Antoinette Hodal, Lori Murphy **PRODUCTION SPECIALIST** Kristin Wovk **DIGITAL PRODUCTION MANAGER** Lisa Stanford **CONTENT SPECIALIST** Kimberley Oster **ADVERTISING PRODUCTION OPERATIONS MANAGER** Deborah Tompkins **DESIGNER, CUSTOM PUBLISHING** Jeremy Hunsinger **SR. TRAFFIC ASSOCIATE** Christine Hall **SPECIAL PROJECTS ASSOCIATE** Sarah Dhere

ASSOCIATE DIRECTOR, BUSINESS DEVELOPMENT Justin Sawyers **GLOBAL MARKETING MANAGER** Allison Pritchard **DIGITAL MARKETING MANAGER** Aimee Apornte **JOURNALS MARKETING MANAGER** Shawana Arnold **MARKETING ASSOCIATES** Tori Velasquez, Mike Romano, Ashley Hylton **DIGITAL MARKETING SPECIALIST** Asleigh Rojanavongse **SENIOR DESIGNER** Kim Hynhn

DIRECTOR AND SENIOR EDITOR, CUSTOM PUBLISHING Sean Sanders **ASSISTANT EDITOR, CUSTOM PUBLISHING** Jackie Oberst

DIRECTOR, PRODUCT & PUBLISHING DEVELOPMENT Chris Reid **DIRECTOR, BUSINESS STRATEGY AND PORTFOLIO MANAGEMENT** Sarah Whalen **ASSOCIATE DIRECTOR, PRODUCT MANAGEMENT** Kris Bishop **PRODUCT DEVELOPMENT MANAGER** Scott Chernoff **PUBLISHING TECHNOLOGY MANAGER** Michael Di Natale **SR. PRODUCT ASSOCIATE** Robert Koepke **SPI ASSOCIATE** Samantha Bruno Fuller

DIRECTOR, INSTITUTIONAL LICENSING Iquo Edim **ASSOCIATE DIRECTOR, RESEARCH & DEVELOPMENT** Elisabeth Leonard **MARKETING MANAGER** Kess Knight **SENIOR INSTITUTIONAL LICENSING MANAGER** Ryan Rexroth **INSTITUTIONAL LICENSING MANAGER** Marco Castellani **MANAGER, AGENT RELATIONS & CUSTOMER SUCCESS** Judy Lillibridge **SENIOR OPERATIONS ANALYST** Lana Guz **FULFILLMENT COORDINATOR** Melody Stringer **SALES COORDINATOR** Josh Haverlock

DIRECTOR, GLOBAL SALES Tracy Holmes **US EAST COAST AND MID WEST SALES** Stephanie O'Connor **US WEST COAST SALES** Lynne Stickrod **US SALES MANAGER, SCIENCE CAREERS** Claudia Paulsen-Young **US SALES REP, SCIENCE CAREERS** Tracy Anderson **ASSOCIATE DIRECTOR, ROW** Roger Gonçalves **SALES REP, ROW** Sarah Lelarge **SALES ADMIN ASSISTANT, ROW** Bryony Cousins **DIRECTOR OF GLOBAL COLLABORATION AND ACADEMIC PUBLISHING RELATIONS**, ASIA Xiaoying Chu **ASSOCIATE DIRECTOR, INTERNATIONAL COLLABORATION** Grace Yao **SALES MANAGER** Danny Zhao **MARKETING MANAGER** Kilo Lan **ASCA CORPORATION, JAPAN** Kaoru Sasaki (Tokyo), Miyuki Tani (Osaka) **COLLABORATION/CUSTOM PUBLICATIONS/JAPAN** Adarsh Sandhu

DIRECTOR, COPYRIGHT, LICENSING AND SPECIAL PROJECTS Emilie David **RIGHTS AND LICENSING COORDINATOR** Jessica Adams **RIGHTS AND PERMISSIONS ASSOCIATE** Elizabeth Sandler **CONTRACTS AND LICENSING ASSOCIATE** Lili Catlett

MAIN HEADQUARTERS
Science/AAAS
1200 New York Ave. NW
Washington, DC 20005

SCIENCE INTERNATIONAL
Clarendon House
Clarendon Road
Cambridge, CB2 8FH, UK

SCIENCE CHINA
Room 1004, Culture Square
No. 59 Zhongguancun St.
Haidian District, Beijing, 100872

SCIENCE JAPAN
ASCA Corporation
Sibaura TY Bldg. 4F, 1-14-5
Shibaura Minato-ku
Tokyo, 108-0073 Japan

EDITORIAL
science_editors@aaas.org

NEWS
science_news@aaas.org

INFORMATION FOR AUTHORS
sciencemag.org/authors/
science-information-authors

REPRINTS AND PERMISSIONS
sciencemag.org/help/
reprints-and-permissions

MEDIA CONTACTS
scipak@aaas.org

MULTIMEDIA CONTACTS
SciencePodcast@aaas.org
ScienceVideo@aaas.org

INSTITUTIONAL SALES AND SITE LICENSES
sciencemag.org/librarian

PRODUCT ADVERTISING & CUSTOM PUBLISHING
advertising.sciencemag.org/
products-services

science_advertising@aaas.org

CLASSIFIED ADVERTISING
advertising.sciencemag.org/
science-careers

advertise@sciencecareers.org

JOB POSTING CUSTOMER SERVICE
employers.sciencereers.org
support@sciencecareers.org

MEMBERSHIP AND INDIVIDUAL SUBSCRIPTIONS
sciencemag.org/subscriptions

MEMBER BENEFITS
aaas.org/membercentral

AAAS BOARD OF DIRECTORS
CHAIR Steven Chu
PRESIDENT Claire M. Fraser
PRESIDENT-ELECT Susan G. Amara
TREASURER Carolyn N. Ainslie
CHIEF EXECUTIVE OFFICER
Sudip Parikh
BOARD Cynthia M. Beall
Rosina M. Bierbaum
Ann Bostrom
Stephen P.A. Fodor
S. James Gates, Jr.
Laura H. Greene
Kaye Husbands Fealing
Maria M. Klawe
Robert B. Millard
Alondra Nelson
William D. Provine

BOARD OF REVIEWING EDITORS (Statistics board members indicated with \$)

Adriano Aguzzi, U. Hospital Zürich
Takuzo Aida, U. of Tokyo
Leslie Aiello, Wenner-Gren Foundation
Deji Akinwande, UT Austin
Judith Allen, U. of Manchester
Marcella Alsan, Harvard U.
Sebastian Amigorena, Institut Curie
James Analytis, UC Berkeley
Trevor Archer, NIEHS, NIH
Paola Ariotta, Harvard U.
Johan Auwerx, EPFL
David Awschalom, U. of Chicago
Clare Baker, U. of Cambridge
Nenad Ban, ETH Zürich
Franz Bauer, Pontificia U. Católica de Chile
Ray H. Baughman, U. of Texas at Dallas
Carlo Beenakker, Leiden U.
Yasmine Belkaid, NIAID, NIH
Philip Benfey, Duke U.
Gabriele Bergers, VIB
Kiros T. Berhane, Columbia U.
Bradley Bernstein, Mass. General Hospital
Joseph J. Berry, NREL
Alessandra Biffi, Harvard Med. School
Peer Bork, EMBL
Chris Bowler, Ecole Normale Supérieure
Ian Boyd, U. of St. Andrews
Emily Brodsky, UC Santa Cruz
Ron Brookmeyer, UCLA (\$) **\$**
Christian Büchel, UKE Hamburg
Dennis Burton, Scripps Res.
Carter Tribley Butts, UC, Irvine
György Buzsáki, New York U. School of Med.
Blanche Capel, Duke U.
Annmarie Carlton, U. of California, Irvine
Nick Chater, U. of Warwick
M. Keith Chen, UCLA
Zhijian Chen, UT Southwestern Med. Ctr.
Ib Chorkendorff, Denmark TU
James J. Collins, MIT
Robert Cook-Deegan, Arizona State U.
Alan Cowman, Walter & Eliza Hall Inst.
Carolyn Coyne, U. of Pittsburgh
Roberta Croce, VU Amsterdam
Ismaila Dabo, Penn State U.
Jeff L. Dangl, U. of North Carolina
Chiara Darao, Caltech
Nicolas Dauphas, U. of Chicago
Christian Davenport, U. of Michigan
Frans de Waal, Emory U.
Claude Desplan, New York U.
Sandra Díaz, U. Nacional de Córdoba
Ulrike Diebold, TU Wien
Hong Ding, Inst. of Physics, CAS
Dennis Discher, U. of Penn.
Jennifer A. Doudna, UC Berkeley
Raissa M. D'Souza, UC Davis
Bruce Dunn, UCLA
William Dunphy, Caltech
Christopher Dye, U. of Oxford
Scott Edwards, Harvard U.
Todd Ehlers, U. of Tübingen
Jennifer Elisseeff, Johns Hopkins U.
Tim Elston, U. of North Carolina
Andrea Encalada, U. San Francisco de Quito
Nader Egheta, U. of Penn.
Karen Ersche, U. of Cambridge
Barry Everitt, U. of Cambridge
Vanessa Ezenwa, U. of Georgia
Michael Feuer, The George Washington U.
Toren Finkel, U. of Pittsburgh Med. Ctr.
Gwenn Flowers, Simon Fraser U.
Peter Fratzl, Max Planck Inst. Potsdam
Elaine Fuchs, Rockefeller U.
Eileen Furlong, EMBL
Jay Gallagher, U. of Wisconsin
Daniel Geschwind, UCLA
Karl-Heinz Glassmeier, TU Braunschweig
Ramon Gonzalez, U. of South Florida
Sandra González-Bailón, U. of Penn
Elizabeth Grove, U. of Chicago
Nicolas Gruber, ETH Zürich
Hua Guo, U. of New Mexico
Kip Guy, U. of Kentucky College of Pharmacy
Taekjip Ha, Johns Hopkins U.
Christian Haass, Ludwig Maximilians U.
Sharon Hammes-Schiffer, Yale U.
Wolf-Dietrich Hardt, ETH Zürich
Louise Harra, U. College London
Jian He, Clemson U.
Carl-Philipp Heisenberg, IST Austria
Ykä Helariutta, U. of Cambridge
Janet G. Hering, Eawag
Hans Hilgenkamp, U. of Twente
Kai-Uwe Hinrichs, U. of Bremen
Deirdre Hollingsworth, U. of Oxford
Lora Hooper, UT Southwestern Med. Ctr.
Fred Hughson, Princeton U.
Randall Hulet, Rice U.
Auke IJsspeert, EPFL
Akiko Iwasaki, Yale U.
Stephen Jackson, USGS and U. of Arizona
Kai Johnsson, EPFL
Peter Jonas, IST Austria
Matt Kaeblerlein, U. of Washington
William Kaelin Jr., Dana-Farber Cancer Inst.
Daniel Kammen, UC Berkeley
V. Narry Kim, Seoul Nat. U.

Robert Kingston, Harvard Med. School
Nancy Knowlton, Smithsonian Institution
Etienne Koechlin, Ecole Normale Supérieure
Alex L. Kolodkin, Johns Hopkins U.
Julija Krupic, U. of Cambridge
Thomas Langer, Max Planck Inst. Cologne
Mitchell A. Lazar, U. of Penn.
Wendell Lim, UC San Francisco
Jianguo Liu, Michigan State U.
Luis Liz-Marzán, CIC bioGUNE
Omar Lizardo, UCLA
Jonathan Losos, Washington U. in St. Louis
Ke Lu, Chinese Acad. of Sciences
Christian Lüscher, U. of Geneva
Jean Lynch-Stieglitz, Georgia Inst. of Tech.
Fabienne Mackay, QIMR Berghofer
Anne Magurran, U. of St. Andrews
Asifa Majid, U. of York
Oscar Marin, King's College London
Charles Marshall, UC Berkeley
Christopher Marx, U. of Idaho
David Masopust, U. of Minnesota
Geraldine Masson, CNRS
C. Robertson McClung, Dartmouth College
Rodrigo Medellín, U. Nacional Autónoma de México
Graham Medley, LSHTM
Jane Memmott, U. of Bristol
C. Jessica Metcalf, Princeton U.
Baohua Mi, UC Berkeley
Edward Miguel, UC Berkeley
Tom Misteli, NCI, NIH
Yasushi Miyashita, U. of Tokyo
Alison Motsinger-Reif, NIEHS, NIH (\$) **\$**
Danielle Navarro, U. of New South Wales
Daniel Nettle, Newcastle U.
Daniel Neumark, UC Berkeley
Beatriz Noheida, U. of Groningen
Helga Nowotny, Vienna Sci., Res. & Tech. Fund
Rachel O'Reilly, U. of Birmingham
Harry Orr, U. of Minnesota
Pilar Ossorio, U. of Wisconsin
Andrew Oswald, U. of Warwick
Isabella Pagano, Istituto Nazionale di Astrofisica
Margaret Palmer, U. of Maryland
Elizabeth Levy Paluck, Princeton U.
Jane Parker, Max Planck Inst. Cologne
Giovanni Parmigiani, Dana-Farber Cancer Inst. (\$) **\$**
Daniel Pauly, U. of British Columbia
Samuel Pfaff, Salk Inst. for Biological Studies
Julie Pfeiffer, UT Southwestern Med. Ctr.
Philip Phillips, UIUC
Matthieu Piel, Institut Curie
Kathrin Plath, UCLA
Martin Plenio, Ulm U.
Katherine Pollard, UC San Francisco
Elvira Poloczanska, Alfred Wegener Inst.
Julia Pongratz, Ludwig Maximilians U.
Bruce Poulin, CNRS
Jonathan Pritchard, Stanford U.
Félix A. Rey, Institut Pasteur
Trevor Robbins, U. of Cambridge
Roger Rojelli, Imperial College London
Amy Rosenzweig, Northwestern U.
Mike Ryan, UT Austin
Shimon Sakaguchi, Osaka U.
Miquel Salmeron, Lawrence Berkeley Nat. Lab
Nitin Samarth, Penn State U.
Jürgen Sandkühler, Med. U. of Vienna
Erica Ollmann Saphire, La Jolla Inst.
Alexander Schier, Harvard U.
Wolfram Schlenker, Columbia U.
Susannah Scott, UC Santa Barbara
Rebecca Sear, LSHTM
Anuj Shah, U. of Chicago
Vladimir Shalaeff, Purdue U.
Jie Shan, Cornell U.
Beth Shapiro, UC Santa Cruz
Jay Shendure, U. of Washington
Steve Sherwood, U. of New South Wales
Brian Shoichet, UC San Francisco
Robert Siliciano, Johns Hopkins U. School of Med.
Lucia Silvotti, U. College London
Alison Smith, John Innes Centre
Richard Smith, U. of North Carolina (\$) **\$**
Mark Smyth, QIMR Berghofer
Pam Solitis, U. of Florida
John Speakman, U. of Aberdeen
Tara Spies-Jones, U. of Edinburgh
Allan C. Spradling, Carnegie Institution for Sci.
V. S. Subrahmanian, Dartmouth College
Ira Tabas, Columbia U.
Sarah Teichmann, Wellcome Sanger Inst.
Rocio Titunik, Princeton U.
Shubha Tole, Tata Inst. of Fundamental Res.
Wim van der Putten, Netherlands Inst. of Ecology
Reinhold Veuglers, KU Leuven
Bert Vogelstein, Johns Hopkins U.
Kathleen Voets, U. of Minnesota
David Wallach, Weizmann Inst. of Sci.
Jane-Ling Wang, UC Davis (\$) **\$**
Jessica Ware, Amer. Mus. of Natural Hist.
David Waxman, Fudan U.
Jonathan Weissman, UC San Francisco
Chris Wikle, U. of Missouri (\$) **\$**
Terrie Williams, UC Santa Cruz
Ian A. Wilson, Scripps Res. (\$) **\$**
Yu Xie, Princeton U.
Jan Zaenen, Leiden U.

Science serves as a forum for discussion of important issues related to the advancement of science by publishing material on which a consensus has been reached as well as including the presentation of minority or conflicting points of view. Accordingly, all articles published in Science—including editorials, news and comment, and book reviews—are signed and reflect the individual views of the authors and not official points of view adopted by AAAS or the institutions with which the authors are affiliated.

Dark skies and bright satellites

Most ground-based observatories require a dark night sky to uncover answers to some of the most fundamental questions about the nature of our Universe. However, a number of companies and governments are in various stages of planning or deploying bright satellites in low-Earth orbit (or LEOsats) in greater numbers than ever before. These “megaconstellations” will fundamentally change astronomical observing at visible wavelengths. Nighttime images will be contaminated by streaks caused by the passage of Sun-illuminated satellites. If proposals calling for 100,000 or more LEOsats are realized, no combination of mitigations will be able to fully avoid the negative impact on astronomy.

This threat comes at a time when new technology offers unprecedented scientific opportunities, all requiring access to dark skies. One example is the Vera C. Rubin Observatory, which is nearing completion. Its Legacy Survey of Space and Time (LSST) will soon offer a dramatic new view of the changing sky. Rubin Observatory will employ the 8.4-m Simonyi Survey Telescope and the 3200-megapixel LSST Camera to capture about 1000 images of the sky, every night, for 10 years. A single 30-s exposure will reveal distant objects that are about 40 million times fainter than those visible with the unaided eye. The observatory’s combination of a large light-collecting area and field of view is unparalleled in the history of astronomy, which is why the project was the top ground-based priority for U.S. astronomers in the 2010 National Academies Decadal Survey of Astronomy and Astrophysics. LSST six-color images will contain data for about 20 billion ultrafaint galaxies and a similar number of stars, and will be used for investigations ranging from cosmological studies of the Universe to searches for potentially hazardous Earth-impacting asteroids. However, the discoveries anticipated from Rubin and other observatories could be substantially degraded by the deployment of multiple LEOsat constellations.

The most exciting science to come out of current and planned astronomical facilities may be the discovery of types of objects and phenomena not yet observed or predicted. Such profound surprises have the potential to revolutionize our understanding of every field from exobiology to cosmology. Rubin Observatory’s LSST, for example, opens the prospect of observing how ultra-

faint objects change over time. It is precisely this kind of astronomy that is most at risk from image artifacts arising from LEOsat megaconstellations. These satellites scatter sunlight for several hours after sunset or before sunrise, are relatively close and bright, and thus can affect ground-based telescopes observing at visible wavelengths. Constellations in orbits well above 600 km will be illuminated by the Sun all night long.

Astronomers worldwide are seeking ways to diminish the satellites’ most damaging effects—the focus of a recent virtual workshop* sponsored by the U.S. National Science Foundation—and are collaborating with SpaceX (in particular, the Rubin Observatory), the first operator to launch a substantial constellation of LEOsats. SpaceX has shown that satellite operators can reduce reflected sunlight through satellite orientation, Sun shielding, and surface darkening. A joint effort to obtain higher-accuracy public data on the predicted location of individual satellites could help astronomers point their instruments to avoid some of the interference.

Although all of these measures are helpful, there are no guarantees, and the research community is left to hope for good corporate citizenship. Future constellations owned and operated by foreign governments pose a different sort of challenge. Although there are international regulations covering radio-frequency

interference, there are no such regulations in place for visible-frequency light pollution from space.

Earth orbit is a natural resource without environmental protections, and we are now witnessing its industrialization. Currently there are about a thousand bright LEOsats, but that may be just the beginning. Proposals to expand telecommunications and data relay to serve new technologies like self-driving cars could lead to a 100-fold increase in the number of LEOsats in the next decade. The American Astronomical Society is working with astronomy stakeholders, commercial satellite operators, and international organizations to begin to forge policy on light pollution from space. It is unclear how long this will take and how effective it can be. What is clear is that without productive industry-observatory collaboration, voluntary operator compliance with best practices for mitigation, and subsequent regulatory action, we are slated to lose a clear view of the Universe and its secrets.

—Anthony Tyson and Joel Parriott

Anthony Tyson

is the Rubin Observatory chief scientist and a professor of Physics and Astronomy at the University of California, Davis, CA, USA. tyson@physics.ucdavis.edu

Joel Parriott

is the deputy executive officer and director of Public Policy at the American Astronomical Society, Washington, DC, USA. joel.parriott@aaas.org

“...we are slated to lose a clear view of the Universe and its secrets.”

*C. Walker *et al.*, *Bull. AAS* **52** (2020); <https://doi.org/10.3847/25c2feb.346793b8>.



LSAMP-NICE international research experiences transform underrepresented STEM students into global scientists and citizens

Like many undergraduates pursuing a science, technology, engineering, and mathematics (STEM) degree, Maggie Fox couldn't quite figure out how to add an international studies course to her packed schedule of classes, labs, and independent research. So when she received an email while on winter break asking if she'd like to do research in France, she quickly and furtively tapped out her reply on her phone during her sister's holiday dance recital.

"Do I need to know how to speak French?" she asked. "No!" came the quick reply.

"Then sign me up!" she typed back, ignoring her mother's raised eyebrows. The email came from Shanise Kent, the director of the Louis Stokes Alliances for Minority Participation (LSAMP) program at Binghamton University, part of the State University of New York (SUNY) LSAMP alliance. Fox had joined the Binghamton LSAMP group to connect with other students of color like herself who were STEM majors.

Fox spent that next summer doing materials science research on conductive polymers at the University of Grenoble in France. "At that point, I was unsure about my future decisions—do I apply for graduate school, go for a research job, or teach high school?" recalls Fox. "It was a once-in-a-lifetime chance to explore another area of research in another country."

It was also a true exchange of scientific knowledge and culture—Fox shared how to do a vapor polymerization method with the Grenoble group, and they taught her how to grow silicon nanotree structures. She learned new

research techniques and had the freedom to plan her own experiments.

"The experience sold me on applying to graduate school, because they treated me like a graduate student there," says Fox, now in her third year as a Ph.D. student at University of California, Los Angeles, studying sustainable materials and energy storage systems.

The Louis Stokes Regional NSF International Center of Excellence (LSAMP-NICE) serves to facilitate those connections and promote opportunities, just as the fortuitous email to Fox's phone did, so that both undergraduate and graduate students who are historically underrepresented in STEM careers may participate in significant international research collaborations. LSAMP-NICE blends the best practices and networks built by nearly 30 years of LSAMP alliance institutions with the financial and logistical support of U.S. National Science Foundation (NSF) programs and collaborating institutions around the globe (see box). LSAMP-NICE also provides competitive faculty awards to U.S.-based research advisors so they can collaborate and build partnerships with laboratories overseas; connects students to the practical support they need to secure travel visas and housing; and promotes the involvement of students underrepresented in STEM in international collaborative research—an integral part of the LSAMP-NICE mission.

Students who traveled to France, Saudi Arabia, and Costa Rica have shared about how their experiences abroad encouraged them to continue careers in research, boosted their confidence, and helped them grow into

global citizens whose research will make significant impacts on the world.

"In this age of globalization, it is imperative that underrepresented minority students be given the opportunity to do international research," says Martha Mondoa-Tchounwou, LSAMP-NICE co-principal investigator and director of the Scholars Academy and Student Support Services at Jackson State University in Mississippi. "LSAMP-NICE provides a bridge between international research institutions and minority-serving institutions to make it easier for students to study abroad, receive meaningful international experiences, and gain vital knowledge and cultural skills that will make them global citizens."

Emmanuel Gras, a researcher and organic chemist at CNRS (French National Center for Scientific Research) and coordinator for the U.S/France/Belgium International Research Experiences for Undergraduates (iREU) Site in Translational Chemistry, says that every scientist learns from meeting people from other countries and cultures and that these exchanges are beneficial for both the students and their host laboratories. "We get students with different training and backgrounds who strengthen their abilities in a different environment, and the U.S. students are always so enthusiastic that they bring an exquisite energy to our research teams."

Making research careers a reality

Like Fox, Anthony Keyes had the opportunity to do a 3-month summer research internship in France at the University of Bordeaux and then returned to complete a Master's degree within the same French laboratory. Keyes was a prime candidate because he had already done research as an undergraduate at Jackson State University in organic nanoparticles. LSAMP-NICE matched Keyes to an organic polymer chemistry group in Bordeaux that was developing iron oxide nanoparticles for targeted delivery of anticancer drugs.

"From a research perspective, that summer was the first time I felt like a scientist," says Keyes, now in a Ph.D. program at the University of Houston, Texas. "I had a clear goal on where the project was headed and I was given a large amount of independence, and we published the work in a peer-reviewed journal."

After finishing her first summer of research as an environmental science student at United Tribes Technical College in Bismarck, North Dakota, Kimberlee Blevins had the chance to do 2 weeks of research in Costa Rica through the All Nations LSAMP. Wrapping up collecting

"The experience sold me on applying to graduate school, because they treated me like a graduate student there."

– Maggie Fox



and analyzing data on how bee body size was related to foraging distances, she was primed to do more research. "I was hooked on the research bug, and doing international research was the next challenge I wanted to take on," says Blevins.

Blevins joined a project to analyze camera-trap photos of an invasive ginger plant to see which birds and mammals were pollinating the plants. The trip to Costa Rica reinforced her desire to help solve global problems through her tribal ties to the Mandan, Hidatsa, and Arikara Nation reservation lands. She is pursuing a Master's degree in environmental science at Sitting Bull College in Fort Yates, North Dakota, to investigate the health and environmental impacts of oil and gas extraction.

Through another LSAMP-NICE-facilitated trip in January, Casandra Salinas competed in the Ninth Annual Undergraduate Poster Competition at King Abdullah University of Science and Technology (KAUST) in Thuwal, Saudi Arabia. The week spent presenting her research, networking with other student researchers from around the world, and learning about KAUST and Saudi Arabia, convinced Salinas that she should apply to microbiology Ph.D. programs abroad as well as in the United States for the next phase of her research career.

"I love traveling and I was pretty stoked about the chance to present my research," says Salinas.

Louis Stokes Alliances for Minority Participation (LSAMP)

Across the United States, the 57 Louis Stokes Alliances for Minority Participation (LSAMP) provide professional development and academic and financial support for both undergraduate and graduate students from historically underrepresented minority groups in science, technology, engineering, and mathematics (STEM) disciplines. Created in 2018, the Louis Stokes Regional NSF International Center of Excellence (LSAMP-NICE) is specifically charged with broadening underrepresented student participation in international collaborative research. LSAMP-NICE is a collaboration of four institutions: Salish Kootenai College, a tribal college in Pablo, Montana (Steve Dupuis, LSAMP-NICE PI); Jackson State University, a historically black university in Jackson, Mississippi (Glake Hill and Martha Mondoa-Tchounwou, co-PIs); Louisiana State University, an R1, or research-intensive, institution in Baton Rouge, Louisiana (Zakiya Wilson-Kennedy, co-PI); and the University of Illinois at Chicago, an R1 and Hispanic-serving institution (Denise Yates, co-PI). All LSAMP projects are funded through the NSF Broadening Participation initiative.

Punching holes in imposter syndrome

But Salinas' confidence hasn't always run so high. She credits her mentors in the Oklahoma LSAMP alliance with helping build her up to a place where presenting her research to an international audience seemed normal.

As someone who was born in the United States, but raised in rural Mexico, Salinas keenly felt like she didn't fit in as a student researcher. "It felt like I should be working in the agricultural fields or in fast food. I didn't see people like me in research," she says. But OK-LSAMP directors Brenda Morales and Jason Kirksey, who is also vice president for institutional diversity at Oklahoma State University, flipped her perspective. "They made me see the significance of my contributions to research."

For Salinas, getting to Saudi Arabia on her own would have been out of the question, but the experience helped

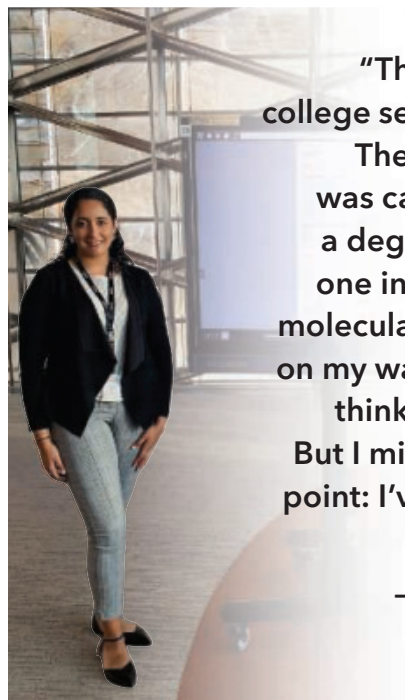
her overcome her doubts and her imposter syndrome. "The idea of going to college seemed not doable. Then I didn't believe I was capable of finishing a degree, especially not one in biochemistry and molecular biology," she says. "Even on my way to KAUST, I was thinking, 'I'm so lucky!'" But I missed an important point: I've actually worked for this."

High cultural exchange rates

Of course, cultural exchanges happen beyond laboratory walls too. Fox and Keyes both traveled extensively through Europe and developed friendships with other student researchers that carried forward into graduate school.

The students from the All Nations LSAMP alliance who traveled with Blevins to Costa Rica had a chance to visit with the indigenous Boruca community to learn about their history, see their dyed-fabric arts, and share a meal. The visit left a deep impression on Blevins. "Sometimes the issue of tribal lands rights feels victimizing, as if you are the only tribe fighting these issues," she says. "It was mind-blowing to hear about another tribe's land-rights struggles in a different country."

Salinas came away with unforgettable memories: "You don't really understand other cultures until you immerse yourself in them and are fully surrounded by the environment," she says. Salinas shared a late-night Arabian coffee chat with two Saudi Arabian students exploring the region's views on women, culture, and religion.



"The idea of going to college seemed not doable. Then I didn't believe I was capable of finishing a degree, especially not one in biochemistry and molecular biology . . . even on my way to KAUST, I was thinking, 'I'm so lucky!' But I missed an important point: I've actually worked for this."

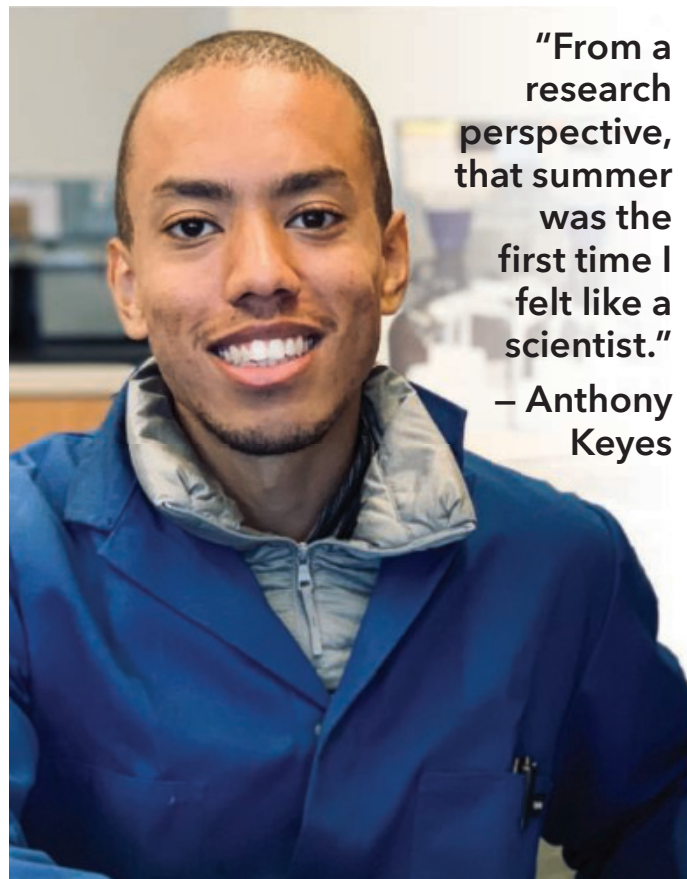
– Casandra Salinas

Lucy Okumu, director of KAUST's international office, says part of the mission of the university is to foster exchanges between scientists around the globe. "We recognize that financial constraints are a big barrier for top students going forward in research careers," she says. The poster competition, she says, builds awareness among those students that there is an opportunity to study at a world-class institute like KAUST and receive full financial support.

These students came away from their travels with a sharper sense that solving global research challenges, such as climate change or the need for pandemic vaccines, requires them to participate as both global scientists and citizens. "The LSAMP students are just like sponges," says Gras. "They are very open-minded and get everything they can from their stay abroad."

Global currency for changing minds

Going into his fourth year of doctoral studies, Keyes already has three first-author publications to his credit. He has been developing new polymerization platforms to synthesize novel block copolymers that could help in recycling and reusing mixed plastics for new materials. But in addition to newfound confidence, while in France,



**"From a research perspective, that summer was the first time I felt like a scientist."
— Anthony Keyes**

Keyes also found his voice as an advocate for minority scientists.

As a Black man, Keyes often found himself answering questions about diversity initiatives such as LSAMP-NICE. He explained the importance of promoting minority participation in research by pointing to the larger French lab group, which was run by five men and one woman, all white. "If you can't see yourself in the professors you work for doing research, then that is a huge problem," says Keyes. "It's disheartening for minorities like me to navigate science when our voices are not being heard, and leaders in the field do not mirror the diverse range of us who aspire to be scientists."

Having these conversations is uncomfortable, he says, but they need to happen: "I was very outspoken—it was one of the key skills I polished in France. It's not just minorities, however, who should learn to initiate these tough conversations." Everyone, he says, needs to discuss issues of systemic racism in academic science.

Similarly, Blevins explains that students attending tribal colleges in the United States often don't see themselves as world-traveling researchers. "Our extended families are very close-knit," she says, adding that students rarely leave home for university studies, much less the country.

But her participation in LSAMP programs broadened Blevins' horizons on the impact researchers can make globally and in their own communities. "We are so focused with my own tribe's concerns, but seeing the problems that farmers face with pollinators or those that another country has with an invasive species brings it full circle for me as a researcher," she says. She recognizes the challenges of having the Bakken oil field and extraction infrastructure in the Fort Berthold Reservation's backyard, and she knows that the environmental and health impacts of oil and gas extraction must be addressed—not only for the Mandan, Hidatsa, and Arikara Nation, but also globally.

"Every country has a global issue that needs solving," says Blevins. "Tribal and other underrepresented STEM students bring a different perspective, and that's required when doing research—you want to look at a problem from as many angles as possible."

Sponsored by

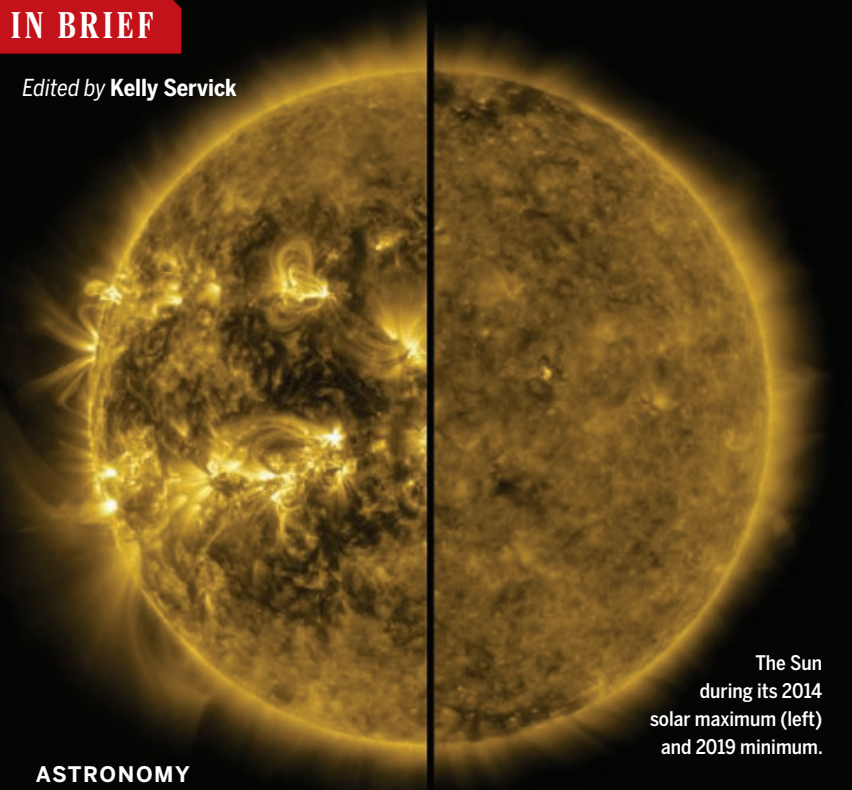


“We will be forever thankful for the 12 crews ... risking their lives defending our scientific treasure.”

Sam Hale, chairman of the Mount Wilson Institute Board of Trustees, in a statement after the Mount Wilson Observatory was declared safe from California's Bobcat fire.

IN BRIEF

Edited by Kelly Servick



The Sun during its 2014 solar maximum (left) and 2019 minimum.

ASTRONOMY

A new solar cycle dawns

The Sun's waxing and waning activity, manifested in sunspot numbers and blasts of radiation and particles, has officially entered the next of its roughly 11-year cycles, NASA and the National Oceanic and Atmospheric Administration (NOAA) announced last week. Solar activity passed a minimum in December 2019, meaning Solar Cycle 25 has been underway for nearly 1 year. Observatories on the ground and in space study the Sun's outpourings meticulously, to both understand its workings and give warnings if one of those blasts is heading our way. A direct hit could disrupt power grids and communications, knock out satellites, and threaten astronauts, especially on the Moon, outside Earth's protective magnetic field, where astronauts may venture as early as 2024. Preparations have begun for the projected maximum activity in 2025: NASA will study solar radiation levels at the Moon with its Gateway lunar orbiting station, while NOAA plans to place its Space Weather Follow-On satellite upstream from Earth to give early warning of incoming blasts.

Sea ice hits near-record low

POLAR SCIENCE | Arctic sea ice dropped below 4 million square kilometers for only the second time in modern history, reaching its seasonal bottom at 3.74 million square kilometers on 15 September, the National Snow and Ice Data Center announced this week. Because of a warming climate, the minimum ice cover has shrunk over the past few decades by an area equal to the size of Alaska, Texas, and Montana—combined. Although the ice extent in 2012 was even lower than this year, scientists have shown the melt is now being driven not only by the warmer atmosphere, but also by the upward advance of a deep layer of warm Atlantic water, previously held beneath the cold surface layer (*Science*, 28 August, p. 1043).

CDC backtracks on testing

POLICY | The U.S. Centers for Disease Control and Prevention (CDC) last week reversed highly criticized guidance suggesting people who were exposed to someone with COVID-19 don't need a test if they don't have symptoms. Public health experts denounced the 24 August guidance as the result of political interference, noting that those who don't feel sick can still spread the virus. The new language, published on 18 September, says anyone who has had close contact with an infected person should get tested. The update came 2 days after the departure of two political appointees from CDC's parent agency, the Department of Health and Human Services (HHS)—top spokesperson Michael Caputo and science adviser Paul Alexander. Both tried to silence CDC officials who spoke out about the seriousness of the pandemic, according to emails uncovered by *The New York Times*. HHS announced this week that Alexander had been permanently let go and Caputo would take a 60-day medical leave.

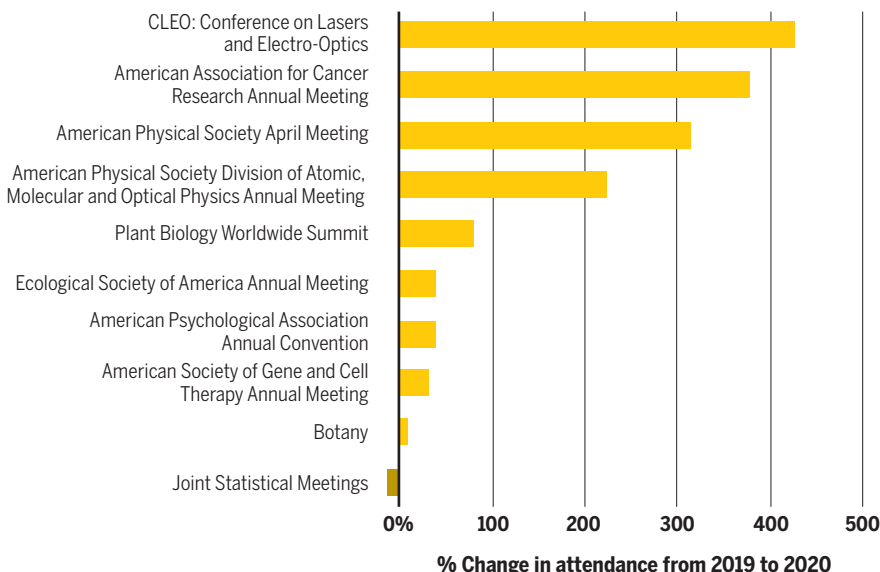
U.S. vaccine distrust grows

COVID-19 | Public confidence in a coronavirus vaccine has plunged in the United States over the past 4 months amid

SCIENTIFIC MEETINGS

Digital gatherings draw crowds

As the COVID-19 pandemic forced many summer conferences to adopt virtual formats, the option to attend from home—often with discounted or free registration—led to surges in participation. A survey by *Science* of 10 U.S.-based meetings of scientific societies across a variety of disciplines showed that most saw higher attendance than in previous years. Many also saw increased international participation, the survey revealed.



concerns that testing is being rushed. In an early September poll of 10,000 people, released last week by the Pew Research Center, just 51% said they are certain or likely to take a COVID-19 vaccine once it's available. In a Pew poll in early May, 72% had given similar answers. Three-quarters of all respondents said it was very or somewhat likely that a vaccine would be released before its effectiveness and safety were fully understood. Both Republicans (69%) and Democrats (82%) were more worried vaccine approval would move too quickly than too slowly. President Donald Trump has said a vaccine could be released to the general public in October—just before the November presidential election and far sooner than predicted by several of his top scientific advisers.

Ig Nobels honor odd science

PRIZES | The Ig Nobel Prize ceremony, an annual celebration of quirky and comical discoveries, carried on despite the pandemic in an online event. The *Annals of Improbable Research*, the science humor magazine that hosts the event, selected bugs as this year's theme, though the 10 winning teams hailed from diverse fields. The entomology

prize went to an investigation of why so many researchers in the field are themselves afraid of spiders. (Despised traits included their fast, unpredictable movements and their many legs.) Winners of the acoustics prize studied the mechanisms of alligator vocalization by sticking the reptiles in helium-filled chambers to raise the pitch of their bellows. Nobel laureates presented the awards and joined professional singers in the debut performance of a miniopera called *Dream, Little Cockroach*.

IBM shares quantum road map

QUANTUM COMPUTING | For 20 years scientists have said they'll someday build a full-fledged quantum computer able to perform useful calculations that would overwhelm any conventional supercomputer. Last week, IBM made its aspirations more concrete by announcing a "road map" for the development of its quantum computers, including the goal of building by 2023 one containing 1000 quantum bits, or qubits. That machine would be big enough to spot and correct the myriad errors that normally plague qubits. IBM's current largest quantum computer, revealed this month, contains 65 qubits. IBM also plans to build

BY THE NUMBERS

3245

Confirmed cases of brucellosis in Lanzhou, China, following a 2019 leak of bacteria in gas from a pharmaceutical factory.

177.4

August water level in meters of lakes Michigan and Huron, beating record highs set in 1986 for the eighth straight month.

5.6 million

Estimated weight in tons of synthetic microfiber pollution traced to clothes washing since 1950. (*PLOS ONE*)

a 1-million-qubit quantum computer at some unspecified date. Google has its own plan to build a 1-million-qubit quantum computer within 10 years but has not published a timeline.

The Lancet tweaks review process

PUBLISHING | Three months after retracting a high-profile COVID-19 paper, editors at *The Lancet* last week announced policy changes meant to keep flawed studies using large medical data sets from slipping past peer review again. The now-retracted study found serious risks to the antimalarial drug hydroxychloroquine using hospital patient data from the small Chicago-based company Surgisphere. Observers questioned the study's large sample size and details about patient demographics and dosing, and *The Lancet* retracted the paper when Surgisphere declined to make underlying data available (*Science*, 12 June, p. 1167). The new policies include stricter standards for the data science expertise of peer reviewers. Authors must now certify that more than one of them has accessed and verified their study's underlying data, and must detail what data they will share, the criteria for access, and how data will be made available.



A new study may help explain why men, like this patient in an Italian intensive care unit, are more likely than women to develop life-threatening COVID-19.

COVID-19

Flawed interferon response spurs severe illness

Antibodies or mutations that cripple key antiviral protein underlie 14% of severe cases

By **Meredith Wadman**

From the first months of the COVID-19 pandemic, scientists baffled by the disease's ferocity have wondered whether the body's vanguard virus fighter, a molecular messenger called type I interferon, is missing in action in some severe cases. Two papers published online in *Science* this week confirm that suspicion. They reveal that in a significant minority of patients with serious COVID-19, the interferon response has been crippled by genetic flaws or by rogue antibodies that attack interferon itself.

"Together these two papers explain nearly 14% of severe COVID-19 cases. That is quite amazing," says Qiang Pan-Hammarström, an immunologist at the Karolinska Institute.

Tadatsugu Taniguchi, a pioneering interferon scientist and emeritus professor at the University of Tokyo, calls the discoveries "remarkable." He says they highlight the "critical" role of type I interferons in

SARS-CoV-2 infection and the development of potentially lethal COVID-19.

Co-author Isabelle Meyts, a pediatric immunologist at the University Hospitals Leuven, was struck by one paper's finding that rogue antibodies underlie COVID-19 in 10% of gravely ill patients: "There has never been any infectious disease explained at this level by a factor in the human body. And it's not an isolated cohort of Europeans. Patients are from all over the world, all ethnicities." Another finding, that 94% of the patients with interferon-attacking antibodies were male, also helps explain why men face higher risk of severe disease.

The paired studies have immediate practical implications. Synthetic interferons, long used to treat other diseases, might help some at-risk patients, as might other therapies aimed at removing the damaging antibodies. A common kind of antibody test could be readily developed and return answers in hours. Those found to be

at high risk of developing severe COVID-19 could take precautions to avoid exposure or be prioritized for vaccination, says Elina Zuniga, an immunologist who studies interferons at the University of California, San Diego.

The findings also raise a red flag for plasma donations from recovered patients.

Because it may be rich in antibodies to the virus, "convalescent plasma" is already given to some patients to fight the infection. But some donations could harbor the interferon-neutralizing antibodies. "You should eliminate these patients from the pool of donors," Zuniga says. "You definitely don't want to be transferring these auto-

antibodies into another person." Type I interferons are made by every cell in the body and are vital leaders of the antiviral battle early in infection. They launch an immediate, intense local response when a virus invades a cell, triggering infected cells to produce proteins that attack the

Science's
COVID-19
reporting is
supported by the
Pulitzer Center
and the
Heising-Simons
Foundation.

virus. They also summon immune cells to the site and alert uninfected neighboring cells to prepare their own defenses.

In one study, Jean-Laurent Casanova, an infectious disease geneticist at Rockefeller University, and his team examined blood samples from 987 gravely ill patients from around the world. In 10.2% of the patients, the researchers identified antibodies that attacked and neutralized the patients' own type I interferon. A subgroup of affected patients had extremely low or undetectable blood levels of this interferon. Lab studies confirmed the antibodies knocked the interferon out of action and cells exposed to the patients' plasma failed to fend off invasion by the new coronavirus.

None of the 663 people in a control group with mild or asymptomatic SARS-CoV-2 infection had those damaging antibodies. The antibodies were also scarce in the general population, showing up in only 0.33% of more than 1200 healthy people tested. "What this means is that at least 10% of critical COVID-19 is an autoimmune attack against the immune system itself," Casanova says.

The preponderance of male patients was a surprise, because women have higher rates of autoimmune disease. "Our favorite hypothesis is that it is an X-linked recessive trait," Casanova says. "Women with two X chromosomes are protected and men, with one, are not." Supporting that suspicion, one woman with a rare condition that silences one X chromosome was among the severely ill patients with autoantibodies.

If these striking results hold up, they might also help explain the increased vulnerability of older people to severe COVID-19: Half the gravely ill patients with autoantibodies were older than 65.

The second paper found genetic flaws in patients that led to the same end result: a grossly inadequate interferon response to SARS-CoV-2 infection. The team sequenced DNA from 659 critically ill COVID-19 patients and from 534 controls with mild or asymptomatic disease. They examined 13 genes, chosen because flaws in them impair the body's production or use of type I interferon; mutations in the genes underlie life-threatening influenza or other viral illnesses. The researchers found that 3.5% of the critically ill patients harbored rare mutations in eight of those genes. In patients for whom blood samples were available, interferon levels were vanishingly small. No members of the control group carried any of the mutations. "This is the first paper to pin down indisputably

disease-causing mutations underlying severe COVID-19," Pan-Hammarström says.

But it's "probably the tip of the iceberg," says Paul Hertzog, an interferon expert at the Hudson Institute of Medical Research. Many other damaging mutations, interferon related and not, may influence the development of severe COVID-19, he says.

Zuniga notes that none of the patients who made antibodies against interferon or had the mutations had a history of life-threatening viral illnesses requiring hospitalization. "This suggests that we are more reliant on type I interferons to protect ourselves against SARS-CoV-2 versus other viral infections," she says. "That makes it important to try therapies aimed at boosting type I interferon responses."

Dozens of randomized clinical trials are now deploying interferons against SARS-CoV-2 (*Science*, 10 July, p. 125). One, led by Tom Wilkinson at the University of Southampton, reported promising findings in a small group of hospitalized COVID-19 patients. But synthetic interferons won't help patients who harbor mutations that prevent interferons from working, or those with antibodies that attack them.

Some researchers caution that the interferon-neutralizing antibodies could be a cause, rather than a consequence, of severe COVID-19. "It's possible that they develop during the disease," says Miriam Merad, an immunologist at the Icahn School of Medicine at Mount Sinai. That would explain why

the patients hadn't faced life-threatening viral infections before, she says.

But Casanova, who has made a career of discovering mutations that confer susceptibility to infectious diseases, says there is a strong case for causality. He points out that preexisting blood samples from a handful of patients showed they had the antibodies in their blood before contracting SARS-CoV-2. He argues that, in response to infection, it's unlikely that the body could quickly generate the high levels of anti-interferon antibodies his team saw.

Yanick Crow, a clinical geneticist at the University of Edinburgh who studies interferon signaling, calls the antibody paper "shocking," in part because men were so much more likely than women to carry the rogue antibodies. Tests screening for the antibodies can and should be rapidly developed, he says, and will quickly reveal whether the new findings hold up. Given tens of millions of cases worldwide, he says, "10% is such a high figure and the implications are very important." ■

**"At least 10%
of critical
COVID-19 is an
autoimmune
attack."**

Jean-Laurent Casanova,
Rockefeller University

VOICES OF THE PANDEMIC

Fighting to be counted

The pandemic has fueled Abigail Echo-Hawk's quest for health data on Indigenous people in the United States

By **Lizzie Wade**

Abigail Echo-Hawk can't even count how many times she's been called a troublemaker. It's happened at conferences, workshops, and even after she testified before Congress—all places where she has advocated for the full and ethical inclusion of American Indians and Alaska Natives in public health data. "I didn't used to know what to say," she says. "Now, my answer is, 'Is calling for justice making trouble?'"

As the director of the Urban Indian Health Institute (UIHI) and the chief research officer for the Seattle Indian Health Board, Echo-Hawk has been working for years with Indigenous people, mostly in cities, across the United States to collect data about their communities. She has also advised the Centers for Disease Control and Prevention (CDC), the National Institutes of Health, and many universities on best practices for analyzing data about American Indian and Alaska Native communities. Now, the COVID-19 pandemic has given Echo-Hawk's work even more urgency.

The virus has taken a disproportionate toll on many Indigenous communities in the United States. But its full impact is unclear because of problems Echo-Hawk has long fought to correct, including racial misclassification and the exclusion of Indigenous communities from data sets and analyses used to make health policy decisions.

"Abigail has highlighted the inadequacy of, the restricted access to, and the delays in receiving data" about how COVID-19 is affecting Indigenous people in the United States, says Spero Manson, director of the Centers for American Indian and Alaska Native Health at the Colorado School of Public Health, who is Pembina Chippewa. "But it all builds on her prior work."

Echo-Hawk, who is a citizen of the Pawnee Nation of Oklahoma, grew up in rural Alaska. She credits her interest in public health to the values she saw modeled by the leaders and members of her tribal com-

munities. “They think about the health and well-being of an entire community in a very holistic way,” Echo-Hawk says.

She had a different experience after moving to Seattle for college and seeking prenatal care for her first pregnancy at a local hospital. When a medical assistant found out that Echo-Hawk was Indigenous, she began to aggressively question her about drinking and drug use. (Echo-Hawk was doing neither.) “That was very traumatic for me ... I was treated in a way that a lot of people of color are, and that is with disdain, discrimination, and outright racism. And it inhibited my care,” she says.

She didn’t see a doctor again until her second trimester, when she went to the Seattle Indian Health Board. There she was welcomed, trusted, and treated with respect. That experience set Echo-Hawk on a path that eventually led to studying health policy at the University of Washington, Bothell, and working at the research program Partnerships for Native Health, now at Washington State University. She became director of UIHI in 2016.

“The system of colonialism in the United States has created, and continues to increase risk factors for, poor health outcomes in Native communities,” Echo-Hawk says. The U.S. government removed many Indigenous communities from their lands and confined them to reservations. Many didn’t have access to medical care and were cut off from their traditional diets and lifestyles, including spiritual practices that were tied to their homelands. Today, American Indians and Alaska Natives have higher rates of obesity, diabetes, asthma, and heart disease than white Americans, as well as higher rates of suicide. The system of oppression in the United States, Echo-Hawk says, “has built a perfect environment to kill us in a pandemic.”

But data showing the pandemic’s full impact on Indigenous communities across the country have not been collected, and accessing the information that does exist can be an uphill battle. Citing privacy concerns, for example, CDC initially denied tribal epidemiology centers, including UIHI, access to data about testing and confirmed COVID-19 cases, even though it was making those data available to states. What’s more, data collected by tribes, local and state health departments, and national agencies are often wildly inconsistent, says Desi Rodriguez-Lonebear, a social demographer at the University of California,

Los Angeles, and a citizen of the Northern Cheyenne Nation. “I cannot tell you with any sort of certainty the number of positive cases of COVID-19 on my reservation right now,” she says. “It’s shocking.”

It also reflects an old pattern, Rodriguez-Lonebear says. “For so long, data has been used against our people.” For example, the U.S. census, which began in 1790, excluded all American Indians until 1860, and didn’t count those living on reservations until 1900. The census data were then used to justify the invasion and settlement of supposedly empty land, Rodriguez-Lonebear says.

Today, American Indians and Alaska Natives make up about 2% of the U.S. popula-

classified as “other.” When UIHI did its own analysis of maternal mortality, it found that urban American Indian mothers were 4.2 times more likely to die during or shortly after pregnancy than non-Hispanic white mothers.

Echo-Hawk is pushing for similar detail on COVID-19 cases. Before the pandemic, she traveled the country working with Indigenous communities and training scientists at universities and other institutions to change their data collection and analysis practices. Now, she can’t leave Seattle because of the pandemic, but she’s working up to 15 hours a day, 7 days a week. “This is probably the most troubling time ever in my career,” she says. Echo-Hawk and others pushed CDC to give tribal health authorities access to COVID-19 cases—with some success. Still, the data are “a sliver” of what she asked for, she says. “The federal government is failing to uphold their end of the bargain,” Rodriguez-Lonebear agrees. CDC did not respond to a request for comment.

Echo-Hawk is a co-author on a recent article in the *Morbidity and Mortality Weekly Report* that found American Indians and Alaska Natives were 3.5 times more likely to be diagnosed with COVID-19 than non-Hispanic white people. “That is a gross underreporting,” she says, because the study could only analyze data from the 23 states that reported patients’ race and ethnicity over 70% of the time. “The data is a national disgrace,” and the gaps affect all communities of color, Echo-Hawk says. “How can decisions be made in the United States to prevent, intervene, and treat COVID-19, when you can’t even truly tell what populations are most affected?”

“Data can be used as a weapon to further marginalize and harm communities of color,” especially Indigenous communities, agrees Kelly Gonzales, a citizen of the Cherokee Nation who studies the effects of systemic racism and colonialism on health at the Oregon Health & Science University–Portland State University School of Public Health. As a founding member of the independent Black, Indigenous, and People of Color (BIPOC) Decolonizing Research and Data Council, she draws on Echo-Hawk’s work to design and teach methods of data collection and analysis that advance racial justice. “On days where doing this work in the context of ongoing white supremacy and colonial violence feels really challenging and impossible, I remember her doing this work, and I remember I’m not alone.” ■



“If you eliminate us in the data, we no longer exist.”

Abigail Echo-Hawk, Urban Indian Health Institute

tion but are often left out of national data analyses or marked as statistically insignificant. “I see being eliminated in the data as an ongoing part of the continuing genocide of American Indians and Alaska Natives. If you eliminate us in the data, we no longer exist,” Echo-Hawk says.

One way this erasure happens is through racial misclassification, Echo-Hawk says. Documents such as hospital intake forms might not give people the option to identify as American Indian or Alaska Native, lumping them into an “other” category. Similarly, CDC reports maternal mortality data by three racial categories: white, Black, and Hispanic. All other races are



Health care workers like these, in Jakarta, Indonesia, would be first to get a vaccine under a World Health Organization arrangement.

COVID-19

Despite obstacles, WHO unveils plan to distribute vaccine

Nations with nearly two-thirds of world's population have joined, but not the United States, Russia, or China

By Kai Kupferschmidt

The World Health Organization (WHO) this week announced advances in its effort to ensure the entire world, not just wealthy countries, will benefit from successful COVID-19 vaccines. It reported that 156 countries have joined its plan to buy and distribute the vaccines. It also unveiled a mechanism through which it plans to allocate vaccine doses, aiming “to end the acute phase of the pandemic by the end of 2021.”

“It is a huge success to have the equivalent of 64% of the world's population signed up,” says Alexandra Phelan, a global health specialist at Georgetown University. But China, Russia, and the United States are absent from the list of partners in WHO's plan, known as the COVID-19 Vaccines Global Access (COVAX) Facility. Their absence reflects “the deeply unequal power dynamics in global health,” Phelan says. It poses financial challenges for the plan and raises fears that some high-income countries will hoard early vaccine supplies for their own populations. WHO is also grappling with how to fairly share what, at first, is sure to be an inadequate supply of vaccine.

“As of today, 64 higher income countries, including 29 economies operating as Team Europe, have submitted legally binding

commitments to join the COVAX Facility,” Seth Berkley, head of GAVI, the Vaccine Alliance, said at a 21 September press conference. Those countries, which include Canada, Japan, and New Zealand, will pay for their vaccine doses. Another 38 higher income countries are expected to sign on.

“The fact that the U.S. is not part of this conversation at all, as far as I can tell, is incredibly distressing,” says Ashish Jha, dean of Brown University's School of Public Health. Berkley said COVAX hopes to work with every country.

Many questions remain about how much COVAX will achieve. So far, donors have committed just \$700 million of the \$2 billion COVAX hopes to raise this year to pay for vaccine doses for its 92 participating lower income countries. And it is not clear how the deals many wealthy countries have already made with vaccine manufacturers will impact WHO's plans. The deals, says Alex Harris of the Wellcome Trust, could mean countries “won't need COVAX so much themselves, and therefore might not provide sufficient financing for the non-self-financing countries.”

Such bilateral deals pose a threat to the plan, WHO's Mariângela Simão concedes, but negotiations on many of them were underway when COVAX was being set up.

WHO's “fair allocation mechanism” pro-

poses distributing vaccine purchased by COVAX in two phases. In the first phase, all participating countries would receive vaccine doses proportional to their population: initially, enough vaccine to immunize 3% of their people, with the first doses intended for frontline health care and social care workers. Then, doses would be delivered to all countries until 20% of their population was covered. WHO expects those doses to go to people at highest risk from COVID-19: elderly people and those with comorbidities.

The plan's second phase would favor specific countries, which would receive vaccine based on urgency of need. WHO suggests two criteria for deciding priority: how fast the virus is spreading and whether other pathogens, such as influenza or measles, are spreading at the same time; and how vulnerable a country's health system is, based on metrics such as occupancy of beds in hospitals.

Ezekiel Emanuel, a bioethicist at the University of Pennsylvania, criticizes WHO's approach to the first phase, saying countries with the highest need should top the list from the start. He compares the situation to a doctor facing an overflowing emergency room. “The doctor doesn't go out into the waiting room and say: ‘I'm giving 3 minutes to everybody sitting in the waiting room.’ The doctor says: ‘All right, who's got the most serious illness? ... I'm going to attend to you first.’” At the moment, he says, sending vaccine to South Korea, New Zealand, or many African countries with low case rates would not do much to reduce deaths from COVID-19.

But WHO's Bruce Aylward notes that new outbreaks can suddenly pop up: “Remember, we are dealing with a ubiquitous threat (the virus) and ubiquitous vulnerability (highly susceptible high-risk populations).”

Allocating some vaccine to every participating country may have been necessary politically, Jha says. “I think [WHO is] probably balancing between trying to get enough people protected and trying to create enough of a sense of buy-in that people are going to be willing to chip in.” Emanuel says he understands WHO's position, “but we shouldn't confuse politics with ethics.”

For now, though, politics is crucial. “The real question is: When the first vaccine comes online, who will get those doses?” Harris says. “COVAX now needs to secure deals for their member countries that will work alongside other countries' existing bilateral deals so that all countries get some early vaccine doses, rather than some countries getting all.” ■

COVID-19

Turkey targets critics of its pandemic response

Researchers and physicians who question data or policies face lengthy investigations

By **Kristen McTighe**

In April, Kayihan Pala, a prominent public health expert at Uludağ University in northwestern Turkey, was shocked to find himself the target of a criminal complaint. Pala, a member of the COVID-19 monitoring group of the Turkish Medical Association (TTB), had given an interview to a local website and shared research that showed the number of cases and deaths from the coronavirus were much higher than the government had reported. The complaint, filed by the governor of Bursa province, accused him of “misinforming the public” and “causing panic.”

Saying it was his job to speak out about a burgeoning health crisis, Pala called for the charges to be dismissed. Instead, the prosecutor’s office asked administrators at the university to investigate. Only after a monthslong investigation and national and international pressure did the university conclude on 1 September that Pala had acted within his duty.

“I am a public health scientist and I have to talk about this pandemic locally, nationally, and internationally,” Pala says. “It should not be a crime.”

Yet his case is far from unique. Critics say Turkish authorities are using judicial harassment and administrative investigations to stifle criticism and control information about the crisis. Since March, they have launched investigations against doctors, including leaders of local TTB chapters, after they discussed the government’s health policy and coronavirus information. “Our colleagues have revealed the scientific facts,

nothing beyond that,” says TTB Secretary General Bülent Nazım Yılmaz. A spokesperson for Turkey’s Ministry of Health did not respond to a request for comment.

Turkey, a country of 82 million, has reported just over 300,000 COVID-19 cases so far and more than 7500 deaths. In June, the government lifted a partial lockdown, although independent doctors and medical associations warned the reopening was premature. In early August, TTB claimed its data showed the true number of confirmed COVID-19 cases in the country was higher than official figures and accused the government of not being transparent. Turkey’s Ministry of Health has denied the allegations.

Health Minister Fahrettin Koca recently warned that the country is facing an increase in cases and deaths and has implemented extra control measures, but medical associations say the government is still stifling information about the pandemic. Turkey has not regularly released case and death numbers broken down by city, for instance, and has not answered scientists’ requests to provide data detailing cases by demographic groups, such as among the country’s large refugee population or the working class.

The government has also declared that all COVID-19-related research must be approved by the Ministry of Health. The announcement, in April, sparked outrage and was widely seen as intended to deny independent scientists access to detailed data. “We are asking for more data and more [measures to prevent the spread of the virus],” Pala says. “This is why they are mad about people who are speaking right now.”

In the southeastern city of Şanlıurfa, hard hit by COVID-19, authorities have pressed forward with an investigation of the Şanlıurfa Medical Chamber’s co-chair, Ömer Melik, and its secretary general, Osman Yüksekayla. Melik was first summoned by police and accused of spreading fear and panic in early April after posting the number of COVID-19 cases in the city on the medical chamber’s official Twitter account. (Although social media have come under fire for spreading misinformation in some countries, they have been a popular and crucial tool for independent doctors and scientists to inform the public in Turkey.)

Later that month, Melik was detained again with Yüksekayla after the chamber highlighted the deaths of medical workers, raised concerns over the number of coronavirus cases in local prisons, and warned on Twitter that medical workers lacked adequate protective equipment.

Melik tells *Science* that police said a government circular stated that only Health Ministry officials were permitted to share coronavirus-related information. When he asked to see the circular, they refused, he says. “Our work was accurate and this is not a criminal situation,” Melik says. A court date has not yet been set in the case.

“If we are not clear about what is happening, and people don’t know what is going on, it makes the situation even worse and the virus spreads faster,” says Özgür Deniz Değer, former co-chair of the Van Medical Chamber. Değer was summoned by police in March after an interview in which he criticized authorities for not including political prisoners when releasing detainees from jails where COVID-19 could spread. In May, he was summoned again over a tweet that tagged Turkey’s minister of health and questioned the accuracy of the government’s health care worker death toll. He was accused of issuing “threats to create fear and panic among the people.”

Two months later, Değer was informed the charges had been dropped, but he says the ordeal has caused him to self-censor. “This investigation against me was dropped, but it doesn’t mean that [authorities] won’t start a new one because of new [social media] posts,” he says. ■



Protesters gather in Bursa, Turkey, on 21 July to support Kayihan Pala, who was accused of “causing panic.”

Kristen McTighe is a journalist based in Seattle.

PHOTO: MEDICAL CHAMBER OF BURSA



Researchers found curved slickenlines at nine exposures of the Kekerengu fault in New Zealand.

PALEOSEISMOLOGY

Curved scour marks trace the directions of ancient quakes

“Slickenlines” etched in rocks could help refine shaking hazard for cities near the ends of faults

By Paul Voosen

Many of the world’s most dangerous earthquake faults are a silent menace: They have not ruptured in more than a century. To gauge the hazard they pose to buildings and people, geologists cannot rely on the record of recent strikes, captured by seismometers. Instead, they must figure out how the faults behaved in the past by looking for clues in the rocks themselves, including slickenlines, scour marks along the exposed rock face of a fault that can indicate how much it slipped in past earthquakes.

Now, researchers in New Zealand say slickenlines, when curved, can also reveal which end of a fault slipped first. “This is important information to know,” says Jean Paul Ampuero, a seismologist at the California Institute of Technology who was not involved in the work. Knowing how an earthquake ruptured in the past could help seismologists refine hazard assessments for cities, such as Los Angeles and Istanbul, that sit at the end of known faults. That’s because earthquakes beam their energy in the direction of rupture, Ampuero says. “If an earthquake is coming toward you, it’s coming to kick you in the face.”

Earthquakes don’t happen all at once. Rather, the slip between rocks begins

at one spot on the face of the fault—the hypocenter—and travels along it, like a zipper being unzipped. As the rupture advances, the earthquake waves it generates pile up and intensify, like the siren of an approaching ambulance. Los Angeles lies at the northern terminus of the southern San Andreas fault, Ampuero notes. “If it breaks north, toward LA, that would be pretty bad.”

The researchers first noticed the curved slickenlines after the 7.8-magnitude Kaikōura earthquake, which struck New Zealand’s South Island in 2016. It was a chaotic event: The quake propagated from the southeast to the northeast and its energy jumped from fault to fault, causing dozens of them to slip and shake. One, the Kekerengu, crosses a series of canyons, creating more than a dozen exposures that revealed the marks of rock scraping against rock. Soon enough, the team noticed a consistently curved pattern in these striations on one side of the fault, says Jesse Kearsse, a doctoral student in earthquake geology at Victoria University of Wellington and co-author of the work. “It was like a rainbow.”

More than 2 decades ago, Paul Spudich, a seismologist who died last year, had seen the same pattern in slickenlines from a Japanese earthquake. But no one had shown that such curves indicated anything about the rupture’s direction. Kearsse showed his

findings to Yoshihiro Kaneko, an earthquake dynamicist at GNS Science, New Zealand’s national geoscience research center. Kaneko thought his models could reproduce the motion that caused such an arch. When they fed his model with the Kekerengu data, the same shapes appeared. As in the real world, they formed on the side of the fault that had slipped toward the northeast.

The model also suggested how the arches form. The fault slip was mostly horizontal, but once the rupture reached the surface, no overlying rock constrained its slight upward motion. That allowed the side of the fault traveling with the rupture to bend slightly upward before leveling off. “It gets dragged off course by the seismic waves and makes an arch,” Kearsse says.

That work, which Kearsse and Kaneko published last year in *Geology*, covered just one earthquake. Kearsse then plunged himself into the literature, unearthing 60 large historical earthquakes that had reached the surface and been documented by a geologist. Of those, one-third had curved slickenlines. Only eight of those 20 had the other constraints Kearsse and Kaneko needed to test their model, like the earthquake’s hypocenter. But for all eight, the location of the curving slickenlines corresponded to the rupture direction predicted by their model, regardless of the earthquake’s magnitude or fault type, they reported in a paper published last month in the *Journal of Geophysical Research*. “It’s really compelling,” says Katherine Scharer, a paleoseismologist at the U.S. Geological Survey. “I’d love to see people go out after every rupture and see if they can document this.”

If similar slickenlines are discovered for older faults, that won’t immediately translate to better risk assessments, cautions Laura Wallace, a geodetic scientist also at GNS Science. Just because a fault ruptured in one direction in the past does not necessarily mean it will break in the same direction again. There are physical reasons to suggest that might be true, but the modern record is simply too short to say for sure. “It’s a huge question,” she says.

Slickenlines may hold the answer to that question, too, Scharer says. Not every fault has the right soft mudstones to preserve these lines, and even those that do likely only retain the last rupture. But under just the right conditions, a fault might capture multiple ruptures, she says, giving researchers a chance to look for sets of curved slickenlines that indicate the directions of multiple earthquakes. “It’s a precious moment of time being recorded.” ■

PHYSICS

The short, strange life of quantum radar

In spite of military interest, quantum mechanics won't defeat stealth technologies

By **Adrian Cho**

You might call Jeffrey Shapiro the reluctant godfather of quantum radar. Twelve years ago, the electrical engineer at the Massachusetts Institute of Technology (MIT) helped develop the key concept underlying this scheme to dramatically increase radar's sensitivity. But even he doesn't think the technology will work. "There's just a lot of problems that make it hard for me to believe that this system is going to be of any use," Shapiro says. So he is both bemused and dismayed by the attention other researchers and funding agencies continue to lavish on it.

A mini-arms race is unfolding in the supposed field, initiated by press reports in 2016 that China had built a quantum radar—potentially threatening the ability of stealthy military aircraft to hide in plain sight from conventional radars. "I started working on this because there were government people coming to me and saying, 'There are reports of quantum radar coming out of China. Is this real?'" says Christopher Wilson, a physicist at the University of Waterloo in Canada. His group and others have demonstrated elements of a quantum radar scheme, but only in limited experiments that a nonquantum system can still match.

The quantum radar story began in 2008, when Seth Lloyd, a quantum engineer at MIT, unveiled his concept of quantum illumination (*Science*, 12 September 2008, p. 1433). Lloyd argued that you could more easily detect an object against a bright background if, instead of merely reflecting light off it, you exploited a quantum connection between particles called entanglement. Every photon has a frequency that determines its energy. Quantum theory says, weirdly, that a photon can have multiple frequencies at once—until it's measured and "collapses" randomly to one frequency or another. Even weirder, two such

photons can then be entangled so that their frequencies, although uncertain, are correlated: They are sure to be identical whenever they're measured.

Lloyd calculated that an observer could more easily pick out an object by generating entangled pairs, shining one photon toward the object, keeping the other, and then measuring the retained and returning photons together in a particular way. Essentially, the entanglement correlations would make it harder to mistake a background photon for one reflected off a target. The signal to noise ratio would scale with the amount of entanglement: The more frequencies spanned by each photon in an entangled pair, the stronger the signal.

Lloyd's calculation relied on a highly idealized form of entanglement. So that same year, he, Shapiro, and colleagues redid it for the real entangled light pulses that experimenters can generate with a special crystal that converts a single higher frequency pulse to two entangled pulses at lower frequencies. The pulses have no defi-

nite number of photons—just an average number—and they are "noisy," like radio static. But thanks to the entanglement, the noise in the two pulses is highly correlated.

The researchers compared the sensitivity of a detector relying on the entangled pulses with a conventional one sending out single pulses of laser light, also known as coherent states. They found that the quantum effects boosted the signal-to-noise ratio by just a factor of four, less than they hoped for. "We were slightly disappointed," says Si-Hui Tan, now a quantum information theorist at Horizon Quantum Computing. "Coherent states, they're just so damned good!" she says.

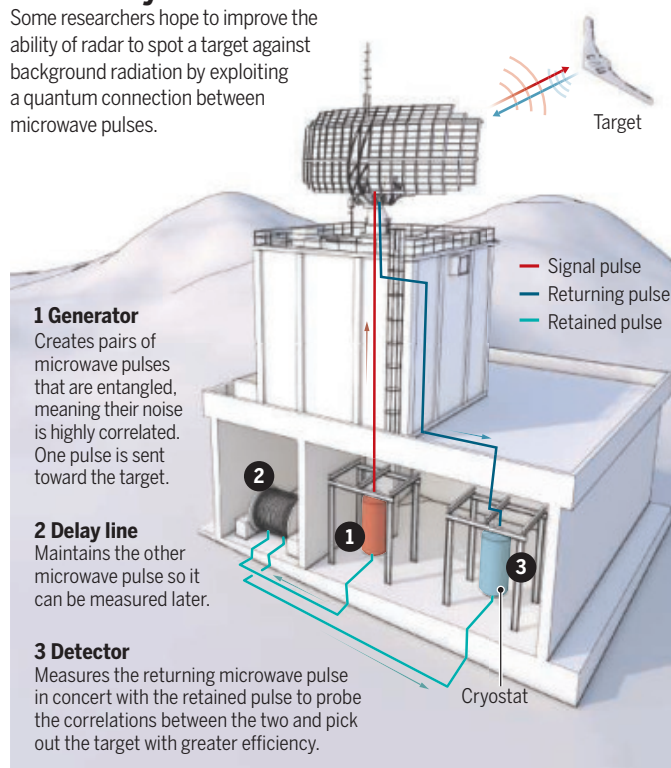
Still, the calculation gave experimenters a target. In 2015, researchers at MIT demonstrated quantum illumination at optical frequencies, realizing a 20% increase in signal to noise. But that experiment had a major limitation. The whole idea was to detect an object against a bright background, but there's very little optical background at room temperature—your surroundings don't glow visibly. So the MIT team had to generate artificial background light.

Things are different in the microwave band, where radar works, says Johannes Fink, an experimental physicist at the Institute of Science and Technology Austria. At room temperature, microwaves stream from everything, even the air. "People are interested in the microwave because the background is always present," he says. Stealth technologies hide military planes by suppressing their reflectivity at microwave frequencies so that the glow of the surroundings masks the plane's reflections.

Quantum illumination seemed to promise a way to defeat stealth technologies. However, demonstrating the scheme with microwaves has proved daunting. Physicists can generate pairs of entangled microwave pulses from single ones using, instead of a crystal, a gizmo called a Josephson parametric converter. But that device only works at temperatures near absolute zero, which requires working within cryostats cooled with liquid helium.

A visionary scheme

Some researchers hope to improve the ability of radar to spot a target against background radiation by exploiting a quantum connection between microwave pulses.



Still, in 2019 Wilson and colleagues demonstrated that they could generate entangled microwaves and use them to detect an object within the same cryostat, as they reported in March 2019 in *Applied Physics Letters*. Fink; Shabir Barzanjeh, a physicist now at the University of Calgary; and colleagues performed a similar experiment, but amplified the signal pulse and ferried it out of the cryostat to detect a room temperature object, as they reported on 8 May in *Science Advances*.

But to really make the scheme work, physicists must also preserve the retained microwave pulse until the reflected pulse (or the background replacing it) returns. Then, both pulses can be measured together in a way that enables the quantum waves to interfere. So far, however, nobody has done that. Instead, they've measured the retained pulse immediately and the returning pulse later, which in the experiments wipes out any gain from the quantum correlations.

Even if experimenters can overcome the technical hurdles, quantum radar would still suffer from a fatal weakness, researchers say. The entangled pulses of microwaves provide an advantage only when the broadcast pulses are extremely faint. The extra quantum correlations fade from prominence if pulses contain significantly more than one photon—which is overwhelmingly the case in real radar. “If you crank up the power, you won't see any difference between the quantum and the classical,” Barzanjeh says. And cranking up the power is a much easier way to improve the sensitivity.

Such considerations suggest quantum radar will never be deployed for long-range uses such as tracking airplanes, says Fabrice Boust, a physicist at France's aerospace agency, ONERA, who specializes in radar. And whatever system China may have developed, it almost certainly isn't a quantum radar as commonly conceived, he says. “I am convinced that when they announced their quantum radar it was not working,” Boust says. “But they knew they would get a reaction.”

Fink says his personal goal remains scientific: demonstrating in the laboratory the true advantage—however small it may be—of entanglement for detecting objects hidden by glare. But the dream of fielding a quantum radar to detect stealth aircraft will likely fade away, says Giacomo Sorelli, a theorist at the Sorbonne University. “Taking out the long-range application of the technology will surely take out a lot of the interest of funding agencies,” he says.

Shapiro is less sure. This week, he notes, researchers again discussed quantum radar in a special session of the online Radar Conference of the Institute of Electrical and Electronics Engineers. ■

CLIMATE SCIENCE

Sizing up a green carbon sink

Studies zero in on forests' potential to fight warming

By **Gabriel Popkin**

Forests are having their moment. Because trees can vacuum carbon from the atmosphere and lock it away in wood, governments and businesses are embracing efforts to fight climate change by reforesting cleared areas and planting trees on a massive scale. But scientists have warned that the enthusiasm and money flowing to forest-based climate solutions threaten to outpace the science.

Two papers published this week seek to put such efforts on a firmer footing. One study quantifies how much carbon might be absorbed globally by allowing forests cleared for farming or other purposes to regrow. The other calculates how much carbon could be sequestered by forests in the United States if they were fully “stocked” with newly planted trees. Each strategy has promise, the studies suggest, but also faces perils.

To get a worldwide perspective on the potential of second-growth forests, an international team led by ecologist Susan Cook-Patton of the Nature Conservancy (TNC) assembled data from more than 13,000 previously deforested sites where researchers had measured regrowth rates of young trees. The team then trained a machine-learning algorithm on those data and dozens of variables, such as climate and soil type, to predict and map how fast trees could grow on other cleared sites where it didn't have data.

A TNC-led team had previously calculated that some 678 million hectares, an area nearly the size of Australia, could support second-growth forests. (The total doesn't include land where trees might not be desirable, such as farmland and ecologically valuable grasslands.) If trees were allowed to take over that entire area, new forests could soak up one-quarter of the world's fossil fuel emissions over the next 30 years, Cook-Patton and colleagues report in *Nature*. That absorption rate is 32% higher than a previous estimate, based on coarser data, produced by the Intergovernmental Panel on Climate Change. But the total carbon drawdown is 11% lower than a TNC-led team estimated in 2017.

The study highlights “what nature can do all on its own,” Cook-Patton says. And

it represents “a lightning step forward” in precision compared with earlier studies, says geographer Matthew Fagan of the University of Maryland, Baltimore County, who was not involved in the work.

But, Fagan adds, “Natural regrowth is not going to save the planet.” One problem: There is often little economic incentive for private landowners to allow forests to bounce back. Under current policies and market pricing, “nobody will abandon cattle ranching or agriculture for growing carbon,” says Pedro Brancalion, a forest expert at the University of São Paulo in Piracicaba, Brazil. And even when forests get a second life, they often don't last long enough to store much carbon before being cleared again. Fagan notes that even in Costa Rica, renowned as a reforestation champion for doubling its forest cover in recent decades, studies have found that

half of second-growth forests fall within 20 years.

Given such realities, some advocates are pushing to expand tree planting in existing forests. To boost that concept, a team of researchers at the U.S. Forest Service (USFS) quantified how many additional trees U.S. forests could hold. Drawing on a federal inventory, they found that more than 16% of forests in the continental United States

are “understocked”—holding fewer than 35% of the trees they could support. Fully stocking these 33 million hectares of forest would ultimately enable U.S. forests to sequester about 18% of national carbon emissions each year, up from 15% today, the team reports in the *Proceedings of the National Academy of Sciences*. But for that to happen, the United States would have to “massively” expand its annual tree-planting efforts, from about 1 billion to 16 billion trees, says lead author Grant Domke, a USFS research forester in St. Paul, Minnesota.

Cook-Patton says planting trees might make sense in some places, but natural regeneration, where possible, provides more bang for the buck. “For any given site,” she says, “we should always ask ourselves first: ‘Can the forest regenerate naturally, or can we do something to help?’” ■

“Can the forest regenerate naturally, or can we do something to help?”

Susan Cook-Patton,
the Nature Conservancy

Gabriel Popkin is a journalist in Mount Rainier, Maryland.

SEEKING A NICHE

Costa Rica is producing a new generation of skilled tropical biologists. But many can't find jobs at home





By **Jocelyn Kaiser**, on Mount Chirripó in Costa Rica

Framed by drifting clouds, ecologist Andrea Vincent surveyed the hot tub-size dome her students had erected here at nearly 3800 meters, on Costa Rica's highest peak. "We did it!" she exulted. Vincent's team from the University of Costa Rica (UCR) had made the steep 15-kilometer hike up to this tropical alpine landscape—known as a páramo—in a bid to understand how global warming might affect the mosaic of shrubs and grasses. The team had built 20 of the open-topped domes, which block the winds that buffet the slopes, thus slightly warming the plants inside and mimicking conditions they might experience in the future. "There are interesting questions here," Vincent says. One is whether the páramo will be overrun by the oak trees now restricted to lower, warmer elevations, threatening its biodiversity.

Setting up the experiment in February marked a professional milestone for the 39-year-old Vincent: It was her first major project as a principal investigator on a grant from Costa Rica's government, after years of working as a collaborator with other scientists, often from the United States. "It's really cool when it's your intellectual child," she says. And she's pleased that her project is part of a network of similar studies taking place in Ecuador and Colombia. "It's *ciencia criolla*," she boasts—a term of pride for projects led by scientists from Latin America.

Costa Rica's renowned biodiversity has made it a go-to destination for field biologists from around the world. But despite its relatively small population of just 5 mil-

lion, the country has also been successful at nurturing its scientific talent in recent decades. And Vincent, who grew up mostly in the capital of San José and trained in Europe, is one of a growing number of Costa Rican scientists who have returned home to launch their careers. It's a trend the government has encouraged, in part by filling open slots at universities with Ph.D.-level scholars, including some promised jobs before they were sent abroad for advanced schooling.

The result, Vincent says, is a new generation of Costa Rican scientists that is better trained and more ambitious, especially in her field of tropical biology. They are no longer satisfied playing support roles for visiting researchers. "A lot of people are hungry to do research that is competitive at the international level," Vincent says.

The blossoming has a downside, however: Although Vincent and other Costa Rican biologists have managed to build careers at home, the country is struggling to absorb all of the researchers it is producing. "There is no room in Costa Rica's universities for the number of scientists who are coming back," says plant ecologist Oscar Rocha, a Costa Rican working at Kent State University in Ohio. "A lot of well-trained scientists are now working for field stations or programs that are training undergraduates," he says, instead of leading projects.

Granted, researchers in many nations face a scarcity of faculty jobs. But it's an especially painful paradox given the natural riches beckoning scientists in Costa Rica. "A lot of us were pushed [to excel] in a good sense," says insect ecologist Fernando Soley Guardia, who earned a Ph.D. in Australia and is now

A new corps of Costa Rican biologists is studying the country's rich biodiversity, including this montane forest. Andrea Vincent (right) is running experiments that explore how climate warming might alter tropical alpine ecosystems.

PHOTOS (LEFT TO RIGHT): GERRY ELLIS/MINDEN PICTURES; J. KAISER/SCIENCE

teaching courses at UCR and the Organization for Tropical Studies (OTS), a nonprofit research and education organization based in the United States and Costa Rica (see sidebar, p. 1561). “Now, a lot of us want to be back here, to do research where we learned from the environment. But there’s not enough space.”

ALTHOUGH DEFINITIVE statistics aren’t available, observers say it’s clear that Costa Rica’s growing pool of Ph.D. tropical biologists marks a departure from 30 years ago. Then, for example, just 13 of 32 faculty at the UCR School of Biology had a doctorate. Now, 80% hold that degree, and a Ph.D. is mandatory for new hires.

Rocha, who is 62, experienced that transformation firsthand. While earning a master’s degree at UCR in the 1980s, he worked as a manager at La Selva, a research station some 80 kilometers north of San José run by OTS. The exposure to visiting scientists helped inspire Rocha to go abroad; he earned a Ph.D. from Pennsylvania State University in the United States in 1990. He then returned to Costa Rica and later became chair of UCR’s School of Biology.

In that job, Rocha promoted efforts to send Costa Rican students abroad to Ph.D. programs—to avoid “inbreeding,” he says—and then lure them back. His department bolstered training in the analytical skills students needed to qualify for foreign programs. Faculty worked to place them with colleagues in the United States and Europe, and helped students win funding from foreign sources. Under a system called *reserva de plaza*, Costa Rican universities also directly funded graduate studies abroad for some students, if they agreed to return to a reserved university job. “The ball started rolling,” Rocha says.

Many of the biologists who have emerged from such efforts have moved beyond the taxonomy and descriptive science that has long been a tradition in Costa Rica. Vincent, for example, pursues broader, hypothesis-driven research as UCR’s first ecosystem ecologist, working to reveal how physical processes like geochemical cycles shape organisms and ecosystems. “There was a sense long ago that we were more like passionate technicians,” says forest ecologist Roberto Cordero, of the National University of Costa Rica, who at 58 is part of Rocha’s generation. “Now, we are demanding more and providing more insights.”



Adrián Pinto is probing symbiotic bacteria, such as those living in leafcutter ants’ fungal gardens, for medically useful compounds.

MICROBIAL ECOLOGIST ADRIÁN PINTO, 42, is one member of this new generation. Earlier this year, he stood in his lab on the UCR campus in San José peering into glass boxes housing leafcutter ants that he uses to educate schoolchildren. Some of the busy ants carried leaf fragments, others tended a brown fungal structure. Pinto’s graduate research at the University of Wisconsin (UW), Madison, showed how bacteria in the ants’ fungal gardens fix nitrogen, or convert it from the air into a biologically usable form; the work was published in *Science* in 2009. He then returned to Costa Rica, where he had a job awaiting at UCR because of the *reserva* system.

Pinto has shifted his focus from the nitrogen-fixing role of such bacteria toward mining them for useful chemicals. “Here basic research is very hard to fund,” he says. He and two co-investigators now lead a 22-person team devoted, in large part, to probing Costa Rica’s insect ecosystems for compounds that might be useful in medicine. (Biologists found one promising antibiotic, dubbed selvamycin, in a leafcutter ant garden at La Selva.) “It’s

a great country for microbial ecology,” Pinto says.

Pinto is a rarity in Costa Rica: He’s also a co-principal investigator on a U.S. National Institutes of Health grant with researchers at UW. His lab screens bacteria for antimicrobial activity, then ships promising leads to UW for expensive animal studies. Pinto “has created a really good model for how to be successful” in Costa Rica, says UW evolutionary biologist Cameron Currie.

Other returning biologists have focused on conserving Costa Rica’s vulnerable species. Gilbert Alvarado, 37, a wildlife pathologist who studies threatened tropical frogs, earned his Ph.D. in Brazil. Now at UCR, Alvarado has helped rediscover several populations, and one entire species, of frogs in Costa Rica that were thought to have been wiped out in the 1980s and 1990s by a fungus called chytrid, which has killed amphibians worldwide. He and U.S. collaborators recently used Costa Rican museum specimens to show chytrid was present in the nation’s frogs a half-century ago, suggesting it spread slowly or evolved to become more lethal. He is now raising chytrid-resistant frogs in the lab that will be released to shore up vulnerable populations.

UCR evolutionary biologist Beatriz Willink, 32, who came back to Costa Rica 2 years ago after a Ph.D. in Sweden, is pursuing more fundamental research. She has studied why damselflies evolved certain colors to attract mates. She returned home not only because Costa Rica’s ecology abounds “with questions,” but also because she feels a moral obligation to teach here, attracted by “the idea that people from all backgrounds in this small Latin American country can have this great publicly funded education.”

ALTHOUGH VINCENT, Pinto, Alvarado, and Willink have secured tenure-track positions, many other Costa Rican researchers are finding it difficult to land satisfying jobs. “I know people who are extremely qualified and have published lots of good papers who are just waiting in line,” Willink says.

One obstacle, several scientists say, is Costa Rica’s *reserva* system. Its intent, to lure back and retain talent by assuring doctoral candidates a job, once made sense, they say. (Only Vincent did not get her job this way.) But now, with an abundance of

A tropical research treasure faces difficult times

As a new generation of tropical biologists rises in Costa Rica (see main story, p. 1558), an institution that has propelled many of their careers has fallen on hard times. The Organization for Tropical Studies (OTS), a 57-year-old nonprofit that runs education programs and field stations in Costa Rica, this year began to emerge from a financial quagmire only to face disruptions caused by the coronavirus pandemic.

U.S. scientists drawn to Costa Rica for its vast biological diversity founded OTS in 1963, backed by a consortium of six U.S. universities and the University of Costa Rica (UCR). Its original 8-week basic graduate course for tropical biology, designed in part by renowned U.S. ecologist Daniel Janzen, is legendary—many U.S. and Latin American tropical biologists have taken it. OTS has “played an incredibly important role in tropical biology,” says Rakan Zahawi of the University of Hawaii, Manoa, a former OTS station director.

OTS’s flagship field site at La Selva in northern Costa Rica, which includes 1600 hectares of lowland rainforest, is one of the world’s top tropical field stations. Studies there have yielded 6000 and counting papers on topics from forest dynamics to insect-plant relationships. Although some Costa Rican scientists have at times seen La Selva and the two other OTS stations as “gringo enclaves,” as a 2002 history put it, they are now meeting places for biologists from across the Americas. “We love OTS and La Selva,” says microbial ecologist Adrián Pinto of UCR. “It’s a treasure for us.”

But OTS’s always-precarious finances, largely covered by dues from its roughly 50 member institutions, as well as gifts, grants, student tuition, and visitors, took a nosedive in the past decade. OTS leaders largely blame competition from similar

undergraduate courses offered in Costa Rica by U.S. universities, a possible decline in interest from students in lengthy field stays, and a breakup with Duke University, OTS’s longtime U.S. headquarters. (The University of Connecticut is now its U.S. partner for undergraduate courses.) Annual operating deficits ran as high as \$1.6 million over the past 4 years, on annual spending of up to \$8 million. Its \$16 million endowment shrank by \$1.7 million.

In 2017, a new director, Sandy Andelman, slashed staff to save \$300,000 in salaries, causing employee morale to plunge. Last year, OTS put its Costa Rican undergraduate program on hold—only a South African program on savanna ecology continued.

Those measures helped get OTS out of its hole. Now, “We’re actually doing OK,” says OTS President and CEO Beth Braker, who is on leave from Occidental College. This year, OTS will have its first balanced budget in 4 years, says OTS board chair George Middendorf. And the organization is about to launch a fundraising campaign and is planning new graduate courses.

But COVID-19 poses a new threat. Just as leaders were poised to rebuild and hire for key positions, COVID-19 shut out visiting scientists and forced course cancellations. Although Costa Rica recently opened its borders to some visitors, OTS revenues from station fees and in-person courses will likely remain below usual levels until at least June 2021.

When OTS emerges from its crisis, a new agreement with UCR should help make it sustainable, OTS and UCR leaders say. It will “reaffirm ... a relationship of mutual trust,” says Pinto, who is UCR interim vice president for research. Maintaining OTS is important for Costa Rica, says OTS board member and former UCR Rector Gabriel Macaya: “It has been a very important bridge for research in many different ways.” —J.K.

researchers trained overseas who are ready to compete for academic jobs, the *reserva* seems a bit “outdated,” says evolutionary biologist Marcelo Araya-Salas, a non-*reserva* Ph.D. who is job hunting in Costa Rica.

In a bid to stay active while waiting for a job to open up, some Ph.D.-level scientists are working for conservation organizations or teaching, in some cases squeezing in research part time. For instance, Jimena Samper-Villareal teaches and works on seagrass ecology and restoration at UCR’s marine science center in a staff scientist position that hovers between one-quarter and three-quarter time each year. She came back in 2016 after her Ph.D. in Australia so her two young kids could be close to family. But there are “very limited opportunities in Costa Rica,” Samper-Villareal says, and she’s “trying to keep my publications up” while watching for an opening.

Some researchers have opted to try to wait things out in postdoctoral positions abroad. Other have joined Costa Rica’s science diaspora, taking faculty positions in the United States or elsewhere instead of trying to return, Rocha notes.

Whether the job crunch will ease in the future is unclear. A shortage of funding has reduced the number of Costa Ricans receiving scholarships to pursue doctoral degrees; at UCR they dropped from nearly 50 a year in 2016 to just 22 last year. That could reduce the competition for jobs. But the same funding shortage could limit jobs at home. The country now spends about 0.4% of its gross domestic product on science, down slightly from previous years when its economy was stronger.

Another factor is a university pension system that appears to be discouraging older faculty from retiring and creating new openings, says geneticist Gabriel Macaya, a former UCR rector. One solution would be for research universities to set aside more funds to hire scientists for nontenured, full-time positions, Macaya says.

Some senior scientists who have mentored this next generation are dismayed. “It is troubling to see good young people with good training not being able to employ their talents,” says William Eberhard, a leading U.S. evolutionary biologist who joined the UCR faculty in 1979 and retired about

5 years ago. “And it is especially frustrating when one has invested time and effort in helping them get to where they are.”

Among Eberhard’s undergraduate students was Soley Guardia, who went on to study how assassin bugs use clever strategies to catch web-weaving spiders for his Ph.D. in Australia. Soley Guardia now wants to do comparative research with Costa Rican species of these aggressive predators, but hasn’t yet found a tenure-track position. He says his twin brother Mariano, a biogeographer, is in the same situation.

Soley Guardia speaks wistfully of the prominent scientists, some from outside Costa Rica, who influenced him. “It was good to have that exposure,” he says. “Now we’re kind of self-sustaining in a good way. We come up with our own ideas.”

But he fears he won’t be able to follow through on them if he stays in his homeland. “The bad thing,” he says, “is we’re aspiring to do science at the level of developed countries without the money to pay for it.” ■

Travel for this story was supported by the International Center for Journalists in Washington, D.C.

INSIGHTS

PERSPECTIVES

MICROBIOLOGY

Transformative tools for parasitic flatworms

Schistosome single-cell atlas and genome-wide functional dissection reveal druggable targets

By Timothy J. C. Anderson¹ and Manoj T. Duraisingh²

Schistosomes, a type of parasitic flatworm, are complex multicellular pathogens with an oversized and probably underestimated impact on human health. Schistosomiasis is one of the “neglected” tropical diseases, named in part because of a perceived lack of tools to probe parasite biology. On pages 1649 and 1644 of this issue, Wang *et al.* (1) and Wendt *et al.* (2), respectively, show that this neglect is unwarranted. With creative use of postgenomic and parasitological approaches, these authors uncover previously unknown aspects of schistosome biology, highlight avenues for

intervention, and provide new resources for the field. Wang *et al.* report a loss-of-function screen that reveals numerous essential genes and identify small-molecule inhibitors of two kinases required for muscle development. Wendt *et al.* unveil a single-cell atlas for adult schistosomes, unearthing a gut stem cell lineage that can be targeted to eliminate egg production and pathology.

Parasitic worms infect more than 1 billion people globally, particularly in resource-poor countries (3). They include parasites from two major phyla: the nematodes and platyhelminths (or flatworms—flukes and tapeworms). Parasitic worm infections cause anemia and stunting and impede cognitive development in children, affect

the development of immunity and allergies, increase susceptibility to HIV and progression to AIDS, and result in many obstructive pathologies. Schistosome blood flukes infect more than 200 million people and cause widespread morbidity and more than 200,000 deaths globally every year (4).

Schistosomes have complex life cycles and fascinating biology; they use both vertebrate and aquatic snail hosts and assume six morphologically distinct developmental, replicative, and sexual morphologies (5). In the

¹Texas Biomedical Research Institute, San Antonio, TX 78227, USA. ²Harvard T.H. Chan School of Public Health, Boston, MA 02139, USA. Email: mduraisi@hsph.harvard.edu; tanderso@txbiomed.org

Paired male (pink) and female (green) adult schistosomes live in the veins surrounding the intestines. The micrograph is colored to distinguish the sexes. Adult worms are about 1 cm long.



Reducing infection, and pathology, of schistosomiasis relies on regular targeted or mass administration of the drug praziquantel (PZ), which was developed 50 years ago. However, PZ treatment typically leaves 30% of people positive for schistosome eggs, and the drug is ineffective against juvenile worms (7). Worryingly, resistance to PZ is suspected in the field (8) and is easily selected for in the laboratory (9). This makes the reliance on PZ monotherapy risky, and new interventions are needed, either to replace or to use in combination with PZ. Both Wang *et al.* and Wendt *et al.* provide a plethora of targets and pathways to prime a pipeline for therapeutic development.

Fortunately, the complete life cycle of schistosome parasites—particularly *S. mansoni*, the focus of both studies—is easily maintained in the laboratory using rodent and snail hosts, there is a growing molecular and cell biological toolkit (10, 11), gene manipulation is possible (12), and genetic mapping studies can be conducted (13). Genome sequences are available for all three major species of schistosomes that infect humans and a growing number (>100) of other parasitic worm genomes, which facilitates comparative genomic studies to predict molecules and pathways of interest (14). Wang *et al.* and Wendt *et al.* exploit genomic information to develop two powerful approaches to functionally probe schistosome biology: large-scale RNA interference (RNAi) screens and single-cell gene expression atlases, respectively. Not only do the authors demonstrate the feasibility of applying these approaches to *S. mansoni* but they also conduct extensive functional analysis to reveal exciting features of parasite biology.

Wang *et al.* targeted the expression of ~2320 schistosome genes, of which 195 were critical for parasite attachment and 66 were critical for stem cell maintenance. They also identified a large number of genes that were essential for adult viability and development. Their analysis provides a treasure trove of possible therapeutic targets for further investigation and was enriched for genes in the ubiquitin proteasome system and muscle development. Many of the essential genes that were identified have orthologs that are not essential in model organisms, suggesting a distinctive biology of fluke parasites that cannot be inferred from studies of invertebrate model organisms, such as the nematode worm *Caenorhabditis elegans* or fruit flies (*Drosophila melanogaster*), or even from the free-living flat-worm *Schmidtea mediterranea*.

Although the functional RNAi screen identified a long list of essential genes, Wang *et al.* prioritized genes by examining the list

for druggability with existing compounds. This allowed experimental validation of proteins involved in the ubiquitin proteasome system (p97) and muscle development (TAO and STK25 kinases) as drug targets. Small-molecule inhibitors with limited host toxicity were identified from a library of U.S. Food and Drug Administration–approved molecules, providing an impetus for drug development. Encouragingly, treatment with these small molecules resulted in worm mortality *in vivo*.

Wendt *et al.* provide an elaborate picture of schistosome body structure and development through the creation of a single-cell atlas of schistosome adult parasites. The resolution is high, with 68 cell populations mapping to almost all of the known tissues of the worm, and spatial distributions of different cell lineages are described using *in situ* hybridization methods and electron microscopy. This descriptive work generates many tantalizing observations that will inspire future functional and cell biology analyses. There are lineages of ciliated neu-



Schistosoma mansoni egg with a characteristic spine is captured with differential interference contrast microscopy. Host immune reactions to eggs lodged in the liver result in pathology in infected people.

human host, male and female adult schistosomes—the focus of the studies by Wang *et al.* and Wendt *et al.*—reside in pairs in the mesenteric veins around the intestines (see the micrograph, above) and can evade immune destruction for up to 40 years. During this time, they lay millions of eggs: Those that do not escape the body through feces or urine elicit strong host immune responses and cause severe pathology when lodged in host tissue (6). In the case of *Schistosoma mansoni* infections, granulomas form in the liver, leading to liver failure and death (see the micrograph, right). Interventions that eliminate adult worms or block egg production are required to prevent transmission and eliminate pathogenesis.

ral cells with unknown functions, whereas other neural markers show left-right asymmetry in gene expression. In addition to identifying cells that make up key organs such as the nervous system and the sexual organs, the authors follow their fundamental interest in stem cells and examine the fate of a newly discovered stem cell lineage involved in gut formation. Detailed functional analysis reveals a central role for the hepatocyte nuclear factor 4 (*hnf4*) gene not only in gut development but also in feeding and egg production. This study reveals gut development as a key point of intervention that results in a decrease in adult size and fecundity, eliminating the egg-induced pathology of schistosomiasis.

Particularly powerful in these studies is the combination of new and old approaches to schistosome biology. Cioli *et al.* first showed that adult worms can be surgically implanted in rodents in the 1980s (15). By treating adult worms with RNAi in vitro and then implanting them in mice, both studies directly examine the impact of repressing the expression of specific genes on parasite survival within a host. Such strategic use of new and old methodologies makes a seemingly difficult organism extremely tractable.

Researchers are now equipped with a long list of essential genes and a comprehensive single-cell atlas of adult worms for functional analysis and future screens. An immediate challenge is the prioritization of targets for drug development or as vaccine antigens, which will be based on criteria beyond essentiality. Are there conserved targets that are druggable at different development stages? Will population variation present a hurdle to effectiveness? One far-reaching impact will be the ability to translate insights from these screens to less experimentally and genetically tractable parasitic worms. This may be possible for the related flatworm parasites (tapeworms and other flukes) but will be more challenging for the more phylogenetically distant parasitic nematodes.

The advent of postgenomic functional studies and tools in parasitic worms allows new comparative approaches. Rather than overzealous reliance on model organisms to infer aspects of parasite biology, it is now possible to directly compare developmental processes in parasites and their free-living relatives to examine how these organisms differ. Wang *et al.* and Wendt *et al.* go much further than identifying drug targets, supporting the premise that it is critical to understand the basic biology of pathogens before designing strategies to kill them. ■

REFERENCES AND NOTES

1. J. Wang *et al.*, *Science* **369**, 1649 (2020).
2. G. Wendt *et al.*, *Science* **369**, 1644 (2020).
3. P. J. Hotez *et al.*, *J. Clin. Invest.* **118**, 1311 (2008).
4. M. A. Verjee, *Res. Rep. Trop. Med.* **10**, 153 (2019).
5. D. P. McManus *et al.*, *Nat. Rev. Dis. Primers* **4**, 13 (2018).
6. E. Hams, G. Avioli, P. G. Fallon, *Front. Immunol.* **4**, 89 (2013).
7. R. Bergquist *et al.*, *J. Infect. Dis. Poverty* **6**, 75 (2017).
8. S. D. Melman *et al.*, *PLOS Negl. Trop. Dis.* **3**, e504 (2009).
9. F. F. Couto *et al.*, *Mem. Inst. Oswaldo Cruz* **106**, 153 (2011).
10. P. J. Skelley, A. Da'dara, D. A. Harn, *Int. J. Parasitol.* **33**, 363 (2003).
11. J. N. Collins, J. J. Collins III, *Methods Mol. Biol.* **1463**, 35 (2017).
12. W. Ittiprasert *et al.*, *eLife* **8**, e41337 (2019).
13. T. J. C. Anderson, P. T. LoVerde, W. Le Clec'h, F. D. Chevalier, *Trends Parasitol.* **34**, 982 (2018).
14. A. Coghlan *et al.*, *Nat. Genet.* **51**, 163 (2019).
15. D. Cioli, L. Pica Mattoccia, *Am. J. Trop. Med. Hyg.* **33**, 80 (1984).

10.1126/science.abe0710

IMMUNOLOGY

Preventing pores and inflammation

Metabolite-directed modification of pore-forming cell death protein limits inflammation

By Robert J. Pickering and Clare E. Bryant

Inflammation is a tightly regulated process that is essential for host protection against infections. When it is dysregulated, however, inflammation becomes damaging, causing many common diseases such as sepsis, arthritis, asthma, and diabetes. Some programmed cell death pathways, such as pyroptosis and necroptosis, induce inflammation in response to pathogens or sterile stimuli. The pyroptosis executioner protein gasdermin D is cleaved by the cysteine protease caspases 1, 4, 5, or 11 (1, 2). This produces a toxic amino-terminal fragment that forms pores in membranes, which lyses cells and releases inflammatory mediators (3). On page 1633 of this issue, Humphries *et al.* (4) reveal a switch whereby dimethyl fumarate (DMF), a drug that is used to treat inflammatory conditions such as multiple sclerosis, succinates critical cysteine residues in gasdermin D to prevent its cleavage, inhibit pyroptosis, and protect against severe inflammation in mice.

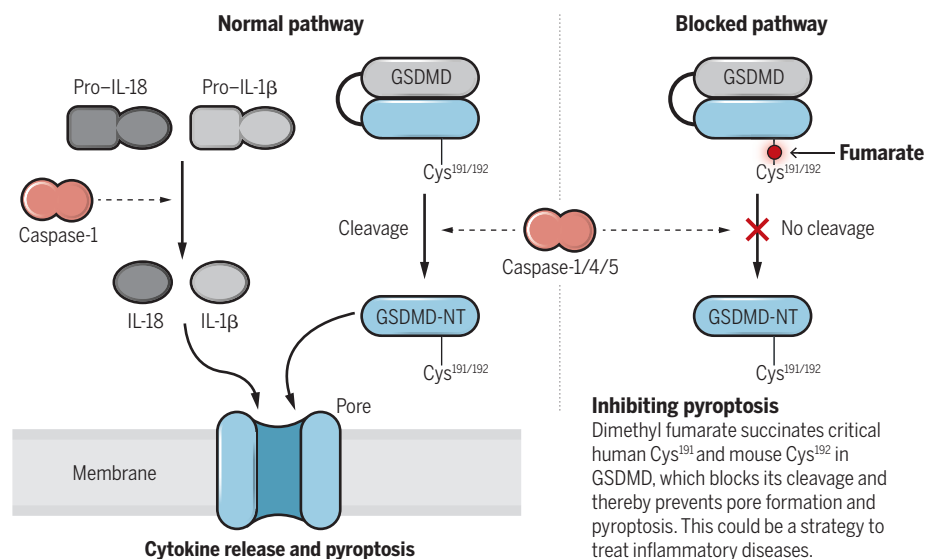
Gasdermin D is cleaved by caspases

through the action of macromolecular inflammatory protein signaling complexes called inflammasomes (1). Canonical inflammasomes are formed when a cytosolic receptor such as a NOD-like receptor (NLR)—for example, NLRP3—binds to a ligand (pathogenic or endogenous), leading to the formation of a signaling platform that activates caspase 1 through proximity-induced dimerization (5). This process cleaves gasdermin D but also results in the cleavage of pro-interleukin 1 β (pro-IL-1 β) and pro-IL-18 into their mature forms (1). Gasdermin D pore formation, and the subsequent pyroptotic lysis of the cells, allows the release of these mature cytokines and a number of other damaging molecules to perpetuate inflammation (6). Noncanonical inflammasomes, activated by the binding of the bacterial lipid lipopolysaccharide to caspase 4 or 5 (in humans) or 11 (in mice), also results in gasdermin D cleavage, and this in turn leads to activation of NLRP3 and canonical inflammasome formation (5).

Canonical NLRP3 inflammasome formation is linked to many chronic inflamma-

Inflammatory cell death

Upon inflammasome activation, caspases are released that cleave gasdermin D (GSDMD) and produce an amino-terminal fragment (GSDMD-NT). This fragment forms pores in the cellular membrane, inducing pyroptosis and release of inflammatory cytokines such as interleukin 18 (IL-18) and IL-1 β .



tory diseases, including type 2 diabetes, Alzheimer's disease, and gout, so inhibition of this pathway is of considerable therapeutic interest (7). Inhibition of noncanonical inflammasome activation protects against sepsis and associated systemic inflammation (7), conditions that occur when the host response against infection (bacterial or viral) is dysregulated and becomes hyperactive. Sepsis is often intractable—for example, in severe coronavirus disease 2019 (COVID-19) (8)—and despite multiple clinical trials, no successful treatments for sepsis have been developed. This has resulted in, understandably, waning enthusiasm by the pharmaceutical industry to develop drugs to treat sepsis.

Inhibiting gasdermin D activation could represent a new strategy to target inflammatory conditions, especially because it is downstream of both canonical and noncanonical inflammasomes (9). Disulpharim, a drug already in clinical use for alcohol addiction, covalently modifies human Cys¹⁹¹ and mouse Cys¹⁹² in gasdermin D, resulting in prevention of pore formation but not its cleavage, protecting against sepsis in rodents (10). This drug is being tested in the DISCO clinical trial for patients with severe COVID-19 infections (NCT04485130). Humphries *et al.* show that succination of the same cysteines by DMF inhibits both gasdermin D processing and pore formation, reducing inflammatory conditions in mice (see the figure). These data confirm that inhibiting gasdermin D is promising, even for severe inflammatory conditions, and maybe this will tempt pharmaceutical companies, particularly in the context of the severe COVID-19 systemic inflammation syndrome, to revisit sepsis as an unmet medical need.

Immunometabolism studies clearly show that metabolic reprogramming of cells underpins the anti-inflammatory effects of a number of therapeutic molecules (11). A number of important posttranslational modifications by endogenous metabolites modulate inflammatory pathways (11). DMF and its clinically relevant metabolite monomethyl fumarate, for example, succinate glyceraldehyde-3-phosphate dehydrogenase (GAPDH) to inactivate its enzyme activity, downregulating aerobic glycolysis to prevent immune activation. This shifts the balance from inflammatory toward regulatory cell types (12). Fumarate, from which DMF is derived, is a metabolic intermediate of the Krebs cycle (downstream of glycolysis), and so its inactivation of GAPDH may be an endogenous negative feedback loop (12). The identification of gasdermin D as another target of fumarate-mediated succination expands the

repertoire of fumarate substrates and helps to explain some of the immunomodulatory effects of DMF. The intersection between metabolism and regulation of inflammasome biology is now well established, with metabolites regulating IL-1 β production and multiple links between mitochondrial metabolism and NLRP3 activity (13).

Many bacteria and viruses activate diverse inflammasomes, with pyroptosis thought to be an important aspect of the response to control infections (6). Efficient release of IL-1 β and IL-18 from the cell requires gasdermin D pores (6), which makes it challenging to precisely differentiate between what is a pyroptotic-dependent or proinflammatory cytokine-dependent process. Pyroptosis is only one of a diverse array of cell death pathways that are increasingly linked to important functions in infection and immunity. The close interrelationship between cell death pathways, particularly those associated with caspase activity, probably arises because cell death is an essential process, and so redundancy is required if one pathway is lost or dysfunctional. In a *Salmonella* infection model, for example, ablation of caspases 1, 11, 12, and 8 as well as RIPK3 (receptor-interacting serine/threonine-protein kinase 3)—which limits pyroptosis, necroptosis, and apoptosis—is required to see a profound deficit in the ability of the host to control bacterial load (14). How these pathways are regulated and potential hierarchies in caspase activity are beginning to emerge, with caspase 8 being a key player and possibly controlled from a PANoptosome multiprotein cell death complex (15). How inhibiting, as opposed to genetically ablating, one cell death pathway affects the activity of another remains to be determined. The collision of immunometabolism with inflammatory cell death presents exciting prospects not only for new developments in the biology of infection and immunity but also for potential anti-inflammatory therapeutic interventions. ■

REFERENCES AND NOTES

1. P. Broz *et al.*, *Nat. Rev. Immunol.* **20**, 143 (2020).
2. N. Kayagaki *et al.*, *Nature* **526**, 666 (2015).
3. X. Liu *et al.*, *Nature* **535**, 153 (2016).
4. F. Humphries *et al.*, *Science* **369**, 1633 (2020).
5. P. Broz, V. M. Dixit, *Nat. Rev. Immunol.* **16**, 407 (2016).
6. J. Lieberman *et al.*, *Sci. Immunol.* **4**, eaav1447 (2019).
7. D. Chauhan *et al.*, *Immunol. Rev.* **297**, 123 (2020).
8. J. Wang *et al.*, *J. Leukoc. Biol.* **108**, 17 (2020).
9. J. K. Rathkey *et al.*, *Sci. Immunol.* **3**, eaat2738 (2018).
10. J. J. Hu *et al.*, *Nat. Immunol.* **21**, 736 (2020).
11. E. M. Pålsson-McDermott *et al.*, *Cell Res.* **30**, 300 (2020).
12. M. D. Kornberg *et al.*, *Science* **360**, 449 (2018).
13. C. L. Holley, K. Schroder, *Clin. Transl. Immunology* **9**, e01109 (2020).
14. M. Doerflinger *et al.*, *Immunity* **53**, 533 (2020).
15. P. Samir *et al.*, *Front. Cell. Infect. Microbiol.* **10**, 238 (2020).

ACKNOWLEDGMENTS

C.E.B. is supported by Wellcome Trust Investigator award 108045/Z/15/Z.

Departments of Medicine and Veterinary Medicine, University of Cambridge, Cambridge, UK. Email: ceb27@cam.ac.uk

ARCHAEOLOGY

The last pieces of a puzzling early meeting

Y chromosomes transferred from *Homo sapiens* to Neanderthals between 350,000 to 150,000 years ago

By Mikkel Heide Schierup

Since the sequencing of the first Neanderthal and Denisovan genomes, genetic evidence has revealed an increasing number of admixture events between *Homo sapiens* and these archaic humans. However, scientists have lacked detailed information about Y chromosome sequences from our two closest relatives. Now, on page 1653 of this issue, Petr *et al.* (1) report intricate DNA sequencing data for Y chromosomes from less-than-well-preserved bones of male Neanderthals and Denisovans.

Most scientific focus has been on genetic admixture from Neanderthals into *H. sapiens* ~40,000 to 60,000 years ago (soon after the so-called main out-of-Africa event) (see the figure). This meeting resulted in the 1.5 to 2% of the Neanderthal-genome fragments present in the nuclear genomes of all non-Africans today (2). Gene flow between *H. sapiens* and Neanderthals was initially surprising, because earlier studies of mitochondrial DNA found no signs of gene flow (3). Furthermore, the sex chromosomes display a different pattern from that of autosomes, with no introgression of Neanderthal Y chromosomes into *H. sapiens* and less-than-expected introgression of the X chromosome. Because mitochondria and Y chromosomes represent single nonrecombining entities, they may have been lost by random genetic drift. The mitochondrion is transmitted by mothers alone, whereas Y chromosomes are transmitted from father to son. Thus, the lack of introgression of one or the other (but not both) could also result from sex differences between who had children together (for example, no mitochondria transfer occurs if Neanderthal fathers, but not mothers, contributed genetic material).

Bioinformatics Research Centre, Aarhus University, DK-8000 Aarhus C, Denmark. Email: mheide@birc.au.dk

Subsequent to these studies, evidence has accumulated that suggests a much earlier meeting between *H. sapiens* and Neanderthals in which the main gene flow went in the opposite direction (*H. sapiens* to Neanderthals), first based on nuclear genomes (4) and later from mitochondrial data (5) (see the figure). This event affected only Neanderthals and not Denisovans. The gene flow to the nuclear genome was likely only 3 to 6% (6). However, all sequenced Neanderthal mitochondria are much more similar to the human mitochondrion than either are to the Denisovan mitochondrion, suggesting a total replacement of this organelle and evidence that *H. sapiens* females contributed to gene flow. The event has been difficult to date, but an upper bound of about 350,000 years ago can be derived from the genetic divergence of the mitochondrion and a lower bound of about 150,000 years ago from evidence that this gene flow event is shared among all sequenced Neanderthals.

Until the new study by Petr *et al.*, archaeologists had only limited Y chromosome data from two Neanderthals (7) and no information on exchanges of Y chromosomes during the early meeting. The main reason is that the three fully sequenced Neanderthal individuals (8–10) and the single fully sequenced Denisovan individual (11) all happen to be females; no bones with a similar quality of noncontaminated DNA from archaic males were identified. Thus, Petr *et al.* used a capture-based DNA sequencing approach to enrich for Y chromosome sequences in less well-preserved bones from males. They succeeded in getting usable Y chromosome sequences from three male Neanderthals and two male Denisovans. The results mirror exactly the findings from the mitochondrion study—complete replacement of Neanderthal Y chromosomes (and no replacement of Denisovan Y chromosomes) with *H. sapiens* Y chromosomes (see the figure). The molecular dating falls well within the estimates from the mitochondrion and nuclear studies, making it a parsimonious explanation that all admixtures are from the same event.

The new study solves important questions but fosters even more new ones. It unequivocally shows that both male and female *H. sapiens* contributed to gene flow, suggesting that both *H. sapiens* and Neanderthal populations accepted children of mixed heritage. Researchers do not yet have genetic evidence from *H. sapiens* bones outside of Africa for the

period in question, but it seems likely that they will show evidence of Neanderthal admixture. There are no genetic traces of the *H. sapiens* population from the meeting 350,000 to 150,000 years ago in present day humans except for small pieces of the genome that *H. sapiens* eventually got back from Neanderthals in the much later meeting.

A rapid and total replacement of both the Y chromosome and mitochondrion seems too much of a coincidence to be

“...both male and female *H. sapiens* contributed to gene flow, suggesting that both *H. sapiens* and Neanderthal populations accepted children of mixed heritage.”

driven by chance alone, especially given the relatively small contribution of *H. sapiens* to the Neanderthal nuclear genome. Some form of natural selection must have contributed. It is as yet anyone's guess what the selective agent might have been. Because both the Y chromosome and mitochondrion are inherited as nonrecombining units, it is exceedingly difficult to locate targets of natural selection on them.

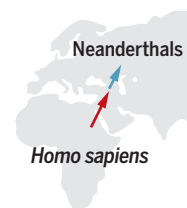
Neanderthals likely had a much lower population size than *H. sapiens* during the 500,000 to 700,000 years of separation (9), making Neanderthals more prone to the accumulation of harmful genetic variants. Petr *et al.* use simulations of accumulations of deleterious variants on the Neanderthal Y chromosome that cause it to have a lower fitness than the *H. sapiens* Y chromosome. The results show that under reasonable parameter assumptions, this process could explain the replacement; but the authors emphasize that this is a possibility and not proof. By the same argument, scientists could expect selection for the *H. sapiens* fragments in the nuclear genome. However, this is not suggested from the low percentage of *H. sapiens* fragments in the Neanderthal nuclear genome. Thus, other selective forces private to the Y chromosome might be at play. Recent results suggest complex replacements of modern human Y chromosomes after the last out-of-Africa event, which are indicative of recurrent positive selection by an unknown agent (12). Y chromosomes have very fast and structurally complex evolution (13), and their variation is associated strongly with male fertility. The introgression patterns of X, the Y chromosome partner, also differs notably between the two gene flow events, with Neanderthal accepting more *H. sapiens* X chromosomes in the early meeting and vice versa in the later meeting. This is the same qualitative pattern seen for the Y chromosome. Thus, another possibility is that the X and Y chromosomes of *H. sapiens* and Neanderthals did not fit well together during male meiosis, and this affected male fertility. Sequencing of male Neanderthal bones from the critical period between 150,000 and 300,000 years ago might resolve these questions. ■

Gene flow in two meetings

(Top) A small group of *Homo sapiens* left Africa for Europe (red arrow), where they transferred genes to Neanderthals (blue arrow) and later went extinct. (Bottom) A second, larger group of *Homo sapiens* left Africa for Europe (thick red arrow), where they received genes from Neanderthals who later went extinct (blue arrow, flow in opposite direction). The tables show the amount of each type of genetic material transferred after the two migrations. ka, thousand years.

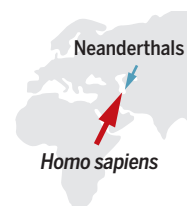
● People transfer ● Gene transfer

Gene flow from *Homo sapiens* to Neanderthals (200 to 300 ka ago)



GENOME COMPONENT	REPLACEMENT (%)
Mitochondrial DNA	100
Y chromosome	100
X chromosome	4–8
Autosomes	3–6

Gene flow from Neanderthals to *Homo sapiens* (40 to 80 ka ago)



GENOME COMPONENT	REPLACEMENT (%)
Mitochondrial DNA	0
Y chromosome	0
X chromosome	<1
Autosomes	15–2

REFERENCES AND NOTES

1. M. Petr *et al.*, *Science* **369**, 1653 (2020).
2. S. Sankararaman, S. Mallick, N. Patterson, D. Reich, *Curr. Biol.* **26**, 1241 (2016).
3. M. Krings *et al.*, *Cell* **90**, 19 (1997).
4. M. Kuhlwilm *et al.*, *Nature* **530**, 429 (2016).
5. C. Posth *et al.*, *Nat. Commun.* **8**, 16046 (2017).
6. M. J. Hubisz, A. L. Williams, A. Siepel, *PLOS Genet.* **16**, e1008895 (2020).
7. M. Hajdinjak *et al.*, *Nature* **555**, 652 (2018).
8. F. Mafessoni *et al.*, *Proc. Natl. Acad. Sci. U.S.A.* **117**, 15132 (2020).
9. K. Prüfer *et al.*, *Science* **358**, 655 (2017).
10. K. Prüfer *et al.*, *Nature* **505**, 43 (2014).
11. M. Meyer *et al.*, *Science* **338**, 222 (2012).
12. P. Hallast *et al.*, *Hum. Genet.* **10.1007/s00439-020-02204-9** (2020).
13. L. Skov, H. Schierup; Danish Pan Genome Consortium, *PLOS Genet.* **13**, e1006834 (2017).

10.1126/science.abe2766



Owls, such as this Eurasian Eagle-Owl (*Bubo bubo*), as well as crows and pigeons have brain organization—and probably cognitive ability—that is similar to mammals.

NEUROSCIENCE

Birds do have a brain cortex—and think

Like mammals, birds have a pallium that sustains correlates of consciousness

By **Suzana Herculano-Houzel**

The term “birdbrain” used to be derogatory. But humans, with their limited brain size, should have known better than to use the meager proportions of the bird brain as an insult. Part of the cause for derision is that the mantle, or pallium, of the bird brain lacks the obvious layering that earned the mammalian pallium its “cerebral cortex” label. However, birds, and particularly corvids (such as ravens), are as cognitively capable as monkeys (1) and even great apes (2). Because their neurons are smaller, the pallium of songbirds and parrots actually comprises many more information-processing neuronal units than the equivalent-sized mammalian cortices (3). On page 1626 of this issue, Nieder *et al.* (4) show that the bird pallium has neurons that represent what it perceives—a hallmark of consciousness. And on page 1585 of this issue, Stacho *et al.* (5) establish that the bird pallium has similar organization to the mammalian cortex.

The studies of Nieder *et al.* and Stacho *et al.* are noteworthy in their own ways, but not because either is the first demonstration of

close parallels between mammalian and bird pallia. That neuroscientists still refer to how bird cognition happens “without a cerebral cortex” (6), as Nieder *et al.* have done themselves (4), is a testament to how neuroscience has grown so much that specialists in different subfields often are not familiar with each other’s findings, even when groundbreaking.

Stating that birds do not have a cerebral cortex has been doubly wrong for several years. Birds do have a cerebral cortex, in the sense that both their pallium and the mammalian counterpart are enormous neuronal populations derived from the same dorsal half of the second neuromere in neural tube development (7). The second neuromere is important: The pallium of birds and mammals lies posterior to the hypothalamus, the true front part of the brain, which is then saddled in development by the rapidly bulging pallium. Owing to the painstaking, systematic comparative analyses of expression patterns of multiple homeobox (Hox) genes that compartmentalize embryonic development, it is now understood that in both birds and mammals, the pallium rests on top of all the neuronal loops formed between spinal cord, hindbrain, midbrain, thalamus, and hypothalamus.

In both birds and mammals, the pallium is the population of neurons that are not a necessary part of the most fundamental cir-

cuits that operate the body. But because the pallium receives copies, through the thalamus, of all that goes on elsewhere, these pallial neurons create new associations that endow animal behavior with flexibility and complexity. So far, it appears that the more neurons there are in the pallium as a whole, regardless of pallial, brain, or body size, the more cognitive capacity is exhibited by the animal (8). Humans remain satisfyingly on top: Despite having only half the mass of an elephant pallium, the human version still has three times its number of neurons, averaging 16 billion (9). Corvids and parrots have upwards of half a billion neurons in their pallia and can have as many as 1 or 2 billion—like monkeys (3).

Additionally, it has been known since 2013 that the circuits formed by the pallial neurons are functionally organized in a similar manner in birds as they are in mammals (10). Using resting-state neuroimaging to infer functional connectivity, the pigeon pallium was shown to be functionally organized and internally connected just like a mouse, monkey, or human pallium, with sensory areas, effector areas, richly interconnected hubs, and highly associative areas in the hippocampus and nidopallium caudolaterale. The nidopallium caudolaterale is the equivalent of the monkey prefrontal cortex (10), the portion of the pallium that is the seat of

Department of Psychology, Department of Biological Sciences, Vanderbilt Brain Institute, Vanderbilt University, Nashville, TN, USA. Email: suzana.herculano@vanderbilt.edu

PHOTO: MASSIMILIANO STICCA/MINDEN PICTURES

the ability to act on thoughts, feelings, and decisions, according to the current reality informed by the senses.

Now, adding to their resting-state neuroimaging tool set the power and high resolution of polarized light microscopy to examine anatomical connectivity, Stacho *et al.* show that the pallia of pigeons and owls, like that of mice, monkeys, and humans, is criss-crossed by fibers that run in orthogonal planes. Repeated imaging of the brain with light shone at different orientations revealed that fibers within and across bird pallial areas are mostly (although not exclusively) organized at right angles, reminiscent of the orthogonal tangential and radial organization of cortical fibers in mammals (17). The broad-minded neuroscientist with some knowledge of developmental biology might not find this surprising; what would be the alternative, a spaghetti-like disorganized jumble of fibers? But then again, the mantra that “birds do not have a cortex” even though they share pallial development and organization with mammals has been repeated so exhaustively that recognizing that columns and layers are actually observed—visible under polarized light if not to the naked eye—brings new hope that this mantra will join the ranks of myth.

If the bird pallium as a whole is organized just like the mammalian pallium, then it follows that the part of the bird pallium that is demonstrably functionally connected like the mammalian prefrontal pallium (the nidopallium caudolaterale) should also function like it. Nieder *et al.*, who established previously that corvids, like macaques, have sensory neurons that represent numeric quantities (12), now move on to this associative part of the bird pallium. They find that, like the macaque prefrontal cortex, the associative pallium of crows is rich in neurons that represent what the animals next report to have seen—whether or not that is what they were shown.

This representation develops over the time lapse of 1 to 2 s between the stimulus disappearing and the animal reporting what it perceived by pecking at a screen either for “yes, there was a stimulus” or for “no, there was no stimulus,” depending on a variable contingency rule. The early activity of these neurons still reflects the physical stimulus presented to the animal, which indicates that they receive secondhand sensory signals. However, as time elapses and (presumably) recurrent, associative cortical circuits progressively shape neuronal activity, the later component of the responses of the same neurons predicts instead what the animal then reports: Did it see a stimulus that indeed was there, or did it think the stimulus was there enough to report it—even if it was not? Future studies will certainly delve into more

complex mental content than simply “Was it there or not?” but concluding that birds do have what it takes to display consciousness—patterns of neuronal activity that represent mental content that drives behavior—now appears inevitable.

Because the common ancestor to birds (and non-avian reptiles) and mammals lived 320 million years ago, Nieder *et al.* infer that consciousness might already have been present then—or might have appeared independently in birds and mammals through convergent evolution. Those hypotheses miss an important point: how fundamental properties of life present themselves at different scales. The widespread occurrence of large mammalian bodies today does not mean that ancestral mammals were large (they were not), nor do the nearly ubiquitous folded cortices of most large mammals today imply that the ancestral cortex was folded [it was not (13)]. The physical properties that make self-avoiding surfaces buckle and fold as they expand under unequal forces apply equally to tiny and enormous cortices, but folds only present themselves past a certain size (14). Expansion of the cortical surface relative to its thickness is required for folds to appear. But that does not imply that folding evolved, because the physical principles that cause it to emerge were always there.

Perhaps the same is true of consciousness: The underpinnings are there whenever there is a pallium, or something connected like a pallium, with associative orthogonal short- and long-range loops on top of the rest of the brain that add flexibility and complexity to behavior. But the level of that complexity, and the extent to which new meanings and possibilities arise, should still scale with the number of units in the system. This would be analogous to the combined achievements of the human species when it consisted of just a few thousand individuals, versus the considerable achievements of 7 billion today. ■

REFERENCES AND NOTES

1. E. L. MacLean *et al.*, *Proc. Natl. Acad. Sci. U.S.A.* **111**, 2140 (2014).
2. C. Kabadayi, L. A. Taylor, A. M. P. von Bayern, M. Osvath, *R. Soc. Open Sci.* **3**, 160104 (2016).
3. S. Olkowicz *et al.*, *Proc. Natl. Acad. Sci. U.S.A.* **113**, 7255 (2016).
4. A. Nieder *et al.*, *Science* **369**, 1626 (2020).
5. M. Stacho *et al.*, *Science* **369**, eabc5534 (2020).
6. O. Güntürkün, T. Bugnyar, *Trends Cogn. Sci.* **20**, 291 (2016).
7. L. Puellès, M. Harrison, G. Paxinos, C. Watson, *Trends Neurosci.* **36**, 570 (2013).
8. S. Herculano-Houzel, *Curr. Opin. Behav. Sci.* **16**, 1 (2017).
9. S. Herculano-Houzel, *The Human Advantage* (MIT Press, 2016).
10. M. Shanahan, V. P. Bingman, T. Shimizu, M. Wild, O. Güntürkün, *Front. Comput. Neurosci.* **7**, 89 (2013).
11. V. J. Wedeen *et al.*, *Science* **335**, 1628 (2012).
12. A. Nieder, *Curr. Opin. Behav. Sci.* **16**, 8 (2017).
13. T. B. Rowe, T. E. Macrini, Z.-X. Luo, *Science* **332**, 955 (2011).
14. B. Mota, S. Herculano-Houzel, *Science* **349**, 74 (2015).

SPECTROSCOPY

Intense x-rays can be (slightly) exciting

Imaging of neutral “survivor” atoms excited by x-ray blasts fights radiation damage

By Thomas Pfeifer

Since their discovery by Röntgen (1) in 1895, x-ray imaging and spectroscopy have revolutionized disciplines as diverse as astrophysics, materials science, chemistry, and the life sciences. However, in the medical context, x-rays are also known for their darker side: They damage tissue. Although even that destructive nature is turned into a benefit in radiation therapy, on a fundamental level, x-rays damage atoms from the inside out: They typically kick out deeply bound electrons, punching a “core hole” into the atom. This unstable situation unleashes a cascade of electronic relaxation events that turn neutral atoms into ions, thus breaking chemical bonds in molecules or creating defects in solids. On page 1630 of this issue, Eichmann *et al.* (2) show how to outpace the radiation damage of x-rays on the fundamental, single-atom level. They detect neutral neon atoms that are just slightly excited, not damaged. Counterintuitively at first, this process benefits from the extremely intense x-rays supplied by a free-electron laser (FEL).

The proof-of-principle setup used by the authors is a simple, elegant realization of a light-matter interaction experiment (see the figure). After a beam of atoms collides with the intense x-ray flashes of the FEL, all of the ions are deflected away, but the remaining neutral atoms hit a position-sensitive detector that is set such that only excited atoms trigger a signal. A characteristic shape on the detector (an “I” marking the spot instead of an “X”) identifies all of the atoms undergoing stimulated x-ray Raman scattering.

Absorbing one x-ray photon creates an unstable core hole (the seed of atomic dam-

Max Planck Institute for Nuclear Physics (MPIK), 69117 Heidelberg, Germany. Center for Quantum Dynamics, Universität Heidelberg, 69120 Heidelberg, Germany. Email: thomas.pfeifer@mpi-hd.mpg.de

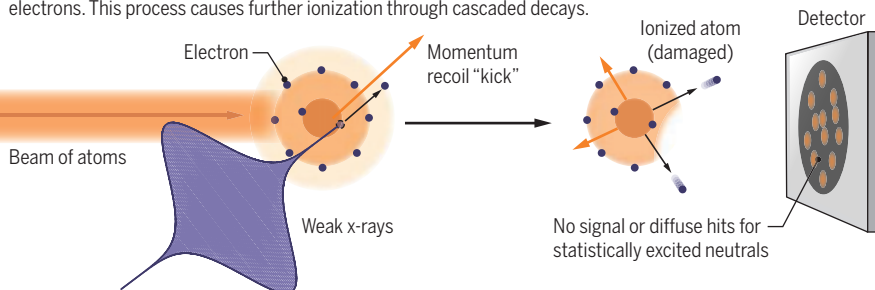
10.1126/science.abe0536

Different x-ray responses

X-rays normally ionize or highly excite atoms out of their core shells. Eichmann *et al.* show how intense x-ray pulses can create only slightly excited neutral atoms formed by promotion of core electrons to high valence states, a key step for site-selective triggering of chemical reaction dynamics.

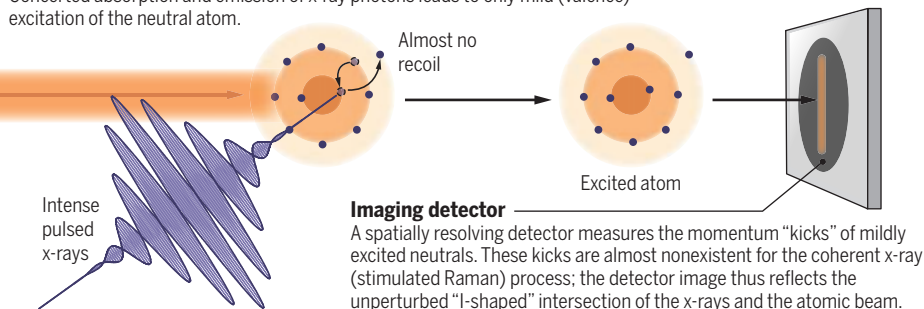
Damaged atoms

When a “normal” x-ray (single photon) is absorbed by an atom, it knocks out core electrons. This process causes further ionization through cascaded decays.



More intense but gently exciting

Intense x-rays can move two electrons through a “nonlinear” two-photon process. Concerted absorption and emission of x-ray photons leads to only mild (valence) excitation of the neutral atom.



age), but stimulated emission of a photon into that same x-ray pulse immediately fills the hole with another outer electron from the same atom, essentially instantly “healing” the atom. This process creates a mildly excited neutral atom that has obtained a soft kick or push along the laser direction, as if it had only interacted with a non-ionizing photon of much lower energy. Atoms undergoing other natural (i.e., statistical) decay processes, such as spontaneous emission of photons or electrons, will suffer a large momentum kick, and thus will be displayed as a diffuse halo on the detector. The nearly negligible momentum transfer of the x-ray-stimulated Raman process, by contrast, arises from the almost perfect compensation of momenta of the co-propagating absorbed and re-emitted photons in the combined nonlinear process of coherent excitation and stimulated emission, respectively.

Stimulated x-ray Raman scattering in a dense medium has previously been observed by a collective (propagation-based) experiment (3). By contrast, Eichmann *et al.* experimentally isolate, extract, and detect exclusively the individual “survivor particles” that were excited but remained neutral in the intense x-ray flash. In the previous approach, the signal light was co-propagating with the intense x-rays and

thus limited the detection of weak signals, whereas neutral-momentum imaging allows a background-free detection with single-particle sensitivity.

One key to the success of this experiment was the high repetition rate of what is currently the world’s most powerful x-ray laser, the European XFEL (EuXFEL) at Schenefeld near Hamburg. With effectively 1000 shots per second and their method to isolate just the atoms undergoing the x-ray-stimulated Raman process, Eichmann *et al.* could optimize the exciting x-ray-atom interaction. The extreme sensitivity of their recoil-imaging approach allowed the fine-tuning of the x-ray properties to maximize the desired “gentle” nonlinear x-ray excitation relative to competing spontaneous decay channels, such as fluorescence or Auger electron decay. By varying the photon energy and intensity of EuXFEL, they obtained an already impressive relative yield of ~10% for the stimulated versus spontaneous Raman processes, which was also confirmed and understood by theoretical modeling. This understanding also showed that the limitations are “just” machine parameters of the FEL. Efficiency could be much improved, such that the stimulated Raman process is favored over the spontaneous Raman process by a factor of >10. What’s still missing

are suitable ways of controlling x-rays that are partly in place at lower-energy FELs (4). Their translation to hard-x-ray FELs would then even allow coherent-control approaches for quantum-state manipulation, such as stimulated Raman adiabatic passage (STIRAP) (5), while also addressing and selectively steering all electrons of an atom down to its core.

A range of opportunities can be expected from this fundamental-physics result. The observed interaction merges x-ray element specificity from core electrons (6) with the chemically relevant excitations of valence orbitals and thus provides a powerful tool for analytical spectroscopy. The authors calculate that signals can be massively enhanced by using two-color modes of operation with few-femtosecond pulse durations, and indeed x-ray FELs are currently being developed in this direction.

The use of two sets of two-color pulses [in the best case with attosecond duration (7)] that take advantage of FEL coherence effects in resonant atomic absorption (8) would allow time-resolved probing of electrons excited at a given atom on one end of a molecule and traveling to a “target” atom on the other end of the molecule. This process is predicted to occur on time scales of only a few femtoseconds (9, 10). The method would implement two-dimensional spectroscopy with x-rays—as conceived quite some time ago (11)—but, as is less commonly known, the signal could consist of massive particles rather than light, as a proof-of-principle experiment at much lower frequencies recently showed (12).

Our improved understanding of fundamental x-ray light-matter interaction keeps driving another revolution, namely comprehensive control and engineering of well-defined quantum states and dynamics of matter on a (sub-)atomic level. The work of Eichmann *et al.* is part of an evolving skill set for taming the darker side of x-rays. The result will be sharper tools to control their exciting properties. ■

REFERENCES AND NOTES

- W. C. Roentgen, *Nature* **53**, 274 (1896).
- U. Eichmann *et al.*, *Science* **369**, 1630 (2020).
- C. Weninger *et al.*, *Phys. Rev. Lett.* **111**, 233902 (2013).
- E. Ferrari *et al.*, *Nat. Commun.* **7**, 10343 (2016).
- K. Bergmann, H. Theuer, B. W. Shore, *Rev. Mod. Phys.* **70**, 1003 (1998).
- K. Siegbahn, *Science* **217**, 111 (1982).
- J. T. O’Neal *et al.*, *Phys. Rev. Lett.* **125**, 073203 (2020).
- T. Ding *et al.*, *Phys. Rev. Lett.* **123**, 103001 (2019).
- L. S. Cederbaum, J. Zobeley, *Chem. Phys. Lett.* **307**, 205 (1999).
- F. Remacle, R. D. Levine, *Proc. Natl. Acad. Sci. U.S.A.* **103**, 6793 (2006).
- I. V. Schweigert, S. Mukamel, *Phys. Rev. Lett.* **99**, 163001 (2007).
- S. Roeding, T. Brixner, *Nat. Commun.* **9**, 2519 (2018).

10.1126/science.abd6168

POLICY FORUM

REGULATION: COVID-19

Self-experimentation, ethics, and regulation of vaccines

DIY COVID-19 vaccines raise legal and ethical questions

By **Christi J. Guerrini¹**, **Jacob S. Sherkow^{2,3,4}**,
Michelle N. Meyer^{5,6}, **Patricia J. Zettler⁷**

As the coronavirus disease 2019 (COVID-19) pandemic continues to sweep the globe, several groups have been working to develop and self-administer unapproved, unproven interventions that they describe as vaccines for COVID-19 (*1–4*). Some of the interest in these do-it-yourself (DIY) approaches apparently stems from a belief that self-experimentation is never subject to time-consuming ethics board review or regulation, such as by the U.S. Food and Drug Administration (FDA). This belief is legally and factually incorrect, and the misunderstanding has potentially important public health implications. Any failure by the FDA to regulate DIY vaccines would permit vaccines of dubious safety and effectiveness to endanger public health and would signal a lowering of standards that—in an age blighted by vaccine skepticism and during a highly politicized pandemic—could undermine public trust in all vaccines, however developed (*5*). Further, some self-experimentation can qualify as human subjects research that is required to undergo ethics review, by law or institutional policy. Even when ethics review is not required, citizen scientists must take seriously their heightened ethical responsibilities when promoting DIY interventions, especially those with potentially serious public health and societal effects, such as COVID-19 vaccines. Given the proliferation of citizen science efforts to fight COVID-19 and the general confusion (even among sophisticated scientists) that surrounds the regulation of DIY research, regulatory leadership is badly needed.

“THE FDA CAN’T STOP YOU”

In July 2020, six months after the first case of COVID-19 was confirmed in the United States, scientists associated with the Rapid Deployment Vaccine Collaborative (RaDVaC) reported administering to themselves a product of their own making that was intended to be a vaccine against the disease.

As described in the group’s white paper, the putative intranasal vaccine consists of synthetic peptides that mimic those of severe acute respiratory syndrome coronavirus 2 (SARS-CoV-2), the virus that causes COVID-19, and is designed to elicit only a local immune response (*6*).

By its own account, RaDVaC is engaged in “citizen science,” which broadly describes activities having a scientific aim that invite public participation. RaDVaC’s chosen research path—which involves a homemade intervention, an evolving protocol, and unclear plans for collecting and analyzing outcomes data—is in contrast to traditional paths to vaccine development, which require randomized controlled trials (RCTs) with well-defined endpoints, such as demonstrated immune responses, and protocols concerning the retention and use of data.

Although some citizen scientists have antiregulatory leanings, RaDVaC has explained that it is not anti-FDA. Rather, its stated mission is a humanitarian one, animated by a belief that open, crowdsourced vaccine efforts will hasten the widespread availability of a potentially life-saving vaccine through development activities that it believes are not subject to FDA regulation (*6*). To that end, RaDVaC published on the internet instructions on how to self-manufacture and self-administer its DIY vaccine. RaDVaC also has provided materials for those activities, reporting as of several weeks ago the delivery of vaccine materials to 70 individuals (*1*). RaDVaC has made clear to potential users that its vaccine has not been reviewed or approved by the FDA. It also believes, as one of its leading scientists stated, “If you are just making it and taking it yourself, the FDA can’t stop you” (*1*).

RaDVaC is not alone. A small group of biohackers known as Project McAfee—after the antiviral software—reconstructed and injected themselves with a vaccine previously tested only in monkeys (*2*). Other known DIY COVID-19 vaccine efforts in the United States include a biohacker who self-administered a DIY vaccine that has reportedly been taken by at least 10 other

people (*3*) and a microbiologist and founder of a small biotech company who sold and administered an unapproved vaccine to about 30 people (*4*). Given the global reach of the disease and widespread involvement of citizen scientists in biomedical activities, other efforts are likely under way, both in the United States and elsewhere.

THE FDA AND SELF-EXPERIMENTATION

In the United States, it is true that the FDA’s authority does not extend to some instances of self-experimentation, for which there is a long tradition in medicine, including vaccine self-experimentation (*7, 8*). But self-experimentation, for the FDA’s purposes, is a narrow category. The FDA’s jurisdiction would not extend to a citizen scientist insufflating an experimental vaccine that they created entirely from materials around their house. Nor would it extend to the distribution of only information about a DIY vaccine, such as suggestions for where to acquire materials or instructions for making and self-administering it (*9*).

However, the FDA does have jurisdiction over other forms of self-experimentation

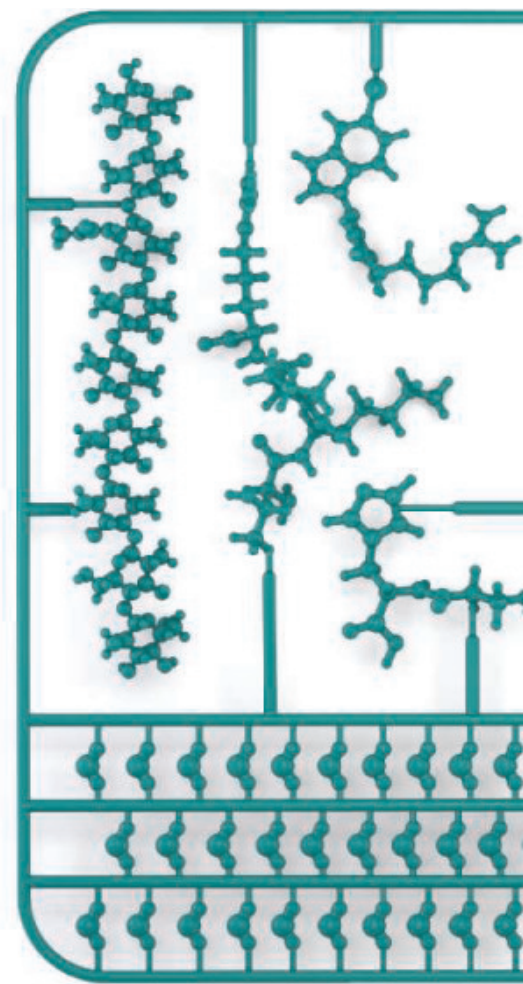
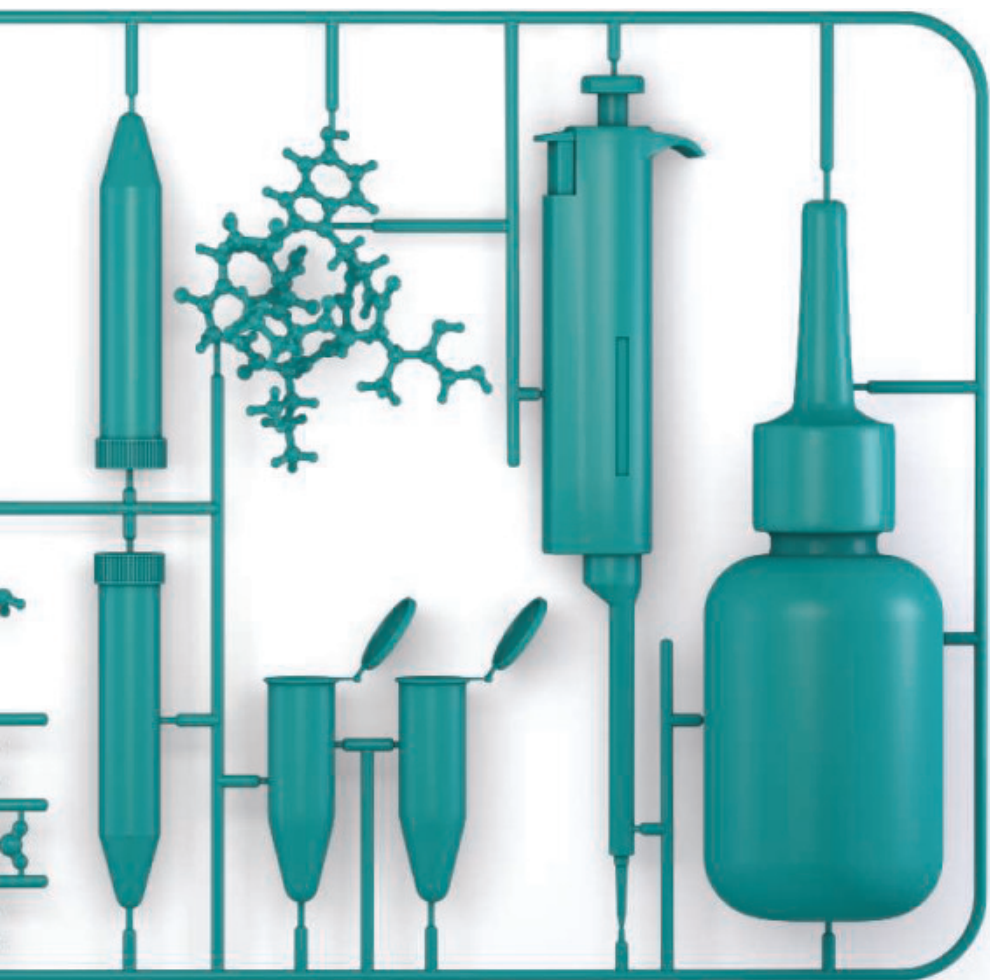


ILLUSTRATION: V. ALTOUNIAN/SCIENCE



tation. Under U.S. federal law, the FDA is authorized to regulate vaccines that cross state lines. This includes not only the final product itself but also more mundane intermediate components, such as reagents (9). The FDA's authority covers such vaccines regardless of whether they are developed by traditional industry players or citizen scientists; administered by a health professional or the patient; or, in many cases, sold for money or freely given away. The FDA's authority is meant to be broad and national in scope rather than leaving things to a fractured pattern of state regulation or jurisdiction that turns on fine technicalities of how money may or may not have changed hands. This ensures that manufacturers and distributors do not easily escape expert public health oversight. Distributing materials intended for the self-manufacture of any vaccine therefore falls squarely within the FDA's jurisdiction

and its public health mission.

Other self-experimentation projects have similarly crossed the line into FDA-regulated product development. For example, in late 2017, in response to concerns about DIY gene-editing kits, the FDA stated that any distribution of gene editing materials intended for use in humans qualifies as gene therapy subject to the FDA's requirements (10). This reach of the FDA's authority is justified. When self-experimenters provide interventions or their components to others who might follow in their footsteps, this has a serious potential to injure other experimenters, among other negative externalities.

THE COMMON RULE AND ETHICS

An FDA-authorized Investigational New Drug (IND) application permits unapproved drugs (and their components) to legally cross states lines and be investigated

in humans, subject to certain requirements, including approval by an Institutional Review Board (IRB). Additionally, even with respect to DIY vaccines outside the FDA's authority, research with human participants is independently regulated in the United States by the Common Rule when the research is federally conducted or funded. Most self-experimentation is neither, but research institutions' own policies generally subject all human participant research in which the institution is "engaged" to the Common Rule's requirement of advance review by an IRB. IRBs help ensure that a study's risks are reasonable in relation to its expected benefits and that participants provide voluntary, informed consent. So long as a self-experiment meets the Common Rule's definition of "research" and the self-experimenter's institution is engaged in that research—say, because it occurs on institutional property or uses institutional resources—self-experimentation likely requires IRB review (11). RaDVaC's early systematic efforts to develop their product clearly meet this definition of research, but there is no evidence that any research institution was engaged in it.

Whether or not required by federal law or institutional policy, the kind of independent, prospective review that IRBs provide is ethically important, especially for public health interventions. Although the harms of some DIY interventions tend to be confined to the researchers themselves, DIY vaccines have the potential to harm others, directly and indirectly.

Those potential harms are evident. Both users and bystanders are harmed by ineffective vaccines when users' false reassurance that they are immune from infection causes them to take risks that they might not otherwise take, such as traveling in crowds. Users of a DIY vaccine might also be unwilling or ineligible to participate in future clinical trials for traditional vaccines. The COVID-19 pandemic has already seen widespread off-protocol use of unproven interventions frustrate attempts to rigorously evaluate those or other interventions (12). At the same time, polls show that many are reluctant to take any COVID-19 vaccine. If scientists—and especially those with elite training or affiliations—herald a readily available vaccine, those who are not hesitant might refuse to take the risk of enrolling in a trial and being randomized to placebo.

¹Center for Medical Ethics and Health Policy, Baylor College of Medicine, Houston, TX, USA. ²College of Law, University of Illinois at Urbana-Champaign, Champaign, IL, USA. ³Carl R. Woese Institute for Genomic Biology, University of Illinois at Urbana-Champaign, Urbana, IL, USA. ⁴Center for Advanced Studies in Biomedical Innovation Law, University of Copenhagen Faculty of Law, Copenhagen, Denmark. ⁵Center for Translational Bioethics and Health Care Policy and Steele Institute for Health Innovation, Geisinger Health System, Danville, PA, USA. ⁶Geisinger Commonwealth School of Medicine, Scranton, PA, USA. ⁷Moritz College of Law, The James Comprehensive Cancer Center and Drug Enforcement and Policy Center, Ohio State University, Columbus, OH, USA. Email: guerrini@bcm.edu; jsherkow@illinois.edu; mmeyer@geisinger.edu; zettler.25@osu.edu

Making an untested DIY vaccine accessible to the general public also runs the risk, as RaDVaC's white paper acknowledges, that lay users might injure themselves as a result of improper preparation, incorrect administration, or heightened allergic or other reactions. These risks raise questions about whether such users are able to give meaningful consent to a DIY vaccine. As demonstrated by reports of desperate individuals drinking cleaning products in an effort to prevent or treat COVID-19, not all individuals attracted to DIY vaccines will have the technical know-how to safely engage in self-experimentation or will invest the time to learn how to do so. Experts can sometimes suffer from a curse of knowledge that leads them to underestimate the risk that less sophisticated users may flub their instructions.

Last, it is concerning that RaDVaC apparently hopes for its DIY vaccine to be very widely adopted but has not disclosed any plans for systematically establishing its safety or efficacy, such as through RCTs. During a pandemic, it is tempting to believe that an intervention that shows early promise has been "proven enough" to justify widespread use (13). Those who are intellectually invested in an intervention may be especially so tempted, perhaps even deeming RCTs, which randomize some participants to placebo, unethical (14). All scientists must resist the temptation to view the rigorous study of COVID-19 vaccine safety and effectiveness as a bureaucratic step that can be skipped. Research that enables us to confidently conclude that a vaccine is safe and effective will take time, whether or not it is overseen by the FDA. But that research, simply, is critical.

ROLES FOR THE FDA AND SCIENTISTS

Given the risks to public health from unsafe or ineffective vaccines, regulatory leadership is needed. First, the FDA should issue a statement clarifying both its authority over, and its intent to regulate, DIY COVID-19 vaccines, as it did with DIY gene-editing kits. This statement should include, at a minimum, clarification that vaccine research, manufacture, distribution, and administration—by anyone—can be subject to regulation. For those activities within its jurisdiction, the FDA has a range of enforcement tools available to it, including sending Warning Letters and imposing civil and criminal penalties. Indeed, the FDA has already sent a Warning Letter to one company, North Coast Biologics, whose founder sold and administered an unapproved COVID-19 vaccine to friends

(4). Explaining how the FDA intends to enforce its authority against citizen science groups can help give fair warning to those who might underestimate the scope of FDA jurisdiction as well as reassure those who are not likely to face enforcement actions.

Although appropriate enforcement of the FDA's authority is critical, the objective should not be to stop all citizen sci-

"Although appropriate enforcement of the FDA's authority is critical, the objective should not be to stop all citizen science research..."

ence research; that would be futile given the popularity and reach of citizen science. But more importantly, such a strategy would imprudently deny society the many benefits of citizen science, including its potential contributions to scientific discovery (9, 15). In recognition of these benefits, the FDA should consider ways to support citizen science research while promoting trust in FDA and research processes, including establishing new channels for engaging with citizen scientists working on COVID-19 solutions. One possibility is to designate FDA staff knowledgeable about citizen science objectives and communities to field questions from citizen scientists, provide feedback on their projects (such as through pre-IND meetings, which are an established way for the FDA to discuss product development plans), and, as necessary, help citizen scientists connect with other staff within the FDA with relevant scientific expertise. More citizen scientists would be encouraged to reach out to the FDA if it were easy for them to identify an office to call with questions. This would require the person speaking with them to be genuinely invested in helping them—even if that ultimately means explaining how a project might violate FDA rules.

By adopting a transparent, collaborative approach to citizen science, the FDA can encourage trust, which is particularly important right now amid concerns about political interference with the FDA's work. At the same time, the FDA can stay apprised of promising solutions that may emerge from these communities, as well as their failures. During a pandemic, this is precisely the kind of information that regulatory authorities should want to know—and without delay.

Although many citizen scientists appear to take seriously the ethical responsibilities associated with their activities, it is important to recognize that those responsibilities expand when public health is at

stake, such as with COVID-19 vaccine development. Characterizing or positioning research as self-experimentation does not eliminate risks to bystanders or the collective good. Given those potential risks, citizen scientists who are involved in open vaccine development and testing efforts outside of traditional scientific institutions should seek review by an independent

IRB. The cost is not necessarily prohibitive for all projects and should be prioritized the same as critical safety equipment. Ethical and efficient development of a vaccine shown to be safe and effective against COVID-19, and broad dissemination of such a vaccine, are goals we all

share and should be able to work together to achieve. ■

REFERENCES AND NOTES

1. A. Regalado, *MIT Tech. Rev.* 29 July 2020; www.technologyreview.com/2020/07/29/1005720/george-church-diy-coronavirus-vaccine.
2. K.V. Brown, *Bloomberg* 25 June 2020; www.bloomberg.com/news/articles/2020-06-25/one-biohacker-s-improbable-bid-to-make-a-diy-covid-19-vaccine.
3. The Thought Emporium, *YouTube* 24 July 2020; <https://www.youtube.com/watch?v=HjDH6bXF4ow&t=67m47s>.
4. H. Murphy, *New York Times* 1 September 2020.
5. A. Shah, P.W. Marks, S.M. Hahn, *JAMA* **324**, 931 (2020).
6. P. Estep et al., "SARS-CoV-2 (2019-nCoV) vaccine" (RaDVaC, 2020); <https://radvac.org/wp-content/uploads/2020/07/White-Paper-SARS-CoV-2-vaccine-ver-2-3-2.pdf>.
7. A.B. Weisse, *Tex. Heart Inst. J.* **39**, 51 (2012).
8. F. Fenner et al., in *Smallpox and Its Eradication* (World Health Organization, 1988), pp. 245–276.
9. C.J. Guerrini, G.E. Spencer, P.J. Zettler, *North Carol. Law Rev.* **97**, 1399 (2019).
10. FDA, Information about self-administration of gene therapy (21 November 2017); www.fda.gov/BiologicsBloodVaccines/CellularGeneTherapyProducts/ucm586343.htm.
11. M.N. Meyer, *J. Law Med. Ethics* **48** (suppl. 1), 60 (2020).
12. R.M. Califf, A.F. Hernandez, M. Landray, *JAMA* **324**, 625 (2020).
13. A.J. London, J. Kimmelman, *Science* **368**, 476 (2020).
14. S. Sayare, *New York Times Mag.* 12 May 2020; www.nytimes.com/2020/05/12/magazine/didier-raoult-hydroxychloroquine.html.
15. P.J. Zettler, C.J. Guerrini, J.S. Sherkow, *Science* **365**, 34 (2019).

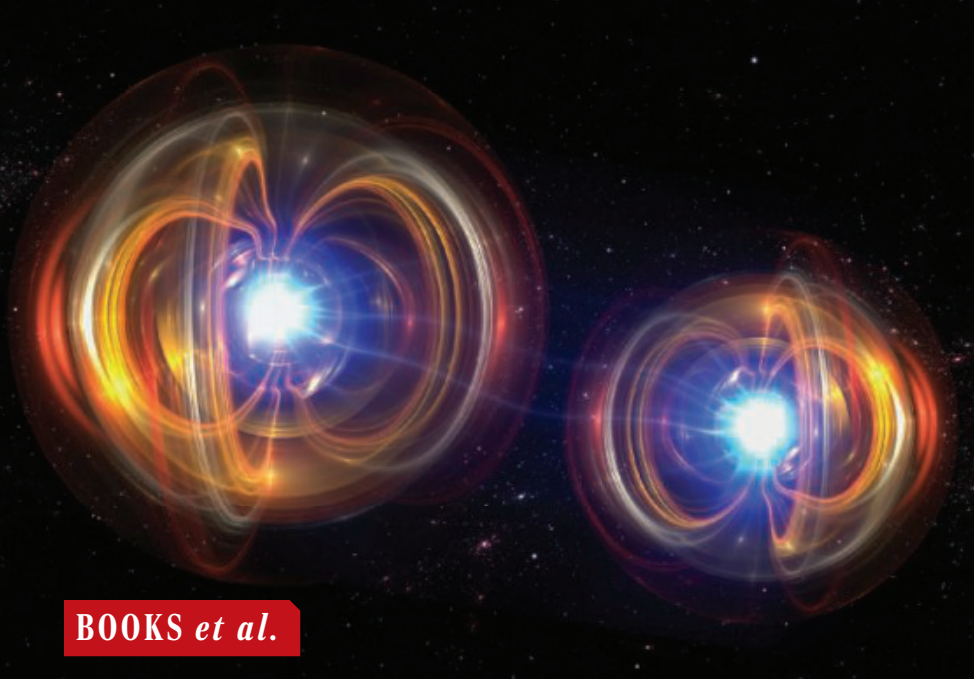
ACKNOWLEDGMENTS

Funding: C.J.G.'s involvement in development of this manuscript was funded by National Human Genome Research Institute grant K01-HG009355 (C.J.G., principal investigator). All authors contributed to the conceptualization, drafting, and critical revision of the manuscript. **Competing interests:** M.N.M. reports having had conversations, for a brief period of time in early April 2020, with some members of what would become RaDVaC in which she provided comments consistent with this article. She also reports having served, from 2014 to 2019, on the Board of Directors of PersonalGenomes.org, a 501(c)(3) founded by George Church, a member of RaDVaC. All other authors declare no competing interests. C.J.G. and P.J.Z. report having participated in conversations with citizen scientists interested in establishing oversight mechanisms for citizen science.

Published online 17 September 2020

10.1126/science.abe1963

sciencemag.org **SCIENCE**



BOOKS *et al.*

QUANTUM MECHANICS

Understanding quantum cause and effect

Correlations at a distance needn't necessarily be "spooky"

By Allen Stairs

If you read a randomly selected non-technical account of quantum entanglement, you will likely be told that measuring a particle in one place can instantly change another particle elsewhere, no matter the distance between the two. Surprisingly, this is something that Paul Halpern never claims in his new book, *Synchronicity*. As the title implies, the central concept of his century-spanning tale is "synchronicity," a term coined by psychoanalyst Carl Jung, who was inspired by conversations with physicists Albert Einstein and Wolfgang Pauli, to connote an "acausal connecting principle." Quantum correlations, in Halpern's view, are a special case of synchronicity.

The book weaves together two themes, the first being the centuries-long development of the notion of causality. Halpern does not explicitly define causality, but it is what Einstein had in mind when he spoke of the principle of contiguity: influence propagating at finite speed without leaping over gaps. Electromagnetism is a paradigm case. The book's other theme is the history of various noncausal explanatory schemes. Some of these veer toward wishful

thinking (for example, Kepler's attempt to fit the orbits of the planets into a scheme based on the five Platonic solids) or outright woo (for example, Pythagorean number mysticism or some of Jung's more extravagant claims about archetypes). But others provide deep insights into the physical world.

Halpern devotes a chapter to symmetry arguments, giving lay readers a window into a critical feature of physical theory and an introduction to the brilliant mathematician Emmy Noether. Explanations of connection that rely on symmetry are noncausal, but Halpern is also open to other acausal forms of explanation. For him, quantum entanglement begs to be understood as a kind of acausal connection. Much of the chapter called "Reality's Rodeo" is devoted to this topic and to John Bell's celebrated theorem, which postulates that ordinary causal explanations cannot account for quantum correlations.

Correlations between outcomes of measurements performed on entangled particles inspired the idea of "spooky action at a distance." However, correlation at a distance needn't necessarily be spooky. If a particle's behavior is determined by the local environment and by properties the particle acquired at its source—if it satisfies

Quantum entanglement begs to be understood as a kind of acausal connection, argues Halpern.

so-called "local realism"—then it is conceivable that the source could orchestrate correlations between what is inscribed in each of a pair of particles.

Bell showed that this idea cannot be extended to quantum mechanics. He uncovered constraints on how probabilistic correlations can be knit together by local realistic models. Such models predict statistics that obey what we now call "Bell inequalities," but these statistics are inconsistent with quantum theory, and experimental data support quantum theory.

Halpern favors an acausal, synchronistic approach to quantum correlations, although just what that might amount to is still an open question. There are serious arguments to be made for thinking that quantum correlations require superluminal action at a distance, but that does not sound like synchronicity. David Bohm's development of de Broglie's pilot wave theory, which posits high-dimensional waves that guide quantum particles, incorporates such influences. However, Halpern notes that Bohm's later work develops the idea of an "implicate order" underlying space-time. This may be a better fit for the idea of synchronicity. Some physicists even believe that quantum entanglement might be the ultimate source of space-time. If so, causality would rest on entanglement.

More generally, instead of looking for an explanation for quantum entanglement, we might consider it part of our basic explanatory machinery. Quantum states fit together in Hilbert space, an elegant abstraction from ordinary physical space that Halpern describes fancifully as akin to "a kind of network of utility corridors behind the scenes of an active office building." If each of two particles is represented by a Hilbert space, the only way to build a Hilbert space for the pair guarantees the existence of entangled states, with their attendant unorthodox statistical predictions.

So-called spooky correlations could exist in such a scenario without causal mechanisms.

Whatever one's position, *Synchronicity* is an entertaining read and provides a valuable service. Although they are important, causal mechanisms are not the only tools available for understanding the world. The book invites nonspecialists to widen their appreciation of the range of what explanation in science could amount to. ■



Synchronicity
Paul Halpern
Basic Books, 2020.
304 pp.

The reviewer is at the Department of Philosophy, University of Maryland, College Park, MD 20742, USA. Email: stairs@umd.edu

10.1126/science.abe0805

ARCHAEOLOGY

The race to decipher Egyptian hieroglyphs

A pair of scholars recount the rivalry that defined efforts to interpret the Rosetta stone

By **Andrew Robinson**

The Rosetta stone, inscribed in 196 BCE during the reign of the Greco-Egyptian ruler Ptolemy V and discovered in Egypt by engineers of Napoleon Bonaparte's army in 1799, is a bilingual inscription written in two of the ancient Egyptian scripts—hieroglyphic and demotic—and the Greek alphabet. From 1815 to 1823, it served as the key that unlocked the decipherment of the Egyptian hieroglyphs through the largely independent labors of the English polymath Thomas Young and the French linguist and archaeologist Jean-François Champollion, who is generally regarded as the founder of Egyptology.

Numerous Rosetta stone-related academic and popular studies have been published, including various biographies of both Champollion and Young, who strongly differed in intellectual outlook and personality. *The Riddle of the Rosetta* offers further commentary on these two individuals, their scholarship, and their rivalry, based on almost a decade of research by the book's authors, Jed Buchwald and Diane Greco Josefowicz.

By comparing the Rosetta stone's hieroglyphic and demotic inscriptions, Young correctly concluded in 1815 that demotic script consisted of "imitations of the hieroglyphics...mixed with the letters of the alphabet." He next read the hieroglyphic name of Ptolemy on the stone by analyzing it phonetically, justifying this approach on the grounds that it was a non-Egyptian name. But, like the ancient Greeks and Romans, Young wrongly assumed that the native Egyptian words in the hieroglyphic script were probably nonphonetic, representing ideas rather than sounds.

In April 1821, Champollion categorically stated in a misguided publication (which

he later withdrew) that the three ancient Egyptian scripts—hieroglyphic, hieratic, and demotic—represented things or ideas, not sounds. He reaffirmed this belief in October 1822 on the first page of his most famous publication, *Lettre à M. Dacier*: "I hope it is not too rash for me to say that I have succeeded in demonstrating that these two forms of writing [hieratic and demotic] are neither of them alphabetic, as has been so generally thought, but ideographic, like the hieroglyphs themselves, that is to say, depicting the ideas and not the sounds of the language."

Although Champollion's statement seemed to exclude even the slightest possibility of a



The French linguist Jean-François Champollion (left) ultimately cracked the Rosetta code, aided by earlier insights provided by the English polymath Thomas Young (right).

phonetic element in Egyptian scripts, this appears to have been unintentional, because he made one crucial exception in the *Lettre*, undoubtedly influenced by Young's prior work: Hieroglyphs could represent sounds when used phonetically to write foreign proper names in cartouches. This allowed Champollion to justify the *Lettre*'s phonetic transliterations of the cartouches of many foreign rulers of Egypt, such as Alexander, Cleopatra, and Ptolemy, and its celebrated list of hieroglyphic and demotic "phonetic signs" supposedly used for writing only these foreign names.

Soon after, however, Champollion radically changed his mind about the Egyptian scripts upon reading the name of Ramesses,

The Riddle of the Rosetta

Jed Z. Buchwald and
Diane Greco Josefowicz
Princeton University Press,
2020. 576 pp.



a historically known, native Egyptian pharaoh, written in a cartouche—a possibility hinted at by Young in 1819. Having applied his growing hieroglyphic "alphabet" to many native Egyptian words, Champollion was thrilled to find that it produced credible transliterations of them that were recognizable from Coptic vocabularies. In April 1823, he announced to the Academy of Inscriptions in Paris that there was, after all, a major phonetic hieroglyphic component that had existed long before the Greco-Roman period—the essential insight that enabled his decipherments in Egypt in 1828–29.

In my view, as a biographer of both Champollion and Young, the single most fascinating aspect of the decipherment is that both a polymath and a specialist were required. Young's myriad-mindedness provided some vital clues early on, but unlike Champollion, Young was far from obsessed with ancient Egypt. His versatility obstructed him from making further progress. Conversely, Champollion's single-mindedness hindered him from spotting these clues, but once they

were in place, his tunnel vision allowed him to begin to perceive the system behind the signs. What a pity that the two scholars, despite being in touch, never truly collaborated. (The "intemperate" Champollion refused to admit his debt to Young.)

Combining exhaustive excavation of British and French archives with eclectic biographical elements, this valuable new book explains, so far as the surviving evidence allows, the twists and turns behind the perpetually fascinating decipherment. Although aimed primarily at scholars of this subject, the book will surely intrigue any reader attracted to the ethos of the Enlightenment. ■

The reviewer is the author of *The Last Man Who Knew Everything* (Oneworld Publications, 2007) and *Cracking the Egyptian Code* (Oxford Univ. Press, 2012).
Email: andrew@andrew-robinson.org



LETTERS

India's state of Bihar suffers from floods that will likely become more frequent with climate change.

Edited by Jennifer Sills

India needs an effective flood policy

Several Indian states are currently suffering from devastating floods that have killed hundreds and rendered millions homeless (1, 2). Flooding in the state of Bihar has been a chronic problem for decades (3), but few concrete steps have been taken to effectively manage these deluges. For the past 50 years, the government policy in the Kosi River Basin—a river known for flooding—has been to build new embankments and reinforce old ones (4) without properly taking environmental and geomorphic factors into consideration. Himalayan rivers carry a tremendous amount of sediments, and the embankments severely constrict the river flow, resulting in massive siltation in the channel beds, which at some locations are now higher than the adjacent floodplains (5). The geomorphic transformation due to embankments has made flooding worse (4).

Climate change will result in even more destructive floods in the future (6). The Bihar government acknowledged this trend in their disaster management plan for 2015 to 2030 (7) yet has taken no concrete science-based steps to address the growing threat. This year, for example, the government blamed Nepal for the devastating floods (8), and the official mitigation policy remained centered on embankments (9).

It is imperative that the government adopt strategies grounded in robust science to minimize future flood damage. For example, reconnecting parts of the river to its historical floodplain could mitigate harm from flooding. Where substantial riverbed aggradation has occurred, silt should be removed from the channel to ensure that it is below the floodplain. Where appropriate, embankments should be removed or lowered to distribute flood water over a larger area. Remaining embankments should be set farther back from the river to provide additional areas to accommodate flooding as well as areas where water can be safely diverted from the main channel and into the former floodplain. This “room for the river” approach has been successful elsewhere (10). The project should be developed in collaboration with all relevant stakeholders, including those across state and international borders, and it should be designed to account for relevant risk factors such as the probability of high-magnitude floods and the future changes in precipitation, streamflow, population, land cover, and flood frequency and magnitude.

The recurring floods in Bihar in the past decades have been devastating. Bihar has lost 3% of its gross state domestic product due to flooding (11) and is among the poorest Indian states (12). India's most vulnerable people will suffer even more due to climate change if sustainable long-term strategies are not adopted with urgency. Implementing such a project would be challenging and expensive; an effective plan is likely to have

substantial monetary costs and may require relocating large numbers of people away from floodplains. However, the benefits of such a project have been shown to outweigh the costs and challenges (10).

Yusuf Jameel^{1*}, Mason Stahl², Shahryar Ahmad³, Abhinav Kumar⁴, Gaëlle Perrier⁵

¹Department of Civil and Environmental Engineering, Massachusetts Institute of Technology, Cambridge, MA 02139, USA. ²Department of Geology, Union College, Schenectady, NY 12308, USA. ³Department of Civil and Environmental Engineering, University of Washington, Seattle, WA 98195, USA. ⁴Department of Chemistry, The University of Texas at Austin, Austin, TX 78712, USA. ⁵Department of Sociology, University of Utah, Salt Lake City, UT 84112, USA. *Corresponding author. Email: yjameel@mit.edu

REFERENCES AND NOTES

1. “Monsoons slam South Asia, displacing millions in Bangladesh and India,” *The New York Times* (2020).
2. “Bihar: Destroyed lives and submerged homes in flood-hit India,” *BBC News* (2020).
3. J. A. Rorabacher, *Econ. Polit. Wkly.* **43**, 45 (2008).
4. R. Sinha, G. V. Bapalu, L. K. Singh, B. Rath, *J. Indian Soc. Remote Sens.* **36**, 335 (2008).
5. R. Sinha et al., *J. Hydrol.* **570**, 156 (2019).
6. H. Ali, P. Modi, V. Mishra, *Weather Clim. Extrem.* **25**, 100212 (2019).
7. Government of Bihar, “Roadmap for disaster risk reduction 2015–2030” (2015); <http://disastermgmt.bih.nic.in/BCDRR20152030.htm> [in Hindi].
8. “Bihar Floods: Parliamentary Standing Committee questions Bihar Government over floods, but officials blame Nepal: Sources,” *NDTV* (2020).
9. Government of Bihar, Water Resources Department (2015); www.fmiscwrbihar.gov.in:8090/Plan_New_Flood_ProWrk.aspx.
10. S. L. Postel, *Replenish: The Virtuous Cycle of Water and Prosperity* (Island Press, 2017).
11. Y. Parida, S. Saini, J. R. Chowdhury, Economic growth in the aftermath of floods in Indian states. *Environ. Dev. Sustain.*, 10.1007/s10668-020-00595-3 (2020).
12. Government of India, National Institution for Transforming India, SDG India Index and Dashboard, iTech Mission (2019); <https://sdgindiaindex.niti.gov.in/#/ranking> (click the second tab at the top: “No Poverty”).

10.1126/science.abe2962

Traditional Knowledge underlies One Health

The degradation of natural environments is a major driver of disease spread from animals to humans (1). The One Health strategy, which links human, animal, and environmental health, has been central to discussions about recovering from the coronavirus disease 2019 (COVID-19) pandemic and preventing the spread of the next zoonotic disease (2). However, scientists and policy-makers often overlook evidence that the One Health paradigm is already embedded in Indigenous values, worldviews, and laws (3). To maximize the effectiveness of the One Health approach, Indigenous principles and inputs should inform both the way it is taught in emerging One Health academic programs and university courses and its application (4) from the Arctic (5) to the tropics.

Traditional Knowledge held by Indigenous Peoples is not only a knowledge system; it is also a process (6) by which resilience to past environmental change and previous disease outbreaks was achieved. Traditional Knowledge holders are intimately familiar with environmental histories and with ways of living respectfully and reciprocally with the land (7). With this knowledge and these processes, they can guide adaptation strategies and ecological restoration plans to achieve sustainability, aided by Western science (8).

The vital role of Indigenous Peoples' lands and the success of Indigenous environmental stewardship in sustaining thriving habitats and biodiversity are well documented (9). The numbers of bird, mammal, reptile, and amphibian species on lands that are managed or co-managed by Indigenous Peoples are equal to or higher than the numbers of species on protected lands (10). Investment in Indigenous Protected and Conserved Areas (11, 12), Indigenous guardian programs, and land-based education are essential to a One Health agenda.

As we mobilize knowledge for recovery and reimagine the ways in which we live and consume in the wake of COVID-19—and amid the ongoing climate and biodiversity emergencies—partnering with holders of Traditional Knowledge can help drive systemic change by transforming our relationships with the Earth and with each other.

Joe Copper Jack^{1*}, Jared Gonet², Anne Mease³, Katarzyna Nowak^{3,4*}

¹Traditional Knowledge Holder, Whitehorse, YT Y1A 4M5, Canada. ²Yukon University/University of Alberta, Whitehorse, YT Y1A 5K4, Canada. ³Canadian Parks and Wilderness Society,

Whitehorse, YT Y1A 2C9, Canada. ⁴The Safina Center, Setauket, NY 11733, USA.

*Corresponding author. Email: ticho69@northwestel.net; knowak02@gmail.com

REFERENCES AND NOTES

1. Secretariat of the Convention on Biological Diversity, "Global Biodiversity Outlook 5" (2020); <http://cbd.int/gbo/gbo5/publication/gbo-5-en.pdf>.
2. J. H. Amuasi *et al.*, *Lancet* **395**, 1543 (2020).
3. K. Hueffer, M. Ehrlander, K. Etz, A. Reynolds, *Int. J. Circumpolar Health* **78**, 1607502 (2019).
4. S. Montesanti, W. E. Thurston, in *Case Studies in One Health: Solving Complex Problems in a Changing World*, S. Cork *et al.*, Eds. (5m Publishing, 2015), chap. 28.
5. Sustainable Development Working Group (SDWG) and Arctic Council, "One Health: Operationalizing One Health in the Arctic: Achievements report" (2017); <https://oaarchive.arctic-council.org/bitstream/handle/11374/1956/One-Health-Report-for-May-2017-final-SA0-edit.pdf>.
6. F. Berkes, *J. R. Soc. New Zealand* **39**, 151 (2009).
7. R. W. Kimmerer, in *Traditional Ecological Knowledge*, M. K. Nelson, D. Shilling, Eds. (Cambridge University Press, 2018), chap. 3.
8. F. Mazzocchi, *Anthropocene Rev.* **7**, 77 (2020).
9. C. J. O'Bryan *et al.*, *Conserv. Biol.* doi.org/10.1111/cobi.13620 (2020).
10. R. Shuster *et al.*, *Environ. Sci. Pol.* **101**, 1 (2019).
11. Indigenous Circle of Experts, "We rise together: Achieving pathway to Canada Target 1 through the creation of Indigenous Protected and Conserved Areas in the spirit and practice of reconciliation" (2018); https://static1.squarespace.com/static/57e007452e69cf9a7af0a033/t/5ab94aca6d2a7338ecb1d05e/1522092766605/PA234-ICE_Report_2018_Mar_22_web.pdf.
12. T. T. Tran *et al.*, *Biol. Conserv.* **241**, 108271 (2020).

COMPETING INTERESTS

J.C.J. is senior policy and planning coordinator at the Yukon Land Use Planning Council. J.G. is president of the Board of the Yukon Conservation Society.

10.1126/science.abe2401

Swiss law would weaken wildlife protection

In September 2019, the Swiss parliament approved a change to the law on hunting and protection of wild mammals and birds (1). The modified law is likely to substantially harm already threatened species. In response, concerned citizens collected signatures to trigger a referendum vote. On 27 September, the people of Switzerland will decide whether the country will enact this law (2).

The proposed change to the law introduces a new category of species called "protected but hunted," which includes the wolf (*Canis lupus*) and the ibex (*Capra ibex*). The new rules would allow people to cull the wolf population, the latest minimum count of which is 70 (3), during 5 months of the year. The hunting season of the ibex would be extended from 3 to 4 months.

Checks and balances in wildlife conservation would be methodically weakened by the change. The list of "protected but

hunted" species will be open to changes by executive decrees of the Federal Council, without requiring parliamentary approval. Nature protection organizations will have fewer opportunities to litigate against decisions to hunt. The modification would further reduce federal power over hunting by delegating decisions to kill "protected but hunted" species to the cantonal states.

The law would also disregard science and conservation efforts by introducing justifications for hunting "protected but hunted" species that are based on hazard criteria. Hunting of species in that category would be allowed for unspecified hunting reasons, to keep populations at an arbitrarily suitable level, to prevent damages to livestock and infrastructure before any damage has occurred, and because the animals attract the attention of people. The hunting of "protected but hunted" species would be allowed even in strictly protected game reserves.

These legal changes were proposed despite the United Nations' call for a focused effort on biodiversity goals in 2020 (4). They are an affront to the principle of non-regression of environmental laws (5). Switzerland, one of the world's wealthiest countries, should oppose narrow sectorial interests and work to preserve and restore biodiversity.

Raphaël Arlettaz^{1*} and Guillaume Chapron²

¹Institute of Ecology and Evolution, University of Bern, 3012 Bern, Switzerland. ²Department of Ecology, Swedish University of Agricultural Sciences, 73091 Riddarhyttan, Sweden.

*Corresponding author.

Email: raphael.arlettaz@iee.unibe.ch

REFERENCES AND NOTES

1. Confédération Suisse, "Loi fédérale sur la chasse et la protection des mammifères et oiseaux sauvages: Modification du 27 septembre 2019" (2020); www.admin.ch/opc/fr/federal-gazette/2019/6267.pdf [in French].
2. Le Conseil Fédéral, "Modification de la loi sur la chasse" (2020); <https://www.admin.ch/gov/fr/accueil/documentation/votations/20200927/modification-de-la-loi-sur-la-chasse.html> [in French].
3. K. Vogt *et al.*, "Vingt-cinq ans de présence du loup en Suisse: Bilan intermédiaire" (KORA Bericht Nr. 91f. 2020); www.kora.ch/fileadmin/file_sharing/5_Bibliothek/52_KORA_Publikationen/520_KORA_Berichte/KORA_Bericht_91_F_25_ans_du_loup_en_Suisse.pdf [in French].
4. I. Andersen, "2020 resolutions for nature" (United Nations Environment Programme, 2020); www.unenvironment.org/news-and-stories/video/2020-resolutions-nature.
5. M. Prieur, in *Elgar Encyclopedia of Environmental Law*, M. Faure, Ed. (Edward Elgar Publishing Limited, 2018), pp. 251–259.

COMPETING INTERESTS

R.A. is a member of the committee of Fauna.v.s. the Valais Society for Wildlife Biology. G.C. is a member of the IUCN Large Carnivore Initiative for Europe, IUCN Canid Specialist Group, and IUCN Cat Specialist Group.

10.1126/science.abe6191



AAAS NEWS & NOTES

Interest in online voting has risen during the COVID-19 pandemic.

Internet voting remains insecure, says AAAS EPI Center

The center has worked with U.S. policy-makers to suggest scientifically sound alternatives

By **Andrea Korte**

Many Americans turn to the internet for shopping, banking and—particularly in the midst of a historic pandemic—schooling and work. Is voting online next? Although some policy-makers and election officials are researching or piloting programs to allow voters to cast their ballots via computer or mobile app, nearly every expert in the field of election security agrees: Internet voting is not secure, and it is unlikely to be any time in the foreseeable future.

Current technologies cannot guarantee the “secrecy, security, and verifiability” of any ballot sent over the internet, leaving online voting systems vulnerable to vote manipulations and privacy breaches, according to a comprehensive 2018 report by the National Academies of Science, Engineering, and Medicine.

The American Association for the Advancement of Science’s Center for Scientific Evidence in Public Issues, which gathers and distills scientific information for policy audiences, is focused on making sure decision-makers are aware of the latest scientific evidence on the dangers of online voting.

The EPI center’s previous work on voting technology and security issues had focused mostly on the accessibility and security concerns associated with different types of electronic voting systems, as well as the importance of statistically sound postelection audits to ensure that results can be verified. Internet voting had been under the center’s umbrella of “the future of voting,” but with the 2020 election approaching and interest in online voting increasing, the EPI Center has emphasized this facet of election security to let decision-makers know that’s where online voting belongs—in the far future.

“Internet voting is one thing that everyone in election security tends to agree on,” said Steve Newell, who leads the EPI Center’s voting technology and security outreach. “There are areas of disagreement, but there’s really not much on internet voting. Everyone from the ACLU to The Heritage Foundation to the Brennan Center for Justice is pretty much on the same page here.”

Experts within the federal government agree. In May, the Department of Homeland Security’s Cybersecurity and Infrastructure

Security Agency, the FBI, the U.S. Election Assistance Commission, and the National Institute of Standards and Technology issued a joint risk assessment, warning that allowing voters to submit their completed ballots over the internet is high-risk.

This unified stance on the dangers of online voting means that the EPI Center has been able to work with a number of other organizations and experts to amplify their voices and share the scientific evidence with policy-makers. This spring, for instance, the EPI Center teamed with allied organizations to provide evidence on a bill in Puerto Rico that would have implemented internet voting in the territory as early as this year and opened it to all voters by 2024.

Building on a range of outreach efforts like letters and webinars, the EPI Center, along with ACLU Puerto Rico, Verified Voting, the Brennan Center, and University of Michigan computer scientist J. Alex Halderman, met virtually in May with the office of Puerto Rico Governor Wanda Vázquez Garced to share the latest scientific evidence that shows internet voting is insecure. When the bill arrived on Vázquez Garced’s desk the next week, she vetoed it.

In a 14 May tweet, Vázquez Garced called for an amended version of the bill, one that takes into account “las preocupaciones sobre la seguridad del voto por internet”—“concerns about the security of online voting.”

“Scientific evidence can be incredibly useful in policy-making, but too often, it is undervalued and can sometimes be difficult to access or understand,” said Michael Fernandez, director of the center, during a recent Q&A with AAAS members. “We make it easier for policy-makers and other decision-makers to access relevant scientific evidence and then integrate that evidence into their decision-making process.”

The outreach in Puerto Rico is just a fraction of the work that the EPI Center has done around the country related to internet voting. In April, the center joined with other groups and experts to send letters to governors, secretaries of state, and state election officials letting them know that internet voting is not secure. The bulk of their efforts are targeted at the local and county level, where many of the decisions related to elections are made. Since launching its effort on election security in 2019, the EPI Center has focused on providing information to more

AAAS NEWS & NOTES

than 1,000 election officials in 772 counties in 13 states, said Kathryn McGrath, the center's communications director.

In Georgia, for instance, when DeKalb County's council passed a resolution in July to research and expand access to online voting, the EPI Center reached out to the county commissioners to share the evidence that online voting is insecure, Newell said.

"This is just such a wonderful manifestation of the vision of the EPI Center and what it was meant to do—providing that help to policy-makers and bringing evidence-based decision-making into policy," said Sudip Parikh, CEO of AAAS and executive publisher of the *Science* family of journals.

The EPI Center team recognizes that policy-makers and election officials have many concerns to balance, Newell added. Along with election security, decision-makers are mindful of a host of other issues, such as funding and equitable access.

"There are genuine concerns about making sure that everyone has access to the ballot—it's incredibly important," said Newell. "We've seen in America disparities in voting going back a very long way. Those are real concerns we need to address, but internet voting unfortunately really isn't the solution to them." In fact, he said, disparities and equity issues could be exacerbated by implementing widespread online voting in a digitally divided country.

Accordingly, the EPI Center makes sure that policy-makers and election officials are aware of alternative options that address some of the concerns that are driving interest in internet voting—and what the science says about those options. This summer, the center

coauthored a report with the nonprofit Free Speech for People, "Leveraging Electronic Balloting Options Safely and Securely During the COVID-19 Pandemic," which recommends ways for jurisdictions to safely send blank ballots to voters through the internet. Remote ballot marking systems, for instance, allow voters to print their ballot, mark their choice by hand with a pen, and send the completed ballot in via the mail or deposit it in a dropbox. Voters with disabilities who are unable to mark a ballot by hand can mark their ballot electronically, then print and submit it. Either way, these options avoid the most significant security challenges of internet voting, which occur when voters submit their choices through any internet-connected device.

The EPI Center is also recommending that jurisdictions prepare to expand access to two scientifically sound alternatives to internet voting: mail-in ballots and early voting, both of which allow voters to avoid close contact with large groups of other voters on Election Day.

"There's a lot of conversation around mail-in ballots, but there's still essentially no evidence to actually support them being controversial," said Newell. "The FBI recently stated that there is no organized fraud in vote by mail, and this is supported by the existing evidence."

The EPI Center's outreach about the insecurity of internet voting and the benefits of alternative voting options is bolstered by new research all the time. They are making sure decision-makers know that the evidence shows that mail-in ballots confer no partisan advantage on either Democrats or Republicans, as found in a study published 26 August in *Science Advances*.

"Who's more excited about technological progress than AAAS, an organization of scientists?" said Newell. "Unfortunately, the science shows that the technology for online voting is not where it needs to be."

2020 Mike Hogg Award and Lecture

Recognizing Cato T. Laurencin, M.D., Ph.D.

MD Anderson Cancer Center extends congratulations to Cato T. Laurencin, M.D., Ph.D., on being named the 2020 Mike Hogg Award recipient.

A scientist, a practicing surgeon, and one of two designated University Professors at the University of Connecticut, Laurencin is being recognized for his pioneering and ongoing contributions in regenerative engineering toward the reformation of damaged or missing tissues, as well as his group's advances in biomaterials, stem cell science, nanotechnology and drug delivery systems.

Laurencin's lecture, titled Regenerative Engineering: A Convergence Approach for Addressing Grand Challenges, will be delivered virtually this year.

The event is sponsored by the Mike Hogg Fund and hosted by MD Anderson's Division of Education and Training.



THE UNIVERSITY OF TEXAS
MD Anderson
Cancer Center

Making Cancer History®

RESEARCH

IN SCIENCE JOURNALS

Edited by Michael Funk

IMMUNE SYSTEMS

Reconfiguring an immune response

The deep sea is a vast and generally empty environment. Finding a mate can thus be difficult. In response to this situation, one group of deep-sea denizens, the anglerfishes, have evolved a system in which males attach to females, in some cases permanently, through fusion of tissues and connection of circulatory systems. Such attachment greatly challenges the immune systems of the fish. Swann *et al.* found that these challenges have been met by the evolution of increasingly reduced immune responses among anglerfish species, including the loss of what have been considered essential vertebrate responses. These shifts suggest that vertebrate immune systems may be more flexible over evolutionary time than was previously thought. —SNV

Science, this issue p. 1608

A female anglerfish of the species *Haplophryne mollis* supports a dorsally fused male fish, an arrangement requiring immune system changes.



PROTEIN DESIGN

Logic at the cell surface

A major challenge in medical interventions is to target only diseased cells. Although there are biomarkers characteristic of certain cancers, for example, it is unlikely that a single marker can specify a particular cell type. Lajoie *et al.* addressed this problem by designing protein switches called Co-LOCKR that bind to antigens on the cell surface and activate through a conformational change only when there is a precise combination of antigens.

They designed switches that can perform AND, OR, and NOT logic. On the path toward applying this technology, they used Co-LOCKR to direct chimeric antigen receptor T cells to tumor cells expressing specific antigens. —VV

Science, this issue p. 1637

CORONAVIRUS

A dynamic viral spike

Efforts to protect human cells against severe acute respiratory syndrome coronavirus 2 (SARS-CoV-2) have focused on the trimeric spike (S) protein.

Several structures have shown a stabilized ectodomain of the spike in its prefusion conformation. Cai *et al.* now provide insight into the structural changes in the S protein that result in the fusion of the viral and host cell membranes. They purified full-length S protein and determined cryo-electron microscopy structures of both the prefusion and postfusion conformations. These structures add to our understanding of S protein function and could inform vaccine design. —VV

Science, this issue p. 1586

CORONAVIRUS

Modeling SARS-CoV-2 in mice

Among the research tools necessary to develop medical interventions to treat severe acute respiratory syndrome coronavirus 2 (SARS-CoV-2) infections, high on the list are informative animal models with which to study viral pathogenesis. Gu *et al.* developed a mouse model in which a SARS-CoV-2 strain was infectious and could cause an inflammatory response and moderate pneumonia. Adaptation of this

viral strain in the mouse appeared to be dependent on a critical amino acid change, Asn⁵⁰¹ to Tyr (N501Y), within the receptor-binding domain of the viral spike protein. The new mouse model was used to study neutralizing antibodies and a vaccine candidate against the virus. —PNK

Science, this issue p. 1603

GRAPHENE

Making metallic ribbons

In its usual two-dimensional form, graphene does not have an energy gap in its electronic structure. However, one-dimensional ribbons made of the material are semiconducting and making them metallic is tricky. Rizzo *et al.* developed a strategy for synthesizing metallic graphene nanoribbons and demonstrated their metallicity using scanning tunneling spectroscopy. These metallic graphene nanoribbons may be useful for exploring exotic quantum phases in a single dimension. —JS

Science, this issue p. 1597

CHEMICAL PHYSICS

Duality of roaming mechanism in H₂CO

The phenomenon of roaming in chemical reactions (that is, bypassing the minimum energy pathway from unlikely geometries) has attracted a great deal of attention in the chemical reaction dynamics community over the past decade and still demonstrates unexpected results. Using velocity-map imaging of state-selected H₂ products of H₂CO photodissociation, Quinn *et al.* discovered the bimodal structure of rotational distribution of the other product fragment, CO. Quasiclassical trajectories showed that this bimodality originates from two distinctive reaction pathways that proceed by the trans or cis configuration of O—C—H···H, leading to high or low rotational excitations of CO, respectively. Whether such a mechanism is present in the many other chemical reactions for which roaming reaction

pathways have been reported is yet to be determined. —YS

Science, this issue p. 1592

ALCOHOL ADDICTION

Tipsy microglia binge on synapses

Alcohol abuse has detrimental cognitive and behavioral consequences. Binge drinking is associated with anxiety in humans and, in mice, activates resident phagocytic immune cells in the brain called microglia. Socodato *et al.* found that a binge-drinking protocol in male mice induced microglia to selectively scavenge excitatory synapses between neurons in the prefrontal cortex. The loss of these connections did not cause neuronal death during the study but instead depressed neurotransmission and increased anxiety-like behaviors in the mice. —LKF

Sci. Signal. **13**, eaba5754 (2020).

CLIMATE CHANGE

Antarctic ice sheet melting and climate

The massive West Antarctic Ice Sheet (WAIS) is now melting at an accelerated rate in response to anthropogenic greenhouse gas emissions, and exactly how this will affect global climate remains poorly understood. Widely available predictive global climate models do not adequately account for ice sheet physics. Using a newly developed model that incorporates ice sheet thermodynamics, Rogstad *et al.* explored the potential effects of WAIS melting on the global climate. Their model not only predicts a significantly greater increase in subsurface ocean temperatures near the WAIS margins than earlier models but also suggests that simultaneous decreases in air and ocean surface temperature, as well as expanded sea ice, will delay previously predicted increases in global warming by several decades. —KVH

Sci. Adv. **10**, 1126/sciadv.aaz1169 (2020).

IN OTHER JOURNALS

Edited by **Caroline Ash**
and **Jesse Smith**

CONSERVATION

Dogs return to the show

The ancient dogs of Oceania include several lineages with Asian ancestry that have since evolved across the South Pacific for more than 3000 years. These include the Australian dingo, but also many less well known and mostly extinct varieties such as the New Zealand kuri. New Guinea singing dogs comprise a small, and highly inbred, population in captivity and are generally believed to be extinct in the wild. Surbakti *et al.* bring a ray of hope with their finding that populations of so-called highland wild dogs living at high altitudes are indeed true New Guinea singing dogs. Genomic analysis of samples collected from several dogs show that they are derived from the same lineage as the captive population but contain significantly higher levels of genetic diversity. This finding brings hope for both protection of the species in the wild and for invigorating the captive population. —SNV

Proc. Natl. Acad. Sci. U.S.A. **10**, 1073/pnas.2007242117 (2020).



The New Guinea singing dog, named for its distinctive calls, has been rediscovered in the wild.

PHOTO: EDWARD MYLES/MINDEN PICTURES

SYMBIOSIS

A bacterial battleground

The white button mushrooms that many of us enjoy eating are subject to brown blotch disease caused by the bacterium *Pseudomonas tolaasii*. These bacteria are spread by means of biosurfactants, and damage is caused by a family of pore-forming cyclic lipopeptides called tolaasins. However, protective bacteria are also found on button mushrooms, and Hermenau *et al.* show how helper bacteria of the genus *Mycetocola* protect their host. Metabolic profiling, mass spectroscopy, structural characterization, and infection assays show that tolaasin is linearized by the helper bacteria. The authors also identify the enzyme responsible and show that a biosurfactant involved in pathogen spreading is also a cyclic lipopeptide that is neutralized by linearization. Understanding these protective mechanisms could allow the development of biocontrol strategies to stop spoilage. —VV

Proc. Natl. Acad. Sci. U.S.A. 10.1073/pnas.2006109117 (2020).

ECOLOGY

Identifying the weakest links

Faced with mass extinction, how do we prioritize conservation needs? Disruption of pollination could compromise reproduction for many plant species, and reduction of seed dispersal could have devastating effects for many tree species. All organisms interact, some very specifically, but we understand little about how the functional disruption of one partner influences the resilience of a community. Simmons *et al.* mapped species interactions involved in 41 pollination and seed dispersal communities to find vulnerabilities. Although specialist links were more vulnerable to habitat loss, they also found that the more vulnerable interactions made the greatest contributions to community tolerance. Thus, identifying the most vulnerable links between

PLANT BIOCHEMISTRY

Carotenoids drive chromoplast development

Carotenoid-rich cellular structures called chromoplasts are a source of the rich reds and yellows in the fruits and flowers of plants. Similar to green, photosynthetic chloroplasts, chromoplasts derive from plastids but are distinct in structure and development. Llorente *et al.* found that expressing an enzyme in leaf chloroplasts that causes enrichment of the carotenoid precursor phytoene disrupted photosynthesis and led to structural changes consistent with chloroplast-to-chromoplast differentiation. This intervention may mimic natural cues for chromoplast development and could be a route to increasing the carotenoid content of green vegetables. —MAF

Proc. Natl. Acad. Sci. U.S.A. 117, 21796 (2020).

The vivid red and yellow colors of some flowers and fruits, such as tomatoes, are produced by carotenoid-rich cellular structures called chromoplasts.



species could become important targets for conservation. —CA

PLOS Biol. 18, e3000843 (2020).

STEM CELLS

Identity by association

Tissue homeostasis and regeneration after injury involve coordinated dynamics for the self-renewal and differentiation of cells. Generally, cells that remain in their niche retain self-renewing activity, whereas cells that leave the niche take on a specific cell fate. Using CRISPR-Cas9 genome editing, live-cell imaging, and RNA interference-mediated gene knockdown, Gordon *et al.* examined the interactions among germ cells of *Caenorhabditis elegans*, the distal tip cell niche, and the adjacent Sh1 sheath cells that surround the gonad. Thin, membranous extensions from the distal tip cell niche and sheath cells touched the undifferentiated germ cells. Cells that touched just the distal tip cell niche remained naïve, whereas cells at the interface divided asymmetrically, with

one daughter cell staying with the distal tip cell niche and remaining naïve and the other becoming surrounded by sheath cells and differentiating. —BAP
eLife 9, e56383 (2020).

BLACK HOLES

Merging across the black hole mass gap

Stellar mass black holes form in supernovae, and theory predicts that they have a maximum of about 65 solar masses. Supermassive black holes with millions of solar masses are widely observed in the centers of galaxies but how they formed remains a topic of debate. The LIGO Scientific Collaboration and Virgo Collaboration discuss the gravitational wave event GW190521, finding that it was most likely due to a merger that formed a black hole of about 142 solar masses. This could be an example of the long-sought intermediate-mass black holes. One of the black holes that merged was about 85 solar

masses, itself perhaps the product of an earlier merger, suggesting hierarchical growth. —KTS

Astrophys. J. Lett. 900, L13 (2020).

ORGANIC CHEMISTRY

Cyclopropanes through C–H activation

Despite the strain inherent in triangular carbon rings, these cyclopropane motifs are surprisingly common in natural products and pharmaceuticals. Their synthesis often involves the addition of highly reactive carbenes to C=C double bonds. Clemenceau *et al.* now report an alternative route whereby a palladium catalyst and base pluck hydrogens off of alkyl groups straddling a benzylic center, which then join together to form the third edge of the triangle. The reaction is highly sensitive to the nature of the base, with pivalate yielding the desired product and carbonate leading to a competing cyclobutene motif. —JSY
J. Am. Chem. Soc. 142, 15355 (2020).

REVIEW SUMMARY

IMMUNOLOGY

The science and medicine of human immunology

Bali Pulendran* and Mark M. Davis

BACKGROUND: The mammalian immune system is a remarkable sensory system for the detection and neutralization of pathogens. History is replete with the devastating effects of plagues, and the coronavirus disease 2019 (COVID-19) pandemic is a defining global health crisis of our time. Although the development of effective vaccines has saved many lives, the basic workings of the immune system are complex and require the development of animal models, such as inbred mice. Indeed, research in mice has been enormously productive, and the tremendous insights gleaned have resulted in many Nobel prizes and other accolades. However, past results are not necessarily a reliable guide to the future, and a notable limitation of animal models has been their failure to accurately model some human diseases and their inability to predict human immune responses in many cases. With regard to inbred mice, which have been the principal model of choice for immunol-

ogy, this is likely due to the compromises that were necessary to create a more tractable and reproducible system for experimentation, such as genetic uniformity and lack of pathogen exposure, as well as the fact that mice are evolutionarily quite distinct. These considerations suggest that direct studies of the human immune system are likely to be extremely rewarding, both from a scientific and a medical perspective.

ADVANCES: In the past decade there has been an explosion of new approaches and technologies to explore the human immune system with unprecedented precision. Insights into the human immune response to vaccination, cancers, and viral infections such as COVID-19 have come from high-throughput “omics” technologies that measure the behavior of genes, mRNA (single-cell transcriptomics), proteins (proteomics), metabolites (metabolomics), cells (mass cytometry), and epigenetic modifica-

tions (ATAC-seq), coupled with computational approaches.

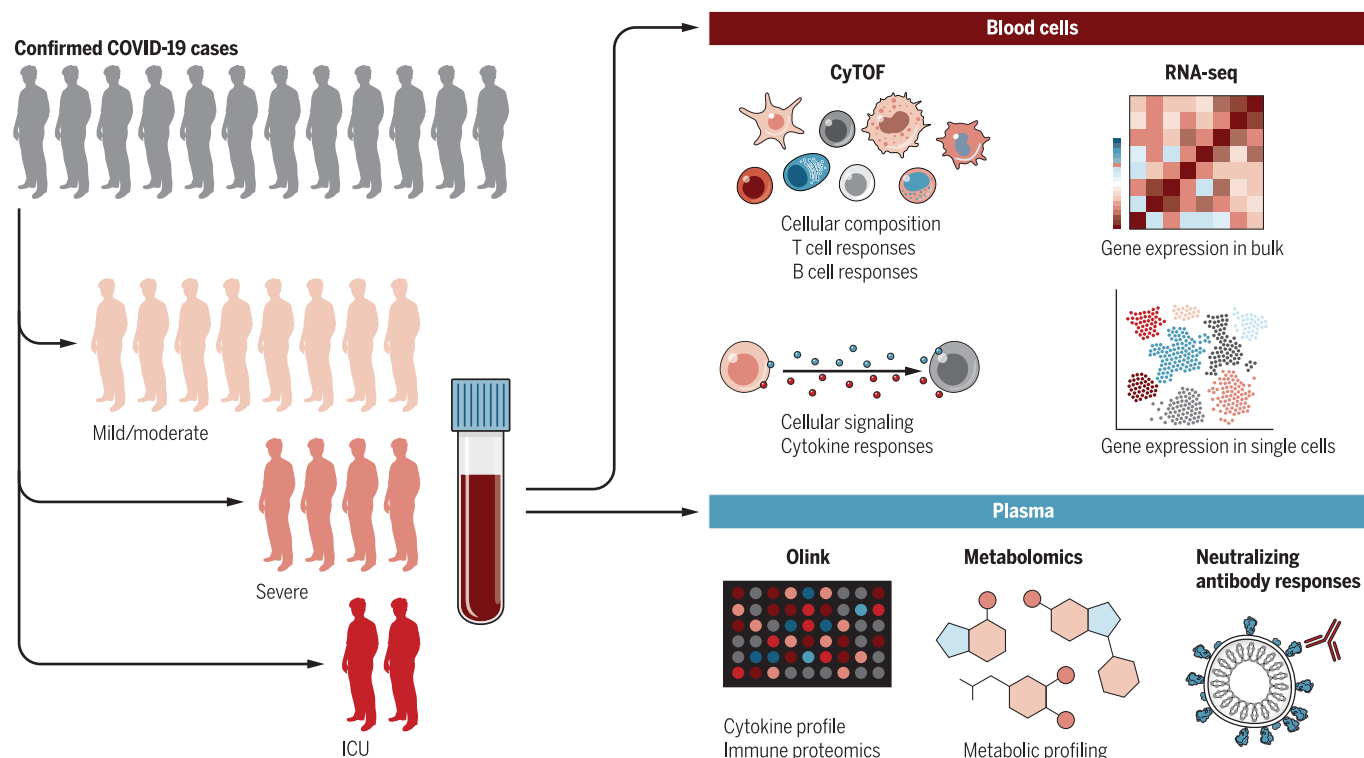
OUTLOOK: Sydney Brenner remarked in 2008, “We don’t have to look for a model organism anymore. Because we are the model organisms.” We propose that studying the immune system in humans, who are genetically diverse and afflicted by a multitude of diseases, offers both a direct link to medicine (i.e., “translation”) and the very real prospect of discovering fundamentally new human biology. New approaches and technology are now making this area much more approachable, but profiling immunity in humans is but the first step. Computational mining of the data and biological validation in animal models or human organoids are essential next steps, in an iterative cycle that seeks to bridge fundamental and applied science, as well as mouse and human immunology, in a seamless continuum of scientific discovery and translational medicine. This will represent a new paradigm for accelerating the development of vaccines and therapeutics. ■

The list of author affiliations is available in the full article online.

*Corresponding author. Email: bpulend@stanford.edu

Cite this article as B. Pulendran, M. M. Davis, *Science* 369, eaay4014 (2020). DOI: 10.1126/science.aay4014

READ THE FULL ARTICLE AT
<https://doi.org/10.1126/science.aay4014>



Probing the human immune response to viral infections. Systems biology techniques can be used to probe the human immune response to viral infections and can define molecular signatures that predict disease severity and illuminate the underlying mechanisms of disease.

ILLUSTRATION: KELLIE HOLOSKI/SCIENCE

RESEARCH ARTICLE SUMMARY

STRUCTURAL BIOLOGY

The endoplasmic reticulum P5A-ATPase is a transmembrane helix dislocase

Michael J. McKenna*, Sue Im Sim, Alban Ordureau, Lianjie Wei, J. Wade Harper, Sichen Shao†, Eunyoung Park‡

INTRODUCTION: Eukaryotic cells contain membrane-bound organelles with distinct identities and functionalities that depend on protein composition. Correct localization of proteins is thus critical for organelle function and cellular homeostasis. The endoplasmic reticulum (ER) and mitochondrial outer membrane are the primary destinations for newly synthesized proteins with hydrophobic transmembrane segments (TMs). Membrane protein localization requires not only high-fidelity protein targeting but also quality control mechanisms that selectively remove mislocalized proteins. At the mitochondrial outer membrane, the ATP-dependent motor protein Msp1/ATAD1 removes some mislocalized transmembrane proteins. By contrast, although protein targeting to the ER is well studied, the mechanisms that remove mistar-

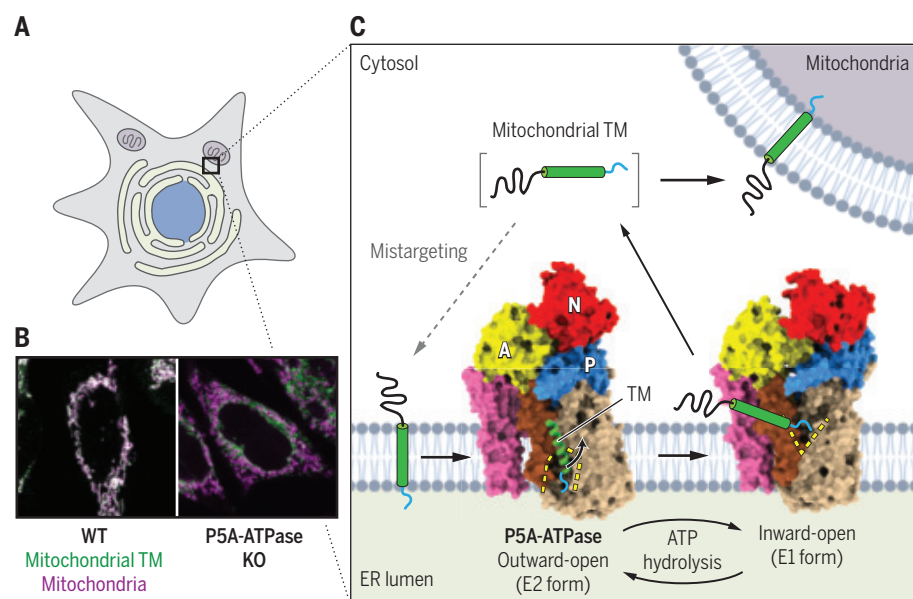
geted transmembrane proteins from the ER membrane are incompletely understood.

RATIONALE: As a model to study membrane protein localization, we focused on tail-anchored proteins, which contain a single C-terminal TM that is necessary and largely sufficient for organelle localization. We reasoned that factors that mediate mitochondrial tail-anchored protein localization would interact directly with nascent proteins. We used an unbiased, site-specific cross-linking and mass spectrometry approach to identify such protein TMs. This approach revealed that the ER-resident orphan P-type pump P5A-ATPase (Spf1 in yeast; ATP13A1 in humans) interacted directly with a mitochondrial tail-anchored protein. Because genetic studies have linked the P5A-ATPase to mitochondrial tail-anchored protein mislocali-

zation, we combined biochemical and structural approaches to define the function and mechanism of the P5A-ATPase.

RESULTS: P-type ATPases form a large class of active transporters that are present in all kingdoms of life and predominantly transport ions or lipids across cellular membranes. The P5A-ATPase belongs to a eukaryotic-specific subfamily of P-type ATPases with unknown substrate specificity. We reconstituted membrane protein insertion into organelles in a cell-free system and used site-specific cross-linking to reveal that the P5A-ATPase interacts directly with the TM of a mitochondrial tail-anchored protein. Human cells lacking ATP13A1 showed mislocalization of mitochondrial tail-anchored proteins to the ER and secretory pathway. In vitro assays, newly synthesized mitochondrial tail-anchored proteins aberrantly accumulated in ER vesicles lacking P5A-ATPase activity. This accumulation was due to the impaired extraction of misinserted mitochondrial proteins from ER membranes lacking ATP13A1. Cryo-electron microscopy structures of *Saccharomyces cerevisiae* Spf1 in different conformations at 3.3 to 3.7 Å resolutions revealed that the P5A-ATPase has an atypically large substrate-binding pocket compared with other P-type ATPases with known structures. The pocket alternately opens toward the ER lumen and cytosol while remaining accessible to the lipid bilayer through a lateral opening. Trapping putative substrates for structure determination revealed an additional membrane-spanning density at the lateral opening, which resembles an α -helical TM. Together with proteomics of wild-type and P5A-ATPase knock-out cells, our results indicate that the P5A-ATPase can dislocate moderately hydrophobic TMs with short hydrophilic luminal domains that misinsert into the ER.

CONCLUSION: Our findings define the function of the P5A-ATPase as a dislocase of TMs at the ER membrane. This assignment establishes polypeptides as P-type ATPase transport substrates in addition to ions and lipids. Active dislocation of misinserted proteins from the ER by the P5A-ATPase also represents a previously unknown cellular safeguarding and quality control mechanism that helps maintain ER and mitochondrial homeostasis, possibly explaining the pleiotropic phenotypes linked to P5A-ATPase dysfunction. ■



P5A-ATPase dislocates mistargeted TMs from the ER. (A) Diagram of a eukaryotic cell showing the nucleus (blue), ER (pale green), and mitochondria (pale purple). (B) Immunofluorescence images showing mislocalization of a mitochondrial tail-anchored protein containing the mitochondrial TM OMP25 (green) in P5A-ATPase knock-out cells. A mitochondrial marker (TOM20) is shown in purple. (C) Model for P5A-ATPase-mediated removal of mistargeted TMs from the ER membrane based on cryo-electron microscopy structures showing different conformations of the yeast P5A-ATPase (Spf1; surface representations) and the position of a substrate TM (green ribbon) bound to the outward-open form.

The list of author affiliations is available in the full article online.

*These authors contributed equally to this work.

†Corresponding author. E-mail: sichen.shao@hms.harvard.edu (S.S.); eunyoung_park@berkeley.edu (E.P.)

Cite this article as M. J. McKenna et al., *Science* 369, eabc5809 (2020). DOI: 10.1126/science.abc5809

READ THE FULL ARTICLE AT
<https://doi.org/10.1126/science.abc5809>

RESEARCH ARTICLE SUMMARY

PREBIOTIC CHEMISTRY

Synthetic connectivity, emergence, and self-regeneration in the network of prebiotic chemistry

Agnieszka Wołos*, Rafał Roszak*, Anna Żądło-Dobrowolska*, Wiktor Beker, Barbara Mikulak-Klucznik, Grzegorz Spólnik, Mirosław Dygas, Sara Szymkuć†, Bartosz A. Grzybowski‡

INTRODUCTION: Although hundreds of organic reactions have been validated under consensus prebiotic conditions, we still have only a fragmentary understanding of how these individual steps combined into complete synthetic pathways to generate life's building blocks, which other abiotic molecules might have also formed, how independent reactions gave rise to chemical systems, and how membranes encapsulating these systems came into being. Answering such questions requires consideration of very large numbers of possible synthetic pathways. Starting with even a few primordial substrates—e.g., H₂O, N₂, HCN, NH₃, CH₄, and H₂S—the number of prebioti-

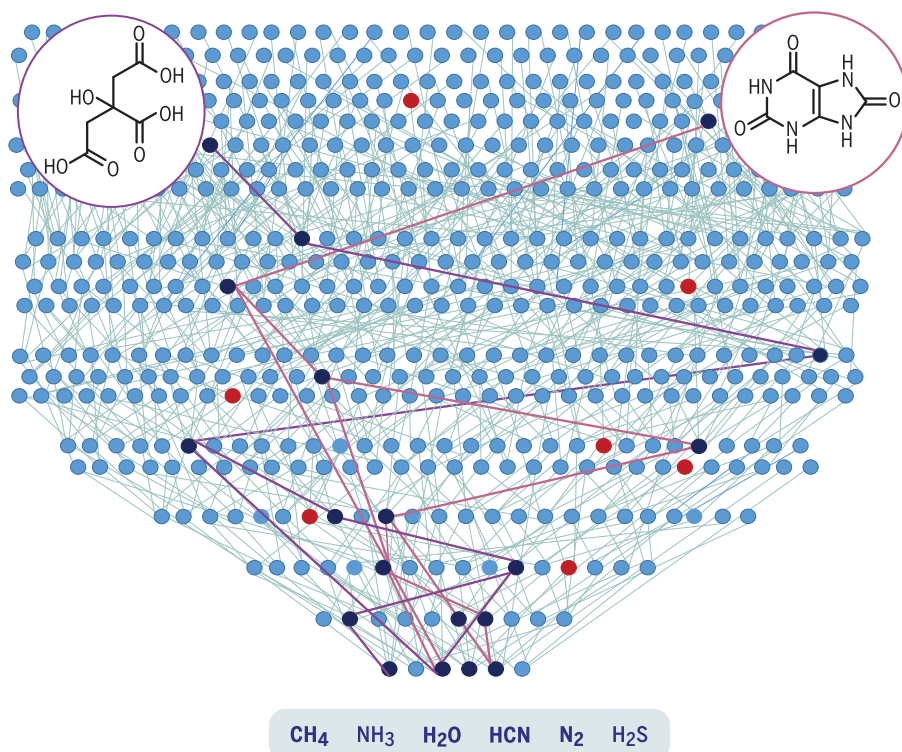
cally synthesizable molecules grows rapidly into the tens of thousands. Detailed analysis of this space and its synthetic connectivity may be beyond the cognition of individual chemists but can be performed by smart computer algorithms.

RATIONALE: We harnessed the power of computer-assisted organic synthesis to map the network of molecules that are synthesizable from basic prebiotic feedstocks. This was done by encoding currently known prebiotic reactions in a machine-readable format, augmenting these reaction transforms with information about incompatible groups and

reaction conditions, and then applying them iteratively to a set of basic prebiotic substrates. The reaction network thus created was queried by algorithms to identify complete synthetic routes as well as those tracing reaction systems—notably, reaction cycles. All calculations were supported by a software application that is freely available to the scientific community.

RESULTS: We demonstrate that this network comprises more abiotic molecules than biotic molecules. The biotic compounds differ from the abiotic compounds in several ways: They are more hydrophilic, more thermodynamically stable, and more balanced in terms of the hydrogen bond donors and acceptors they contain and are synthesizable along routes with fewer changes of conditions. The network contains not only all known syntheses of biotic compounds but also previously unidentified routes, several of which (e.g., prebiotic syntheses of acetaldehyde and diglycine, as well as malic, fumaric, citric, and uric acids) we validated by experiment. We also demonstrate three notable forms of chemical emergence: (i) that the molecules created within the network can themselves enable new types of prebiotic reactions; (ii) that within just a few synthetic generations, simple chemical systems (including self-regenerating cycles) begin to emerge; and (iii) that the network contains prebiotic routes to surfactant species, thus outlining a path to biological compartmentalization. We support these conclusions with experimental results, establishing previously undescribed prebiotic reactions and entire reaction systems—notably, a self-regenerating cycle of iminodiacetic acid.

CONCLUSION: Computer-generated reaction networks are useful in identifying synthetic routes to prebiotically relevant targets and are indispensable for the discovery of prebiotic chemical systems that are otherwise challenging to discern. As our network continues to grow by means of crowd-sourcing of newly validated prebiotic reactions, it will allow continued simulation of chemical genesis, beginning with molecules as simple as water, ammonia, and methane and leading to increasingly complex targets, including those of current interest in the chemical and pharmaceutical industries. ■



Network of prebiotic chemistry. Computer simulation of plausible prebiotic reactions creates a network of molecules that are synthesizable from prebiotic feedstocks and establishes multiple unreported—but now experimentally validated—syntheses of prebiotic targets as well as self-regenerating cycles. In this schematic illustration, light blue nodes represent abiotic molecules, dark blue nodes represent molecules along newly discovered prebiotic syntheses of uric and citric acids, and red nodes represent other biotic molecules.

The list of author affiliations is available in the full article online.

*These authors contributed equally to this work.

†Corresponding author. Email: saszymkuc@gmail.com (S.S.); nanogrybowski@gmail.com (B.A.G.)

Cite this article as A. Wołos *et al.*, *Science* 369, eaaw1955 (2020). DOI: 10.1126/science.aaw1955

S READ THE FULL ARTICLE AT
https://doi.org/10.1126/science.aaw1955

RESEARCH ARTICLE SUMMARY

NEUROSCIENCE

A cortex-like canonical circuit in the avian forebrain

Martin Stacho^{*†}, Christina Herold[†], Noemi Rook, Hermann Wagner, Markus Axer, Katrin Amunts, Onur Güntürkün

INTRODUCTION: For more than a century, the avian forebrain has been a riddle for neuroscientists. Birds demonstrate exceptional cognitive abilities comparable to those of mammals, but their forebrain organization is radically different. Whereas mammalian cognition emerges from the canonical circuits of the six-layered neocortex, the avian forebrain seems to display a simple nuclear organization. Only one of these nuclei, the Wulst, has been generally accepted to be homologous to the neocortex. Most of the remaining pallium is constituted by a multinuclear structure called the dorsal ventricular ridge (DVR), which has no direct counterpart in mammals. Nevertheless, one long-standing theory, along with recent scientific evidence, supports the idea that some parts of the sensory DVR could display connectivity patterns, physiological signatures, and cell type-specific markers that are reminiscent of the neocortex. However, it remains unknown if the entire Wulst and sensory DVR harbor a canonical circuit that structurally resembles mammalian cortical organization.

RATIONALE: The mammalian neocortex comprises a columnar and laminar organization with orthogonally organized fibers that run in

radial and tangential directions. These fibers constitute repetitive canonical circuits as computational units that process information along the radial domain and associate it tangentially. In this study, we first analyzed the pallial fiber architecture with three-dimensional polarized light imaging (3D-PLI) in pigeons and subsequently reconstructed local sensory circuits of the Wulst and the sensory DVR in pigeons and barn owls by means of in vivo or in vitro applications of neuronal tracers. We focused on two distantly related bird species to prove the hypothesis that a canonical circuit comparable to the neocortex is a genuine feature of the avian sensory forebrain.

RESULTS: The 3D-PLI fiber analysis showed that both the Wulst and the sensory DVR display an orthogonal organization of radially and tangentially organized fibers along their entire extent. In contrast, nonsensory components of the DVR displayed a complex mosaic-like arrangement with patches of fibers with different orientations. Fiber tracing revealed an iterative circuit motif that was present across modalities (somatosensory, visual, and auditory), brain regions (sensory DVR and Wulst), and species (pigeon and barn owl). Although

both species showed a comparable columnar and lamina-like circuit organization, small species differences were discernible, particularly for the Wulst, which was more subdifferentiated in barn owls, which fits well with the processing of stereopsis, combined with high visual acuity in the Wulst of this species. The primary sensory zones of the DVR were tightly interconnected with the intercalated nidopallial layers and the overlying mesopallium. In addition, nidopallial and some hyperpallial lamina-like areas gave rise to long-range tangential projections connecting sensory, associative, and motor structures.

CONCLUSION: Our study reveals a hitherto unknown neuroarchitecture of the avian sensory forebrain that is composed of iteratively organized canonical circuits within tangentially organized lamina-like and orthogonally positioned column-like entities. Our findings suggest that it is likely that an ancient microcircuit that already existed in the last common stem amniote might have been evolutionarily conserved and partly modified in birds and mammals. The avian version of this connectivity blueprint could conceivably generate computational properties reminiscent of the neocortex and would thus provide a neurobiological explanation for the comparable and outstanding perceptual and cognitive feats that occur in both taxa. ■

The list of author affiliations is available in the full article online.

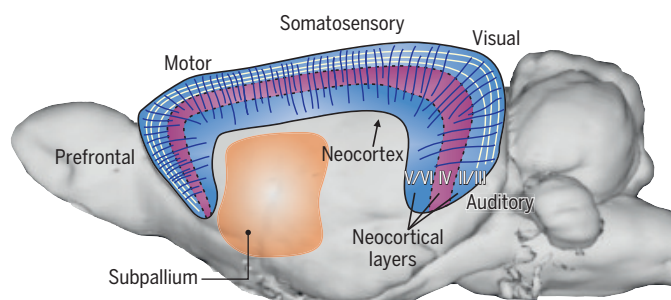
^{*}Corresponding author. Email: martin.stacho@rub.de

[†]These authors contributed equally to this work.

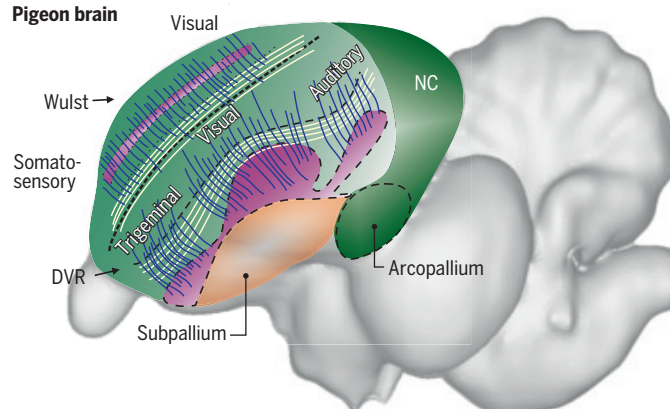
Cite this article as M. Stacho *et al.*, *Science* 369, eabc5534 (2020). DOI: 10.1126/science.abc5534

READ THE FULL ARTICLE AT
<https://doi.org/10.1126/science.abc5534>

Rat brain



Pigeon brain



Fiber architectures of mammalian and avian forebrains. Schematic drawings of a rat brain (left) and a pigeon brain (right) depict their overall pallial organization. The mammalian dorsal pallium harbors the six-layered neocortex with a granular input layer IV (purple) and supra- and infragranular layers II/III and V/VI, respectively (blue). The avian pallium comprises the Wulst and the DVR, which both, at first glance, display a nuclear organization. Their primary sensory input zones are shown in purple, comparable to layer IV. According to

this study, both mammals and birds show an orthogonal fiber architecture constituted by radially (dark blue) and tangentially (white) oriented fibers. Tangential fibers associate distant pallial territories. Whereas this pattern dominates the whole mammalian neocortex, in birds, only the sensory DVR and the Wulst (light green) display such an architecture, and the associative and motor areas (dark green), as in the caudal DVR, are devoid of this cortex-like fiber architecture. NC, caudal nidopallium.

RESEARCH ARTICLES

CORONAVIRUS

Distinct conformational states of SARS-CoV-2 spike protein

Yongfei Cai^{1,2*}, Jun Zhang^{1,2*}, Tianshu Xiao^{1,2}, Hanqin Peng¹, Sarah M. Sterling^{3,4}, Richard M. Walsh Jr.^{3,4}, Shaun Rawson^{3,4,5}, Sophia Rits-Volloch¹, Bing Chen^{1,2†}

Intervention strategies are urgently needed to control the severe acute respiratory syndrome coronavirus 2 (SARS-CoV-2) pandemic. The trimeric viral spike (S) protein catalyzes fusion between viral and target cell membranes to initiate infection. Here, we report two cryo-electron microscopy structures derived from a preparation of the full-length S protein, representing its prefusion (2.9-angstrom resolution) and postfusion (3.0-angstrom resolution) conformations, respectively. The spontaneous transition to the postfusion state is independent of target cells. The prefusion trimer has three receptor-binding domains clamped down by a segment adjacent to the fusion peptide. The postfusion structure is strategically decorated by N-linked glycans, suggesting possible protective roles against host immune responses and harsh external conditions. These findings advance our understanding of SARS-CoV-2 entry and may guide the development of vaccines and therapeutics.

The current coronavirus pandemic is having devastating social and economic consequences. Coronaviruses (CoVs) are enveloped, positive-stranded RNA viruses. They include severe acute respiratory syndrome (SARS) and Middle East respiratory syndrome (MERS), both of which have been associated with significant fatalities (1–3), as well as several endemic common-cold viruses (4). With a large number of similar viruses circulating in bats and camels (5–8), the possibility of additional outbreaks poses major threats to global public health. The current disease, coronavirus disease 2019 (COVID-19), which is caused by a new virus, SARS-CoV-2 (9), has created urgent needs for diagnostics, therapeutics and vaccines. Meeting these needs requires a deep understanding of the structure-function relationships of viral proteins and relevant host factors.

For all enveloped viruses, membrane fusion is a key early step for entering host cells and establishing infection (10). Although it is an energetically favorable process, membrane fusion has high kinetic barriers when two membranes approach each other, mainly because of repulsive hydration forces (11, 12). For viral membrane fusion, free energy to overcome these kinetic barriers comes from refolding of virus-encoded fusion proteins from a primed, metastable prefusion conformational state

to a stable, postfusion state (13–15). The fusion protein for CoV is its spike (S) protein that decorates the virion surface as an extensive crown (hence, “corona”). The protein also induces neutralizing antibody responses and is therefore an important target for vaccine development (16). The S protein is a heavily glycosylated type I membrane protein anchored in the viral membrane. It is first produced as a precursor that trimerizes and is thought to be cleaved by a furin-like protease into two fragments: the receptor-binding fragment S1 and the fusion fragment S2 (Fig. 1A) (17). Binding through the receptor-binding domain (RBD) in S1 to a host cell receptor [angiotensin-converting enzyme 2 (ACE2) for both SARS-CoV and SARS-CoV-2] and further proteolytic cleavage at a second site in S2 (the S2' site) by a serine protease, transmembrane serine protease 2 (TMPRSS2) (18), or the endosomal cysteine proteases cathepsins B and L (CatB/L) are believed to trigger dissociation of S1 and irreversible refolding of S2 into a postfusion conformation, a trimeric hairpin structure formed by heptad repeat 1 (HR1) and heptad repeat 2 (HR2) (19, 20). These large structural rearrangements bring together the viral and cellular membranes, ultimately leading to fusion of the two bilayers.

Since the first genome sequence of SARS-CoV-2 was released (21), several structures have been reported for S protein complexes, including the ectodomain stabilized in the prefusion conformation (22–24) and RBD-ACE2 complexes (25–28) (fig. S1), building upon the previous success of the structural biology of S proteins from other CoVs (20). In the stabilized S ectodomain, S1 folds into four domains, the N-terminal domain (NTD), RBD, and two C-terminal domains (CTDs), and protects the

prefusion conformation of S2, in which HR1 bends back toward the viral membrane (fig. S1, A and B). The RBD samples two distinct conformations, with “up” representing a receptor-accessible state and “down” representing a receptor-inaccessible state. Structures representing the postfusion state of S2 from mouse hepatitis virus (MHV) (fig. S1E) and the one at a lower resolution from SARS-CoV (fig. S1F) suggest how the structural rearrangements of S2 proceed to promote membrane fusion and viral entry (29, 30). Comparison of the pre- and postfusion states reveals that HR1 undergoes a “jackknife” transition that can insert the fusion peptide (FP) into the target cell membrane. Folding back of HR2 places the FP and transmembrane (TM) segments at the same end of the molecule, causing the membranes with which they interact to bend toward each other, effectively leading to membrane fusion. In the previous structures, the regions near the viral membrane were either not present or disordered, yet they all appeared to play critical structural and functional roles (31–35).

To gain further insight, we aimed to determine the pre- and postfusion states of the full-length wild-type S protein of SARS-CoV-2.

Results

Purification of intact S protein

To produce a functional SARS-CoV-2 S protein, we transfected human embryonic kidney (HEK) 293 cells with an expression construct of a full-length wild-type S sequence with a C-terminal Strep-tag (Fig. 1A). These cells fused efficiently with cells transfected with an intact human ACE2 construct even without the addition of any extra proteases (fig. S2), suggesting that the S protein expressed on the cell surfaces is fully functional for membrane fusion. The fusion efficiency was not affected by the C-terminal Strep-tag. To purify the full-length S protein, we lysed the cells and solubilized all membrane-bound proteins in 1% NP-40 detergent. The Strep-tagged S protein was then captured on Strep-tactin resin in 0.3% NP-40. The purified S protein eluted from a size-exclusion column as three distinct peaks in 0.02% NP-40 (Fig. 1B). Analysis by Coomassie blue-stained sodium dodecyl sulfate-polyacrylamide gel electrophoresis (SDS-PAGE) (Fig. 1C) showed that peak 1 contained both the uncleaved S precursor and the cleaved S1/S2 complex; peak 2 had primarily the cleaved but dissociated S2 fragment; and peak 3 included mainly the dissociated S1 fragment, as judged by N-terminal sequencing and Western blot (fig. S3). This was confirmed by negative-stain electron microscopy (EM) (Fig. 1C). Peak 1 showed the strongest binding to soluble ACE2, comparable to that for the purified soluble S ectodomain trimer, and peak 2 showed the weakest binding because it contained mainly the S2 fragment (fig. S4). Although cleavage

¹Division of Molecular Medicine, Boston Children's Hospital, Boston, MA 02115, USA. ²Department of Pediatrics, Harvard Medical School, Boston, MA 02115, USA. ³The Harvard Cryo-EM Center for Structural Biology, Harvard Medical School, Boston, MA 02115, USA. ⁴Department of Biological Chemistry and Molecular Pharmacology, Blavatnik Institute, Harvard Medical School, Boston, MA 02115, USA. ⁵SBGrid Consortium, Harvard Medical School, Boston, MA 02115, USA.

*These authors contributed equally to this work.

†Corresponding author. Email: bchen@crystal.harvard.edu

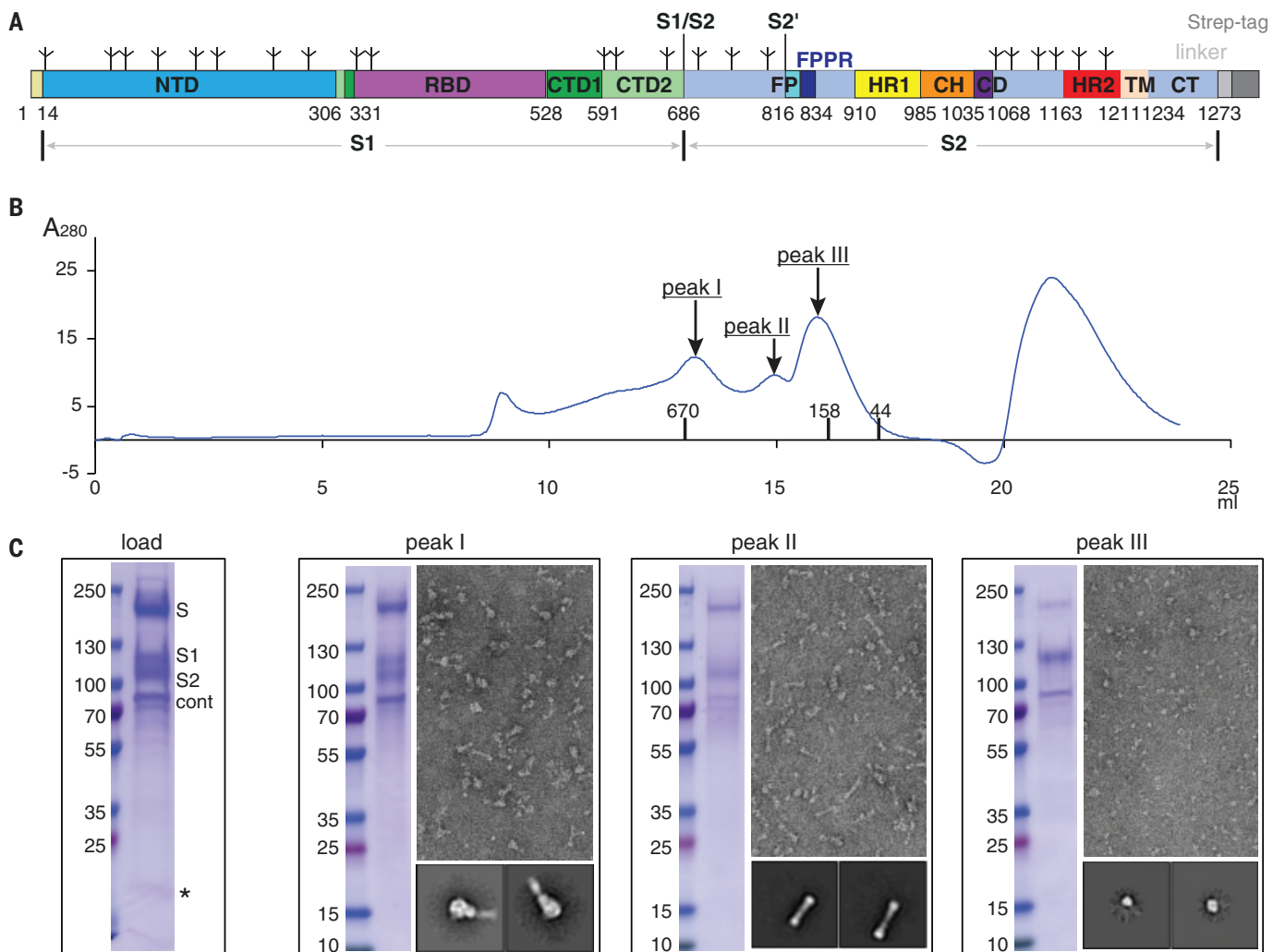


Fig. 1. Preparation of a full-length SARS-CoV-2 spike protein. (A) Schematic representation of the expression construct of full-length SARS-CoV-2 S protein. Segments of S1 and S2 include NTD, RBD, CTD1, CTD2, S1/S2, S2', FP, FPPR, HR1, CH, CD, HR2, TM, CT, and tree-like symbols for glycans. A Strep-tag was fused to the C terminus of S protein by a flexible linker. (B) The purified S protein was resolved by gel-filtration chromatography on a Superose 6 column in the presence of NP-40. The molecular weight standards include thyroglobulin (670 kDa), γ -globulin (158 kDa), and ovalbumin (44 kDa). Three major peaks (peaks I, II,

and III) contain the S protein. (C) Load sample and peak fractions from (B) were analyzed by Coomassie blue-stained SDS-PAGE. Labeled bands were confirmed by Western blot (S, S1, and S2) or protein sequencing (S2 and Cont; S and S1 bands did not give any meaningful results, probably because of a blocked N terminus). Cont, copurified contaminating protein, identified as endoplasmic reticulum chaperone BiP precursor by N-terminal sequencing. *Putative S1/S2-S2' fragment. Representative images and 2D averages by negative-stain EM of three peak fractions are also shown. The box size of 2D averages is ~ 510 Å.

at the S1/S2 (furin) site was clearly demonstrated by protein sequencing of the N terminus of the S2 fragment in peak 2, cleavage at the S2' site was not obvious. In some preparations, we observed a band around 20 kDa, a size expected for the S1/S2-S2' fragment (Fig. 1C). We obtained a similar gel filtration profile when another detergent (dodecyl maltoside) was used to solubilize the S protein (fig. S5), suggesting that the S protein dissociation during gel filtration chromatography is not triggered by any specific detergent. We also identified a major contaminating protein in the preparation as endoplasmic reticulum chaperone binding protein (BiP) precursor (36), which may have a role in facilitating S protein folding.

Cryo-EM structure determination

Cryo-EM images were acquired with selected grids prepared from all three peaks on a Titan Krios electron microscope operated at 300 keV and equipped with a BioQuantum energy filter and a Gatan K3 direct electron detector. RELION (37) was used for particle picking, two-dimensional (2D) classification, 3D classification, and refinement. Structure determination was performed by rounds of 3D classification, refinement, and masked local refinement, as described in the supplementary materials. The final resolution was 2.9 Å for the prefusion S protein and 3.0 Å for S2 in the postfusion conformation (figs. S6 to S9).

Structure of the prefusion S trimer

The overall architecture of the full-length S protein in the prefusion conformation was very similar to the published structures of a soluble S trimer stabilized by a C-terminal foldon trimerization tag and two proline substitutions at the boundary between HR1 and the central helix (CH) in S2 (fig. S1) (22, 23). In our new structure, the N terminus, several peripheral loops, and glycans that were invisible in the soluble trimer structures are ordered (Fig. 2, A and B, and fig. S10A). As described previously, the four domains of the S1 fragment, NTD, RBD, CTD1, and CTD2, wrap around the threefold axis, covering the S2 fragment underneath. The furin cleavage

site at the S1/S2 boundary is in a surface-exposed and disordered loop (Fig. 2B), so it is unclear whether this structure represents the uncleaved or cleaved trimer, although the sample clearly contains both forms (Fig. 1C). Likewise, the S2 fragment has a conformation nearly identical to that in the previous

trimer structures, with most of the polypeptide chain packed around a central three-stranded coiled coil formed by CH, including the connector domain (CD), which links CH and the C-terminal HR2 through an additional linker region. A difference between our structure and the published trimer structures is that

an ~25-residue segment in S2 immediately downstream of the fusion peptide is ordered. The segments HR2, TM, and CT, which were not observed in previous structures, are still not visible.

Several features are different between our structure and the previously described prefusion

Fig. 2. Cryo-EM structure of the SARS-CoV-2 S protein in the prefusion conformation.

(A) The structure of the S trimer was modeled based on a 2.9-Å density map. Three protomers (A, B, and C) are colored in green, blue, and red, respectively. (B) Overall structure of S protein in the prefusion conformation shown in ribbon representation. Various structural components in the color scheme shown in Fig. 1A include NTD, RBD, CTD1, CTD2, FP, FPPR, HR1, CH, and CD. The N terminus, S1/S2 cleavage site, and S2' cleavage site are indicated.

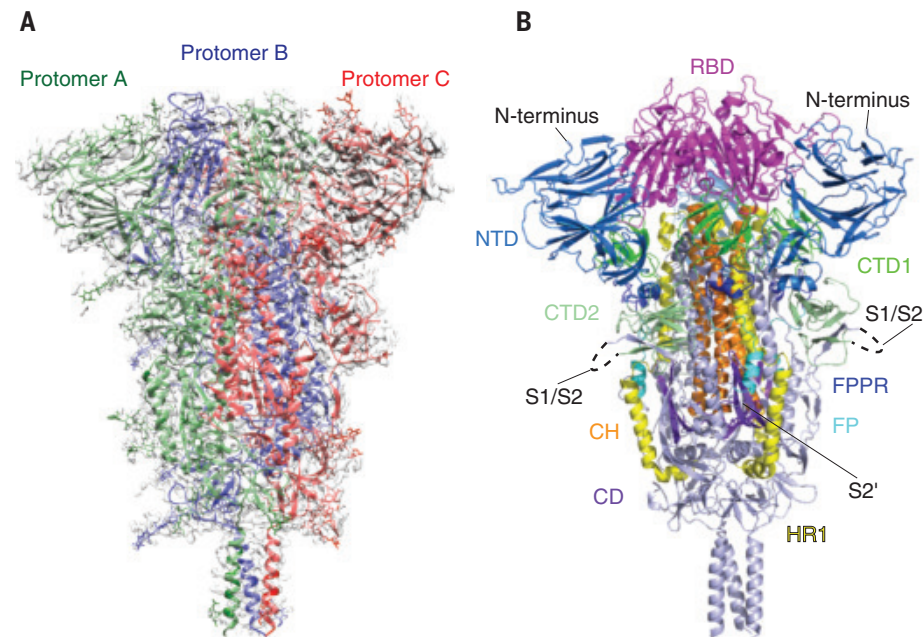
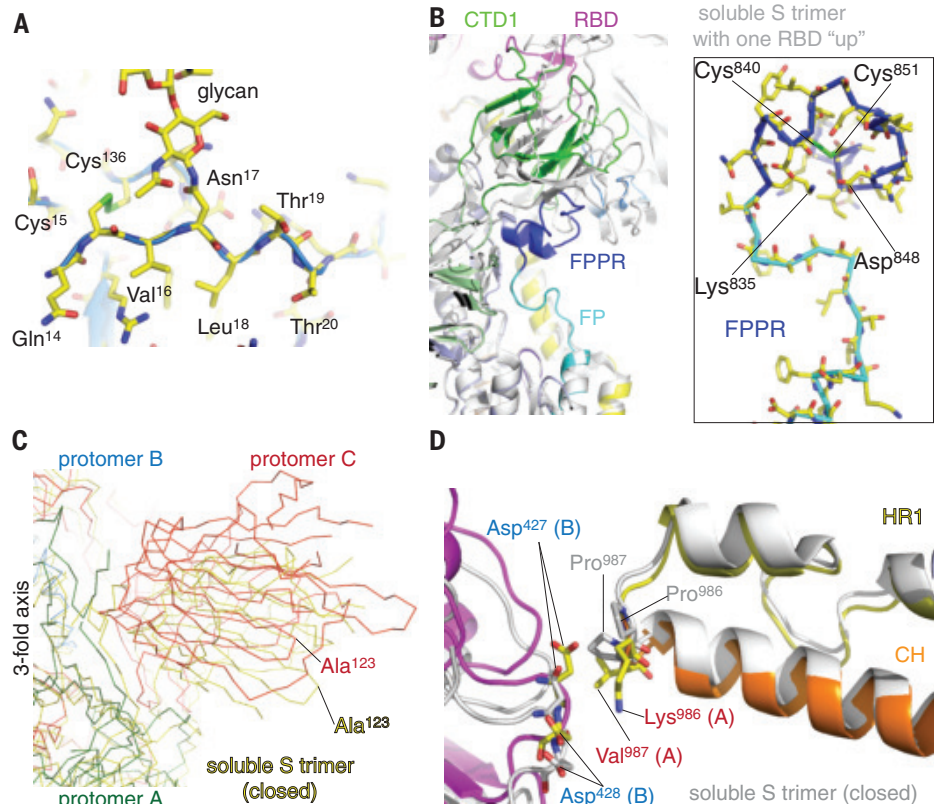


Fig. 3. Selected new features of the SARS-CoV-2 prefusion S trimer.

(A) N-terminal segment of the S protein. The N terminus is at residue Gln¹⁴ after cleavage of the signal peptide. Cys¹⁵ forms a disulfide bond with Cys¹³⁶. We observed good density for the N-linked glycan at Asn¹⁷. (B) A segment immediately downstream of the fusion peptide, designated FPPR, although disordered in the stabilized soluble S ectodomain trimer structure, forms a tightly packed structure, abutting CTD1. The newly identified FPPR structure would clash with CTD1 in the RBD up conformation. Various domains are shown in the color scheme in Fig. 2B. The structure of the soluble S trimer with one RBD in the up conformation (PDB ID: 6vyb) is shown in gray. Box shows a close-up view of the FPPR with the adjacent fusion peptide in both a surface representation and a stick model. (C) The SARS-CoV-2 prefusion S trimer, viewed along the threefold axis, is superposed on the structure of the stabilized soluble S ectodomain trimer in the closed conformation with all three RBDs in the down conformation (PDB ID: 6vxx). Although the S2 region is well aligned, there is a significant shift (e.g., ~12 Å between two Ala¹²³ residues) in S1. (D) Impact of the proline mutations introduced at residues 986 and 987 to stabilize the prefusion conformation. K986P mutation removes a salt bridge between Lys⁹⁸⁶ of one protomer and either Asp⁴²⁷ or Asp⁴²⁸ of another protomer in the trimer interface.



conformations. First, the N terminus in our structure is ordered and adopts a conformation similar to that in SARS-CoV, including a disulfide bond (Cys¹⁵–Cys¹³⁶) and an N-linked glycan at Asn¹⁷ (Fig. 3A) (38). It will be important to confirm whether this region is unfolded with no disulfide bond in the stabilized soluble constructs or if it is folded and simply poorly defined by density despite a disulfide bond, particularly if these constructs are widely used for vaccine studies.

Second, another disulfide-containing segment (residues 828 to 853) immediately downstream of the fusion peptide is also absent from the structures of the soluble ectodomain but ordered in our structure (Fig. 3B). We designate it as the fusion-peptide proximal region (FPPR). The FPPR is disordered in both the closed and RBD-up conformations of the stabilized soluble S trimer. In our full-length structure, it packs rather tightly around an internal disulfide bond between Cys⁸⁴⁰ and Cys⁸⁵¹, further reinforced by a salt bridge between Lys⁸³⁵ and Asp⁸⁴⁸, as well as by an extensive hydrogen bond network. When compared with the RBD-up conformation by superposition of the rest of S2, the FPPR clashes with CTD1, which rotates outward with the RBD in the flipping-up transition. Thus, a structured FPPR abutting the opposite side of CTD1 from the RBD appears to help clamp down the RBD and stabilize the closed conformation of the S trimer. It is not obvious why the FPPR is also not visible in the published, closed S ectodomain structure with all three RBDs in the down conformation (23). Our structure of the full-length S protein suggests that CTD1 is a structural relay between RBD and FPPR that can sense the displacement on either side. The latter is directly connected to the fusion peptide. Lack of a structured FPPR in the stabilized, soluble S trimer may explain why the RBD-up conformation is readily detected in that preparation. In addition, a D614G mutation that was identified in recent SARS-CoV-2 isolates has been suggested to lead to more efficient entry (39, 40). D614 forms a salt bridge with K854 in the FPPR (fig. S10B), supporting a functional role of the FPPR in membrane fusion. In the 3D classification of our prefusion particles from two independent datasets, only one subclass with an RBD flipped up was observed (fig. S6), suggesting that the RBD-up conformation is relatively rare in our full-length S preparation. The map for this subclass was refined to 4.7 Å without C3 symmetry, and we could not model the FPPR. The FPPR is ordered in all other maps that are refined to 3.5 Å or higher resolution.

When we aligned our full-length structure with the soluble S trimer structure by the S2 portion, the three S1 subunits in the soluble trimer structure moved outward, away from the threefold axis, up to ~12 Å in peripheral

areas (Fig. 3C and fig. S11), suggesting that the full-length S trimer is more tightly packed among the three protomers than the mutated soluble trimer. Examining the region near the proline mutations between HR1 and CH, we found that the K986P mutation appeared to eliminate a salt bridge between Lys⁹⁸⁶ in one protomer and either Asp⁴²⁷ or Asp⁴²⁸ in another protomer; thus, the mutation could create a net charge (three for one trimer) inside the trimer interface. This may explain why the soluble trimer with the PP mutation has a looser structure than the full-length S with the wild-type sequence. Whether this loosening leads to disordered FPPRs in the closed trimer will require additional experimental evidence. However, the proline mutations, designed to destabilize the postfusion conformation and strengthen the prefusion structure, may also affect the prefusion structure.

Structure of the postfusion S2 trimer

Three-dimensional reconstruction of the sample from peak 2 yielded a postfusion structure of the S2 trimer, shown in Fig. 4A. The overall architecture of the SARS-CoV-2 S2 in the postfusion conformation is nearly identical to that of the published structure derived from the S2 ectodomain of MHV produced in insect cells (fig. S1) (29). In the structure, HR1 and CH form an unusually long, central, three-stranded coiled coil (~180 Å). The connector

domain, together with a segment (residues 718 to 729) in the S1/S2-S2' fragment, form a three-stranded β sheet, which is invariant between the prefusion and postfusion structures. In the postfusion state, residues 1127 to 1135 join the connector β sheet to expand it into four strands while projecting the C-terminal HR2 toward the viral membrane. Another segment (residues 737 to 769) in the S1/S2-S2' fragment makes up three helical regions locked by two disulfide bonds that pack against the groove of the CH part of the coiled coil to form a short, six-helix bundle structure (6HB-1 in Fig. 4B). It is unclear whether the S2' site is cleaved because it is in a disordered region spanning 142 residues (Fig. 4B), as in the MHV S2 structure. Nevertheless, the S1/S2-S2' fragment is an integral part of the postfusion structure and would not dissociate regardless of cleavage at the S2' site. The N-terminal region of HR2 adopts a one-turn helical conformation and also packs against the groove of the HR1 coiled coil; the C-terminal region of HR2 forms a longer helix that makes up the second six-helix bundle structure with the rest of the HR1 coiled coil (6HB-2 in Fig. 4B). Thus, the long central coiled coil is reinforced multiple times along its long axis, making it a very rigid structure, as evident even from 2D class averages of particles in the cryo-EM images (fig. S8).

A striking feature of the postfusion S2 is its surface decoration by N-linked glycans (Fig. 4C),

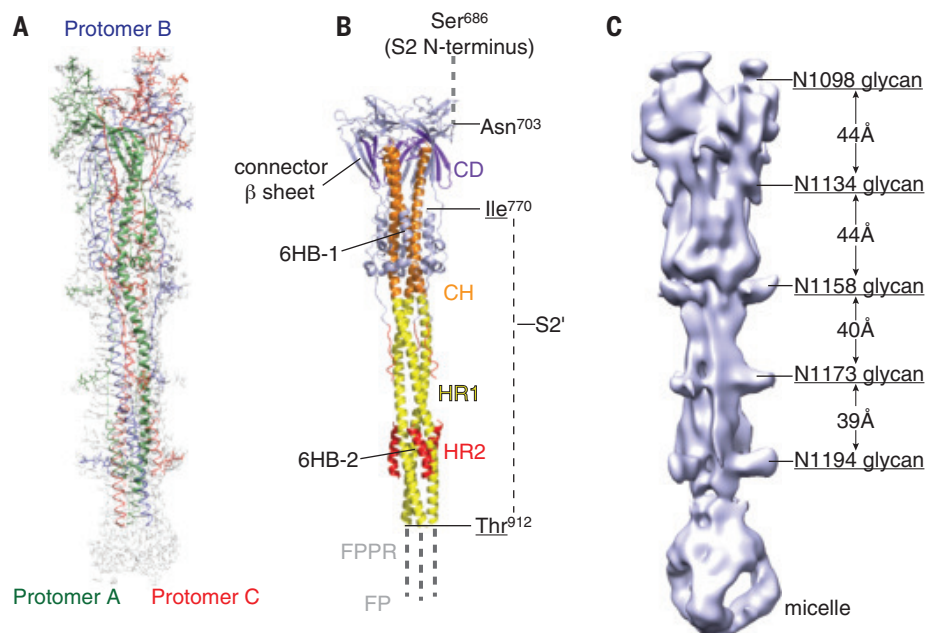


Fig. 4. Cryo-EM structure of the SARS-CoV-2 S2 in the postfusion conformation. (A) The structure of the S2 trimer was modeled based on a 3.0-Å density map. Three protomers (A, B, and C) are colored in green, blue, and red, respectively. (B) Overall structure of the S2 trimer in the postfusion conformation shown in ribbon diagram. Various structural components in the color scheme shown in Fig. 1A include HR1, CH, CD, and HR1. The S2' cleavage site is in a disordered loop between Ile⁷⁷⁰ and Thr⁹¹². Possible locations of the S2 N terminus (S1/S2 cleavage site), FP, and FPPR are also indicated. (C) Low-resolution map showing the density pattern for five N-linked glycans, with almost equal spacing along the long axis.

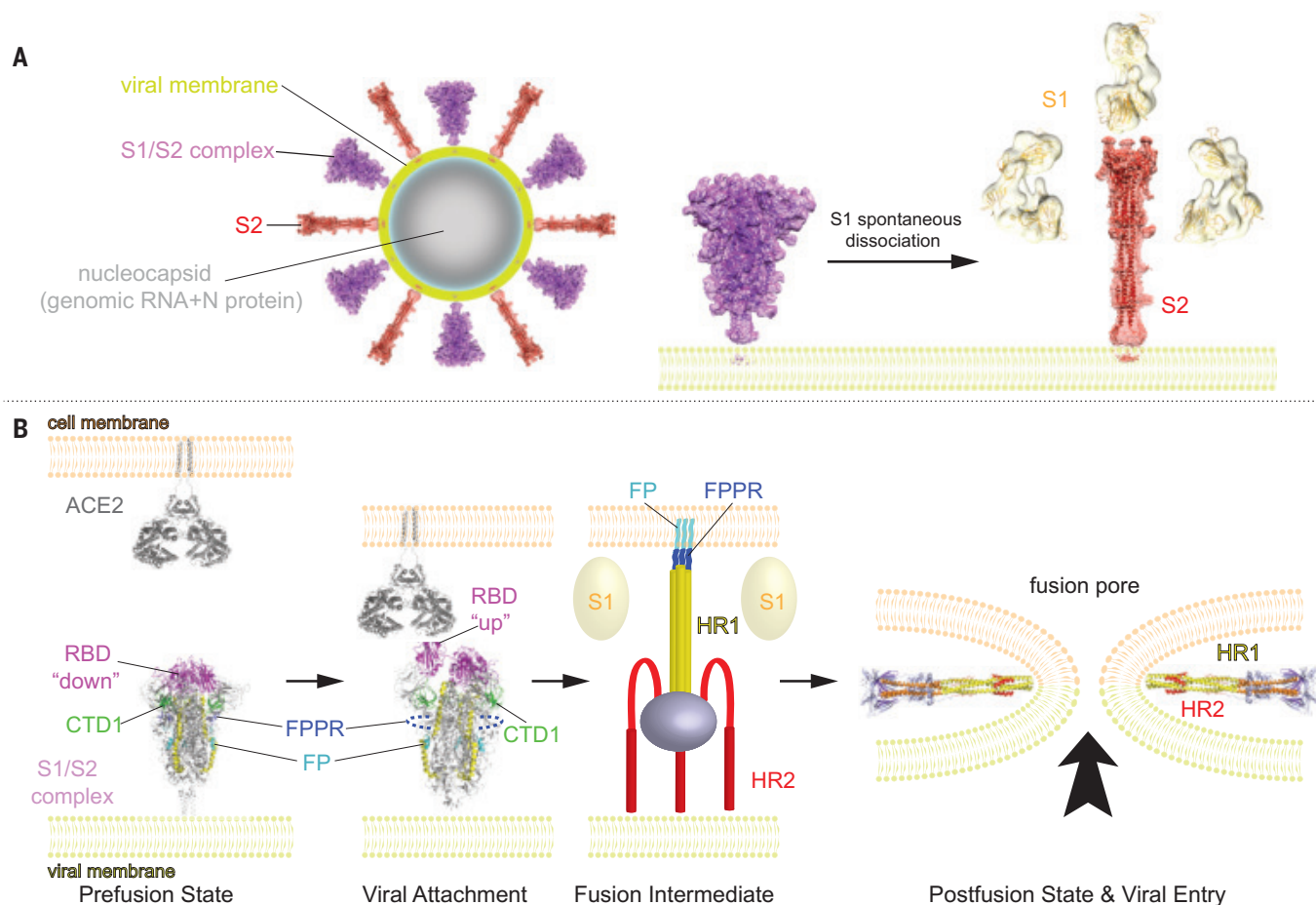


Fig. 5. Model for structural rearrangements of SARS-CoV-2 S protein.

(A) Structural changes independent of a target cell. We suggest that both the prefusion and postfusion spikes are present on the surface of mature virion and the ratio between them may vary. A diagram of the virion is shown. The postfusion spikes on the virion are formed by S2 after S1 dissociates in the absence of ACE2. (B) ACE2-dependent structural rearrangements. Structural transition from the prefusion to postfusion conformation inducing membrane fusion likely proceeds stepwise as follows. First, FPPR clamps down RBD through CTD1 in the prefusion S trimer (this study) but occasionally flips out of

position and allows an RBD to sample the up conformation (PDB ID: 6vyb). Second, RBD binding to ACE2 (PDB ID: 6m17) creates a flexible FPPR that enables exposure of the S2' cleavage site immediately upstream of the adjacent FP. Cleavage at the S2' site, and perhaps also the S1/S2 site, releases the structural constraints on the fusion peptide and initiates a cascade of refolding events in S2, probably accompanied by complete dissociation of S1. Third, the long, central, three-stranded coiled coil forms and HR2 folds back. Finally, the postfusion structure of S2 (this study) forms, which brings the two membranes together, facilitating formation of a fusion pore and viral entry.

also visible in the 2D class averages (fig. S8). Five glycans at residues Asn¹⁰⁹⁸, Asn¹¹³⁴, Asn¹¹⁵⁸, Asn¹¹⁷³, and Asn¹¹⁹⁴ are positioned along the long axis with a regular spacing and four of them aligned on the same side of the trimer. If these glycosylation sites are fully occupied by branched sugars, then they may shield most surfaces of the postfusion S2 trimer. A similar pattern has been described recently (41) for a SARS-CoV S2 preparation derived from a soluble S ectodomain construct produced in insect cells and triggered by proteolysis and low pH. The reason for this decoration is unclear given that a postfusion structure has accomplished its mission and should not need to be concealed from the immune system.

Peak 3 contains primarily the dissociated monomeric S1 fragment, which is the smallest (~100 kDa) and shows the lowest con-

trast in cryo-EM grids of the three particle types we describe. We performed a preliminary 3D reconstruction analysis (fig. S12), further confirming its identity.

Discussion

Architecture of S protein on the surface of SARS-CoV-2 virion

The fact that the cleaved S1/S2 complex dissociates in the absence of ACE2 and that the S2 fragment adopts a postfusion conformation under mild detergent conditions suggests that the kinetic barrier for the conformational transition relevant to viral entry is surprisingly low for this S protein. Whether this observation relates directly to efficient membrane fusion or infection is unclear. Nevertheless, it is noteworthy that the postfusion S2 trimer not only has a very stable and rigid structure, but is also

strategically decorated with N-linked glycans along its long axis as if under selective pressure for functions other than the membrane fusion process. Although some have suggested that viral fusion proteins may further oligomerize in their postfusion conformation to facilitate fusion pore formation (42), the protruding surface glycans of the SARS-CoV-2 S2 make this scenario unlikely. A more plausible possibility is a protective role that the S2 postfusion structure could play if it is also present on the surface of an infectious and mature virion. It may induce non-neutralizing antibody responses to evade the host immune system, and it may also shield the more vulnerable prefusion S1/S2 trimers under conditions outside the host by decorating the viral surface with interspersed rigid spikes (Fig. 5A). Several recent reports have provided some evidence

supporting this possibility. First, EM images of a β -propiolactone-inactivated SARS-CoV-2 virus preparation purified by a potassium tartrate-glycerol density gradient appeared to have lost all S1 subunits, leaving only the postfusion S2 on the virion surfaces (43). Likewise, EM images of a β -propiolactone-inactivated SARS-CoV-2 virus vaccine candidate (PiCoVacc) also showed needle-like spikes on its surfaces (44). Second, spontaneous shedding of SARS-CoV-2 S1 from pseudoviruses in the absence of ACE2 has been reported (39). Third, binding antibodies against S2 are readily detectable in COVID-19 patients (45), suggesting that S2 is more exposed to the host immune system than indicated by the unprotected surfaces on the prefusion structures (22, 23) (Fig. 2). We therefore suggest that postfusion S2 trimers may have a protective function by constituting part of the crown on the surface of mature and infectious SARS-CoV-2 virion (Fig. 5). The postfusion S2 spikes are probably formed after spontaneous dissociation of S1 independently of the target cells.

Membrane fusion

We identify a structure near the fusion peptide, the FPPR, that may play a critical role in the fusogenic structural rearrangements of the S protein. There appears to be cross-talk between the RBD and the FPPR, mediated by CTD1, because a structured FPPR clamps down the RBD whereas an RBD-up conformation disorders the FPPR. Moreover, the FPPR is close to the S1/S2 boundary and the S2' cleavage site and thus might be the center of activities relevant to conformational changes in S. One possibility is that one FPPR occasionally flips out of position due to intrinsic protein dynamics, allowing the RBDs to sample the up conformation. A fluctuation of this kind would loosen the entire S trimer, as observed in modified soluble S trimer constructs (22, 23). Once an RBD is fixed in the up position by binding to ACE2 on the surface of a target cell, a flexible FPPR may enable exposure of the S2' cleavage site immediately upstream of the adjacent fusion peptide. The phenotype of the D614G mutation appears to be consistent with the notion that the FPPR is involved in membrane fusion (39, 40). Cleavage at the S2' site releases the structural constraints on the fusion peptide, which may initiate a cascade of refolding events in S2, including formation of the long, central, three-stranded coiled coil; folding back of HR2; and ultimately membrane fusion. Cleavage at the S1/S2 site allows complete dissociation of S1, which may also facilitate S2 refolding.

Questions regarding membrane fusion remain because the regions near the viral membrane are still not visible in the reconstructions. However, these regions all play critical structural and functional roles. For example, the

conserved hydrophobic region immediately preceding the TM domain, and possibly the TM itself, have been shown to be crucial for S protein trimerization and membrane fusion (37). The cytoplasmic tail, containing a palmitoylated, cysteine-rich region, is believed to be involved in viral assembly and cell-cell fusion (32–35). Whether other viral proteins, such as M protein, may help to stabilize the spike by interacting with HR2 remains an open question. Thus, we still need a high-resolution structure of an intact S protein in the context of the membrane and other viral components to answer such questions.

Considerations for vaccine development

A safe and effective vaccine is the primary medical option to reduce or eliminate the threat posed by SARS-CoV-2. The first round of vaccine candidates with various forms of the S protein of the virus are passing rapidly through preclinical studies in animal models and clinical trials in humans. Our study raises several potential concerns about the current vaccine strategies. First, vaccines using the full-length wild-type sequence of the S protein may produce the various forms in vivo that we have observed here. The postfusion conformations could expose immunodominant, non-neutralizing epitopes that distract the host immune system, as documented for other viruses such as HIV-1 and RSV (46, 47). Second, the approach to stabilizing the prefusion conformation by introducing proline mutations at residues 986 and 987 may not be optimal because the K986P mutation may break a salt bridge between protomers that contributes to trimer stability. The resulting S trimer structure with a relaxed apex may induce antibodies that could not efficiently recognize S trimer spikes on the virus, although it may be more effective in inducing anti-RBD-neutralizing responses than the closed form. Third, considering the possibility that the postfusion S2 is present on infectious virions, vaccines using β -propiolactone-inactivated viruses may require additional quality control tests. Although the PiCoVacc appears to provide protection against challenges in nonhuman primates after three immunizations (44), it is unclear how to minimize the number of the postfusion S2 trimers to avoid batch variations. Structure-guided immunogen design may be particularly critical if SARS-CoV-2 becomes seasonal and returns with antigenic drift, as do influenza viruses (48).

REFERENCES AND NOTES

1. E. de Wit, N. van Doremalen, D. Falzarano, V. J. Munster, *Nat. Rev. Microbiol.* **14**, 523–534 (2016).
2. N. S. Zhong et al., *Lancet* **362**, 1353–1358 (2003).
3. B. Hijawi et al., *East. Mediterr. Health J.* **19**, S12–S18 (2013).
4. V. M. Corman, D. Muth, D. Niemeyer, C. Drosten, *Adv. Virus Res.* **100**, 163–188 (2018).
5. Y. Guan et al., *Science* **302**, 276–278 (2003).
6. B. Hu et al., *PLoS Pathog.* **13**, e1006698 (2017).
7. H. A. Mohd, J. A. Al-Tawfiq, Z. A. Memish, *Virol. J.* **13**, 87 (2016).

8. A. Banerjee, K. Kulcsar, V. Misra, M. Frieman, K. Mossman, *Viruses* **11**, 41 (2019).
9. P. Zhou et al., *Nature* **579**, 270–273 (2020).
10. S. Belouzard, J. K. Millet, B. N. Licitra, G. R. Whittaker, *Viruses* **4**, 1011–1033 (2012).
11. R. P. Rand, V. A. Parsegian, *Can. J. Biochem. Cell Biol.* **62**, 752–759 (1984).
12. V. A. Parsegian, N. Fuller, R. P. Rand, *Proc. Natl. Acad. Sci. U.S.A.* **76**, 2750–2754 (1979).
13. S. C. Harrison, *Virology* **479–480**, 498–507 (2015).
14. M. Kielian, *Annu. Rev. Virol.* **1**, 171–189 (2014).
15. W. Weissenhorn et al., *Mol. Membr. Biol.* **16**, 3–9 (1999).
16. L. Du et al., *Nat. Rev. Microbiol.* **7**, 226–236 (2009).
17. B. J. Bosch, R. van der Zee, C. A. de Haan, P. J. Rottier, *J. Virol.* **77**, 8801–8811 (2003).
18. M. Hoffmann et al., *Cell* **181**, 271–280.e8 (2020).
19. J. K. Millet, G. R. Whittaker, *Proc. Natl. Acad. Sci. U.S.A.* **111**, 15214–15219 (2014).
20. M. A. Tortorici, D. Vesles, *Adv. Virus Res.* **105**, 93–116 (2019).
21. F. Wu et al., *Nature* **579**, 265–269 (2020).
22. D. Wrapp et al., *Science* **367**, 1260–1263 (2020).
23. A. C. Walls et al., *Cell* **181**, 281–292.e6 (2020).
24. R. Henderson et al., *bioRxiv* 2020.05.18.102087 [Preprint]. 18 May 2020. <https://doi.org/10.1101/2020.05.18.102087>.
25. J. Lan et al., *Nature* **581**, 215–220 (2020).
26. R. Yan et al., *Science* **367**, 1444–1448 (2020).
27. J. Shang et al., *Nature* **581**, 221–224 (2020).
28. Q. Wang et al., *Cell* **181**, 894–904.e9 (2020).
29. A. C. Walls et al., *Proc. Natl. Acad. Sci. U.S.A.* **114**, 11157–11162 (2017).
30. W. Song, M. Gui, X. Wang, Y. Xiang, *PLOS Pathog.* **14**, e1007236 (2018).
31. B. Schroth-Diez et al., *Biosci. Rep.* **20**, 571–595 (2000).
32. B. J. Bosch, C. A. de Haan, S. L. Smits, P. J. Rottier, *Virology* **334**, 306–318 (2005).
33. E. Lontok, E. Corse, C. E. Machamer, *J. Virol.* **78**, 5913–5922 (2004).
34. C. M. Petit et al., *Virology* **341**, 215–230 (2005).
35. R. Ye, C. Montalto-Morrison, P. S. Masters, *J. Virol.* **78**, 9904–9917 (2004).
36. S. M. Hurtle, D. G. Bole, H. Hoover-Litty, A. Helenius, C. S. Copeland, *J. Cell Biol.* **108**, 2117–2126 (1989).
37. S. H. Scheres, *J. Struct. Biol.* **180**, 519–530 (2012).
38. R. N. Kirchdoerfer et al., *Sci. Rep.* **8**, 15701 (2018).
39. L. Zhang et al., *bioRxiv* 2020.06.12.148726 [Preprint]. 12 June 2020. <https://doi.org/10.1101/2020.06.12.148726>.
40. Z. Daniloski et al., *bioRxiv* 10.1101/2020.06.14.151357 [Preprint]. 7 July 2020. <https://doi.org/10.1101/2020.06.14.151357>.
41. X. Fan, D. Cao, L. Kong, X. Zhang, *Nat. Commun.* **11**, 3618 (2020).
42. T. Danielli, S. L. Pelletier, Y. I. Henis, J. M. White, *J. Cell Biol.* **133**, 559–569 (1996).
43. C. Liu et al., *bioRxiv* 2020.03.02.972927 [Preprint]. 5 March 2020. <https://doi.org/10.1101/2020.03.02.972927>.
44. Q. Gao et al., *Science* **369**, 77–81 (2020).
45. F. Wu et al., *medRxiv* 2020.03.30.20047365 [Preprint]. 20 April 2020. <https://doi.org/10.1101/2020.03.30.20047365>.
46. J. S. McLellan et al., *Science* **342**, 592–598 (2013).
47. G. Frey et al., *Nat. Struct. Mol. Biol.* **17**, 1486–1491 (2010).
48. J. J. Skehel, D. C. Wiley, *Annu. Rev. Biochem.* **69**, 531–569 (2000).

ACKNOWLEDGMENTS

We thank M. Liao for generous advice; the SBGrid team for technical support; and S. Harrison, M. Liao, A. Carfi, and D. Barouch for critical reading of the manuscript. Negative-stain and cryo-EM data were collected at the Molecular Electron Microscopy Suite and the Harvard Cryo-EM Center for Structural Biology, respectively, at Harvard Medical School. **Funding:** This work was supported by NIH grants AI147884 (to B.C.), 3R01AI147884-01A1S1 (to B.C.), AI141002 (to B.C.), and AI127193 (to B.C. and James Chou), as well as a COVID-19 Award by Massachusetts Consortium on Pathogen Readiness (MassCPR; to B.C.). **Author contributions:** B.C. and Y.C. conceived the project. Y.C. and H.P. expressed and purified the full-length S protein. T.X. expressed and purified soluble ACE2 and performed SPR and cell-cell fusion experiments. Y.C. and J.Z. performed negative-stain EM analysis. J.Z. prepared cryo-EM grids and performed EM data collection with contributions from S.M.S. and R.M.W. J.Z. processed the cryo-EM data and built and refined the atomic models for the prefusion S trimer and the postfusion S2 trimer. Y.C. processed the S1 data. S.R. contributed to data processing for S1 and provided computational support. S.R.-V. contributed to cell culture and protein production. All authors analyzed the data. B.C., Y.C., J.Z., and T.X. wrote the manuscript with input from all other authors. **Competing interests:** The authors

declare no competing interests. **Data and materials availability:** The atomic structure coordinates have been deposited in the RCSB Protein Data Bank (PDB) under the accession numbers 6XR8 and 6XRA, and the electron microscopy maps have been deposited in the Electron Microscopy Data Bank (EMDB) under the accession numbers EMD-22292 and EMD-22293. All materials generated during the current study are available from the corresponding author under a materials transfer agreement with Boston Children's Hospital. This work is licensed under a Creative Commons Attribution 4.0 International (CC BY 4.0) license, which permits unrestricted

use, distribution, and reproduction in any medium, provided the original work is properly cited. To view a copy of this license, visit <https://creativecommons.org/licenses/by/4.0/>. This license does not apply to figures/photos/artwork or other content included in the article that is credited to a third party; obtain authorization from the rights holder before using such material.

SUPPLEMENTARY MATERIALS

science.sciencemag.org/content/369/6511/1586/suppl/DC1
Materials and Methods

Figs. S1 to S12
Table S1
References (49–58)
MDAR Reproducibility Checklist

20 June 2020; accepted 14 July 2020
Published online 21 July 2020
10.1126/science.abd4251

CHEMICAL PHYSICS

Rotational resonances in the H₂CO roaming reaction are revealed by detailed correlations

Mitchell S. Quinn^{1*}, Klaas Nauta^{1*}, Meredith J. T. Jordan², Joel M. Bowman³, Paul L. Houston⁴, Scott H. Kable^{1†}

Since its discovery 16 years ago, roaming has become a ubiquitous mechanism in molecular photochemistry. Its general features are now understood, but little detail is known about how the potential energy surface (PES) determines reaction outcomes. We performed detailed experiments on formaldehyde (H₂CO) photodissociation and determined fully correlated quantum state distributions of the molecular hydrogen and carbon monoxide products. These experiments reveal previously undetected bimodal carbon monoxide rotational distributions. Insights from classical trajectory calculations demonstrate that these features arise from resonances as the PES directs the reaction into *cis* and *trans* O–C–H...H critical geometries, which produce rebound and stripping mechanisms, respectively. These subtle and pervasive effects demonstrate additional complexity in this prototypical roaming reaction, which we expect to be general. They also provide detailed benchmarks for predictive theories of roaming.

Roaming is now an established term in reaction dynamics (1–4) and is accepted as a pervasive feature of chemical reactions (5–17). Notably, roaming reactions bypass any conventional tight-saddle point transition state (TS). In formaldehyde, H₂CO, roaming occurs in the van der Waals region of the H + HCO radical product channel when there is insufficient energy in the relative translational degree of freedom for the radicals to dissociate (5). Instead, the H atom roams about the HCO fragment and abstracts the second H to form H₂ + CO molecular products. This leads to large amplitude in the C–H–H angle coordinate, θ_{CHH} , describing the roaming motion. Because abstraction occurs at large H–H separation, roaming also results in high vibrational excitation of the H₂ acceptor molecular product. These features are characteristic of all roaming reactions. Roaming necessarily involves large-amplitude angular motion in a van der Waals region of the configuration space of the system, and abstraction at large separation leads to highly vibrationally excited acceptor products.

Our chemical and intuitive understanding of roaming has always been guided by high-quality theory. Computational support of roaming has generally been provided by quasiclassical trajectory (QCT) calculations on high-level potential energy surfaces (PESs) (5, 7). However, strictly theoretical analyses are challenging because of the large-amplitude motion, which necessitates sampling large volumes of configuration space and because of the fact that many roaming pathways are in the same region of configuration space as conical intersections (3, 13, 18, 19). Quantum calculations of roaming in a three-atom reaction (20, 21) have provided both support and insight about the large-amplitude nature of roaming. There is also pronounced current interest in using statistical mechanics approaches to roaming dynamics through analysis of phase space—rather than configuration space—which is embedded in QCTs (19, 22–24).

Seminal experiments in 1993 on the unimolecular dissociation of H₂CO showed unexpected bimodality of the CO rotational distribution with a puzzling peak at low quanta of CO angular momentum, $j(\text{CO})$ (25). Bimodality in chemical dynamics is often an indicator of competing chemical or dynamical pathways. Although the more pronounced high- $j(\text{CO})$ signal was well understood in 1993 as characteristic of the conventional tight TS, it was not until 2004 that the low- $j(\text{CO})$ feature was shown

to be a signature of roaming (5). The 2004 experiments were critical in showing that this low- $j(\text{CO})$ peak was correlated with highly vibrationally excited H₂. These results were confirmed in dynamics calculations, which, by examination of the trajectories, were able to identify the roaming pathway. Similar observations of bimodal distributions of final quantum states in the products of a reaction are now often considered to be diagnostic of possible roaming. Although unexpected products are another signature of possible roaming dynamics (11), bimodal distributions are centrally important as they indicate the presence of multiple reaction pathways.

This paper presents additional details of the multimodality of roaming signatures and shows that the previously reported low- $j(\text{CO})$ rotational distribution is itself bimodal. Observation of the bimodality requires the measurement of fully correlated, individual H₂(v, j) states with CO(v, j) states. Although aspects of the correlation between CO and H₂ product quantum states were revealed even in the first roaming paper (5), these observations were derived from interrogation of the CO product, which allowed the H₂ states correlated with individual CO states to be inferred. The correlations between individual H₂ quantum states and the full set of CO states have not been previously revealed. The results in this paper show that the CO rotational state distribution from roaming is itself bimodal. Moreover, this bimodality is present for all CO vibrational states, for every H₂ rotation-vibration state, and for all H₂CO initial states. It is a pervasive feature of roaming in H₂CO. Our observation of multimodality implies previously unidentified, and as yet unexplained, dynamics in the roaming reaction.

Experimental results

The experiments used in this study have largely been described previously (16), except that the H₂ photofragment was detected instead of CO. Briefly, H₂CO in a molecular beam of He was excited by a laser to the 2¹4³ vibrational level of the first excited singlet (S₁) state. See supplementary materials and fig. S1 for relevant details of H₂CO spectroscopy. The nascent, recoiling H₂ photofragments were state-selectively ionized using (2 + 1) resonance enhanced multiphoton ionization (REMPI) via the $E, F\ ^1\Sigma_g^+$ state. An example REMPI

¹School of Chemistry, University of New South Wales, Kensington, NSW, 2052, Australia. ²School of Chemistry, University of Sydney, Sydney, NSW, 2006, Australia. ³Department of Chemistry, Emory University, Atlanta, GA, USA. ⁴Department of Chemistry and Biochemistry, Cornell University, Ithaca, NY, USA.

*These authors contributed equally to this work.

†Corresponding author. Email: s.kable@unsw.edu.au

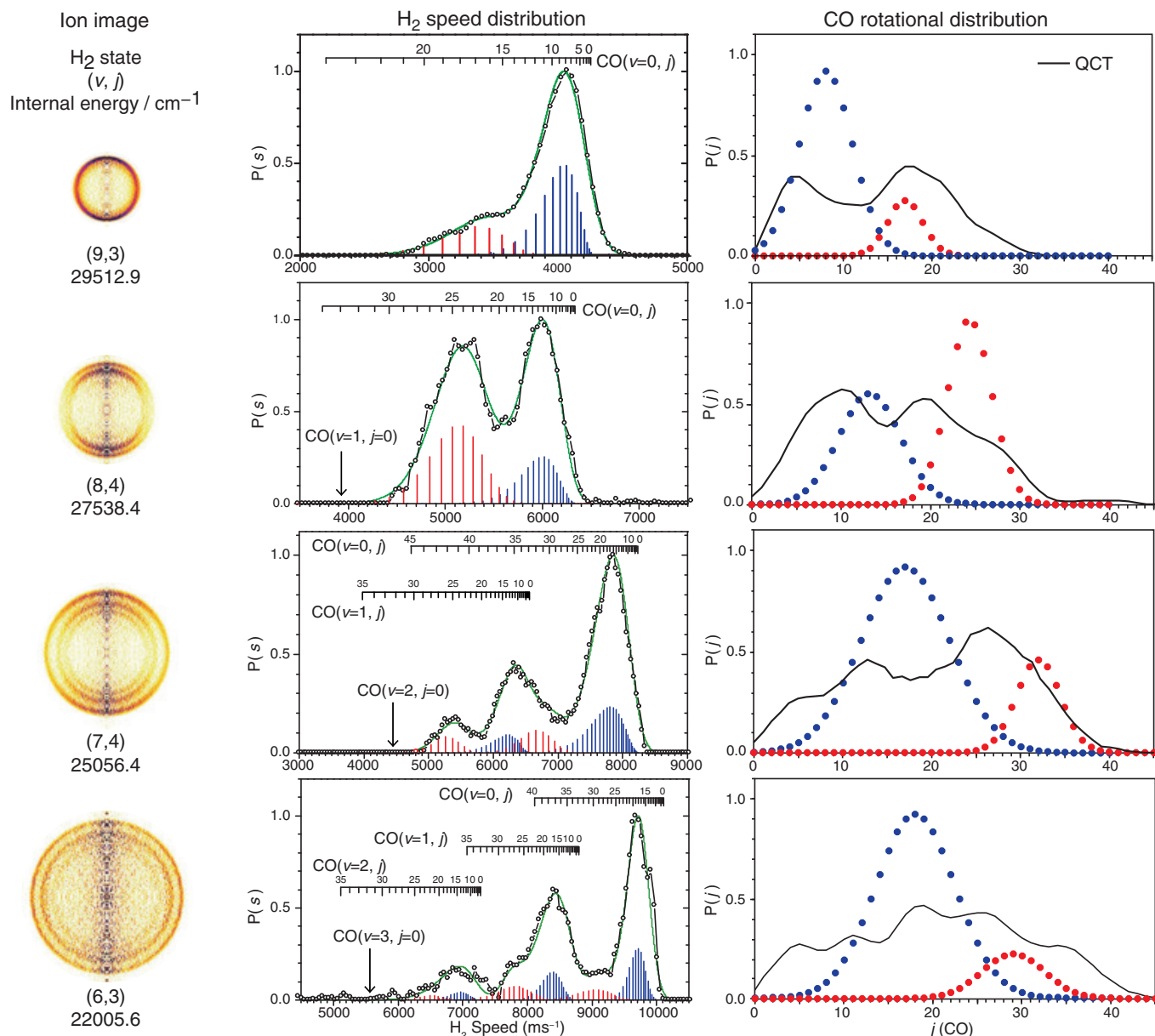


Fig. 1. Experimental data for speed distributions of H_2 in $(v, j) = (9,3)$, $(8,4)$, $(7,4)$, and $(6,3)$, respectively. The left column shows the velocity-mapped image, the center column shows the derived H_2 speed distribution along with a fit to a bimodal Gaussian CO rotational distribution, and the right column shows the fitted CO ($v = 0$) rotational distributions and those obtained from corresponding QCT simulations.

spectrum is shown in fig. S2. Recoiling H_2 ions were mass selected and then recorded on a position-sensitive detector using velocity map imaging (26). A full experimental description is provided as supplementary materials.

Figure 1 shows a selection of velocity-mapped images of H_2 after transforming the raw, two-dimensional image into a slice of the three-dimensional distribution using BASEX (27). The H_2 (v, j) product state is identified under each image. Some of the rings in the images exhibit anisotropy. The origin of this anisotropy is unclear, is sensitive to the initially excited rovibrational state of H_2CO , and will be the subject of further work. Adjacent to each image

is the resultant H_2 speed distribution, which exhibits complex structure. Conservation of energy and linear momentum dictates that this structure is associated with the internal energy of the CO cofragment. It is well established that the roaming reaction in H_2CO produces CO in excited vibrational states (16, 28); however, the observed structure does not correspond (solely) to different vibrational populations. The full set of images and speed distributions for 50 experiments is provided in fig. S2.

The data shown in the top two rows of Fig. 1 probe H_2 ($v = 9, j = 3$) and ($v = 8, j = 4$). In both cases, the high internal energy of H_2 ensures that the CO cofragment can only be formed in

$v = 0$. Any structure in the speed distribution must reflect solely the population distribution in CO rotational states. Although there is insufficient experimental resolution to resolve individual j states, both images clearly show bimodal speed and, hence, $j(\text{CO})$ distributions. Underneath the experimental curves, two model Gaussian j distributions are shown as stick spectra, where j has been transformed into the H_2 speed coordinate. The blue and the red stick spectra represent the lower- and higher- $j(\text{CO})$ components, respectively. Each stick spectrum was convolved with an instrumental function of $\sim 250 \text{ m s}^{-1}$ to account for inherent instrumental resolution and the H_2

Fig. 2. CO rotational energies and impact parameters as a function of available energy.

(A) Average CO rotational energy (E_{rot}) determined from the mean of the Gaussian components shown in Fig. 1 and fig. S2. (B) Approximate impact parameter (see text for details) between recoiling CO and H₂ fragments, calculated from the mean of each Gaussian component. In both panels, the red and blue lines indicate the higher- and lower- j (CO) Gaussian components, respectively.

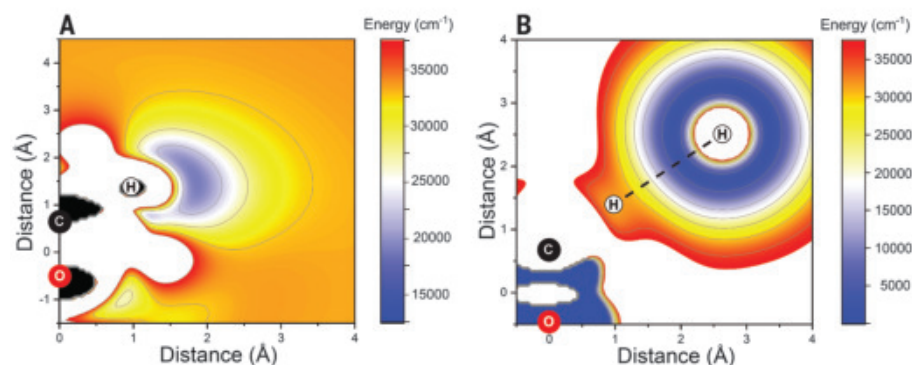
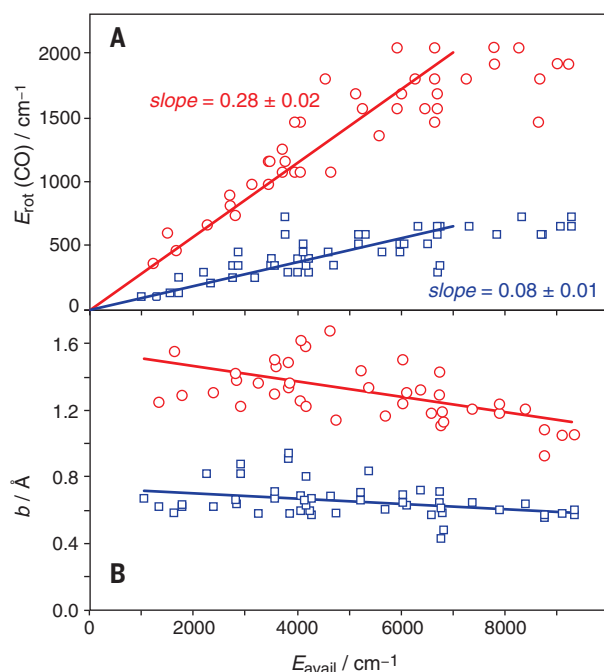


Fig. 3. Two-dimensional slices of the H + HCO PES. (A) Potential experienced by a roaming H atom for HCO in its equilibrium geometry. (B) Potential experienced by the H bound to CO at the critical point where it bonds to the roaming H. Energies are with respect to the H₂CO minimum.

recoil from the ionization step, and the result is shown as the green curve. The Gaussian fitting parameters were varied until the best fit to the experimental data was obtained. Two Gaussian functions provided a better fit to experiment than any other model distribution (see the section on experimental data modeling in the supplementary materials).

The speed distributions for the H₂ (7,4) and (6,3) states in the bottom two rows of Fig. 1 now contain contributions from CO($v = 1,2$) because the H₂ internal energy is commensurately lower. Each distribution was very well fit by two components to the rotational state distribution in each vibrational state, as shown by the stick spectra. Here, again, the blue and red sticks represent the lower- and higher- j components, respectively, and the green curve shows the convolution with the instrumental

function. The CO rotational state distributions determined from the Gaussian fits are shown in the right column of Fig. 1 for CO($v = 0$). Double Gaussian rotational distributions were fit to 50 speed distributions for three initial H₂CO states and H₂ product states spanning $v = 6$ to 9 and $j = 0$ to 12 (fig. S3). In most cases, the low- j component dominates; in a few cases, the high- j component is too weak to fit or lies underneath the low- j component of a higher-lying vibrational state.

The mean j of the low- and high- j (CO) fitted Gaussians—which are shown as blue and red, respectively, in Fig. 1 and fig. S2—was converted to CO rotational energy. This energy, for CO($v = 0$), is plotted as a function of available energy in Fig. 2A. Each component shows a linear trend with $E_{\text{rot}}(\text{CO})$ for the first 7000 cm⁻¹ of available energy, perhaps reaching a pla-

teau at the highest available energies. The slope of each line represents the fraction of available energy found in CO rotation for each component, which reveals that 8 ± 1 and $28 \pm 2\%$ of the available energy is found, on average, in the low- and high- j (CO) components, respectively.

As described in the experimental data modeling section of the supplementary materials, conservation of angular momentum, coupled with very low H₂CO and H₂ angular momentum, ensures that $j(\text{CO}) \approx L = \mu vb$, where L is the orbital angular momentum, μ is the reduced mass, v is the recoil velocity in the center of mass (COM) frame, and b is the impact parameter of the recoiling H₂ and CO fragments. This relationship allows an approximate impact parameter to be determined for the center of each fitted Gaussian component (Fig. 2B), plotted as a function of available energy. Further analysis is given as supplementary materials, with limiting impact parameters shown in fig. S4. Figure 2B shows that the low- j (CO) component corresponds to an impact parameter of ≈ 0.7 Å, and the high- j component corresponds to ≈ 1.3 Å. There is a weak trend toward lower impact parameters across the 1-eV difference in available energy. The consistency of derived impact parameters, across a wide range of available energy, arising from 50 different combinations of H₂CO initial states and H₂ product states is indicative of a consistent feature in the dynamics of the reaction, so we turn to QCTs run on an accurate ab initio PESs for further insight.

QCT results

The 52,800 QCTs calculated in (29) were re-analyzed. These trajectories were run on a high-quality PES (30) at a total energy of 36,223 cm⁻¹ relative to the bottom of the H₂CO well, which corresponds to excitation of the H₂CO 2¹4³ state. Of the 42.8% of the trajectories that gave H₂ + CO products, 13.5% produced H₂ with $v \geq 6$ and were classified as roaming. These roaming trajectories were then examined and analyzed in detail. For each trajectory, the final orbital angular momentum and impact parameter were recorded along with the angular momentum and the vibrational and rotational energy of each of the CO and H₂ products. The classical results were converted to quantum numbers using standard (histogram) binning, with the exception of the H₂ vibrational energy, for which we used Gaussian binning (31). Although Gaussian binning reduced the effective number of trajectories for each H₂(v) (fig. S5), it describes the action associated with each quantum state markedly better and, hence, performs better in terms of conservation of energy and gives minimal blurring of other distributions (31). Further details are provided in the computational methods section of the supplementary materials.

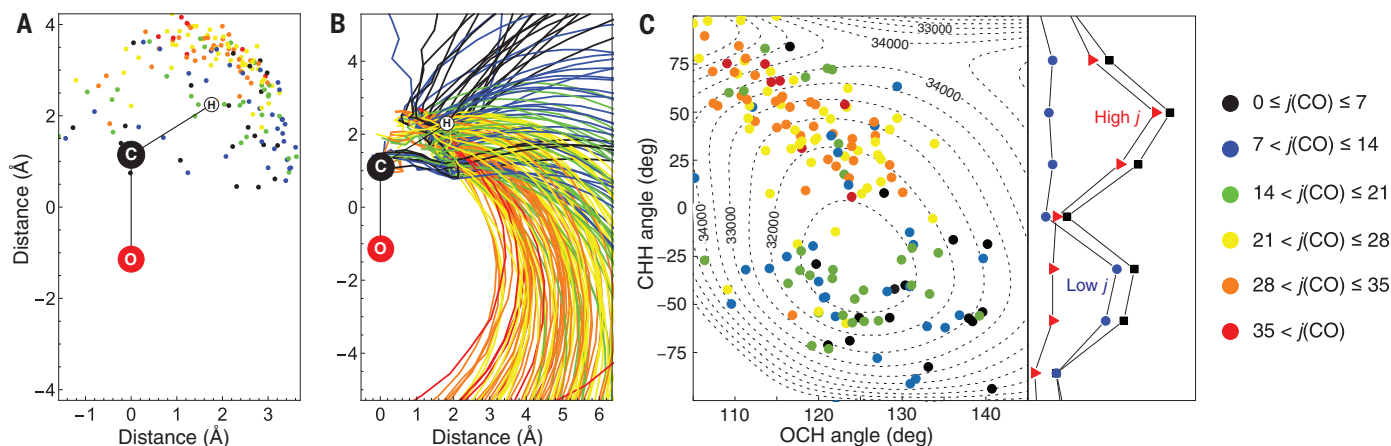


Fig. 4. CO + H₂ roaming exit channel. (A) Plot of position of H₂ COM at the critical point on the PES (see text for details). (B) Trajectories of H₂ COM in the stationary frame of CO after crossing the critical point. (C) H₂ critical point COM projected onto the θ_{OCH} and θ_{CHH} coordinates describing the breaking and forming bonds superimposed on PES contours, with respect to the H₂ CO

minimum, for H–H, C–H, and C–O distances of 2.000, 1.200, and 1.1838 Å, respectively, and all atoms in plane. Trajectories and critical points are color coded to final $j(\text{CO})$, as indicated. On the far right, the overall distribution of critical point θ_{CHH} (black squares), separated into low- $j(\text{CO})$ (blue circles) and high- $j(\text{CO})$ (red triangles) components, is noted.

The right column of Fig. 1 shows the CO rotational state distributions for $v(\text{CO}) = 0$, derived from QCT calculations, for the four (H₂) (v_j) experimental states shown. The QCT distributions are compared with the low- and high- $j(\text{CO})$ Gaussians obtained by modeling the experimental H₂ speed distributions. First, the range of $j(\text{CO})$ states is reproduced well by the QCT calculations. Second, each QCT distribution shows evidence of a bimodal rotational distribution that strongly resembles the experimentally derived distributions. The qualitative agreement between the bimodal experimental and QCT distributions leads us to forensically investigate the trajectories and the PES to seek an explanation. QCT speed distributions corresponding to all experimental data can be found in the supplementary materials.

Discussion

The nature of the PES

A bimodal distribution of product state populations is often indicative of two reaction mechanisms or two pathways to products on a PES. To test whether there are two distinct regions of H₂CO phase space, we closely followed the set of 208 trajectories that led to H₂ ($v = 7, j = 3$) products. Having $E_{\text{avail}} = 6372 \text{ cm}^{-1}$, this state is approximately in the middle of the range of H₂ vibrational and rotational states and available energies.

Figure 3A shows a slice of the PES experienced by the roaming H atom for in-plane interaction with a free HCO moiety—that is, with HCO bond lengths and bond angle equal to those of the isolated radical. The origin is defined as the COM of the CO moiety throughout, and we define the x axis as perpendicular and the y axis as parallel to this bond. The deep H₂CO well lies at a negative x distance and is not shown. A shallower well lies almost along the

CH bond. As the roaming H atom approaches the bound H atom, the PES changes substantially. There is a critical distance of approach of the roaming H atom, at which point the internal H atom becomes unbound to the C atom. Figure 3B shows a two-dimensional slice of this critical point from the perspective of the bound H atom. The energy plateau between the inner H being bound to C and bound to H is shown by orange shading. As the inner H moves away from CO, it experiences a large attractive force toward the free (roaming) H atom, forming the H₂ molecule. This large force leads to extensive H₂ vibrational excitation, which is a well-known signature in H₂CO roaming. After the critical point for each trajectory, the PES continues to change substantially. There is a strong repulsion between the COMs of the nascent CO and H₂ fragments (fig. S6).

Two roaming mechanisms

We examined all 208 trajectories leading to H₂ ($v = 7, j = 3$). In every case, there is a well-defined, critical point at which the internal H atom transfers to the roaming H atom. The H atom is never transferred back to CO. The CO and H₂ fragments recoil directly away from each other along the exit channel and form products, with little further complex interaction (fig. S6). Figure 4A shows these critical points for all trajectories in the H₂ ($v = 7, j = 3$) set projected onto the xy (HCO) plane. The dots represent projections of the H₂ COM and are color coded according to the final j state of the recoiling CO, as shown in the legend. Although not absolute, most low- j trajectories have critical points that lie in a cis-like O–C–H...H geometry, whereas high- j trajectories have critical points that lie more frequently in a trans O–C–H...H geometry.

Figure 4B shows how the trajectories propagate in the exit channel after the critical point—

again showing the H₂ COM position relative to the CO COM. The stationary reference frame of the CO causes the trajectories to be curved, and higher curvature reflects higher final CO angular momentum. Trajectories are color coded in the same way as they are in Fig. 4A. The low- j trajectories starting in cis geometries mostly moved up in the figure and had a smaller final impact parameter between H₂ and CO. Trajectories with high $j(\text{CO})$ starting from trans geometries, on the other hand, headed downward in the figure, with larger resultant impact parameters. Figure S7 shows that final $j(\text{CO})$ is approximately proportional to orbital angular momentum L and hence impact parameter b . The scatter about the linear relationship is a result of nonzero $j(\text{H}_2) = 3$.

The correlation between cis and trans critical point geometries and final $j(\text{CO})$ is shown in Fig. 4C, where the H₂ COM of the trajectory critical points—color coded for final $j(\text{CO})$ —have been projected onto the θ_{OCH} and θ_{CHH} angular coordinates, describing the breaking and forming bonds and superimposed on PES contours. In Fig. 4C, cis and trans critical points have $\theta_{\text{CHH}} < 0$ and $\theta_{\text{CHH}} > 0$, respectively. The trajectory critical points have been binned with respect to θ_{CHH} on the right-hand side of the panel, with the overall distribution (black) separated into low- and high- $j(\text{CO})$ —blue and red symbols—defined as $j(\text{CO}) \leq 21$ and $j(\text{CO}) > 21$, respectively. Figure 4C shows that cis critical points strongly correlate with low- $j(\text{CO})$ products, and trans critical points are strongly correlated with high- $j(\text{CO})$ products.

The QCTs also revealed a mechanistic difference between the low- j and high- j trajectories. As the roaming H atom approaches the bound H of HCO, there is a strong attractive force (Fig. 3A). From the point of view of abstraction reactions, a cis O–C–H...H configuration leads

to a rebound reaction with a small impact parameter, whereas a trans configuration leads to a stripping reaction with a large impact parameter. Thus, trans critical point configurations produced more CO rotation. Four typical rebound and stripping trajectories are shown in fig. S8 and movies S1 to S4.

The origin of bimodality

The QCT results reproduced the range of final $j(\text{CO})$. They showed that reactions that produce low- $j(\text{CO})$ have predominantly cis critical point geometries and demonstrate a rebound-type abstraction reaction. High- $j(\text{CO})$ trajectories, on the other hand, typically have trans critical point geometries and exhibit a stripping-like reaction with a large impact parameter. We can also describe the energetics of the roaming reaction to produce $\text{H}_2 + \text{CO}$. In the entrance channel, there is a substantial well near a linear $\text{C-H}\cdots\text{H}$ geometry (Fig. 3A). At the critical geometry, the CH bond breaks on a high-energy plateau (Fig. 3B) such that the H_2 product is formed with high vibrational energy, and then, in the exit channel, there is a repulsive force leading to the final molecular products (fig. S6).

Figure 4C shows the importance of θ_{CHH} . Our hypothesis of the origin of the bimodality is that this coordinate may be considered to be a bending coordinate of the roaming H atom about the breaking CH bond. The coordinate is crucial because the roaming H atom must roam from the H_2CO well on the opposite side of the molecule to the critical roaming configuration. This necessarily involves large-amplitude motion in—and hence velocity associated with—the θ_{CHH} coordinate. Abstraction of the bound H atom takes place when the roaming H reaches a critical $\text{H}\cdots\text{H}$ distance of ~ 2 Å (Fig. 3B). Figures 3A and 4C also show that the minimum energy geometry has near-linear C-H-H , and the θ_{CHH} bending potential is approximately harmonic. As shown in Fig. 4C, the critical points for abstraction occurred more often when the H atom had slowed to a stop at the classical turning points of the θ_{CHH} potential—i.e., at cis and trans geometries, which will occur in resonance with the classical θ_{CHH} angular frequency. There is also a minimum in the distribution of trajectory critical points at the near-linear C-H-H angle, which corresponds to the minimum energy PES well shown in Fig. 4C. Thus, abstraction was less probable when the roaming H atom passed through the minimum energy configuration with substantial velocity. This is classical behavior, and it explains why the QCTs could qualitatively reproduce the distinct impact parameter distribution and hence the bimodality in the $j(\text{CO})$ distribution.

There is a commensurate quantum mechanical explanation, which arises straightforwardly from quantum-classical correspondence. As the roaming H atom starts an oscillation in

the θ_{CHH} coordinate, a bound wave function is transiently established. All bending wave functions except $v = 0$ have maxima at the extremities. In this case, the minimum in θ_{CHH} is close to linear, so the extremities correspond to cis and trans geometries. This bending wave function—likely a mix of many different quanta of the van der Waals bending vibration, but not $v = 0$ —is projected onto the final CO product state distribution. The projection of a bending wave function in the parent molecule onto the final product rotational state distributions of the products is known as the rotation reflection principle (32, 33), and the bimodal CO rotational distribution can be considered to arise from resonances of the θ_{CHH} partial wave expansion.

Summary and outlook

Detailed velocity-mapped imaging measurements of the H_2 product of H_2CO dissociation have made it possible to measure the correlations between individual vibrational and rotational states of the H_2 and individual vibrational and rotational states of the CO products. Although previous results (29) have shown that the roaming and TS pathways to molecular products have different CO rotational distributions, our results—obtained by focusing on high-vibrational ($v \geq 6$) levels of the H_2 —demonstrate that the CO rotational distribution for the roaming pathway is itself also bimodal. The measurement and the associated QCT calculations provide additional insights into the roaming process: The high rotational states of CO from roaming come from a trans $\text{O-C-H}\cdots\text{H}$ critical configuration, whereas the low rotational states come from a cis configuration. A simple physical picture is that the former leads to a large impact parameter stripping abstraction of the H in HCO by the roaming H atom, whereas the latter leads to a small impact parameter rebound abstraction. We hypothesized that the bimodality arises from a reflection of the wave function for bending the θ_{CHH} coordinate.

Large-amplitude motion in the bending coordinate comprising the breaking and forming bonds is a prerequisite for roaming reactions. This motion arises precisely because of the roaming mechanism. We therefore expect bimodality to be a feature of all roaming reactions. Testing this hypothesis will be a challenge for theoretical and experimental chemistry. The quantitative reproduction of the state-specific experimental correlations would be an extremely stringent test of the quality of a PES and of any theoretical method.

REFERENCES AND NOTES

1. A. G. Suits, *Acc. Chem. Res.* **41**, 873–881 (2008).
2. J. M. Bowman, B. C. Shepler, *Annu. Rev. Phys. Chem.* **62**, 531–553 (2011).
3. S. Maeda, T. Taketsugu, K. Ohno, K. Morokuma, *J. Am. Chem. Soc.* **137**, 3433–3445 (2015).
4. A. G. Suits, *Annu. Rev. Phys. Chem.* **71**, 77–100 (2020).

5. D. Townsend *et al.*, *Science* **306**, 1158–1161 (2004).
6. P. L. Houston, S. H. Kable, *Proc. Natl. Acad. Sci. U.S.A.* **103**, 16079–16082 (2006).
7. B. R. Heazlewood *et al.*, *Proc. Natl. Acad. Sci. U.S.A.* **105**, 12719–12724 (2008).
8. J. G. López *et al.*, *J. Am. Chem. Soc.* **129**, 9976–9985 (2007).
9. J. Mikosch *et al.*, *Science* **319**, 183–186 (2008).
10. J. Zhang *et al.*, *J. Phys. Chem. Lett.* **1**, 2747–2752 (2010).
11. E. Kamarchik, L. Koziol, H. Reisler, J. M. Bowman, A. I. Krylov, *J. Phys. Chem. Lett.* **1**, 3058–3065 (2010).
12. R. Sivaramakrishnan *et al.*, *J. Phys. Chem. A* **115**, 3366–3379 (2011).
13. M. P. Grubb *et al.*, *Science* **335**, 1075–1078 (2012).
14. K. L. K. Lee *et al.*, *Chem. Sci.* **5**, 4633–4638 (2014).
15. A. S. Mereshchenko, E. V. Butaeva, V. A. Borin, A. Eyzips, A. N. Tarnovsky, *Nat. Chem.* **7**, 562–568 (2015).
16. M. S. Quinn, D. U. Andrews, K. Nauta, M. J. T. Jordan, S. H. Kable, *J. Chem. Phys.* **147**, 013935 (2017).
17. F. J. J. Cascarini, B. Hornung, M. S. Quinn, P. A. Robertson, A. J. Orr-Ewing, *J. Phys. Chem. A* **123**, 2679–2686 (2019).
18. N. D. Coutinho *et al.*, *J. Phys. Chem. Lett.* **6**, 1553–1558 (2015).
19. F. A. L. Mauguère *et al.*, *Annu. Rev. Phys. Chem.* **68**, 499–524 (2017).
20. A. Li, J. Li, H. Guo, *J. Phys. Chem. A* **117**, 5052–5060 (2013).
21. F. A. L. Mauguère *et al.*, *J. Phys. Chem. A* **120**, 5145–5154 (2016).
22. D. U. Andrews, S. H. Kable, M. J. T. Jordan, *J. Phys. Chem. A* **117**, 7631–7642 (2013).
23. F. A. L. Mauguère, P. Collins, G. S. Ezra, S. C. Farantos, S. Wiggins, *Chem. Phys. Lett.* **592**, 282–287 (2014).
24. F. A. L. Mauguère, P. Collins, G. S. Ezra, S. C. Farantos, S. Wiggins, *J. Chem. Phys.* **140**, 134112 (2014).
25. R. D. van Zee, M. F. Foltz, C. B. Moore, *J. Chem. Phys.* **99**, 1664–1673 (1993).
26. A. T. J. B. Eppink, D. H. Parker, *Rev. Sci. Instrum.* **68**, 3477–3484 (1997).
27. V. Dribinski, A. Ossadtchi, V. A. Mandelshtam, H. Reisler, *Rev. Sci. Instrum.* **73**, 2634–2642 (2002).
28. S. A. Lahankar *et al.*, *Chem. Phys.* **347**, 288–299 (2008).
29. P. L. Houston *et al.*, *J. Chem. Phys.* **147**, 013936 (2017).
30. X. Wang, P. L. Houston, J. M. Bowman, *Phil. Trans. R. Soc. A* **375**, 20160194 (2017).
31. R. Conte, B. Fu, E. Kamarchik, J. M. Bowman, *J. Chem. Phys.* **139**, 044104 (2013).
32. R. Schinke, *J. Chem. Phys.* **84**, 1487–1491 (1986).
33. R. Schinke, *Photodissociation Dynamics* (Cambridge Monographs on Atomic, Molecular and Chemical Physics, Cambridge Univ. Press, 1993).
34. M. Quinn *et al.*, Unprecedented correlation information reveals rotational resonances in the H_2CO roaming reaction, Univ. of New South Wales dataset (Research Data Australia, 2020); <https://doi.org/10.26190/5f0e4db844041>.

ACKNOWLEDGMENTS

Funding: The University of New South Wales and University of Sydney work was supported by the Australian Research Council (DP190102013). M.S.Q. was supported by an Australian postgraduate award. J.M.B. thanks the Army Research Office, DURIP grant (W911NF-14-1-0471), for funding a computer cluster where the trajectory calculations were performed. **Author contributions:** M.S.Q. performed all experiments and data analysis. K.N. assisted with experiments and performed detailed analysis of PES. M.J.T.J. supervised aspects of computational and experimental data analysis. J.M.B. directed construction of PESs and trajectory code. P.L.H. supervised and carried out trajectory calculations. S.H.K. conceived and directed the project and supervised experiments. All authors contributed to the drafting of the manuscript. **Competing interests:** The authors have no competing interests to declare. **Data and materials availability:** All data needed to evaluate the conclusions in the paper are present in the paper or the supplementary materials. Raw data are available at the Australian Research Data Archive (34).

SUPPLEMENTARY MATERIALS

science.sciencemag.org/content/369/6511/1592/suppl/DC1
Materials and Methods
Supplementary Text
Figs. S1 to S8
Tables S1 and S2
References (35–38)
Movies S1 to S4

23 April 2020; accepted 19 July 2020
Published online 6 August 2020
10.1126/science.abc4088

GRAPHENE

Inducing metallicity in graphene nanoribbons via zero-mode superlattices

Daniel J. Rizzo^{1,2*}, Gregory Veber^{3*}, Jingwei Jiang^{1,4*}, Ryan McCurdy³, Ting Cao^{1,4,5}, Christopher Bronner¹, Ting Chen¹, Steven G. Louie^{1,4,†}, Felix R. Fischer^{3,4,6,†}, Michael F. Crommie^{1,4,6,†}

The design and fabrication of robust metallic states in graphene nanoribbons (GNRs) are challenging because lateral quantum confinement and many-electron interactions induce electronic band gaps when graphene is patterned at nanometer length scales. Recent developments in bottom-up synthesis have enabled the design and characterization of atomically precise GNRs, but strategies for realizing GNR metallicity have been elusive. Here we demonstrate a general technique for inducing metallicity in GNRs by inserting a symmetric superlattice of zero-energy modes into otherwise semiconducting GNRs. We verify the resulting metallicity using scanning tunneling spectroscopy as well as first-principles density-functional theory and tight-binding calculations. Our results reveal that the metallic bandwidth in GNRs can be tuned over a wide range by controlling the overlap of zero-mode wave functions through intentional sublattice symmetry breaking.

Extended two-dimensional (2D) graphene is a gapless semimetal, yet when it is laterally confined to nanometer-scale 1D ribbons, a sizable energy gap emerges (1). Unlike carbon nanotubes (which can exhibit metallicity depending on their chirality), isolated armchair and zigzag graphene nanoribbons (GNRs) always feature a band gap that scales inversely with the width of the ribbon (2). This makes GNRs attractive as transistor elements for logic devices at the ultimate limits of scalability (3). However, it is also a limitation because metallic GNRs would be valuable as device interconnects and could create opportunities for exploring Luttinger liquids (4–6), plasmonics (7–9), charge density waves (10, 11), and superconductivity (12, 13) in 1D. GNRs synthesized by means of atomically precise bottom-up fabrication techniques exhibit band gaps that are in good agreement with theoretical predictions (14–18) and are thus ideal platforms for probing atomic-scale sensitivity of electronic properties in 1D structures. It has recently been shown, for example, that bottom-up synthesis can be used to place topologically protected junction states at predetermined positions along the GNR backbone (19–24) that hybridize to form the frontier GNR electronic structure. These localized states (21, 22) each contribute a single unpaired electron at mid gap to the electronic structure (i.e., at $E = 0$), and so judicious

placement of such zero-mode states raises the possibility of creating metallic and magnetic configurations. Thus far, however, only semiconducting GNRs have been fabricated with this technique (19, 20).

Here we demonstrate a general approach for designing and fabricating metallic GNRs using the tools of atomically precise bottom-up synthesis. This is accomplished by embedding localized zero-mode states in a symmetric superlattice along the backbone of an otherwise semiconducting GNR. Quantum mechanical hopping of electrons between adjacent zero-mode states results in metallic bands as predicted by elementary tight-binding electronic structure models (25). Using scanning tunneling spectroscopy (STS) and first-principles theoretical modeling, we find that zero modes confined to only one of graphene's two sublattices (i.e., sublattice-polarized states) result in narrow-band metallic phases that reside at the border of a magnetic instability. The metallic bandwidth of these GNRs, however, can be increased by more than a factor of 20 by intentionally breaking the GNR bipartite symmetry, thus resulting in robust metallicity. This is accomplished by inducing the formation of just two new carbon-carbon bonds per GNR unit cell (each unit cell contains 94 carbon atoms in the bottom-up synthesized GNRs presented here). This marked change in electronic structure from a seemingly minor chemical bond rearrangement arises from the loss of sublattice polarization that accompanies broken bipartite symmetry. This concept provides a useful tool for controlling GNR metallicity and for tuning GNR electronic structure into different physical regimes.

Concept of GNR metallization

Our strategy for designing metallic GNRs uses a theorem based on simple nearest-neighbor tight-binding theory: A piece of graphene with

a surplus of carbon atoms (ΔN) on sublattice A versus sublattice B will have a minimum of $\Delta N = N_A - N_B$ eigenstates localized on the A sublattice at $E = 0$ ("zero modes"). Here N_A (N_B) is the number of atoms residing on sublattice A (B) [see (26) for this theorem's derivation]. This bears resemblance to Lieb's theorem (27) and is also applicable to the behavior of vacancy defects in graphene (28–30). Expanding this idea to 1D GNR systems with a periodic sublattice imbalance (i.e., an imbalance in each unit cell), one can construct a low-energy effective tight-binding model to describe the resulting electronic bands by introducing a parameter, t , that represents electron hopping between adjacent localized zero modes. This concept can be used to design metallic GNRs by providing them with a unit cell that contains a surplus of two carbon atoms on sublattice A ($\Delta N = 2$). Under this construction there are two relevant hopping amplitudes: the intracell hopping amplitude (t_1) and the intercell hopping amplitude (t_2). A tight-binding analysis of this situation leads to the well-known Su-Schrieffer-Heeger (SSH) (25) dispersion relationship for the zero-mode bands:

$$E_{\pm}(k) = \pm \sqrt{|t_1|^2 + |t_2|^2 + 2|t_1||t_2|\cos(k + \delta)} \quad (1)$$

where δ is the relative phase between t_1 and t_2 (which, in general, can be complex numbers). Two bands result here because there are two zero-mode states per unit cell and the energy gap between them is $\Delta E = 2||t_1| - |t_2||$. If the two hopping amplitudes are identical, $|t_1| = |t_2|$, then the energy gap is reduced to zero, and the resulting 1D electronic structure should be metallic.

Synthesis of molecular precursor and sawtooth-GNRs

Using this idea as a guide for creating metallic GNRs, we designed the GNR precursor molecule **1** (Fig. 1A). A graphene honeycomb lattice superimposed onto this molecule reveals that under cyclodehydrogenation, the methyl group carbon atom attached to the central tetracene (highlighted gray in Fig. 1A) will fuse and provide one surplus carbon atom on sublattice A over sublattice B per monomer. Previous step-growth polymerizations of structurally related molecules (20) suggest that the surface polymerization of **1** will place the central tetracene unit in an alternating pattern on either side of the GNR growth axis. If polymerization proceeds in a head-to-tail configuration, then the resulting GNRs feature two additional carbon atoms on sublattice A per unit cell (Fig. 1A). Following cyclodehydrogenation, the anticipated GNR structure is composed of short zigzag edges

¹Department of Physics, University of California, Berkeley, CA 94720, USA. ²Department of Physics, Columbia University, New York, NY 10027, USA. ³Department of Chemistry, University of California, Berkeley, CA 94720, USA. ⁴Materials Sciences Division, Lawrence Berkeley National Laboratory, Berkeley, CA 94720, USA. ⁵Department of Materials Science and Engineering, University of Washington, Seattle, WA 98195, USA. ⁶Kavli Energy NanoSciences Institute at the University of California Berkeley and the Lawrence Berkeley National Laboratory, Berkeley, CA 94720, USA.

*These authors contributed equally to this work.

†Corresponding author. Email: crommie@berkeley.edu (M.F.C.); ffischer@berkeley.edu (F.R.F.); sglouie@berkeley.edu (S.G.L.)

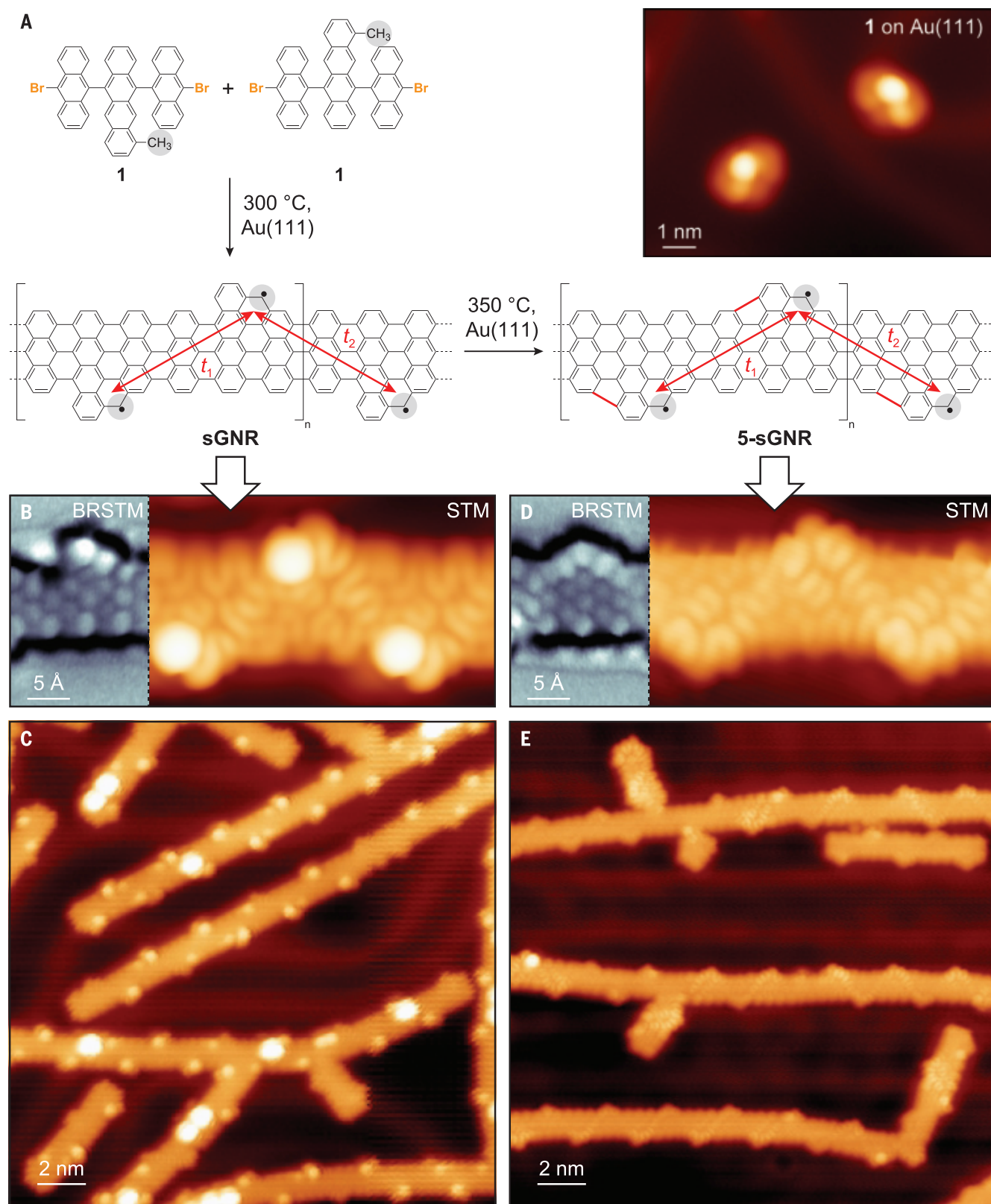


Fig. 1. Bottom-up synthesis of sawtooth-GNRs. (A) Schematic representation of bottom-up growth of both sGNRs and 5-sGNRs from molecular precursor **1**. Inset: STM topograph of two isolated monomers of **1** deposited on Au(111) ($I_t = 30$ pA, $V_s = 1.000$ V). (B) STM topograph of a segment of a sGNR ($I_t = 80$ pA, $V_s = 0.006$ V). Inset shows a bond-resolved STM (BRSTM) image of a cyclized monomer unit

with an intact cove region ($I_t = 110$ pA, $V_s = 0.010$ V, $V_{AC} = 10$ mV). (C) Large-scale image of sGNRs ($I_t = 30$ pA, $V_s = -1.100$ V). (D) STM topograph of a segment of a 5-sGNR ($I_t = 1.5$ nA, $V_s = -0.100$ V). BRSTM image in inset shows how cove regions fuse to form five-membered rings ($I_t = 110$ pA, $V_s = 0.010$ V, $V_{AC} = 10$ mV). (E) Large-scale image of 5-sGNRs ($I_t = 20$ pA, $V_s = 0.010$ V).

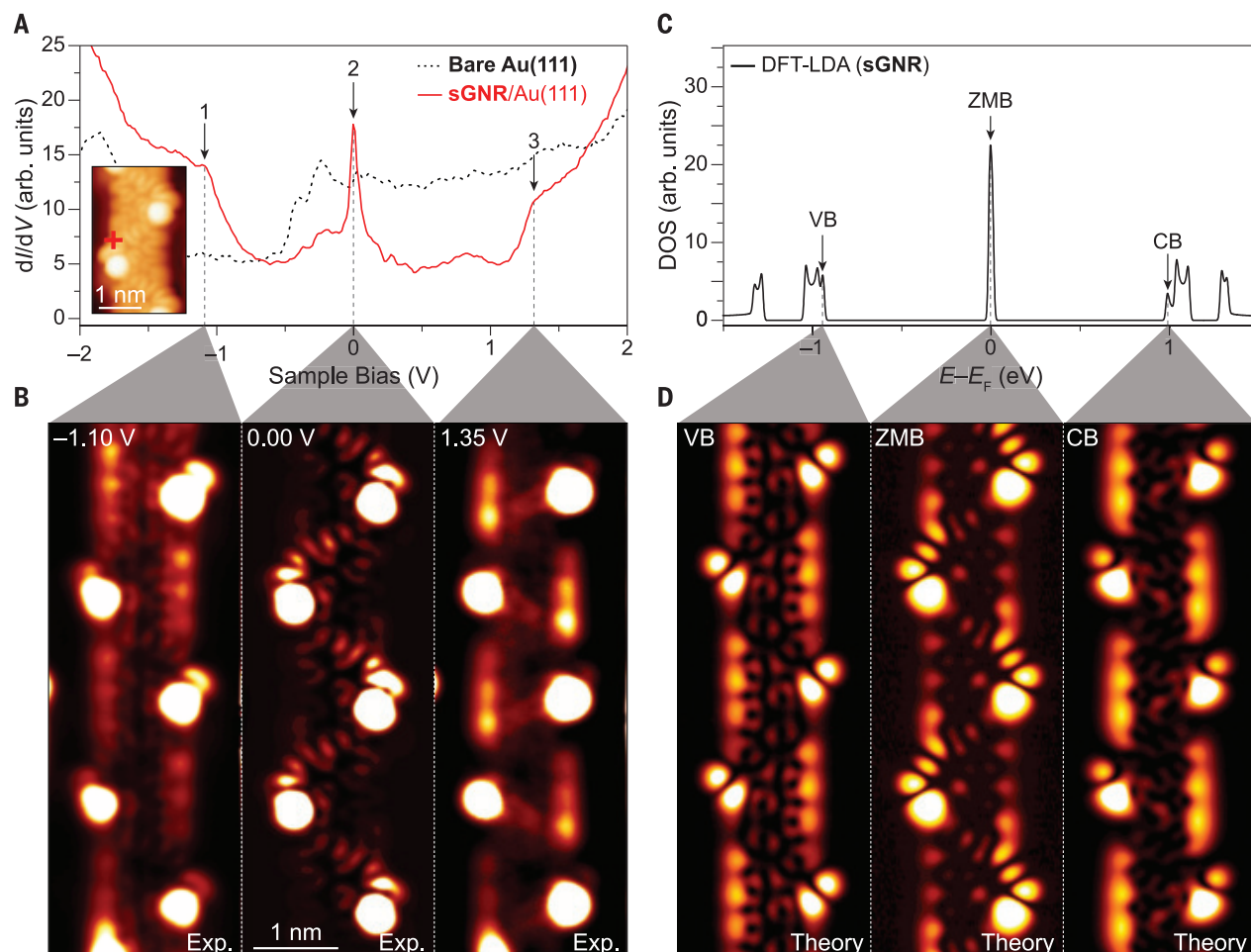


Fig. 2. Electronic structure of sGNRs. (A) dI/dV point spectroscopy of sGNR/Au(111) at the zigzag position marked in the inset. Dashed curve shows bare Au(111) reference spectrum (spectroscopy: $V_{AC} = 10$ mV; imaging: $I_t = 80$ pA, $V_s = 0.006$ V). (B) Constant-height dI/dV maps of sGNRs conducted at the biases indicated in (A) (spectroscopy: $V_{AC} = 20$ mV for states 1 and 3, $V_{AC} = 4$ mV for state 2). Constant-height dI/dV maps were subjected to background

subtraction of substrate LDOS as described in fig. S15 (18, 26). (C) DFT-LDA calculated DOS of the sGNR (spectrum broadened by 10-meV Gaussian). Van Hove singularities near $E - E_F = 0$ merge because of Gaussian smearing. The valence band (VB), zero-mode band (ZMB) and conduction band (CB) energies are indicated by the black arrows. (D) DFT-calculated LDOS of a sGNR at energies shown in (C) (LDOS sampled at a height of 3.5 Å above the plane of the sGNR) (26).

and prominent cove regions (reminiscent of a saw blade) and will herein be referred to as the sawtooth-GNR (sGNR). From the symmetry of the sGNR unit cell, one anticipates that the hopping amplitudes t_1 and t_2 will be equal (Fig. 1A, red arrows), resulting in a metallic band structure for the sGNR. A caveat to this approach is the limited control over head-to-tail surface polymerization, because head-to-head and tail-to-tail polymerizations place the extra carbon atoms on opposite sublattices with inequivalent hopping terms, leading to gapped semiconductors (figs. S1 and S2) (26). In principle, established directional solution-based polymerization techniques (31–33), as well as nascent directional on-surface polymerization strategies (34), could provide a route for promoting the head-to-tail structure, and hierarchical (35, 36) and sterically enforced (19) surface growth could be used to promote

head-to-head and tail-to-tail growth. Furthermore, other precursor designs should be possible that do not rely on directional growth.

Addition of (10-bromoanthracen-9-yl)lithium to a suspension of **3** followed by dehydration of crude diol precursor yielded the molecular precursor **1** for sGNRs (fig. S3) (26). Precursor **1** was then deposited onto a clean Au(111) surface in ultrahigh vacuum (UHV) with the use of a Knudsen cell evaporator (26). Figure 1A shows a representative STM image of two precursor molecules on Au(111). Step-growth polymerization of **1** was induced by heating the surface to 200°C for 20 min, followed by a second annealing step at 300°C for 20 min to complete the cyclodehydrogenation. A topographic STM image of a sGNR segment resulting from head-to-tail polymerization is depicted in Fig. 1B. Prominent periodic bright spots are observed at the locations of the cove

regions owing to the nonplanar conformation induced by the superposition of hydrogen atoms (fig. S4A) (26). Bond-resolved STM (BRSTM) further corroborates the sGNR structure (Fig. 1B). A representative image showing the distribution of head-to-tail (Fig. 1A), head-to-head, and tail-to-tail (fig. S1) segments in the sGNR is depicted in Fig. 1C, which shows each linkage appearing in roughly equal proportions (26).

Prolonged annealing of sGNRs at temperatures >300°C induces a secondary cyclodehydrogenation along the cove regions that leads to the formation of five-membered rings along the edges of sGNRs (Fig. 1A). Although at 300°C this transformation remains a rare event (<30% of cove regions undergo the secondary cyclization), we were able to force the vast majority of cove regions to undergo cyclodehydrogenation by annealing to higher

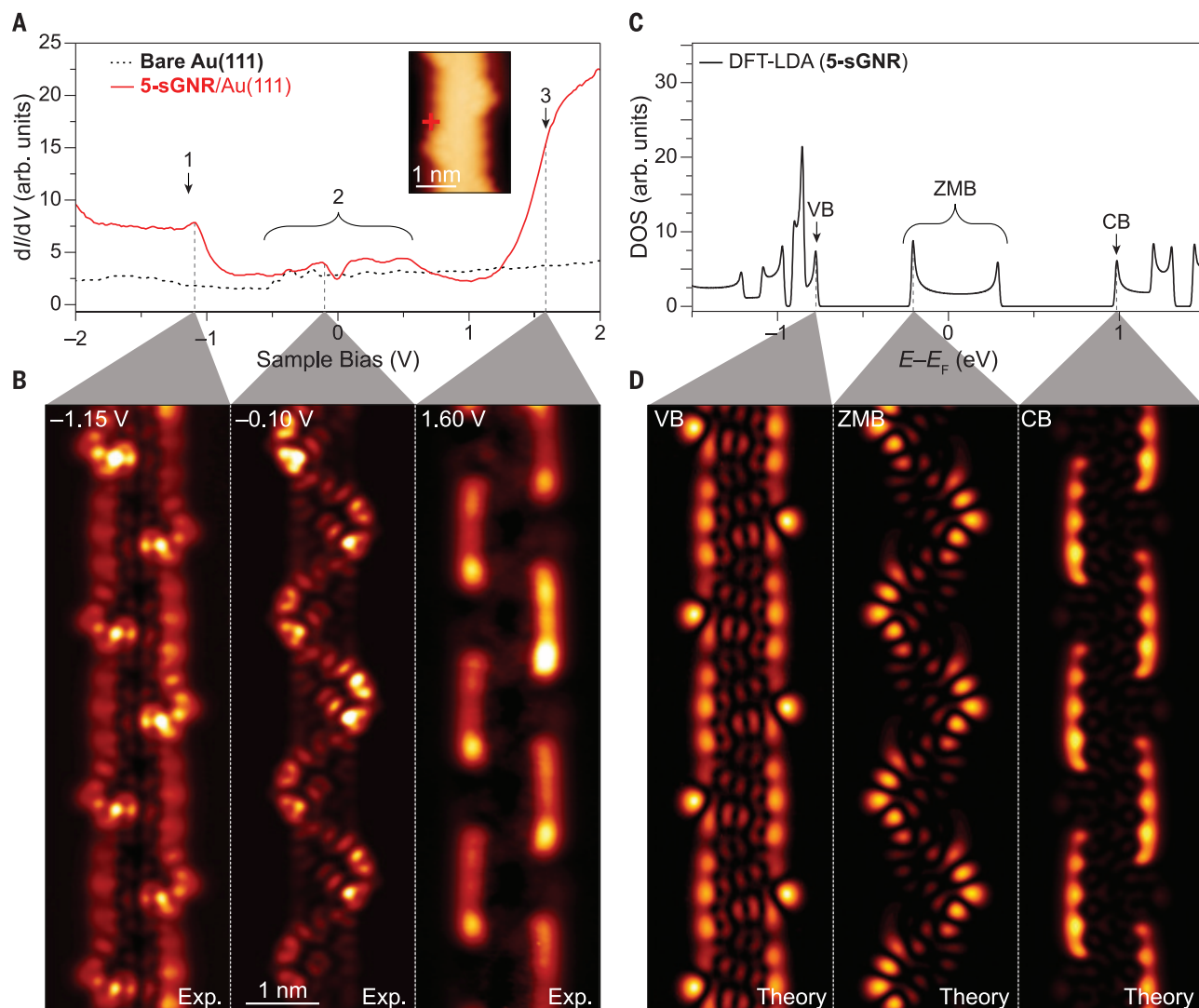


Fig. 3. Electronic structure of 5-sGNRs. (A) dI/dV point spectroscopy conducted on 5-sGNR/Au(111) at the zigzag position marked in the inset. Dashed curve shows bare Au(111) reference spectrum (spectroscopy: $V_{AC} = 10$ mV; imaging: $I_t = 60$ pA, $V_s = -0.100$ V). (B) Constant-height dI/dV maps of 5-sGNRs conducted at the biases indicated in (A) (spectroscopy: $V_{AC} = 20$ mV). Constant-height dI/dV maps were subjected to background subtraction of

substrate LDOS as described in fig. S15 (18, 26). (C) DFT-LDA calculated DOS of the 5-sGNR (spectrum broadened by 10-meV Gaussian). The valence band (VB), zero-mode band (ZMB), and conduction band (CB) energies are indicated by the black arrows. (D) DFT-LDA calculated LDOS of a 5-sGNR at energies shown in (C) (LDOS sampled at a height of 3.5 Å; above the plane of the 5-sGNR) (26).

temperatures ($\sim 95\%$ of cove regions undergo the secondary cyclization at 350°C). The resulting GNRs will herein be referred to as five-sawtooth-GNRs (5-sGNRs) (Fig. 1, D and E). BRSTM imaging of 5-sGNRs unambiguously confirms the presence of five-membered rings along the cove edges of the GNRs (Fig. 1D). The absence of periodic bright spots observed in the topographic STM image of 5-sGNRs (previously attributed to the superposition of hydrogen atoms along the cove edges of sGNRs) further corroborates the structural assignment (fig. S4B) (26).

Scanning tunneling spectroscopy of GNRs

To experimentally determine GNR metallicity, we characterized the electronic structure of

sGNRs using STM spectroscopy. Figure 2A shows a typical dI/dV point spectrum obtained on a sGNR [dI/dV spectroscopy provides a measure of the local density of states (LDOS) beneath the STM tip]. Distinctive features associated with valence band (VB) and conduction band (CB) edges can be seen at $V = -1.07 \pm 0.03$ V (state 1) and $V = 1.36 \pm 0.03$ V (state 3), respectively. Most prominent, however, is the sharp peak in the LDOS (state 2) that is centered near $V = 0$ (E_F) (0.02 ± 0.02 V). This peak continuously spans energies both below and above E_F , a clear signature of a gapless, metallic density of states (DOS). dI/dV imaging of the wave function of these metallic sGNR states shows a characteristic serpentine pattern that snakes back and forth across the

sGNR width (Fig. 2B). The valence and conduction band edge states, by contrast, have their highest intensity along the armchair edges of the GNR (Fig. 2B), consistent with previous measurements of conventional semiconducting GNRs under similar conditions (37, 38). Spectroscopic measurements were also conducted on semiconducting head-to-head and tail-to-tail sGNRs (figs. S5 to S7), which are observed to host topological homojunctions (fig. S6) and metal-semiconductor heterojunctions (fig. S7), as expected from theoretical considerations (26).

A similar experimental analysis was performed on the 5-sGNRs (Fig. 3A). The point spectroscopy of 5-sGNRs was seen to be quite different from that of sGNRs. Although features associated with the valence band edge

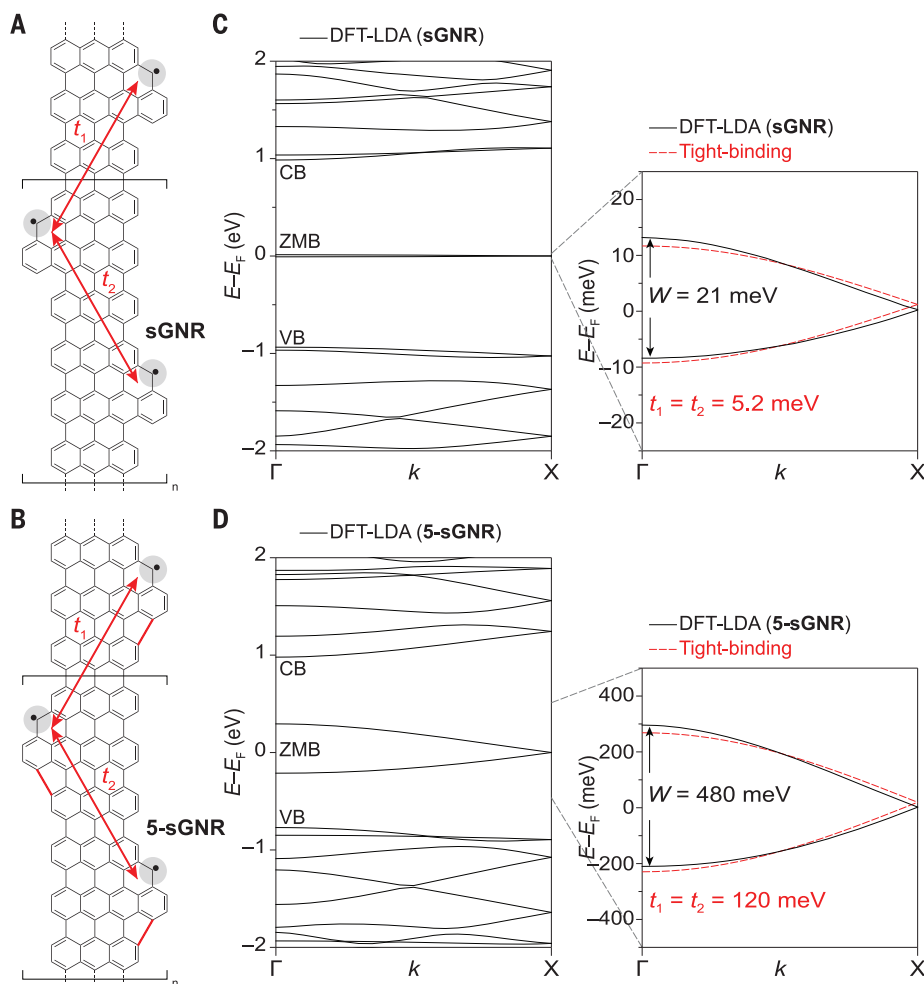


Fig. 4. Zero-mode band structure. Schematic representation of inter- and intracell hopping between localized zero modes embedded in (A) sGNRs and (B) 5-sGNRs. (C) Left: DFT-LDA calculated band structure for sGNRs. The valence, zero-mode, and conduction bands are labeled VB, ZMB, and CB, respectively. Right: Tight-binding fit (red) to DFT-LDA band structure yields the hopping parameters $t_1 = t_2 = 5.2$ meV. (D) The same as (C) but for 5-sGNRs. The hopping parameters for 5-sGNRs (and corresponding bandwidth) are 23 times as large as those for sGNRs (26).

($V = -1.12 \pm 0.03$ V, state 1) and conduction band edge ($V = 1.64 \pm 0.09$ V, state 3) of 5-sGNRs are observed at similar energies when compared to sGNR states, the spectrum of the 5-sGNR does not feature a central peak at $V = 0$ (Fig. 3A). Instead it exhibits a shallow dip at $V = 0$ and a broad DOS feature that spans an energy range above and below E_F . The electronic wave functions corresponding to states 1 to 3 in 5-sGNRs are similar to the corresponding features in sGNRs except for the lack of periodic bright spots associated with the nonplanar cove edges (Fig. 3B). For example, dI/dV images performed at biases near the conduction and valence band edges show the LDOS concentrated at the armchair edges, whereas we observe a serpentine pattern near $V = 0$ (Fig. 3B) that is very similar to the metallic state seen in sGNRs. This state can be observed in dI/dV maps as the sample

bias is swept across the dip at $V = 0$ over a wide energy range (-0.46 V $< V < 0.50$ V) (figs. S8 and S9), including biases where the sGNR ZMB cannot be observed (fig. S10) (26). This implies that 5-sGNRs are also metallic and that the LDOS dip observed near $V = 0$ is not an energy gap but rather a 1D metallic DOS feature resulting from van Hove singularities (see Fig. 3C). The peaks near $V = 0$ associated with the 5-sGNR ZMB shift slightly depending on the tip position during STS experiments (fig. S8D) (26).

Ab initio calculations of GNR electronic structure

We further explored the apparent metallicity of sGNRs by using ab initio density functional theory (DFT). Figure 4C shows the resulting band structure calculated for an isolated sGNR by means of the local density approximation (LDA). Two narrow bands [denoted zero-mode

bands (ZMBs)] are observed bracketing E_F , whereas CB and VB edges can be seen at energies much further from E_F . The two bands bracketing E_F have no bandgap and are fit well by the SSH expression (Eq. 1) with $t_1 = t_2 = 5.2$ meV and $\delta = 0$ (Fig. 4C, red dashed lines), and are also stable against Peierls distortion (39) (as confirmed by supercell calculations). The resulting theoretical DOS (Fig. 2C) shows a single peak centered at E_F , as well as VB and CB peaks at lower and higher energies, respectively, in good agreement with the STM point spectroscopy for sGNRs (Fig. 2A). The theoretical wave function maps (Fig. 2D) match the experimental dI/dV maps obtained at E_F and at the band edge energies, providing further evidence of metallicity in sGNRs.

Although our sGNRs clearly match the metallic predictions of the symmetric SSH model, a potential complication is the very narrow metallic sGNR bandwidth (~ 21 meV). Metals with a high DOS at E_F are often unstable to Mott insulator transitions or magnetic phase transitions as dictated by the Stoner criterion (40, 41). The metallic behavior indicated theoretically may be caused by the spin polarization not being accounted for in our simplified tight-binding or LDA-based calculations. To test for this type of magnetic instability in sGNRs, we calculated the sGNR band structure using the local spin density approximation (LSDA) for an isolated sGNR. The result (fig. S11) shows that the sGNR electronic structure does, in fact, undergo a ferromagnetic phase transition that opens a 200-meV energy gap about E_F (26). We do not see a gap experimentally because of a combined effect of p-doping and surface electric fields induced by the underlying Au(111) substrate. When these are properly accounted for in our DFT calculation, the gap does, indeed, vanish at the LSDA level, and the metallic result is recovered (fig. S11D) (26). Therefore, although it is technically correct to say that sGNR/Au(111) is metallic, our DFT calculation predicts that a substantial energy gap will open up and metallicity will be lost owing to a magnetic phase transition as soon as this sGNR is removed from the Au(111) surface. This represents an interesting and potentially useful 1D magnetic phase transition, but the question remains whether it is possible to engineer a sGNR with more robust metallicity that would not suffer this fate.

This question can be answered by examining the 5-sGNR, whose metallic DOS features are much wider in energy than the narrow peak at E_F seen for sGNRs (Figs. 2 and 3). To clarify the robustness of 5-sGNR metallicity, we also analyzed its electronic structure through ab initio DFT calculations. At the LDA level, the 5-sGNR band structure does, indeed, show a much wider metallic band than the corresponding sGNR band structure (Fig. 4, C and D)

[Perdew-Burke-Ernzerhof (PBE) functionals yield a nearly identical band structure (fig. S12)] (26). When the SSH expression (i.e., the tight-binding result from Eq. 1) is fit to the 5-sGNR DFT-LDA band structure, we find a hopping amplitude of $t_1 = t_2 = 120$ meV, which corresponds to a bandwidth 23 times as large as the sGNR DFT-LDA bandwidth (Fig. 4D, red dashed lines). This is also reflected in the calculated DOS (Fig. 3C), which shows a broad U-shaped feature (with peaks at the band edges characteristic of 1D van Hove singularities), consistent with the experimental minimum in dI/dV intensity observed at $V = 0$ for 5-sGNR point spectroscopy (Fig. 3A). The experimental peaks associated with the 5-sGNR van Hove singularities appear to be additionally broadened, perhaps as a result of substrate hybridization or finite quasiparticle lifetime effects. The theoretical LDOS patterns calculated for the 5-sGNR band-edge and metallic states (Fig. 3D) also correspond well to the 5-sGNR experimental dI/dV images (Fig. 3B). Our DFT calculations of the 5-sGNR at the LSDA level additionally show no signs of magnetism (with or without substrate doping) and are identical to the LDA-based results (fig. S13) (26). We conclude that 5-sGNRs exhibit robust metallicity with a much wider bandwidth than sGNRs, both experimentally and theoretically, and are not expected to undergo a magnetic phase transition upon transfer from Au(111) to an insulator.

Discussion

How does the seemingly small structural difference between 5-sGNRs and sGNRs lead to such a large difference in their electronic behavior? The considerable increase in bandwidth observed for 5-sGNRs is a result of the loss of sublattice polarization of the ZMB electron wave functions. This sublattice mixing occurs because the graphene bipartite lattice symmetry is disrupted by the formation of five-membered rings that fuse the cove regions along the edges of sGNRs. This can be understood by remembering that the two extra atoms added to the sGNR unit cell on sublattice A result in two new localized $E = 0$ eigenstates (zero modes) per unit cell whose wave functions are also confined to sublattice A. This sublattice polarization is preserved in the sGNR Bloch waves for the two in-gap bands (Fig. 5B), and the sGNR bandwidth is determined by the effective amplitude (t_{eff}) for an electron to hop between adjacent zero modes (Fig. 5A). Because the zero modes are all on the same sublattice, it can be shown that $t_{\text{eff}} \propto t'$ where t' is the second nearest-neighbor hopping amplitude of graphene (as there is no zero-mode state density on sublattice B). In the case of 5-sGNRs, however, the bipartite lattice is disrupted by the bond that closes the coves; the zero modes are thus no longer sublattice polarized (fig. S14B) (26). Conse-

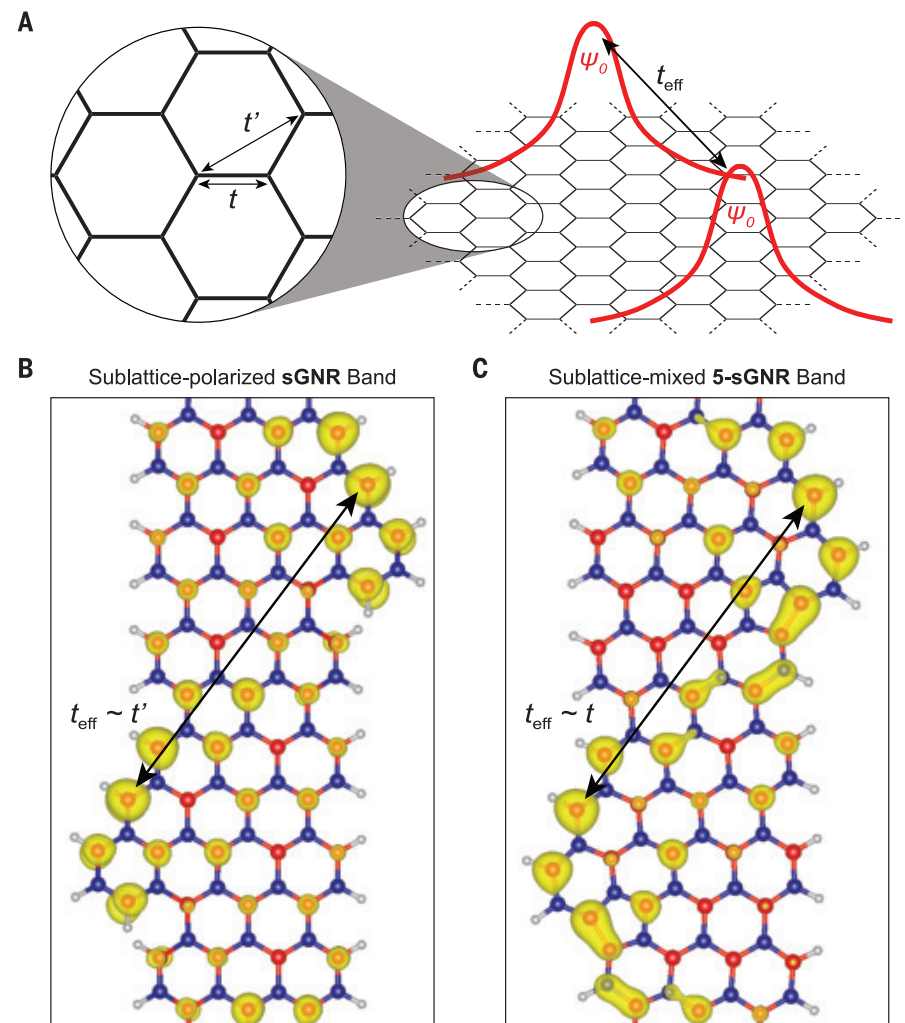


Fig. 5. Zero-mode engineering in sGNRs. (A) Diagram of effective hopping t_{eff} between two localized states (labeled ψ_0) embedded in graphene. Inset: Schematic representation of the first (t) and second (t') nearest-neighbor hopping parameters of graphene. (B) DFT-calculated wave function isosurface of a sGNR for states near $E = 0$ (5% charge density isosurface shown). (C) Same as (B) but for 5-sGNRs. Different sublattices are denoted with different colors (A sublattice in red and B sublattice in blue). The sGNR wave function is completely sublattice polarized, whereas the 5-sGNR wave function is sublattice mixed and more delocalized (26).

quently, the resulting Bloch waves are no longer sublattice polarized [i.e., both sublattices now exhibit state density (Fig. 5C)] and so $t_{\text{eff}} \propto t$, where t is the nearest-neighbor hopping amplitude of graphene (Fig. 5A) [see (26) for additional details]. This explanation is consistent with the ratio of the bandwidths of the two GNRs (~ 23), which falls within the range of accepted values for t/t' (42). The key insight here is that the loss of sublattice polarization (i.e., through intentional fusion of five-membered rings along the cove edges) greatly increases the effective overlap of adjacent localized zero-mode states and strongly enhances the metallic bandwidths, even as the spatial separation between zero modes along the GNR backbone is fixed. This provides a useful design criterion for engineering robust metal-

lic systems from zero-mode superlattices in carbon networks.

Our results provide a general strategy for introducing zero modes into graphene-based materials and reveal the important role of sublattice polarization in controlling the emergent band structure of these systems. This approach creates opportunities for developing nanoscale electrical devices and for exploring electronic and magnetic phenomena in this class of 1D metallic systems.

REFERENCES AND NOTES

1. Y.-W. Son, M. L. Cohen, S. G. Louie, *Phys. Rev. Lett.* **97**, 216803 (2006).
2. L. Yang, C.-H. Park, Y.-W. Son, M. L. Cohen, S. G. Louie, *Phys. Rev. Lett.* **99**, 186801 (2007).
3. G. E. Moore, *Proc. IEEE* **86**, 82–85 (1998).
4. M. Bockrath et al., *Nature* **397**, 598–601 (1999).

5. J. Luttinger, in *Luttinger Model: The First 50 Years and Some New Directions* (World Scientific, 2014), pp. 3–11.
6. J. Voit, *Rep. Prog. Phys.* **58**, 977–1116 (1995).
7. A. R. Goñi et al., *Phys. Rev. Lett.* **67**, 3298–3301 (1991).
8. H. Kataura et al., *Synth. Met.* **103**, 2555–2558 (1999).
9. M. F. Lin, K. W.-K. Shung, *Phys. Rev. B Condens. Matter* **50**, 17744–17747 (1994).
10. P. Mongeau, N. Ong, A. M. Portis, A. Meerschaut, J. Rouxel, *Phys. Rev. Lett.* **37**, 602–606 (1976).
11. G. Grüner, A. Zawadowski, P. Chaikin, *Phys. Rev. Lett.* **46**, 511–515 (1981).
12. Z. K. Tang et al., *Science* **292**, 2462–2465 (2001).
13. I. Takesue et al., *Phys. Rev. Lett.* **96**, 057001 (2006).
14. Y.-C. Chen et al., *ACS Nano* **7**, 6123–6128 (2013).
15. J. Cai et al., *Nature* **466**, 470–473 (2010).
16. L. Talirz et al., *ACS Nano* **11**, 1380–1388 (2017).
17. P. Ruffieux et al., *Nature* **531**, 489–492 (2016).
18. D. J. Rizzo et al., *Nano Lett.* **19**, 3221–3228 (2019).
19. D. J. Rizzo et al., *Nature* **560**, 204–208 (2018).
20. O. Gröning et al., *Nature* **560**, 209–213 (2018).
21. T. Cao, F. Zhao, S. G. Louie, *Phys. Rev. Lett.* **119**, 076401 (2017).
22. Y.-L. Lee, F. Zhao, T. Cao, J. Ihm, S. G. Louie, *Nano Lett.* **18**, 7247–7253 (2018).
23. K.-S. Lin, M.-Y. Chou, *Nano Lett.* **18**, 7254–7260 (2018).
24. J. Jiang, S. G. Louie, Topology Classification from Chiral Symmetry: Chiral Phase Index and Spin Correlations in Graphene Nanoribbons. arXiv:2002.04628 [cond-mat.mtrl-sci] (2020).
25. W. P. Su, J. R. Schrieffer, A. J. Heeger, *Phys. Rev. B Condens. Matter* **22**, 2099–2111 (1980).
26. See supplementary materials.
27. E. H. Lieb, *Phys. Rev. Lett.* **62**, 1201–1204 (1989).
28. M. Ugeda, I. Brihuega, F. Guinea, J. M. Gómez-Rodríguez, *Phys. Rev. Lett.* **104**, 096804 (2010).
29. M. Inui, S. A. Trugman, E. Abrahams, *Phys. Rev. B Condens. Matter* **49**, 3190–3196 (1994).
30. J. J. Palacios, J. Fernández-Rossier, L. Brey, *Phys. Rev. B Condens. Matter Mater. Phys.* **77**, 195428 (2008).
31. G. Li, K.-Y. Yoon, X. Zhong, X. Zhu, G. Dong, *Chemistry* **22**, 9116–9120 (2016).
32. W. Yang, A. Lucotti, M. Tommasini, W. A. Chalifoux, *J. Am. Chem. Soc.* **138**, 9137–9144 (2016).
33. A. Narita et al., *Nat. Chem.* **6**, 126–132 (2014).
34. K.-J. Shi et al., *Org. Lett.* **19**, 2801–2804 (2017).
35. C. Bronner et al., *ACS Nano* **12**, 2193–2200 (2018).
36. C. Bronner et al., *J. Phys. Chem. C* **121**, 18490–18495 (2017).
37. P. Ruffieux et al., *ACS Nano* **6**, 6930–6935 (2012).
38. Y.-C. Chen et al., *Nat. Nanotechnol.* **10**, 156–160 (2015).
39. C. Van Nguyen et al., *J. Electron. Mater.* **46**, 3815–3819 (2017).
40. E. C. Stoner, *Proc. R. Soc. London Ser. A* **165**, 372–414 (1938).
41. E. C. Stoner, *Proc. R. Soc. London Ser. A* **169**, 339–371 (1939).
42. R. Kundo, *Mod. Phys. Lett. B* **25**, 163–173 (2011).
43. <https://www.quantum-espresso.org/>.
44. D. J. Rizzo et al., Data for figures: Inducing Metallicity in Graphene Nanoribbons via Zero-Mode Superlattices, Zenodo (2020); <https://doi.org/10.5281/zenodo.3940702>.

ACKNOWLEDGMENTS

Funding: Research was supported by the Office of Naval Research MURI Program N00014-16-1-2921 (molecular design, STM spectroscopy, band structure); by the U.S. Department of Energy (DOE), Office of Science, Basic Energy Sciences (BES), under the Nanomachine Program award number DE-AC02-05CH11231 (surface growth, image analysis); by the Center for Energy Efficient Electronics Science NSF Award 0939514 (precursor synthesis); and by the National Science Foundation under grants DMR-1508412 (structural relaxation studies) and DMR-1926004 (LSDA simulations), as well as DMR-1839098 (zero-mode analysis). Computational resources were provided by the DOE Lawrence Berkeley National Laboratory's NERSC facility and by the NSF through XSEDE resources at NICS. **Author contributions:** D.J.R., G.V., J.J., S.G.L., M.F.C., and F.R.F. initiated and conceived the research; G.V., R.M., and F.R.F. designed, synthesized, and characterized the molecular precursors; D.J.R., C.B., T.Ch., and M.F.C. performed on-surface synthesis and STM characterization and analysis; J.J., T.Ca., and S.G.L. performed the DFT calculations and the theoretical analysis that predicted and interpreted the STM data. All authors contributed to the scientific discussion. **Competing interests:** The authors declare no competing interests. **Data and materials availability:** The DFT code and pseudopotentials can be downloaded from the Quantum Espresso website (43). For this study, we used version 6.3 for

the theoretical calculations. All data presented in the main text and the supplementary materials can be found in the corresponding Zenodo repository (44).

SUPPLEMENTARY MATERIALS

science.sciencemag.org/content/369/6511/1597/suppl/DC1
Materials and Methods

Supplementary Text
Figs. S1 to S15
References (45–58)

12 June 2019; resubmitted 13 December 2019

Accepted 14 July 2020

10.1126/science.aay3588

CORONAVIRUS

Adaptation of SARS-CoV-2 in BALB/c mice for testing vaccine efficacy

Hongjing Gu^{1*}, Qi Chen^{1*}, Guan Yang^{2*}, Lei He^{1*}, Hang Fan^{1*}, Yong-Qiang Deng^{1*}, Yanxiao Wang², Yue Teng¹, Zhongpeng Zhao¹, Yujun Cui¹, Yuchang Li¹, Xiao-Feng Li¹, Jiangfan Li¹, Na-Na Zhang¹, Xiaolan Yang¹, Shaolong Chen¹, Yan Guo¹, Guangyu Zhao¹, Xiliang Wang¹, De-Yan Luo¹, Hui Wang¹, Xiao Yang², Yan Li³, Gencheng Han³, Yuxian He⁴, Xiaojun Zhou⁵, Shusheng Geng⁶, Xiaoli Sheng⁶, Shibo Jiang^{7†‡}, Shihui Sun^{1†‡}, Cheng-Feng Qin^{1†‡}, Yusen Zhou^{1†§}

The ongoing coronavirus disease 2019 (COVID-19) pandemic has prioritized the development of small-animal models for severe acute respiratory syndrome coronavirus 2 (SARS-CoV-2). We adapted a clinical isolate of SARS-CoV-2 by serial passaging in the respiratory tract of aged BALB/c mice. The resulting mouse-adapted strain at passage 6 (called MASCP6) showed increased infectivity in mouse lung and led to interstitial pneumonia and inflammatory responses in both young and aged mice after intranasal inoculation. Deep sequencing revealed a panel of adaptive mutations potentially associated with the increased virulence. In particular, the N501Y mutation is located at the receptor binding domain (RBD) of the spike protein. The protective efficacy of a recombinant RBD vaccine candidate was validated by using this model. Thus, this mouse-adapted strain and associated challenge model should be of value in evaluating vaccines and antivirals against SARS-CoV-2.

The pandemic of coronavirus disease 2019 (COVID-19) caused by the newly emerged severe acute respiratory syndrome coronavirus 2 (SARS-CoV-2) has become a global health crisis (1–3). In the absence of protective immunity in the whole human population (4), SARS-CoV-2 has exhibited an unprecedented human-to-human transmission capability. Although several vaccine candidates are being currently tested in clinical trials, no commercial COVID-19 vaccine is presently available.

SARS-CoV-2 belongs to the *Betacoronavirus* genus of the *Coronaviridae* family, along with two other closely related highly pathogenic viruses, SARS-CoV and Middle East respiratory

syndrome coronavirus (MERS-CoV). SARS-CoV-2 has a positive-sense, single-stranded RNA genome of 30 kb in length, which is coated by the inner nucleocapsid (N) proteins and an outer envelope made up of membrane (M) and envelope (E) proteins, as well as spike (S) proteins. Like SARS-CoV, the S protein of SARS-CoV-2 mediates viral entry into host cells by binding to their shared receptor, angiotensin-converting enzyme 2 (ACE2), through the receptor-binding domain (RBD) (1). Previously, we and others have demonstrated that the RBD of SARS-CoV and MERS-CoV contain major conformation-dependent neutralizing epitopes and are capable of eliciting potent neutralizing antibodies in immunized animals, thus representing promising targets for vaccine development (5–8).

Small-animal models that recapitulate SARS-CoV-2 infection are urgently needed. Because SARS-CoV-2 does not use mouse ACE2 as its receptor (1), wild-type mice are thought to be less susceptible to SARS-CoV-2. Transgenic mice expressing human ACE2 have been developed by means of different strategies. Such mice have been used previously to study SARS-CoV-2 infection and pathogenesis and to evaluate countermeasures against COVID-19 (9–11). Here, we report the generation of a mouse-adapted strain of SARS-CoV-2 that can productively replicate in the respiratory tract and

¹State Key Laboratory of Pathogen and Biosecurity, Beijing Institute of Microbiology and Epidemiology, Academy of Military Medical Sciences, Beijing 100071, China. ²State Key Laboratory of Proteomics, Beijing Proteome Research Center, National Center for Protein Sciences (Beijing), Beijing Institute of Lifeomics, Beijing 102206, China. ³Institute of Military Cognition and Brain Sciences, Beijing 100850, China. ⁴Institute of Pathogen Biology, Chinese Academy of Medical Sciences and Peking Union Medical College, Beijing 100730, China. ⁵Laboratory Animal Center, Academy of Military Medical Sciences, Beijing 100071, China. ⁶Beijing JOINN Biologics Co., Beijing 100176, China. ⁷Key Laboratory of Medical Molecular Virology (MOE/NHC/CAMS), School of Basic Medical Sciences, Fudan University, Shanghai 200032, China.

*These authors contributed equally to this work.

†Corresponding author. Email: shibojiang@fudan.edu.cn (S.J.); sunsh01@163.com (S.S.); qincf@bmi.ac.cn (C.-F.Q.)

‡These authors contributed equally to this work. §Deceased.

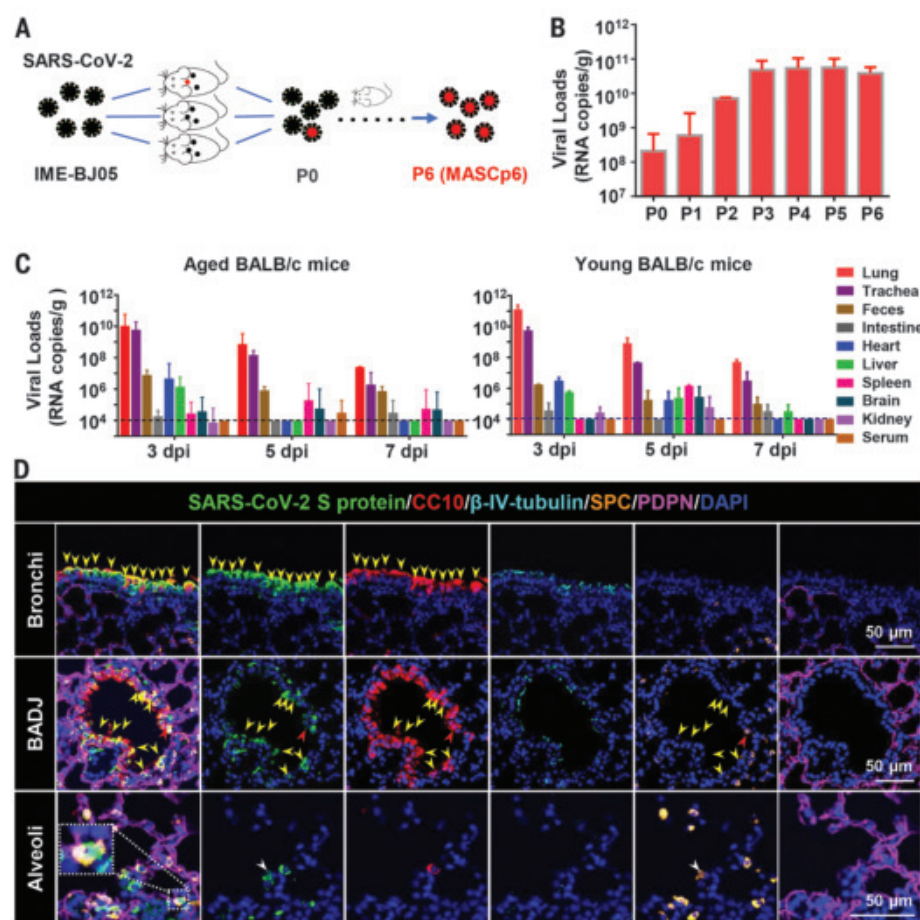


Fig. 1. Generation and characterization of a mouse-adapted strain of SARS-CoV-2 in BALB/c mice.

(A) Schematic diagram of the passage history of SARS-CoV-2 in BALB/c mice. The original SARS-CoV-2 viruses are shown in black, and the adapted viruses are in red. (B) SARS-CoV-2 genomic RNA loads in mouse lung homogenates at P0 to P6. Viral RNA copies were determined by means of quantitative reverse transcription polymerase chain reaction (RT-PCR). Data are presented as means \pm SEM ($n = 2$ to 4 mice per group). (C) Tissue distribution of SARS-CoV-2 viral RNAs in mice infected with MASCp6. Groups of aged and young mice were inoculated with 1.6×10^4 PFU of MASCp6 and sacrificed at 3, 5, or 7 days after inoculation, respectively. Feces, sera, and the indicated tissue samples were collected at the specified times and subjected to viral RNA load analysis by means of quantitative RT-PCR. Dashed lines denote the detection limit. Data are presented as means \pm SEM ($n = 3$ mice per group). (D) Multiplex immunofluorescence staining of mouse lung sections. SARS-CoV-2 S protein (green), CC10 (red), β -IV-tubulin (cyan), PDPN (magenta), SPC (gold), and nuclei (blue). The dash box is magnified at the bottom right corner of the same image. Yellow arrowheads indicate SARS-CoV-2⁺/CC10⁺ cells, red arrow heads indicate SARS-CoV-2⁺/CC10⁺/SPC⁺ cells, and the white arrowheads indicate SARS-CoV-2⁺/SPC⁺ cells.

cause interstitial pneumonia in wild-type immunocompetent mice. Additionally, the protective efficacy of a newly developed recombinant subunit vaccine candidate based on SARS-CoV-2 RBD was assayed by using this mouse challenge model.

Results

Rapid adaption of SARS-CoV-2 in BALB/c mice

To generate a SARS-CoV-2 mouse-adapted strain, the human clinical isolate of SARS-CoV-2 (BetaCov/human/CHN/Beijing_IME-BJ05/2020, abbreviated as IME-BJ05) was serially passaged by means of intranasal inoculation in aged mice (Fig. 1A), as previously

described for SARS-CoV (12). Briefly, 9-month-old BALB/c mice were intranasally inoculated with 7.2×10^5 plaque forming units (PFU) of SARS-CoV-2, and the lung tissues were collected from each passage for viral RNA load analysis at 3 days after inoculation. Substantial viral RNAs ($10^{8.32}$ copies/g) were readily detected after a single passage, which was defined as passage 0 (P0), in the lung homogenate (Fig. 1B). Subsequently, the viral RNA copies in the lung approached $10^{10.68}$ RNA copies/g at passage 3 (P3), which was about 250-fold higher than those at P0 and remained at a similar level during the following passages (Fig. 1B). The final viral stock at passage 6 (P6)

was titrated by means of plaque assays (fig. S1A) and called MASCp6 for further characterization.

To determine whether the increased viral RNA loads in mouse lungs could be attributed to the enhanced infectivity of the virus in mice, we examined the replication kinetics and tissue tropism of MASCp6 in both aged (9 months old) and young (6 weeks old) BALB/c mice. After intranasal inoculation with 1.6×10^4 PFU of MASCp6, high amounts of viral RNAs in the lungs and tracheas were detected at 3, 5 and 7 days after inoculation in all aged mice (Fig. 1C), with peak viral RNA loads of $\sim 10^{10}$ copies/g at 3 days after inoculation, which was comparable with the results from the human ACE2 transgenic mice (10). Viral RNAs were also detected in heart, liver, spleen, and brain, as well as in feces. Marginal viral RNA was detected in the kidney and serum from individual infected mice (Fig. 1C). Similar tissue distribution of SARS-CoV-2 RNA was also seen in the MASCp6-infected young mice (Fig. 1C). Immunostaining of lung section from MASCp6-infected mice showed robust expression of S protein along the airways and at the alveolus in both young and aged mice at 3 and 5 days after inoculation (fig. S1B). To identify the major cell types infected by SARS-CoV-2 in our model, lung sections were further analyzed by means of multiplex immunofluorescence staining for SARS-CoV-2 S protein and specific lung epithelium cell markers. As shown in Fig. 1D, colocalization of CC10⁺ club cells and SARS-CoV-2 S protein were observed predominantly in the bronchi and bronchioles as well as the bronchioalveolar-duct junction (BADJ) of the lungs. Furthermore, SPC⁺ alveolar type 2 (AT2) cells were also costained with S protein in the BADJ and alveoli. However, SARS-CoV-2 S protein was not detected in all β -IV-tubulin⁺ ciliated cells and PDPN⁺ alveolar type 1 (AT1) cells. Thus, club cells and AT2 cells are the major target cells that support SARS-CoV-2 replication in mouse lung in our model.

Characterization of MASCp6 infection in BALB/c mice

To further characterize pathological features in the MASCp6-infected BALB/c mice, lung tissues were collected at 3 or 5 days after inoculation, respectively, and subjected to histopathological analysis by means of hematoxylin and eosin (H&E) staining. Both aged and young BALB/c mice presented with mild to moderate pneumonia after MASCp6 infection (Fig. 2, A and C). In the aged mice, MASCp6 infection caused interstitial pneumonia at 3 days after inoculation, characterized with denatured and collapsed epithelial cells, thickened alveolar septa, alveolar damage, focal exudation and hemorrhage, and activated inflammatory cell infiltration. Vessels were obviously injured, with adherent inflammatory cells and damaged basement

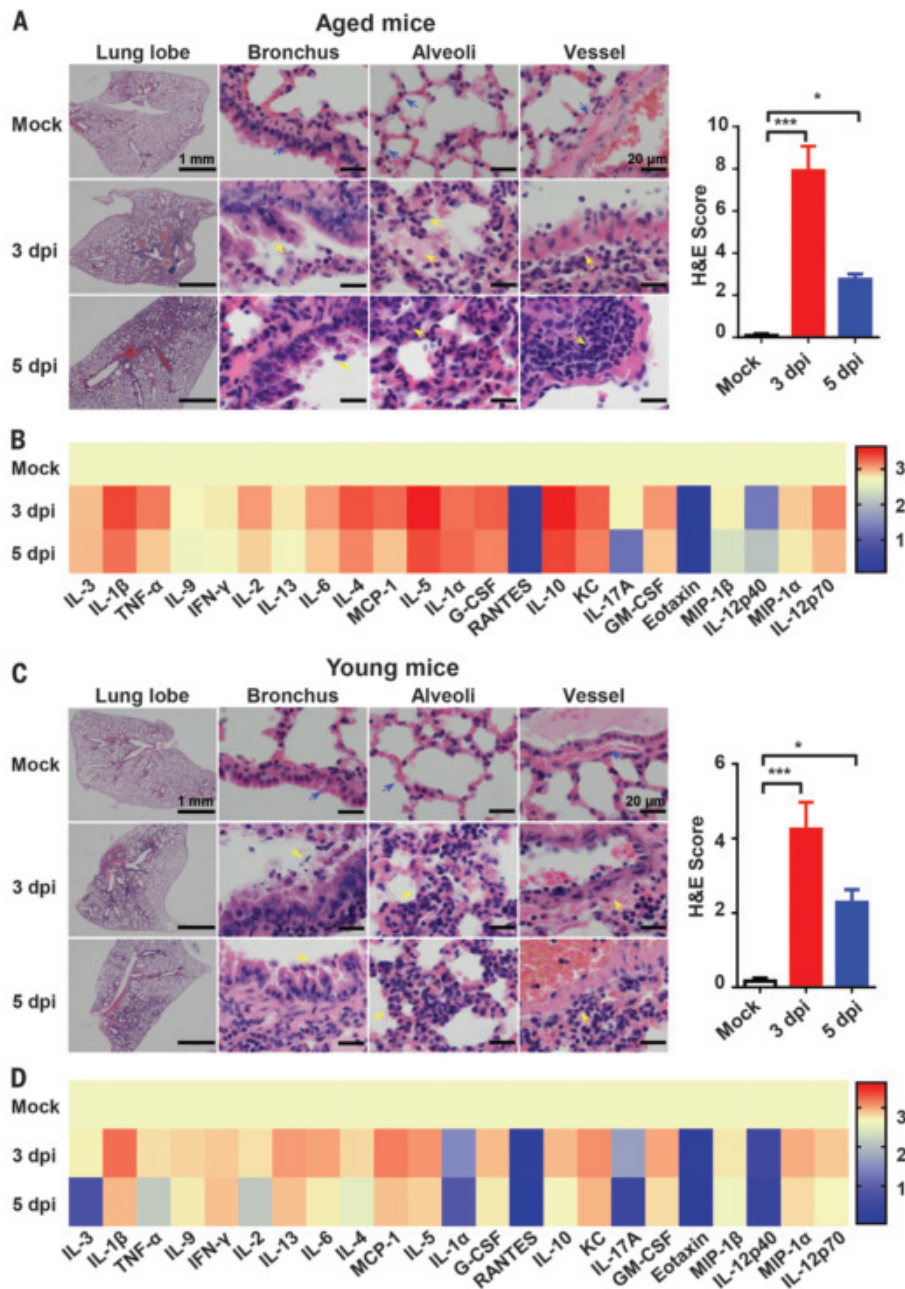


Fig. 2. MASCP6 infection causes pathological lung lesions and inflammatory responses in both aged and young BALB/c mice. (A) H&E staining of lung sections from aged (9 months old) BALB/c mice infected with MASCP6. Blue arrows indicate the normal areas, and yellow arrows indicate damaged areas. Data from semiquantitative analysis of histopathological changes of lung tissues are presented as means \pm SEM ($n = 3$ mice per group). Statistical significance was analyzed by means of Mann-Whitney test. (B) Serum cytokine and chemokine heatmap in MASCP6-infected aged mice. Data are presented as fold change relative to mock infection ($n = 5$ mice per group). (C) H&E staining of lung sections from MASCP6-infected young mice ($n = 3$ mice per group). (D) Serum cytokine and chemokine heatmap in MASCP6-infected young mice ($n = 5$ mice per group). * $P < 0.05$, *** $P < 0.001$.

membrane (Fig. 2A). At 5 days after inoculation, the lung damage was much milder than that seen at 3 days after inoculation (Fig. 2A), suggesting a self-recovering process. In addition, multiplex immunofluorescence staining demonstrated that SARS-CoV-2 infection led to massive cell death, as evidenced with

cleaved caspase-3 staining, at 3 days after inoculation, as well as remarkable inflammatory cell infiltration in CD103⁺ dendritic cells, CD163⁺ macrophages, and CD3⁺ T lymphocytes in the lung of aged mice (fig. S2A). Serum concentrations of inflammatory cytokines—including interleukin-1 β (IL-1 β), IL-6, and

IL-5—were up-regulated upon MASCP6 challenge (Fig. 2B and fig. S3A). As expected, the young mice developed similar but much milder lung damage than that of the aged mice after MASCP6 challenge (Fig. 2C). Similarly, inflammatory cell infiltration (fig. S2B) and serum cytokine response (Fig. 2D and fig. S3B) in the young mice was much weaker than that of aged mice. Additionally, MASCP6 infection caused no obvious changes in the body weight of aged or young mice (fig. S4). Taken together, these results demonstrate that MASCP6 can productively replicate in the lower respiratory tract of wild-type BALB/c mice, resulting in a more severe interstitial pneumonia phenotype in the aged mice.

Identification of adaptive mutations that emerged in MASCP6

To decipher the underlying mechanism for the increased virulence of MASCP6, the complete genome of MASCP6 was subjected to deep sequencing with an Ion Torrent S5Plus sequencer. Compared with the full genome of the original SARS-CoV-2 strain IME-BJ05, MASCP6 contains five nucleotide mutations that are distributed within the ORF1ab, S, and N genes, respectively (Fig. 3A and table S1). The A23063T mutation resulted in a N501Y amino acid substitution in the RBD of the S protein, which is assumed to be responsible for receptor recognition and host range of SARS-CoV-2 (13, 14). (A, alanine; T, threonine; N, asparagine; Y, tyrosine. In the mutants, other amino acids were substituted at certain locations; for example, A23063T indicates that alanine at position 23063 was replaced by threonine.) Structural remodeling also suggested that the N501Y substitution in the RBD of SARS-CoV S protein increased the binding affinity of the protein to mouse ACE2 (Fig. 3B). Immunofluorescence staining supported colocalization of mouse ACE2 and SARS-CoV-2 S protein in the lungs of MASCP6-infected mice (Fig. 3C). To further trace the adaption history of MASCP6, the emergence of N501Y substitution was further analyzed by means of deep sequencing. As expected, all reads from the original IME-BJ05 isolate were pure A23063. T23063 readily emerged after a single passage in one of the three mouse lung homogenates (table S2), and the proportion of A23063T mutation gradually increased during subsequent passages (Fig. 3D). Thus, the increased virulence of SARS-CoV-2 MASCP6 in mice was likely attributed to the rapid emergence of N501Y substitution in the RBD of SARS-CoV-2 S protein.

Validation of the protective efficacy of an RBD-based SARS-CoV-2 subunit vaccine

To validate the utility of this mouse challenge model, we tested the protection efficacy of a recombinant subunit vaccine candidate against COVID-19. Briefly, SARS-CoV-2 RBD (aa 331-524)

fused with a human immunoglobulin G (IgG) Fc at the C terminus (fig. S5A) was expressed in CHO-K1 cells and purified through affinity chromatography and anion exchange chroma-

tography in a good laboratory practice (GLP) laboratory. As expected, the molecular weight of recombinant RBD-Fc was about 47.98 kD, as detected with mass spectroscopy (fig. S4B),

and flow cytometry analysis confirmed that RBD-Fc, not the Fc control, specifically bound to human ACE2 expressed in the stable ACE2/293T cells (fig. S4C) (15).

Fig. 3. MASCP6 carries a distinct amino acid substitution in the RBD of the Spike (S) protein.

(A) Schematic diagram of SARS-CoV-2 genome and all the adaptive mutations identified in MASCP6. Amino acid sequences of the parental IME-BJ05 strain and the MASCP6 strain adjacent to the N501Y mutation are shown. (B) Homology modeling of mouse ACE2 (pink) in complex with SARS-CoV-2 RBD (green) with N501 (left) or Y501 residue (right). (C) Colocalization of SARS-CoV-2 S protein (green) and mouse ACE2 (red) in the lung from SARS-CoV-2-infected mice. The dashed box in the left image is magnified in the three images at the right. (D) The proportion of A23063T mutation in each passage. The mutation threshold was defined as 1% according to the average quality score of sequenced base.

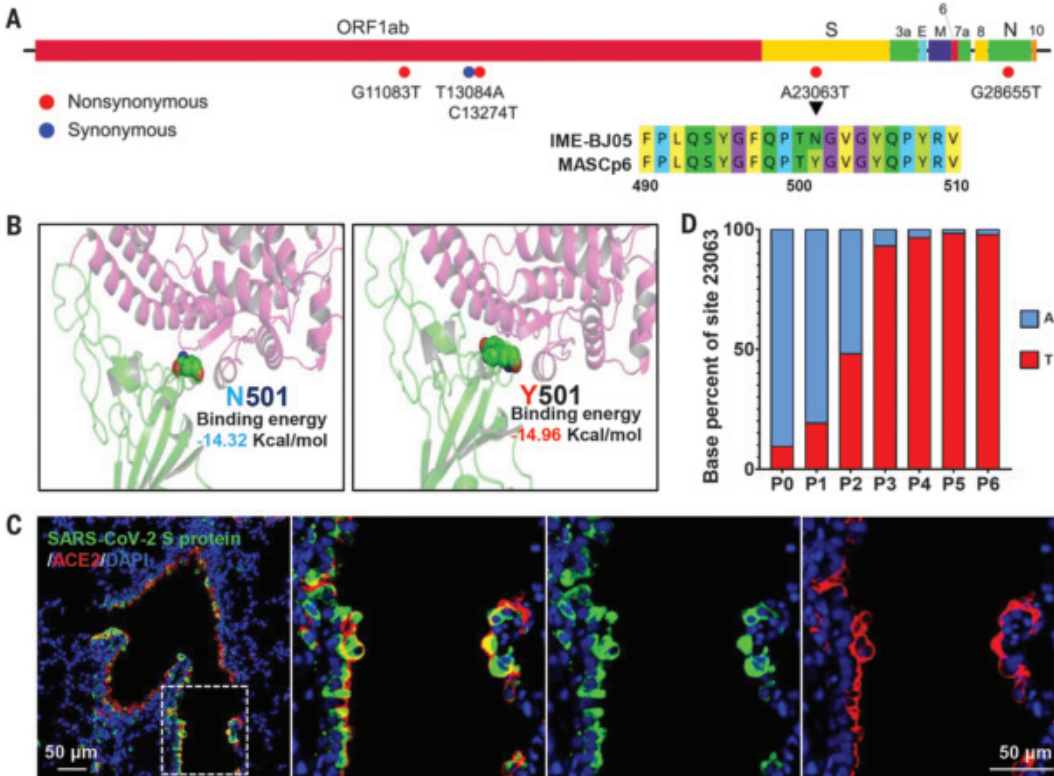
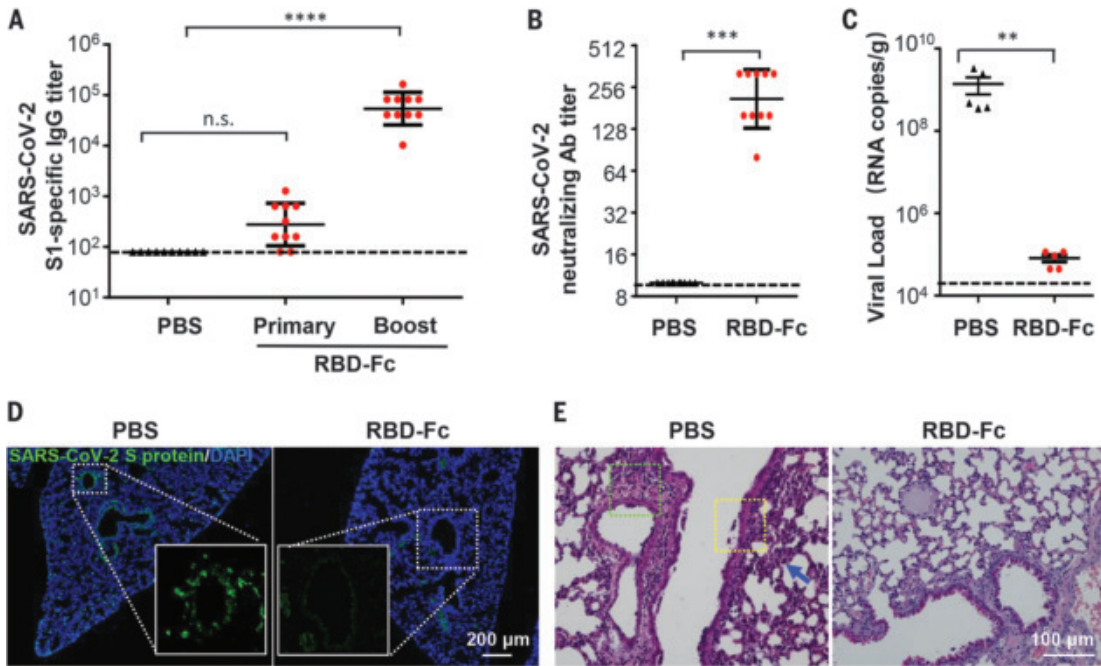


Fig. 4. Protection efficacy of the recombinant RBD-Fc vaccine candidate against MASCP6 challenge in mice.

(A) SARS-CoV-2-specific IgG antibody titers were detected with enzyme-linked immunosorbent assay at 2 weeks after primary and boost immunization, respectively ($n = 10$ mice per group). Statistical significance was analyzed by means of one-way analysis of variance. (B) Neutralizing antibody titers against SARS-CoV-2 were determined with the microneutralization assay at 2 weeks after boost immunization ($n = 10$ mice per group). (C) Viral RNA loads in lung of vaccinated mice were detected at 5 days after MASCP6 challenge ($n = 5$ mice per group). Statistical significance was analyzed by means of Student's t test. (D) Immunofluorescence staining of mouse lung sections for S protein (green) and 4',6-diamidino-2-phenylindole (DAPI) (blue). The dotted boxes are magnified at the bottom of the same image. (E) H&E staining of mouse lung sections. Focal perivascular (green square) and peribronchiolar (yellow square) inflammation and thickened alveolar septa (blue arrow) are indicated. n.s., not significant; $**P < 0.01$, $***P < 0.001$, $****P < 0.0001$.



Female BALB/c mice were then subcutaneously immunized with two doses of recombinant RBD-Fc (10 µg/mouse) at a 2-week interval, and mice immunized with phosphate-buffered saline (PBS) were set as controls. As expected, high levels of SARS-CoV-2-specific IgG antibodies (Fig. 4A) and neutralization antibodies (Fig. 4B) were elicited in all of the RBD-Fc immunized mice at 2 weeks after boost immunization. All immunized mice were then intranasally challenged with MASCP6 (1.6×10^4 PFU), and lung tissues were collected for virological and histopathological analysis at 5 days after challenge. As expected, all the PBS-treated mice sustained high amounts of viral RNA loads in the lung at 5 days after challenge. By contrast, a significant reduction in viral RNA loads (approximately 0.1%) were seen in the lung of RBD-Fc immunized mice compared with the control animals (Fig. 4C). Moreover, immunofluorescence staining for SARS-CoV-2 S protein showed that only a small population of positive cells was detected in the lung from the RBD-Fc-immunized mice, whereas abundant viral proteins were seen in the lung from PBS-immunized mice (Fig. 4D). No apparent pathological damage was observed in the lung of RBD-Fc immunized mice, whereas inflammatory lung injury—with focal perivascular and peribronchiolar inflammation, as well as thickened alveolar septa—were found in the lung of the control mice (Fig. 4E). Taken together, these data indicate that our newly developed mouse model with MASCP6 represents a useful tool for testing the efficacy of COVID-19 vaccine candidates.

Discussion

An ideal animal model for COVID-19 should reproduce the viral replication as well as the clinical outcome observed in COVID-19 patients. Here, we report the rapid adaption of SARS-CoV-2 in BALB/c mice, and the resulting MASCP6 strain not only replicated efficiently in the trachea and lung but also caused interstitial pneumonia and inflammatory responses, reproducing many clinical features observed in COVID-19 patients (16, 17). Upon MASCP6 challenge, SARS-CoV-2 primarily replicated in the respiratory tracts, and viral RNAs peaked in the lungs at 3 days after inoculation and then decayed at 5 and 7 days after inoculation. This result was consistent with other transgenic or humanized mouse models (9, 11). In particular, the aged mice developed more severe lung damage when compared with the young mice upon MASCP6 challenge, which reflects that the mortality and fatality of COVID-19 are strongly skewed toward the elderly (18). Fatality was only reported by Jiang *et al.* (10) in SARS-CoV-2-infected ACE2 transgenic mice. In our challenge model, neither visible clinical symptoms nor body weight loss were recorded throughout the experiments (fig. S4). The challenge

dose used in our experiment was 1.6×10^4 PFU; thus, whether a higher challenge dose of MASCP6 would exacerbate the pathology remains to be determined.

The development of a mouse-adapted strain-based challenge model has been well demonstrated in SARS-CoV and MERS-CoV studies (12, 19, 20). Serial passaging of virus in mouse lungs results in adaptive mutations that increase viral infectivity. The MASCP6 genome contains five mutations in comparison with its parental strain IME-BJ05, and these mutations resulted in four amino acid residue changes in the ORF1ab, S, and N genes, respectively (Fig. 3A). The N501Y mutation seems to provide a more favorable interaction with mouse ACE2 for docking and entry, thus leading to the increased virulence phenotype in mice. Whether the other three mutations, except for N501Y, also regulated viral infectivity remains to be determined. Further investigation with reverse genetics will clarify this issue and could allow the rapid synthesis of a recombinant SARS-CoV-2 with enhanced virulence (21, 22). Additionally, immunostaining results showed that lung club and AT2 cells are major target cells of MASCP6, which is in agreement with previous findings from animal models and COVID-19 patients (11, 23, 24).

Compared with the previously described ACE2 transgenic or humanized mice, our MASCP6-based challenge model uses immunocompetent wild-type mice and can be directly applied to the efficacy evaluation of various vaccine candidates. Immunization with the recombinant subunit vaccine candidate (RBD-Fc) induced high levels (up to 1:320) of neutralizing antibodies against SARS-CoV-2, nearly eliminating viral RNA replication in mouse lungs after MASCP6 challenge (Fig. 4, B and C). The potential correlation between serum neutralizing antibody titers in the vaccinated mice and the protective efficacy highlights the versatility of this convenient and economical animal model. Recently, nonhuman primates, which are closest to humans phylogenetically, have also been used to reproduce SARS-CoV-2 infection, and several vaccine candidates have been validated with promising protection efficacy (25–27). Hamsters, ferrets, and cats are also permissive to SARS-CoV-2 infection (28–30), and the clinical outcome varies from asymptomatic infection to severe pathological lung lesions after SARS-CoV-2 infection. No single animal model for SARS-CoV-2 currently reproduces all aspects of the human disease. Therefore, the establishment of different animal models should greatly expand our understanding of SARS-CoV-2 transmission and pathogenesis and accelerate the development of countermeasures against COVID-19.

REFERENCES AND NOTES

1. P. Zhou *et al.*, *Nature* **579**, 270–273 (2020).

2. L. F. Moriarty *et al.*, *MMWR Morb. Mortal. Wkly. Rep.* **69**, 347–352 (2020).
3. N. Zhu *et al.*, *N. Engl. J. Med.* **382**, 727–733 (2020).
4. N. Vabret *et al.*, *Immunity* **52**, 910–941 (2020).
5. Y. He, H. Lu, P. Siddiqui, Y. Zhou, S. Jiang, *J. Immunol.* **174**, 4908–4915 (2005).
6. L. Du *et al.*, *J. Virol.* **87**, 9939–9942 (2013).
7. L. Du *et al.*, *Vaccine* **25**, 2832–2838 (2007).
8. L. Du *et al.*, *Nat. Rev. Microbiol.* **7**, 226–236 (2009).
9. L. Bao *et al.*, *Nature* (2020).
10. R. D. Jiang *et al.*, *Cell* **182**, 50–58.e8 (2020).
11. S. H. Sun *et al.*, *Cell Host Microbe* **28**, 124–133.e4 (2020).
12. A. Roberts *et al.*, *PLoS Pathog.* **3**, e5 (2007).
13. Y. Wang, M. Liu, J. Gao, *Proc. Natl. Acad. Sci. U.S.A.* **117**, 13967–13974 (2020).
14. C. Yi *et al.*, *Cell. Mol. Immunol.* **17**, 621–630 (2020).
15. W. Tai *et al.*, *Cell. Mol. Immunol.* **17**, 613–620 (2020).
16. E. M. Dufort *et al.*, *N. Engl. J. Med.* **383**, 347–358 (2020).
17. L. Carsana *et al.*, *Lancet Infect. Dis.* **20**, S1473–3099(20)30434-5 (2020).
18. E. Petersen *et al.*, *Lancet Infect. Dis.* **20**, S1473–3099(20)30484-9 (2020).
19. M. Frieman *et al.*, *J. Virol.* **86**, 884–897 (2012).
20. K. Li, P. B. McCray Jr., *Methods Mol. Biol.* **2099**, 161–171 (2020).
21. X. Xie *et al.*, *Cell Host Microbe* **27**, 841–848.e3 (2020).
22. K. H. Dinno *et al.*, *bioRxiv* **081497** [Preprint] 7 May 2020; <https://doi.org/10.1101/2020.05.06.081497>.
23. C. Wang *et al.*, *EBioMedicine* **57**, 102833 (2020).
24. K. P. Y. Hui *et al.*, *Lancet Respir. Med.* **8**, 687–695 (2020).
25. W. Deng *et al.*, *Science* **eaac5343** (2020).
26. Q. Gao *et al.*, *Science* **369**, 77–81 (2020).
27. J. Yu *et al.*, *Science* **eaac6284** (2020).
28. J. Shi *et al.*, *Science* **368**, 1016–1020 (2020).
29. Y. I. Kim *et al.*, *Cell Host Microbe* **27**, 704–709.e2 (2020).
30. S. F. Sia *et al.*, *Nature* (2020).

ACKNOWLEDGMENTS

We thank X. D. Yu and J. J. Zhao for excellent technical and biosafety support. **Funding:** This work was supported by the National Key Plan for Scientific Research and Development of China (2016YFD0500304, 2016YFD0500306, and 2020YFA0707801), the National Natural Science Foundation of China (82041006 and 82041025), the National Science and Technology Major Project of China (2018ZX09711003 and 2017ZX10304402003), and Beijing Municipal Science and Technology Project (Z201100001020004). C.-F.Q. was supported by the National Science Fund for Distinguished Young Scholar (81925025), the Innovative Research Group (81621005) from the NSFC, and the CAMS Innovation Fund for Medical Sciences (2019-I2M-5-049). **Author contributions:** H.G., S.S., Q.C., G.Y., L.H., H.F., Y.-Q.D., Y.W., Y.T., Z.Z., Y.C., Yu.L., X.-F.L., J.L., N.-N.Z., X.Y., S.C., G.Z., G.H., D.-Y.L., and Y.G. performed experiments; X.W., H.W., X.Y., Ya.L., Y.H., X.Z., S.G., and X.S. analyzed data; Y.Z. and C.-F.Q. conceived the project and designed the experiments; Y.Z., C.F.Q., S.S., and S.J. supervised the study and wrote the manuscript with the input of all co-authors. **Competing interests:** The authors declare no competing interests. **Data and materials availability:** The genome sequence of IME-BJ05 and MASCP6 have been deposited in the Genome Warehouse in National Genomics Data Center (<https://bigd.big.ac.cn/gwh/>), BIG, CAS, with the accession nos. GWHACBB010000002 and GWHACBF00000000, respectively. All requests for resources and reagents should be directed to C.-F.Q. (qincf@bmi.ac.cn or qinlab313@163.com) and will be fulfilled after completion of a materials transfer agreement. This work is licensed under a Creative Commons Attribution 4.0 International (CC BY 4.0) license, which permits unrestricted use, distribution, and reproduction in any medium, provided the original work is properly cited. To view a copy of this license, visit <https://creativecommons.org/licenses/by/4.0/>. This license does not apply to figures/photos/artwork or other content included in the article that is credited to a third party; obtain authorization from the rights holder before using such material.

SUPPLEMENTARY MATERIALS

science.sciencemag.org/content/369/6511/1603/suppl/DC1
Materials and Methods
Figs. S1 to S5
Tables S1 and S2

29 April 2020; resubmitted 29 May 2020

Accepted 15 July 2020

Published online 30 July 2020

10.1126/science.abc4730

IMMUNE SYSTEMS

The immunogenetics of sexual parasitism

Jeremy B. Swann^{1*}, Stephen J. Holland¹, Malte Petersen¹, Theodore W. Pietsch², Thomas Boehm^{1*}

Sexual parasitism has evolved as a distinctive mode of reproduction among deep-sea anglerfishes. The permanent attachment of males to host females observed in these species represents a form of anatomical joining, which is otherwise unknown in nature. Pronounced modifications to immune facilities are associated with this reproductive trait. The genomes of species with temporarily attaching males lack functional *aicda* genes that underpin affinity maturation of antibodies. Permanent attachment is associated with additional alterations, culminating in the loss of functional *rag* genes in some species, abolishing somatic diversification of antigen receptor genes, the hallmark of canonical adaptive immunity. In anglerfishes, coevolution of innate and adaptive immunity has been disentangled, implying that an alternative form of immunity supported the emergence of this evolutionarily successful group of vertebrates.

Lophiiform fishes constitute a morphologically diverse assemblage of taxa that share a peculiar and distinctive mode of feeding; it is characterized most notably by a luring apparatus (illicium) derived from a modified first dorsal-fin spine, located on the tip of the snout (Fig. 1A) (1, 2). Of the five suborders found within the lophiiform fishes, the Ceratioidei, or deep-sea anglerfishes, is the most diverse, with 168 known species divided among 11 families and 35 genera (2). Deep-sea anglerfish are found distributed throughout the world's oceans at depths below 300 m and have evolved several adaptations that facilitate their deep-sea lifestyle, chief among which are their distinctive reproductive habits, which involve extreme sexual dimorphism and physical pair formation. Male deep-sea anglerfish are dwarfed compared with their mates—those of some species grow to only 6 to 10 mm standard length (2–4)—and attach themselves (either temporarily or permanently) to the bodies of relatively gigantic females (Fig. 1A). In some taxa, attachment is followed by fusion of epidermal and dermal tissues and, eventually, by connection of the circulatory systems so that the male becomes permanently dependent on the female for nutrients, with the pair becoming a kind of self-fertilizing chimera (2, 5–8).

Sexual parasitism represents a form of naturally occurring anatomical joining (parabiosis), which is otherwise known in nature only from the rare instances of genetically identical conjoined twins (9). From an immunological perspective, the formation of permanent physical attachments between anglerfish pairs is notable: In all other vertebrate species, such a tissue fusion event would be expected to provoke

a potent immune response directed against the “nonself” major histocompatibility complex (MHC) antigens. Typically, successful transplantation of tissues requires the careful cross-matching of donor and recipient MHC haplotypes, together with immunosuppressive drugs to ensure long-term survival of the allogeneic graft (10, 11). Given that some anglerfish species can undergo tissue fusion without eliciting a destructive immune response, we set out to explore immunological adaptations that are associated with sexual parasitism within this suborder of lophiiform fishes. To this end, we considered several possibilities. First, that ceratioid species may consist of genetically identical or closely related clones, in which case the barrier of allorecognition would be removed, allowing successful tissue fusion between individuals of the same species. Second, we hypothesized that ceratioids may be able to identify suitable mates through olfactory assessment of MHC genotype, which we previously found to contribute to mate choice in aquatic and terrestrial species (12, 13). Selecting matching MHC haplotypes before parasitization would be a mechanism to circumvent allogeneic rejection and facilitate long-term attachment and/or tissue fusion. To examine these first two hypotheses, our interest initially focused on the extent of MHC diversity, both among individuals of the same species and between corresponding female and male pairs. We also considered a third hypothesis, that ceratioids might enable sexual parasitism by specific adaptations of the genes underpinning adaptive immune responses, perhaps functionally similar in outcome to the immunological interactions that occur at the feto-maternal interface of the mammalian placenta (14). To examine this latter possibility, we focused our attention on genes with unequivocal orthologies and specific roles in the vertebrate immune system, such as those encoding the CD4 and CD8 coreceptor molecules and the components associated with the antigen receptors of B cells

and T cells, as well as genes required for the generation of their somatically diversified receptor repertoires.

Reproductive modes in ceratioids

The reproductive modes in ceratioids fall into two broad categories. In the first group of species, males attach temporarily to females but never become parasitic; in the second group, males attach permanently to females (2, 4, 8). An important distinguishing feature among sexually parasitizing species is the number of males simultaneously attached to females (2) (Fig. 1B). Females of the three *Cerantias* species studied here (*Cerantias holboelli*, *C. tentaculatus*, and *C. uranoscopus*) almost always have only one attached male; only 2 out of 32 parasitized females have two males attached (1.06 ± 0.06 males per female, mean \pm SEM). By contrast, females of *Cryptopsaras couesii*, a species closely related to *Cerantias*, often ($P = 0.038$; two-tailed *t* test, when compared to *Cerantias*) carry more than one male (1.60 ± 0.20 males per female; $P = 0.014$; two-tailed *t* test, when compared with *Cerantias*), with 12 out of 47 parasitized females having two or more, and up to eight, males attached. Multiple attachments are also frequently observed in the two species of the family Linophrynidae studied here, *Photocorynus spiniceps* [1.76 ± 0.22 males per female ($n = 25$ females)] and *Haplophryne mollis* (1.76 ± 0.22 males per female; $n = 5$ females).

Study population and design

We generated whole-genome shotgun sequences of 31 specimens representing 10 species of Ceratioidei, covering a broad phylogenetic spectrum of this suborder (15) (tables S1 and S2). Among the species known to exhibit temporary attachment, we studied one species each of Himantolophidae (*Himantolophus appeli*), Melanocetidae (*Melanocetus johnsonii*), Diceratiidae (*Diceratias pileatus*), and Gigantactinidae (*Gigantactis vanhoeffeni*); for reference, we use the subscript [TA] as an identifier when discussing the immune genotype of these species. *C. holboelli*, *C. tentaculatus*, and *C. uranoscopus* are identified by [PA1], indicating that males permanently attach to females in a 1:1 mode; *C. couesii*, *P. spiniceps*, and *H. mollis* are identified by [PA_n] to indicate that often multiple males permanently attach to a single female. As controls for the 10 species of the suborder Ceratioidei described above, we examined the genomes of specimens from two further suborders of lophiiform fishes (tables S1 and S2). The suborder Antennarioidei is represented by specimens from two families (Tetrabrachiidae, *Tetrabrachium ocellatum*; and Antennariidae, *Antennarius commerson*), and the suborder Chaunacoidei is represented by *Chaunax abei*. Because males never attach to females in these species, they

¹Department of Developmental Immunology, Max Planck Institute of Immunobiology and Epigenetics, D-79108 Freiburg, Germany. ²School of Aquatic and Fishery Sciences, University of Washington, Seattle, WA 98105-5020, USA. *Corresponding author. Email: boehm@ie-freiburg.mpg.de (T.B.); swann@ie-freiburg.mpg.de (J.B.S.)

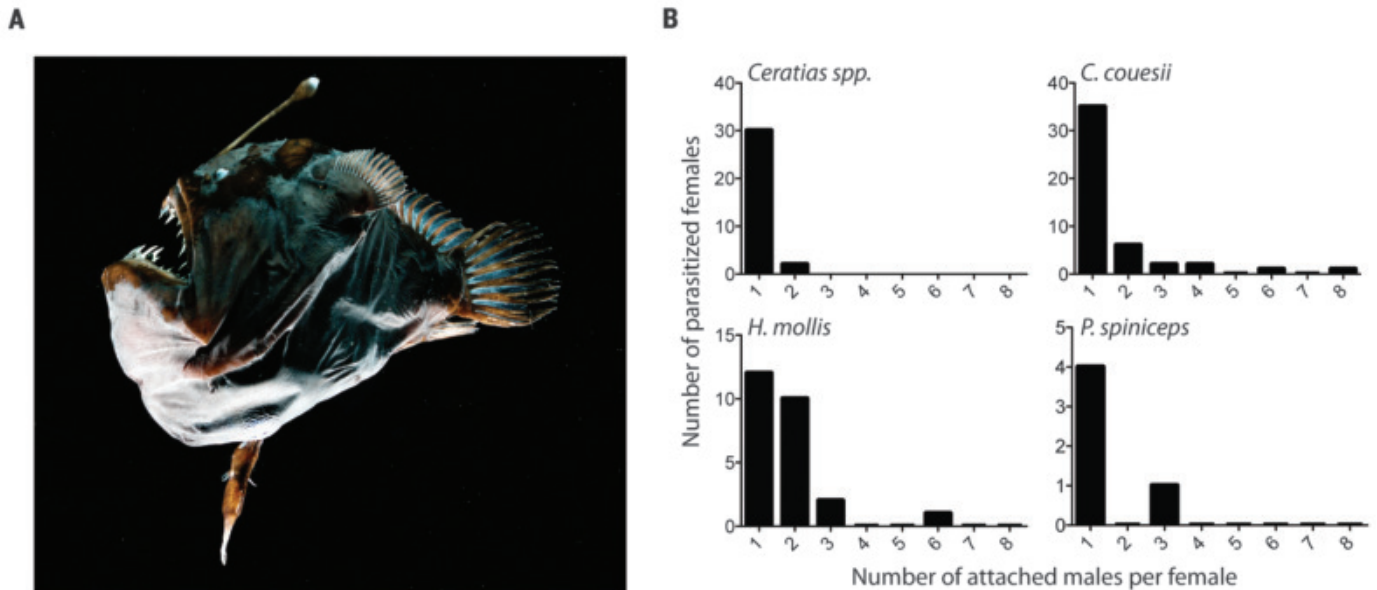


Fig. 1. Sexual parasitism in ceratioid anglerfishes. (A) Parasitized female of *M. johnsonii*. Note the illicium at the forehead and the attached male at the belly. [Photo credit: Edie Widder] (B) Exclusive ([PAI]) and consortial ([PAN]) modes of male parasitism. Data are compiled from (2); for *P. spiniceps*, the parasitized female described here is included.

are given the [NA] identifier. The scarcity of parasitized females, lack of fresh material, and poor quality of archival ceratioid specimens poses a considerable challenge for molecular analysis. We were unable to obtain intact RNA from the specimens available to us and therefore focused our analysis on genomic DNA (tables S1 and S2). Using gene-centered local assemblies (in selected cases confirmed by Sanger sequencing of amplified genomic fragments), we examined the structures and syntenic relationships of a collection of genes with unequivocal orthologies and well-established roles in the vertebrate immune system (table S3).

Diversity of MHC genes in lophiiform fishes

Histocompatibility in jawed vertebrates is governed by haplotype variability in MHC genes, and we therefore began our examination of anglerfish immune systems by exploring the MHC gene content of the various species in our collection, with particular emphasis on male-female pairs where possible. We found that the three nonparasitizing species (*T. ocellatum*_[NA], *A. commersoni*_[NA], and *C. abei*_[NA]) and three of four temporarily attaching species (*D. pileatus*_[TA], *H. appeli*_[TA], and *M. johnsonii*_[TA]) each possess large numbers of different MHC class I genes of the U type (*mhc1u*) but only few genes of the Z type (*mhc1z*) (table S4), which is typical of the situation in Teleostei (16). This diverse *mhc1* repertoire observed in nonattaching and temporarily attaching species was complemented by multiple *mhc2a* alleles (table S4), indicating that a diverse *mhc* gene content does not

represent an immunological barrier to the formation of temporary attachments in most instances.

By contrast, we observed profound changes in the MHC gene status of the six species exhibiting permanent attachment of males to females. Among the three species (*C. holboellii*_[PAI], *C. tentaculatus*_[PAI], and *C. uranoscopus*_[PAI]) that practice permanent exclusive attachment, we found that whereas *mhc2* diversity was maintained (table S4), the *mhc1* gene complement was substantially altered. We detected at most two *mhc1u* genes per *Ceratias* species, whereas an unusually large number of distinct *mhc1z* gene sequences were recovered (table S4). The importance of the apparent contraction of *mhc1u* and expansion of *mhc1z* is, as of now, unknown; however, the substantial shift in *mhc1* gene diversity in anglerfish species that form permanent, exclusive attachments suggests that alteration of antigen-presentation pathways may be required to facilitate tissue fusion.

Loss of MHC diversity was much more substantial among anglerfish species capable of forming permanent, consortial matings. We found no functional versions of *mhc1u* and *mhc1z* genes in the four *C. couesii*_[PAN] specimens sequenced, and although we could detect one or two *mhc2aa* sequences per individual, no *mhc2ab* genes were found in these individuals. In *H. mollis*_[PAN], no functional *mhc1u* and *mhc2a* sequences were found, and a maximum of two alleles each for exons 2 and 3 of *mhc1z* genes were recorded. Of the four specimens of *P. spiniceps*_[PAN] (one fe-

male, three attached males) examined, we noted a lack of detectable *mhc1u* and *mhc2a* sequences; however, each individual possessed one or two alleles of *mhc1z*. Collectively, these results indicate that anglerfish that use permanent consortial pairings are largely depauperate in MHC genes.

Having characterized the *mhc1* and *mhc2* content of the various species in our collection, we turned our attention to the permanently attached pairs from which we were able to obtain DNA from the fusion partners. Examination of the *mhc* haplotypes of exclusive pairs of *C. holboellii*_[PAI] and *C. uranoscopus*_[PAI] revealed that although some overlap in *mhc1* and *mhc2* alleles was detected between the fusion partners, each individual had several specific *mhc1* and *mhc2* alleles not found in their attached mate (Fig. 2A). These results clearly demonstrate that MHC haplotype matching is not essential for tissue fusion between anglerfish. The lack of MHC diversity detected among the anglerfish species that form permanent consortial pairs renders the assessment of MHC haplotype matching between fusion partners largely redundant; however, we note that for the *P. spiniceps*_[PAN] female with three attached males, all members of the consort had the same *mhc1z* allele, with the female having one additional allele. For the *H. mollis*_[PAN] pair, the *mhc1z* alleles differed between the partners.

Overall, our results suggest that anglerfish species that use mating strategies involving permanent attachment have undergone substantial changes to their MHC gene content:

Permanent exclusive pairings are associated with restructuring of the *mhc1* system, whereas the use of a consortial mating strategy is associated with an almost complete loss of both *mhc1* and *mhc2* haplotype diversity. One outlier in our analysis was *G. vanhoeffeni*_[TA]; this species exhibits a general reduction in both *mhc1z* and *mhc2a* diversity relative to other temporarily attaching or nonattaching species (table S4). The reason for this reduction in MHC diversity in a temporarily attaching species is unknown; however, *G. vanhoeffeni*_[TA] exhibits a number of additional immunological abnormalities, setting it apart from other temporarily attaching species (see below).

Pseudogenization of CD8 co-receptor genes
MHC class I-restricted CD8⁺ cytotoxic T cells are key mediators of allograft rejection (17). Given that permanent attachment is associated with loss of *mhc1u* diversity (table S4), we next examined the *cd8a* and *cd8b* genes, which encode the heterodimeric CD8αβ co-receptor that interacts with MHC class I molecules (18). Notably, functional *cd8a* and *cd8b* genes were absent in all six permanently attaching species; in two cases, remnants of the *cd8a* gene could be found in the interval between the genes flanking the tandemly arranged *cd8a* and *cd8b* genes (Fig. 2B and figs. S1 to S3). Moreover, both *cd8* genes were also missing in the genome of *G. vanhoeffeni*_[TA], in line with

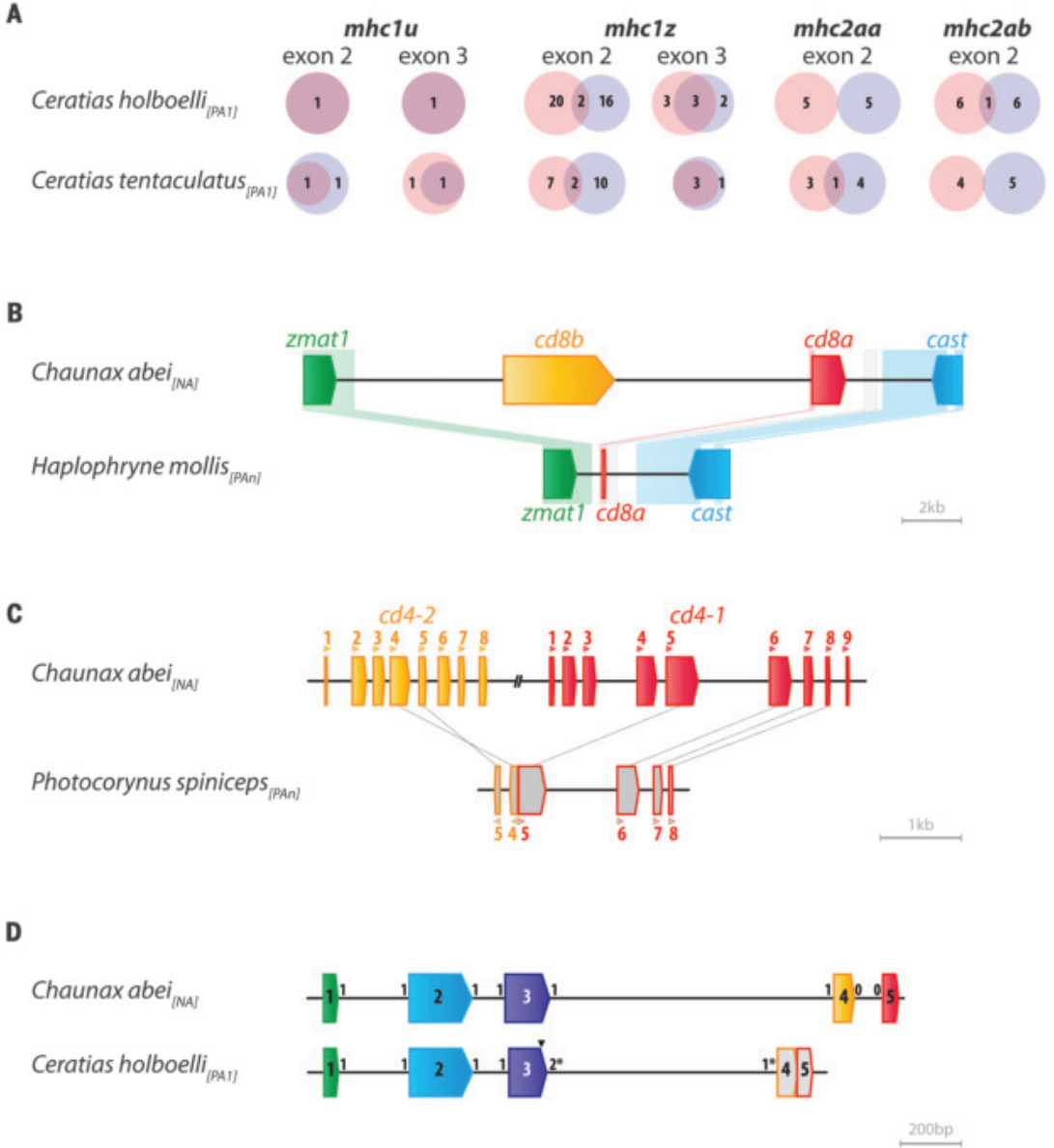
the lack of functional *mhc1u* genes in this species (fig. S1 and table S4), further strengthening its distinctive immunogenetic constellation among the species with a temporary attachment mode. Collectively, these findings suggest that the canonical antigen-specific cytotoxic pathway is impaired in all species distinguished by permanent male attachment. However, the *perforin* gene (table S3), which encodes a key element of the cytotoxic pathway, is present in all genomes analyzed here, suggesting the presence of cytotoxic innate lymphoid cells in these species.

Loss of the CD4 pathway

MHC class II-restricted CD4⁺ helper T cells are also known to play an important role in

Fig. 2. Immunogenetic features of lophiiform fishes.

(A) Number of shared and distinct *mhc* gene alleles in female-male pairs of the two indicated species of *Ceratias*. Blue indicates the male genotype, and pink indicates the female genotype. **(B)** Tandem arrangement of *cd8b* and *cd8a* genes and their flanking genes *zmat1* and *cast*. *H. mollis*_[PAN] retains a short sequence of the 5' end of *cd8a*. The structure of the locus of *C. abei*_[NA] serves as a reference; sequence homologies are indicated as shaded blocks. **(C)** Gene models of *cd4-2* and *cd4-1*. The relative orientation of exons is indicated by arrowheads. Gray lines connect equivalent exons between species. In *P. spiniceps*_[PAN], the *cd4-2* gene has lost all exons except exons 4 and 5, which are found in an inverse orientation; the first four exons of *cd4-1* are deleted, and remnants of others exhibit deleterious sequence alterations. Oblique parallel black lines indicate the omission of intergenic sequence to highlight coding features. **(D)** Gene model of the *cd3gd* gene, which exhibits deleterious changes in *Ceratias* species. Exons are depicted as shaded blocks; internal numbers indicate exon number, whereas numbers flanking the exons indicate the splice phase. A 23-base pair deletion (indicated by a black arrowhead) in exon 3 of the *Ceratias* gene causes a splicing defect, and mismatched splice sites are indicated with an asterisk. In addition, the *Ceratias* *cd3gd* gene exhibits the loss of the intron between exons 4 and 5.



allograft rejection (17), so we next turned to the *cd4-1* and *cd4-2* genes (19) that encode the characteristic co-receptors of the helper T cell lineage (18). We also examined the status of the *cd74* gene, which encodes a specialized chaperone molecule (also known as invariant chain) that facilitates the transport of MHC class II molecules to endosomes, which is an important prerequisite for antigen presentation (20). In all species with a diverse set of *mhc2a* genes (table S4), functional *cd4-1*, *cd4-2*, and *cd74* genes are readily identifiable (figs. S4 to S11). By contrast, *G. vanhoeffeni*_[TA], *C. couesii*_[PAN], *P. spiniceps*_[PAN], and *H. mollis*_[PAN] lack functional versions of the *cd4-1* and *cd4-2* genes (Fig. 2C and figs. S4 to S12); with the exception of *G. vanhoeffeni*_[TA], which possesses a single *mhc2a* gene, the other three species lack functional *mhc2a* genes (table S4). We failed to detect *cd74*-related genes in *P. spiniceps*_[PAN] and *H. mollis*_[PAN]; the *cd74* gene structures in *G. vanhoeffeni*_[TA] and *C. couesii*_[PAN] predict an unusual form of the protein, whose functional properties are unclear (fig. S12). Collectively, it appears that the canonical MHC class II pathway is unlikely to play an important role in immune defense in these four species.

Alterations of the T cell receptor signaling complex

The substantial changes in MHC gene content and the frequent loss of MHC co-receptors among anglerfish that practice permanent attachment suggest that the T cell compartment in these animals is likely to have also undergone considerable changes. In mammals, the heterodimeric T cell receptor, which recognizes peptides presented by MHC molecules with the aid of CD4 or CD8 co-receptors, consists of α and β chains encoded by the *Tcr* and *Tcrb* genes. This antigen-recognition module then associates with a hexameric signaling complex consisting of polypeptides encoded by the *Cd3g*, *Cd3d*, *Cd3e*, and *Cd3z* genes (21); in fishes, the mammalian *Cd3g* and *Cd3d* genes are represented by a single precursor gene, *cd3gd* (22). On binding of the T cell receptor to MHC-peptide complexes, the CD3 complex initiates a signaling cascade that encompasses protein tyrosine phosphorylation of its immunoreceptor tyrosine-based activation motifs (ITAMs) (23). Intact *cd3gd* genes were found in *T. ocellatum*_[NA], *A. commerson*_[NA], *C. abei*_[NA], *H. appeli*_[TA], *M. johnsonii*_[TA], *D. pileatus*_[TA], and *G. vanhoeffeni*_[TA]; however, they could not be detected in *C. couesii*_[PAN], *P. spiniceps*_[PAN], and *H. mollis*_[PAN] (figs. S13 to S15). The three *Ceratias*_[PAI] species share a variant of the *cd3gd* gene that is predicted to encode a protein lacking the characteristic cytoplasmic ITAM (Fig. 2D and figs. S13 to S15). Although it is unknown whether this truncated protein is produced (the internal deletion

in the *cd3gd* gene may lead to nonsense-mediated degradation of the transcript), the variant CD3 signaling complexes of *Ceratias*_[PAI] is predicted to reduce the T cell receptor's overall signaling capacity (24). Because essential components of the cytotoxic pathway (*mhc1u*, *cd8a*, *cd8b*) appear to be missing in *Ceratias*_[PAI], the altered T cell receptor signaling most likely affects the function of the T helper lineage by reducing the magnitude of the antigen-specific antibody responses in these species. We were unable to substantiate the presence of *cd3e* genes in *C. couesii*_[PAN], *P. spiniceps*_[PAN], and *H. mollis*_[PAN]; however, intact genes were identified in all other species, with the exception of *G. vanhoeffeni*_[TA], in which a truncated *cd3e* protein is predicted to lack the ITAM (fig. S16). All species were found to possess intact *cd3z* genes, with the exception of *P. spiniceps*_[PAN], in which an internal deletion leads to the absence of one of the three ITAMs (fig. S17). We presume that retention of the *cd3z* gene in *H. mollis*_[PAN] and *P. spiniceps*_[PAN] is due to a requirement in other signaling complexes, such as those used by innate immune cells (25).

In the absence of complementary transcriptomes, the complexity of the T cell receptor gene loci confounded a definitive inventory of *trc* genes in anglerfishes by analysis of genomic DNA sequences alone. In particular, unambiguous identification of *trdc* and *trgc* constant-region genes was not possible because of their similarities with other immunoglobulin domain-encoding genes. However, we were able to definitively identify *trca* and *trcb* constant-region genes (designated *trac* and *trbc*, respectively) in all species with non-attaching males (INA) and temporarily attaching males (ITA), as well as in species exhibiting permanent exclusive attachments (PAI) (figs. S18 and S19). By contrast, we were unable to confidently identify *trac* and *trbc* genes in any of the species of anglerfishes that exhibit permanent consortial (PAN) pairings. (A poorly supported candidate *trac* gene was detected in two of four *C. couesii*_[PAN] specimens, a *trbc* fragment was detected in *H. mollis*_[PAN], and no evidence of either the *trac* or *trbc* gene was found in *P. spiniceps*_[PAN] genome sequences.) We therefore provisionally conclude that the assembly of a functional $\alpha\beta$ T cell receptor heterodimer is unlikely in anglerfish species that form permanent consortial (PAN) pairings.

Impaired antibody-mediated immunity

Antibody-mediated allograft rejection is a known complication in transplant settings (17, 26) and suggests that in addition to the defects in cellular immunity described above, anglerfish species that use temporary or permanent attachment modes must have evolved mechanisms to avoid humoral rejection of

mates. We therefore examined key genetic elements of the humoral arm of adaptive immunity and began by searching for genes encoding three essential components of the B cell receptor signaling complex, namely, *ighm*, *cd79a*, and *cd79b* (27). We found that with the exception of *H. mollis*_[PAN] and *P. spiniceps*_[PAN], all species possess functional *ighm* (fig. S20), *cd79a*, and *cd79b* genes (Fig. 3, A and B, and figs. S21 to S30). These results indicate that most anglerfish species are expected to be capable of mounting antibody-mediated immune responses; however, at least some species that practice consortial pairings lack an adaptive humoral defense system.

Class switching and germinal center reactions are thought to be critical features of antibody-mediated allograft rejection (28). We therefore investigated the *aicda* gene, which encodes a cytidine deaminase required for immunoglobulin gene hypermutation and class switch recombination (29). Notably, although we found intact *aicda* genes in all three anglerfish species that never form attachments, all 10 ceratioid species (ITA, PAI, and PAN) were found to be *aicda*-deficient (Fig. 3C and figs. S31 and S32). However, remnants of the *aicda* gene could be identified situated between *nat14* and *necap1* flanking genes in several instances, providing evidence that this gene was pseudogenized by deletional mechanisms (Fig. 3C and figs. S31 and S32). By contrast, all species retain two paralogs of *apobec2* (table S3), the members of the cytidine deaminase family most closely related to *aicda* (30), supporting the notion that the loss of *aicda* in ceratioids is a selective event. The loss of *aicda* may represent an immunogenetic adaptation to reduce the risk of allo-immunization reactions (31), thereby facilitating successful repeated temporary attachments by the same or different males; moreover, this modification of the immunogenome may also be beneficial in the situation of permanent attachment.

Collectively, our findings suggest that attenuation of antibody responses may be required to facilitate temporary attachments; however, complete abrogation of antibody-mediated immunity is not required for permanent exclusive (PAI) and consortial (PAN) attachments to occur. In the two lophrynid species, *H. mollis*_[PAN] and *P. spiniceps*_[PAN], the facility of antibody-mediated immunity appears to have been lost, as is evident from the presence of pseudogenized forms of the *cd79a* (Fig. 3A) and *cd79b* (Fig. 3B) co-receptor genes and by our inability to identify sequences related to the constant region of *igm* (fig. S20 and table S3).

Loss of RAG-based somatic diversification of antigen receptors

The findings described above indicate that the immunogenomes of *H. mollis*_[PAN] and

*P. spiniceps*_[PAn] have undergone substantial changes, leading to the absence of canonical antigen-specific T cell receptor and B cell receptor signaling pathways, the cornerstones of the prototypical adaptive immune systems of jawed vertebrates for the past 500 million years (32–35). In the context of the mammalian immune system, the immunogenetic constellation in *H. mollis*_[PAn] and *P. spiniceps*_[PAn] would be consistent with the lethal condition of severe combined immunodeficiency (36). Because this is evidently not the case, we entertained the possibility that the alternative $\gamma\delta$ T cell lineage might play a dominant role in the immune defense system of the two linophrynid species and, by inference, perhaps also for *C. couesii*_[PAn]. However, the lack of crucial elements of the cd3 complex would argue against the presence of a canonical $\gamma\delta$ T cell receptor-CD3 signaling complex in these species.

Whereas compensatory activity of the $\gamma\delta$ T cell lineage cannot be excluded for *C. couesii*_[PAn], it can be confidently ruled out for both

*H. mollis*_[PAn] and *P. spiniceps*_[PAn]. This conclusion is based on the identification of pseudogenized versions of both *rag1* and *rag2* genes (37) in the latter two species (Fig. 4 and figs. S33 to S42). The *rag1* gene, which is encoded in three exons, is disrupted by the invasion of transposable element-related and other types of repetitive sequences in both *H. mollis*_[PAn] and *P. spiniceps*_[PAn] (Fig. 4 and figs. S33 to S41). The *rag2* gene, which consists of a single coding exon and is located immediately adjacent to the *rag1* gene in tail-to-tail configuration in all known jawed vertebrates, has lost most of its coding capacity in *P. spiniceps*_[PAn] because of an interstitial deletion; this leaves behind only short segments of an upstream noncoding segment and a pseudogenized stretch of downstream coding sequences (Fig. 4B). No remnants of *rag2* coding sequences could be found in *H. mollis*_[PAn] (figs. S33 and S42). Collectively, these findings demonstrate that *P. spiniceps*_[PAn] and *H. mollis*_[PAn] have lost the key facilities that characterize classical adaptive immunity of

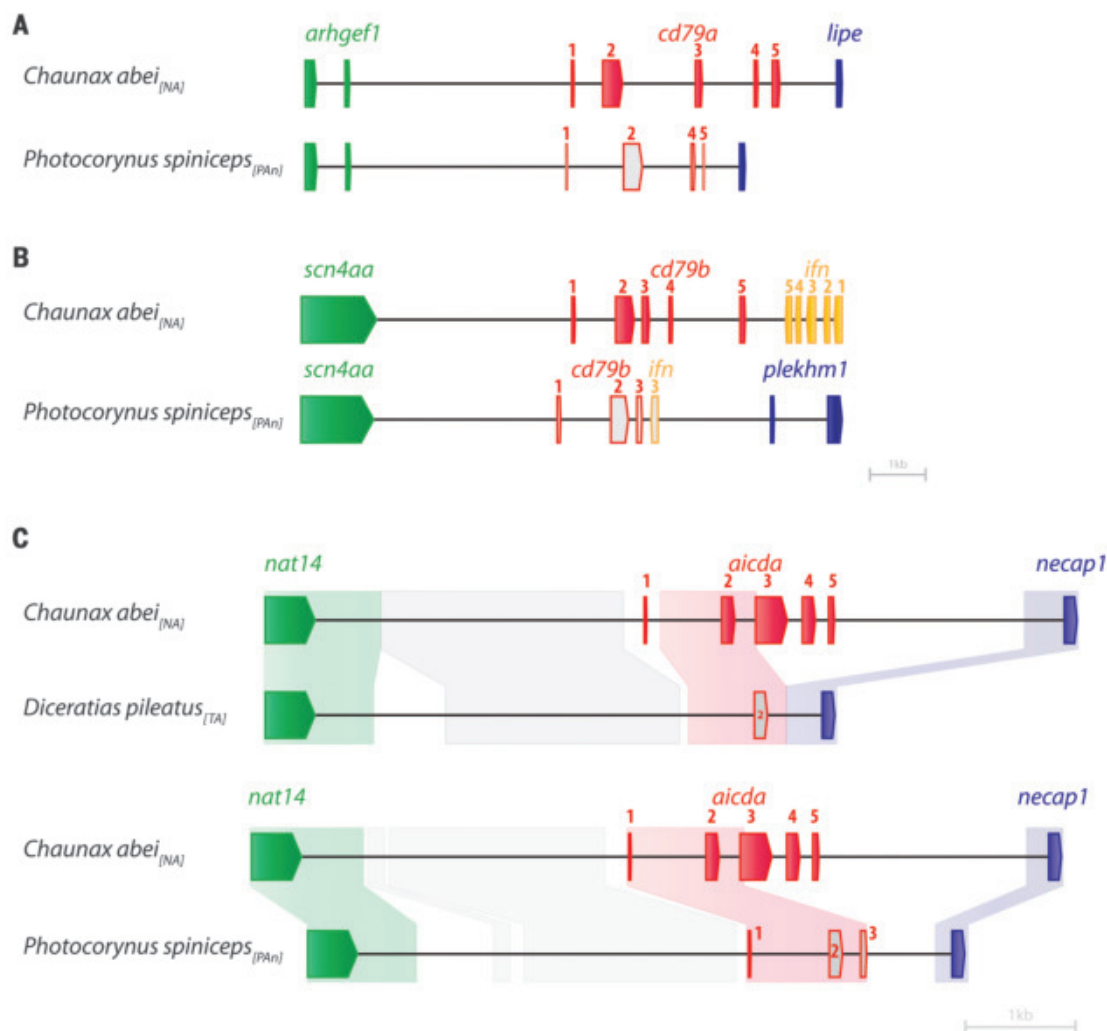
jawed vertebrates (32–35). They lack genes underlying MHC-based antigen-presentation pathways, genes encoding antigen receptors, and the key elements of the machinery required for somatic assembly of antigen receptor genes. Because these species lack functional *aicda* genes, they cannot use an alternative activation-induced cytidine deaminase-mediated diversification mechanism, a process important for antibody repertoire formation in birds and ruminants (38) and assembly of VLR antigen receptor genes in lampreys (39, 40). Moreover, we have been unable to find sequences related to distant members of the *Rag*-like gene family, such as the transib transposase from the insect *Helicoverpa zea* (41), which might be able to cooperate with an endogenous Rag2-like activity to achieve V(D)J recombination (42).

Evolution of sexual parasitism

Of note, no sex-related differences in immune gene content were detected between male and female fish of a given species, indicating that

Fig. 3. Structure of genes in the humoral arm.

(A) Pseudogenization of the *cd79a* gene in *P. spiniceps*_[PAn] through deleterious mutations in exon 2, loss of exon 3, and truncation of exon 5.
(B) Pseudogenization of the *cd79b* gene in *P. spiniceps*_[PAn] through deleterious mutations in exons 2 and 3 and an internal deletion affecting a neighboring type I *ifn* gene.
(C) Pseudogenization of the *aicda* gene in *D. pileatus*_[TA] and *P. spiniceps*_[PAn] through multiple deletions across the gene and deleterious mutations in several exons; sequence homologies are indicated as shaded blocks.



these changes are species-specific and that the evolution of sexual parasitism does not involve the asymmetrical loss of immune genes in different sexes of the same species. Collectively, our work identifies four types of immunogenetic adaptations associated with sexual parasitism in anglerfishes (Fig. 5A). (i) Temporary attachment ([TA]) appears to minimally require reduced antibody responses in the form of absent affinity maturation (*H. appeli*_[TA], *M. johnsonii*_[TA], and *D. pileatus*_[TA]). (ii) Permanent exclusive attachment ([PA1]) is additionally associated with impaired T cell-mediated immune facilities, possibly abolishing cytotoxic immune responses through CD8⁺ αβ T cells and reducing the magnitude of a helper T cell function through alterations of T cell receptor signaling. (iii) In the situation of permanent consortial ([PAn]) attachments, it appears that canonical cytotoxicity must be completely eliminated and antibody responses be severely blunted through loss of both aicda-mediated affinity maturation and helper T cell function (*C. couesii*_[PAn]). (iv) In an extreme variation on this theme, the immunogenomes of *P. spiniceps*_[PAn] and *H. mollis*_[PAn] lack all defining features of RAG-mediated adaptive immunity of jawed vertebrates. *G. vanhoeffeni*_[TA] defies simple classification in this system. The immunogenome of this species appears more aligned with that of permanently attaching species than with that of the other temporary attachers examined here; however, to date, no instances of permanently attached males have been documented for this species, despite relatively extensive sampling (2). The distinctive immunological changes observed in *G. vanhoeffeni*_[TA] could conceivably support a more prolonged period of temporary attachment in this species, or may even be indicative of an intermediate stage on an evolutionary trajectory toward permanent attachment (either [PA1] or [PAn]). At present, it is not possible to resolve the question of whether the observed pattern of gene loss drives attachment mode or vice versa, because a generalized linear model analysis (taking species phylogeny into account) did not reach statistical significance (supplementary methods).

How did sexual parasitism evolve? Are temporary attachment and facultative parasitism precursors to obligate parasitism, or are the former more derived states of the latter? Did obligate parasitism arise more than once? Previous attempts to address these issues have generated phylogenies based on either morphological characters (43) or analysis of mitochondrial genomes (15). Although these distinct approaches yielded phylogenetic trees with differing topologies, both studies surprisingly concluded that permanent sexual parasitism has evolved in multiple instances, with the temporary attachment mode serving as the ancestral state to obligate parasitism. Our new

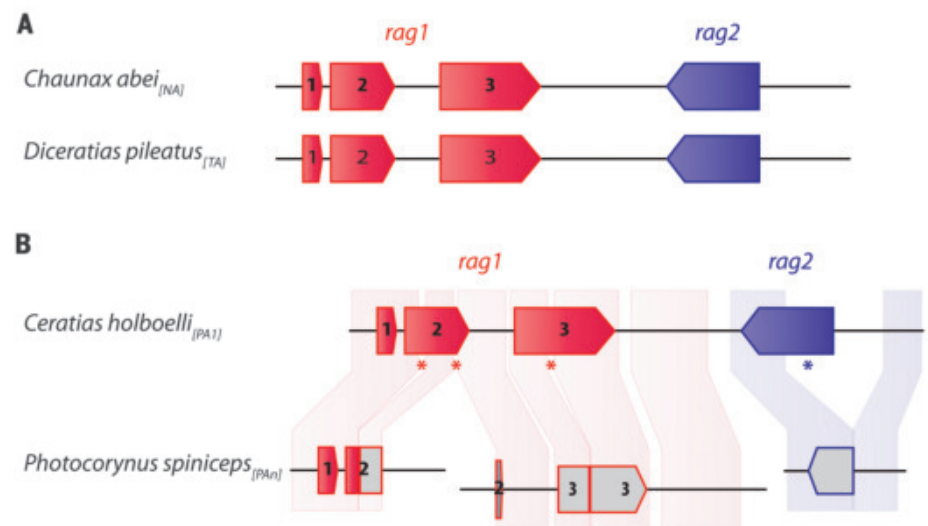


Fig. 4. Deleterious mutations in *rag* genes in species with consortial attachment. (A) Configurations of the intact *rag* loci in *C. abei*_[NA] and *D. pileatus*_[TA], demonstrating the conserved tandem arrangement of *rag1* (red) and *rag2* (blue) genes that is observed in the genomes of all jawed vertebrates reported to date. (B) Compared with the intact *rag1* gene in exclusively permanently attaching *C. holboellii*_[PA1], the *rag1* gene of *P. spiniceps*_[PAn] exhibits a number of deleterious insertions and deletions, resulting in defective coding sequences (indicated by gray shading of exons); the same is true for the pseudogenized *rag2* gene. Deletions resulting in the loss of >100 base pairs of coding sequence (relative to *C. holboellii*_[PA1]) are highlighted by an asterisk underneath the reference gene; sequence homologies are indicated as shaded blocks.

genetic resources provided the opportunity to readdress these findings, this time from the perspective of nuclear-encoded genes. To this end, we turned to the dataset of orthologous paralogy-free exon markers established by Hughes *et al.* in their reconstruction of the phylogeny of ray-finned fishes (44). A total of 946 exons, corresponding to about 86% of the Hughes dataset, were successfully identified in all species included in our study. Phylogenetic reconstruction by Bayesian inference (Fig. 5B) supports the notion that temporal attachment is the ancestral state in Ceratioidei (15, 43). Moreover, grouping the consortial permanent attaching Linophryinae species, *P. spiniceps*_[PAn] and *H. mollis*_[PAn], with the temporarily attaching *G. vanhoeffeni*_[TA] is in line with the phylogenetic reconstruction of Pietsch and Orr that was based on morphological characters (43); this association is also supported by their unusual immune gene constellations. By contrast, the three other temporarily attaching species—*D. pileatus*_[TA], *M. johnsonii*_[TA], and *H. appeli*_[TA]—form a separate monophyletic group, in accordance with their distinct immune genotype, characterized by the lack of antibody affinity maturation.

The paraphyletic constellation of *G. vanhoeffeni*, *P. spiniceps*, and *H. mollis* and the four Ceratiidae species supports the conclusions by Pietsch and Orr (43) and Miya *et al.* (15) of the independent acquisition of permanent attachment of males to females; however, the analy-

sis of additional genomes of other species of this family will be required to strengthen this conclusion.

The sequence of events leading to sexual parasitism and the driving forces behind them remain speculative; however, we view modification of the immune system to curtail allogeneic reactions to be an essential component of the process. Whether the evolutionary advantage of sexual parasitism is itself sufficient to drive changes in the immune system or whether other evolutionary forces first lead to changes in the immune system, which are then exploited for the evolution of sexual parasitism, is an important question to resolve in future studies. The results presented here would suggest that the latter scenario is more likely. For example, *G. vanhoeffeni*_[TA] forms only temporary attachments but exhibits losses of a number of genes (e.g., *cd4*, *cd8*) that could potentially allow the formation of more permanent pairings. The lack of the MHC class II pathway per se is not associated with sexual parasitism, because it has also been described in other species, such as cod (45), the non-parasitizing anglerfish *Lophius piscatorius* (46), and seahorses and pipefishes, which practice male pregnancy (47, 48). We therefore conclude that it is the unprecedented loss of other components of adaptive immunity, as described here, that is associated with the emergence of obligate sexual parasitism in ceratioidei.

New types of vertebrate immune systems

The deep sea is known to harbor rich microbial communities (49) and is also home to unicellular parasites capable of infecting at least some anglerfish species (50). How can fish species subscribing to permanent male parasitism survive despite the loss of antigen-specific cytotoxic activity and antibody affinity

maturation on one end of the spectrum and complete loss of RAG-dependent adaptive immunity on the other end? Although we consider it unlikely, we cannot exclude the possibility that anglerfishes have evolved an entirely new type of adaptive immune system. Rather, we propose that the evolutionary emergence of exclusive and consortial parasitiza-

tion, and the associated loss of several aspects of classical adaptive immunity, was accompanied by reorganization of innate immune defenses to provide efficient protection against pathogens. All ceratioid species possess at least one gene encoding type I interferon (fig. S43), as well as at least one gene encoding interferon γ (fig. S44); likewise, *tnfa* genes were readily identifiable (fig. S45). These findings suggest that key elements of innate immunity are intact. The identification of functional *prf1* (fig. S46) genes suggests that innate cytotoxic functions are present, perhaps mediated by natural killer-like or innate lymphoid cell-like cells (51). In addition, the presence of an ortholog of the *il10* gene (fig. S47), as well as of the gene encoding the common γ chain of the IL2 receptor (*il2rg*) (fig. S48), suggests that important regulatory and effector cytokine-mediated regulatory networks may still be in place. Moreover, the identification of genes encoding effector molecules of the Toll signaling pathway [*myd88* (fig. S49) and *ticam1* (fig. S50)] support the notion of intact innate defenses in ceratioids. It is possible that the immunogenetic adaptations in these fishes represent hard-wired versions of the altered immune response profiles seen in *rag1*-mutant zebrafish (52).

Conclusions

Our study uncovers a surprising degree of evolvability of immune defenses in vertebrates. Our findings challenge the view that once innate and adaptive immune systems have engaged in coevolution, neither arm can be eliminated without detrimental consequences. The nature of immunogenetic adaptations that are associated with such substantial impairments of adaptive immunity are of particular interest from an evolutionary point of view. Key nodes of evolvability of innate immune gene networks may be revealed by a comparison of the components of innate immune systems before (as present in invertebrates), during (as present in the majority of vertebrates), and after (as present in anglerfishes) coevolution with adaptive immunity. Moreover, such studies also hold promise to learn about potential strategies to enhance innate immune defenses in immune-deficient patients. On a more general level, our study highlights the advances that can be made by exploring the vast phenotypic space of vertebrates more fully. We predict that additional variations on the general design of vertebrate immunity will be discovered among the animals occupying the extraordinarily diverse ecological niches and habitats of this planet.

REFERENCES AND NOTES

1. W. Beebe, *Bull. N.Y. Zool. Soc.* **41**, 50–53 (1938).
2. T. W. Pietsch, *Oceanic Anglerfishes* (Univ. of California Press, 2009).
3. W. Watson, H. J. Walker, *Rec. Aust. Mus.* **56**, 139–142 (2004).

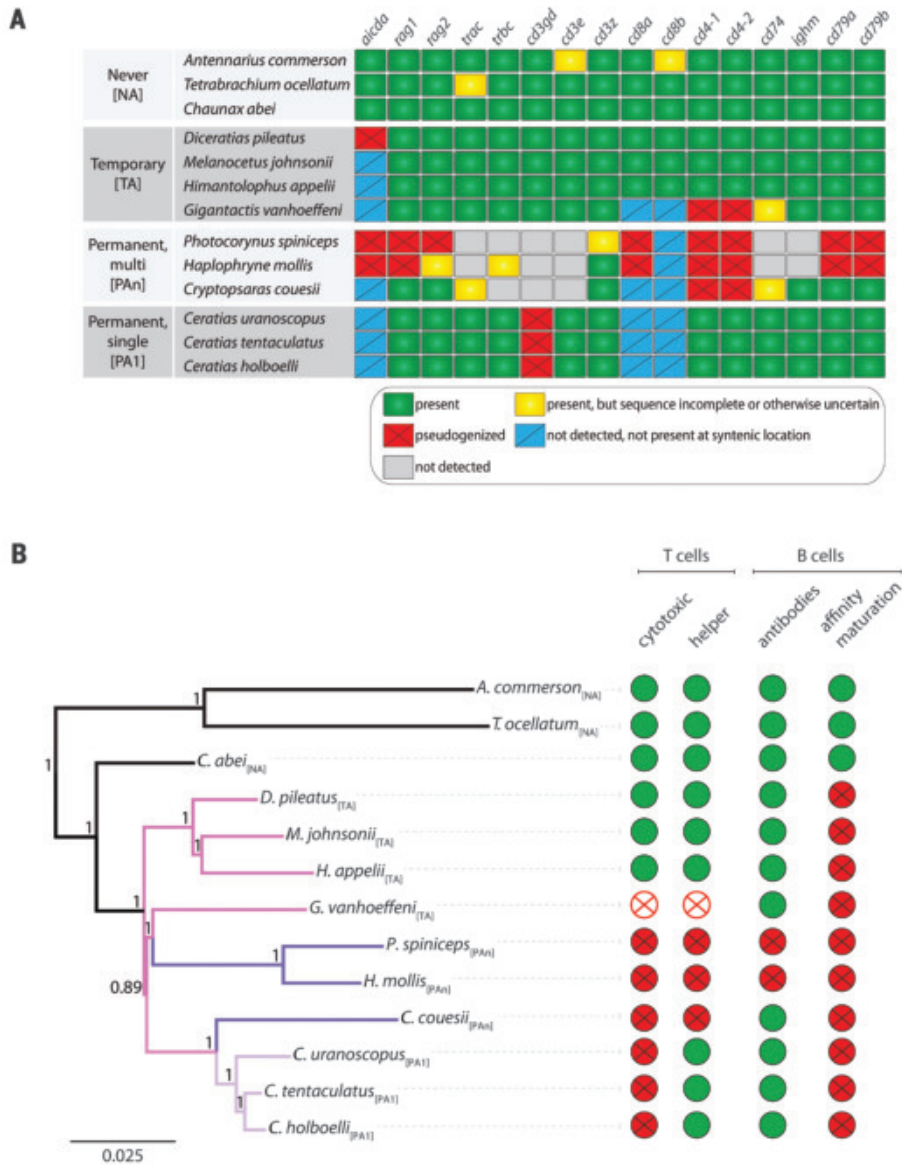


Fig. 5. Immune gene content and phylogenetic relationship of the various anglerfish species examined. (A) Tabular summary of gene content. Green shading indicates the presence of a functional gene, yellow indicates gene models that are incomplete or otherwise uncertain, red indicates the presence of a defective gene, blue indicates genes that were not detected and were additionally demonstrated to be absent from their expected syntenic location, and gray indicates genes for which no evidence was detected. An extended version of the table with notes can be found in the supplementary materials. (B) Bayesian reconstruction of ceratioid phylogeny based on the analysis of 946 orthologous exons (44). The attachment modes are noted next to the species names and are color coded in the phylogenetic tree. Also indicated are the presumed immunological consequences of genetic aberrations. Solid green circles indicate the presence of immune facility, and solid red circles with X's indicate the absence; open red circles with X's indicate that T cell receptors are present but lymphocyte lineage-specific co-receptors are missing.

4. T. W. Pietsch, *Ichthyol. Res.* **52**, 207–236 (2005).
5. C. T. Regan, *Proc. R. Soc. London Ser. B* **97**, 386–400 (1925).
6. O. Munk, E. Bertelsen, *Videnskabelige Meddelelser fra dansk naturhistorisk Forening* **144**, 49–74 (1983).
7. O. Munk, *Acta Zoologica* **81**, 315–324 (2001).
8. T. W. Pietsch, *Copeia* **1976**, 781 (1976).
9. N. W. Nisbet, *Transplant. Rev.* **15**, 123–161 (1973).
10. K. E. Lunsford, A. S. Barbas, T. V. Brennan, *Curr. Opin. Organ Transplant.* **16**, 390–397 (2011).
11. R. J. Duquesnoy, *Curr. Opin. Organ Transplant.* **19**, 428–435 (2014).
12. T. Leinders-Zufall *et al.*, *Science* **306**, 1033–1037 (2004).
13. M. Milinski *et al.*, *Proc. Natl. Acad. Sci. U.S.A.* **102**, 4414–4418 (2005).
14. F. Colucci, *Science* **365**, 862–863 (2019).
15. M. Miya *et al.*, *BMC Evol. Biol.* **10**, 58 (2010).
16. U. Grimholt, *Biology* **5**, 6 (2016).
17. P. N. Rocha, T. J. Plumb, S. D. Crowley, T. M. Coffman, *Immunol. Rev.* **196**, 51–64 (2003).
18. S. Rangarajan, R. A. Mariuzza, *Cell. Mol. Life Sci.* **71**, 3059–3068 (2014).
19. K. J. Laing *et al.*, *J. Immunol.* **177**, 3939–3951 (2006).
20. B. Stockinger *et al.*, *Cell* **56**, 683–689 (1989).
21. D. Dong *et al.*, *Nature* **573**, 546–552 (2019).
22. S. V. Guselnikov, A. M. Najakshin, A. V. Taranin, *Immunogenetics* **55**, 472–479 (2003).
23. A. Alcover, B. Alarcón, V. Di Bartolo, *Annu. Rev. Immunol.* **36**, 103–125 (2018).
24. A. Fischer, G. de Saint Basile, F. Le Deist, *Curr. Opin. Allergy Clin. Immunol.* **5**, 491–495 (2005).
25. A. Moretta *et al.*, *Annu. Rev. Immunol.* **19**, 197–223 (2001).
26. A. Loupy, C. Lefaucheur, *N. Engl. J. Med.* **379**, 1150–1160 (2018).
27. M. R. Gold, M. G. Reth, *Annu. Rev. Immunol.* **37**, 97–123 (2019).
28. M. Chhabra *et al.*, *Front. Immunol.* **9**, 3038 (2019).
29. M. Muramatsu *et al.*, *Cell* **102**, 553–563 (2000).
30. A. Krishnan, L. M. Iyer, S. J. Holland, T. Boehm, L. Aravind, *Proc. Natl. Acad. Sci. U.S.A.* **115**, E3201–E3210 (2018).
31. T. Nakanishi *et al.*, *Transplantation* **99**, 1598–1605 (2015).
32. M. D. Cooper, M. N. Alder, *Cell* **124**, 815–822 (2006).
33. T. Boehm, *Nat. Rev. Immunol.* **11**, 307–317 (2011).
34. T. Boehm, *Curr. Biol.* **22**, R722–R732 (2012).
35. T. Boehm, J. B. Swann, *Annu. Rev. Anim. Biosci.* **2**, 259–283 (2014).
36. A. Fischer, A. Rausell, *Semin. Immunol.* **36**, 13–16 (2018).
37. G. Teng, D. G. Schatz, *Adv. Immunol.* **128**, 1–39 (2015).
38. C. A. Reynaud, A. Dahan, V. Anquez, J. C. Weill, *Cell* **59**, 171–183 (1989).
39. R. Morimoto *et al.*, *Sci. Immunol.* **5**, eaba0925 (2020).
40. T. Boehm *et al.*, *Annu. Rev. Immunol.* **36**, 19–42 (2018).
41. C. G. Hencken, X. Li, N. L. Craig, *Nat. Struct. Mol. Biol.* **19**, 834–836 (2012).
42. L. M. Carmona, S. D. Fugmann, D. G. Schatz, *Genes Dev.* **30**, 909–917 (2016).
43. T. W. Pietsch, J. W. Orr, *Copeia* **2007**, 1–34 (2007).
44. L. C. Hughes *et al.*, *Proc. Natl. Acad. Sci. U.S.A.* **115**, 6249–6254 (2018).
45. B. Star *et al.*, *Nature* **477**, 207–210 (2011).
46. A. Dubin, T. E. Jørgensen, T. Mourm, S. D. Johansen, L. M. Jakt, *Biol. Lett.* **15**, 20190594 (2019).
47. D. Haase *et al.*, *Biol. Lett.* **9**, 20130044 (2013).
48. O. Roth *et al.*, *Proc. Natl. Acad. Sci. U.S.A.* **117**, 9431–9439 (2020).
49. S. Sunagawa *et al.*, *Science* **348**, 1261359 (2015).
50. M. A. Freeman *et al.*, *J. Fish Dis.* **34**, 445–452 (2011).
51. E. Vivier *et al.*, *Science* **331**, 44–49 (2011).
52. Y. Tokunaga *et al.*, *Sci. Rep.* **7**, 7536–10 (2017).
53. J. B. Swann, S. J. Holland, M. Petersen, T. W. Pietsch, T. Boehm, Data for: The immunogenics of sexual parasitism, Zenodo (2020); <https://dx.doi.org/10.5281/zenodo.3835870>.

ACKNOWLEDGMENTS

We thank R. J. Arnold, A. Graham, K. E. Hartel, A. Hay, C. P. Kenaley, M. Miya, J. W. Orr, A. Stewart, and T. T. Sutton for providing tissue samples; K. P. Maslenikov for curatorial assistance; and L. Gerri, F. Mateos, and the MPIIE deep sequencing and bioinformatics units for their help with genome sequencing. Special thanks are extended to E. Widder for allowing us to reproduce her photograph of *M. johnsonii*. **Funding:** This work

was supported by the Max Planck Society, the Ernst Jung Foundation for Science and Medicine, the European Research Council (ERC) under the European Union's Seventh Framework Programme (FP7/2007-2013), ERC grant agreement 323126, and U.S. National Science Foundation grant DEB 03-14637. **Author contributions:** J.B.S., T.W.P., and T.B. designed research; T.W.P. provided tissue samples; J.B.S., S.J.H., and T.B. performed research; J.B.S., S.J.H., M.P., T.W.P., and T.B. analyzed and interpreted data; and T.W.P. and T.B. wrote the paper with input from all other authors. **Competing interests:** The authors have no competing interests. **Data and materials availability:** The data reported in this paper have been deposited in the NCBI Sequence Read Archive (SRA) database (individual accession numbers for BioProject ID PRJNA578585 are listed in table S1) and the GenBank database (accession numbers listed in table S5). Alignments of the 946 exon loci that were used to reconstruct the anglerfish phylogeny are available at Zenodo

(53). All other data are available in the manuscript or the supplementary materials.

SUPPLEMENTARY MATERIALS

science.sciencemag.org/content/369/6511/1608/suppl/DC1
Materials and Methods
Figs. S1 to S53
Tables S1 to S8
References (54–80)
MDAR Reproducibility Checklist
Data S1

22 October 2019; accepted 17 July 2020
Published online 30 July 2020
10.1126/science.aaz9445

REPORTS

SOLAR CELLS

Stable perovskite solar cells with efficiency exceeding 24.8% and 0.3-V voltage loss

Mingyu Jeong^{1*}, In Woo Choi^{2,3*}, Eun Min Go^{4*}, Yongjoon Cho¹, Minjin Kim², Byongkyu Lee¹, Seonghun Jeong¹, Yimhyun Jo², Hye Won Choi², Jiyun Lee⁴, Jin-Hyuk Bae³, Sang Kyu Kwak^{4,†}, Dong Suk Kim^{2,†}, Changduk Yang^{1,†}

Further improvement and stabilization of perovskite solar cell (PSC) performance are essential to achieve the commercial viability of next-generation photovoltaics. Considering the benefits of fluorination to conjugated materials for energy levels, hydrophobicity, and noncovalent interactions, two fluorinated isomeric analogs of the well-known hole-transporting material (HTM) Spiro-OMeTAD are developed and used as HTMs in PSCs. The structure–property relationship induced by constitutional isomerism is investigated through experimental, atomistic, and theoretical analyses, and the fabricated PSCs feature high efficiency up to 24.82% (certified at 24.64% with 0.3-volt voltage loss), along with long-term stability in wet conditions without encapsulation (87% efficiency retention after 500 hours). We also achieve an efficiency of 22.31% in the large-area cell.

To achieve better and cheaper alternative energy, perovskite solar cells (PSCs) have been the front runner among emerging next-generation solar cells. Power conversion efficiency (PCE) exceeding 25% (1) has been achieved in laboratory-scale PSCs by improving the perovskite material formulations (2–5), the device fabrication routines (6–9), and the high-quality film-formation methodologies (10–12) on the basis of a comprehensive understanding of the charge dynamics at the interfacial layers. Most high-performance

PSCs have a sandwich structure composed of a perovskite absorber between a metal oxide-based electron-transporting material (ETM) and an organic hole-transporting material (HTM) (3, 7, 13, 14). Because high-quality perovskite and ETMs can be obtained from various processing methodologies, HTMs are considered to be fundamentally important in further improving PSC performance. Despite efforts to develop better HTMs to replace Spiro-OMeTAD [2,2',7,7'-tetrakis(*N,N*-di-*p*-methoxyphenylamine)-9,9'-spirobifluorene] (15–17), this compound, which was developed by Grätzel *et al.* for solid-state dye-sensitized solar cells more than two decades ago (18), is still recognized as the most efficient HTM in PSCs owing to its amorphous nature, high compatibility with dopants, and energy levels matching those of perovskite. However, it must be chemically doped with hygroscopic dopants to attain efficient hole extraction and sufficient conductivity. Such doping negatively influences the stability of ambient PSCs, thus presenting a major obstacle to truly commercializing

¹Department of Energy Engineering, School of Energy and Chemical Engineering, Perovtronics Research Center, Low Dimensional Carbon Materials Center, Ulsan National Institute of Science and Technology (UNIST), Ulsu-gun, Ulsan 44919, Republic of Korea. ²Ulsan Advanced Energy Technology R&D Center, Korea Institute of Energy Research, Nam-gu, Ulsan 44776, Republic of Korea. ³School of Electronics Engineering, Kyungpook National University, Daegu 41566, Republic of Korea. ⁴Department of Energy Engineering, School of Energy and Chemical Engineering, Ulsan National Institute of Science and Technology (UNIST), Ulsan 44919, Republic of Korea.

*These authors contributed equally to this work.

†Corresponding author. Email: yang@unist.ac.kr (C.Y.); kimds@kier.re.kr (D.S.K.); skkwak@unist.ac.kr (S.K.K.)

PSCs despite PCE being sufficient for practical applications (19–21). Therefore, the PSC community is actively investigating candidate HTMs to replace Spiro-OMeTAD and ultimately achieve stable PSCs simultaneously exhibiting the same or improved performance. Notably, the latest research on cesium cation (Cs^+)–(22, 23), carbon electrode–(24–26), and dopant-free-based PSCs (27, 28) can bring the benefits in improving the device stability but lower PCE levels when compared with that of the Spiro-OMeTAD-based PSC.

Considering the multiple possible aspects of fluorination of the conjugated materials (e.g., lowering energy levels and enhancing molecular packing and hydrophobicity through the induced dipole along the C–F bond), we developed two fluorinated isomeric analogs (Spiro-*m*F and Spiro-*o*F) of Spiro-OMeTAD as HTMs for PSC fabrication and compared their device performance with that of the optimized Spiro-OMeTAD-based PSC. Not only do we report a PCE of 24.82% (certified PCE of 24.64% with 0.3-V loss) achieved from the device fabricated with Spiro-*m*F, but we also show the long-term stability of fluorinated HTM-based devices without encapsulation on exposure to high relative humidity (RH) (87% PCE retention after 500 hours). Furthermore, the Spiro-*m*F-based PSC, with an area of 1 cm^2 , represents an efficiency of 22.31%.

Figure 1A presents the chemical structures of the parent Spiro-OMeTAD and its fluorinated analogs (Spiro-*m*F and Spiro-*o*F). The two fluorinated isomeric HTMs were synthesized through two Buchwald-Hartwig C–N cross-coupling reactions; detailed synthesis and molecular characterization are described in figs. S1 to S7 and materials and methods. Differential scanning calorimetry analysis revealed that the synthesized HTMs exist in both amorphous and crystalline states, as evidenced by the observation of glass-transition and melting temperatures (fig. S8). The ultraviolet-visible absorption (UV-Vis) spectra in Fig. 1B show that, in addition to the absorption band from 300 to 450 nm, the three HTMs feature a slight redshift as the solution transitions to the solid state, which is commonly observed in many organic semiconductors (29–31). Relative to the Spiro-OMeTAD, both new fluorinated isomeric HTMs, especially Spiro-*o*F, display obvious blue-shifted absorption maxima and onsets, thus leading to the net widening of their optical bandgaps (E_g^{opt}), which is attributed to the fluorine atoms generating an inductive electron-withdrawing effect on the aromatic rings of the conjugated backbone (32–34). Cyclic voltammetry (CV) was performed on the HTMs to determine the highest occupied molecular orbital (HOMO) energy levels (fig. S9); the lowest unoccupied molecular orbital (LUMO) energy levels were

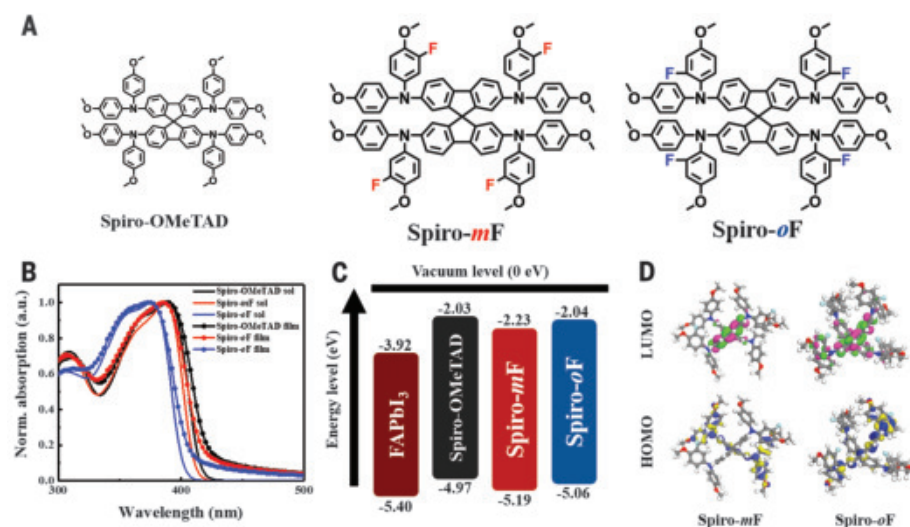


Fig. 1. Optical and electrochemical characteristics and DFT calculation of HTMs. (A) Chemical structures of Spiro-OMeTAD and its fluorinated analogs Spiro-*m*F and Spiro-*o*F. (B) UV-Vis absorption spectra of Spiro-OMeTAD, Spiro-*m*F, and Spiro-*o*F in dilute chlorobenzene solution (sol) and as thin films. a.u., arbitrary units; Norm., normalized. (C) Molecular energy level alignments. (D) Electron density distributions of HOMO and LUMO for Spiro-*m*F and Spiro-*o*F.

derived from the HOMOs and E_g^{opt} . The CV and E_g^{opt} -derived HOMO and LUMO energies are –4.97 and –2.03, –5.19 and –2.23, and –5.06 and –2.04 eV for Spiro-OMeTAD, Spiro-*m*F, and Spiro-*o*F, respectively, thus demonstrating that fluorination can simultaneously lower the HOMO and LUMO levels (Fig. 1C and table S1). These results agree well with the trend estimated from density functional theory (DFT) calculations by using the generalized gradient approximation with Perdew-Burke-Ernzerhof functional (figs. S10 and S11). The same trend is observed for the HOMOs of the doped HTMs (fig. S12). Therefore, in addition to reasonably estimating the enhanced oxidation stability of both fluorinated HTMs, more efficient interfacial hole-transport kinetics are observed compared with that of Spiro-OMeTAD. Moreover, the UV-Vis spectra and CV data indicate a strong fluorine positioning effect, on the optical and electrochemical properties. We also observe clear differences in the DFT-calculated structural conformations and electron distributions of Spiro-*m*F and Spiro-*o*F (Fig. 1D).

After deciphering their intrinsic properties, we used Spiro-*m*F and Spiro-*o*F as HTMs in PSCs fabricated with the conventional n–i–p configuration, specifically fluorine-doped tin-oxide substrate/compact TiO_2 /mesoporous TiO_2 /perovskite layer/HTM/Au (fig. S13); FAPbI_3 was selected as the perovskite layer because of its narrow bandgap (1.48 eV), thus making it suitable for the absorption of near-infrared light and promoting thermal stability (35, 36). For a comparative study, we also prepared a control device under the same conditions, using

Spiro-OMeTAD as the HTM. The HTM chlorobenzene solution containing 4-*tert*-butylpyridine, lithium bis(trifluoromethanesulfonyl)imide, and tris[2-(1H-pyrazol-1-yl)-4-*tert*-butylpyridine]cobalt(III)-tris[bis(trifluoromethylsulfonyl)imide] as dopant additives was deposited by spin-coating on the FAPbI_3 layer. X-ray diffraction (XRD) patterns of the neat FAPbI_3 (fig. S14) show strong diffraction peaks at 14.1° and 28.2° , corresponding to the (001) and (002) crystal planes, respectively, and confirming a dense and ordered perovskite crystal structure. Similar results were observed after the films were spin-coated with the doped HTM solutions, indicating that the HTM processing did not damage the perovskite crystal quality. The optimized thicknesses of the FAPbI_3 and HTM layers were ~ 750 and ~ 270 nm, respectively. Because PSC performance is sensitive to the dopant type and doping conditions, independent device optimization was also undertaken by carefully screening the ratios and amount of dopant additives. Details about the device fabrication and all device data examined herein are included in the supplementary materials.

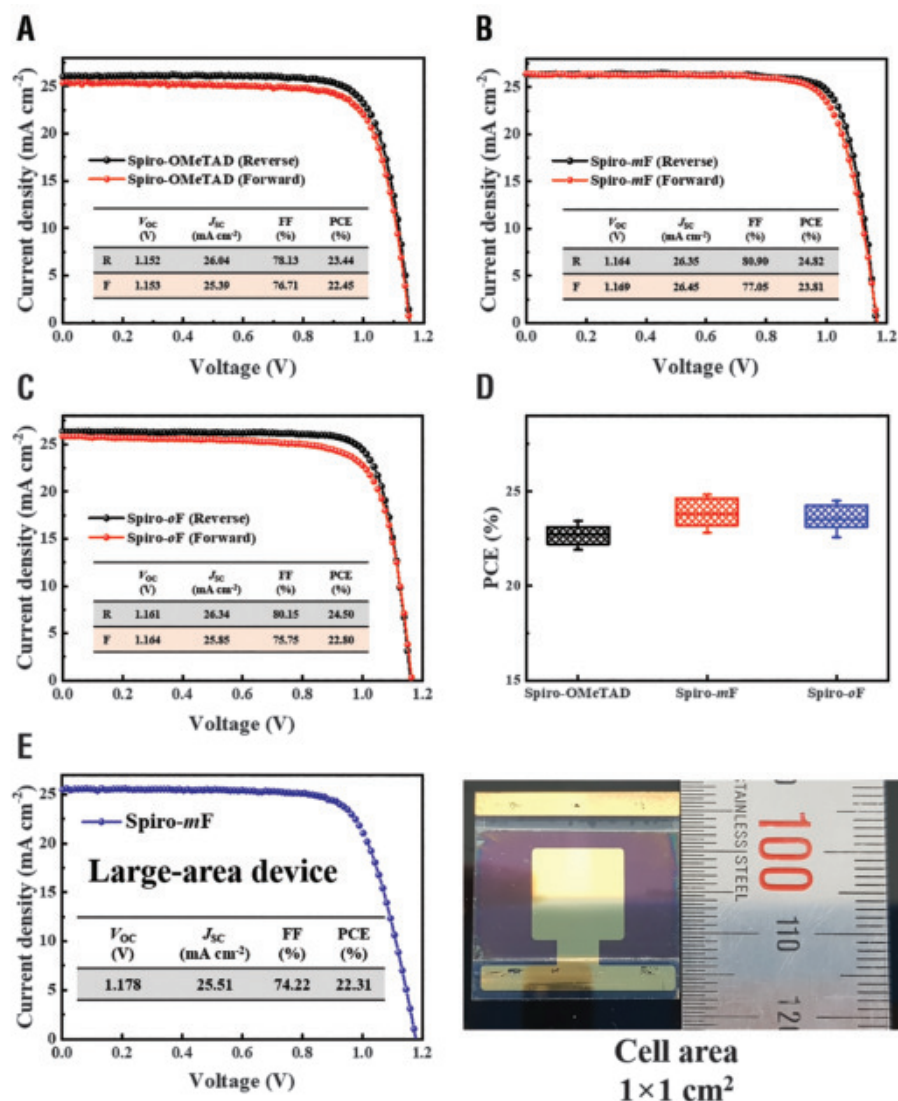
Figure 2 shows the current density-voltage (J - V) curves of the best PSCs for each given HTM under AM 1.5 G simulated solar illumination at 100 mW cm^{-2} ; the corresponding photovoltaic parameters are summarized in table S2. A tiny hysteresis was observed in the J - V scans between reverse and forward scans in all cases. First, under optimized conditions, the control device fabricated with Spiro-OMeTAD achieved a maximum PCE of 23.44% for an area of 0.0819 cm^2 with a short-circuit current density (J_{sc}) of 26.04 mA cm^{-2} , an open-circuit voltage (V_{oc}) of 1.152 V, and a fill factor (FF) of

78.13%; this value is fairly comparable to the previously reported highest PCE of the PSCs in single-junction devices (37–39). Compared with the control device fabricated with doped Spiro-OMeTAD, both fluorinated HTM-based PSCs exhibited nearly identical (J_{SC}) values of 26.34 to 26.35 mA cm^{-2} and slightly superior V_{OC} values over 1.16 V, thus reflecting the lower-lying HOMO levels observed in the CV data. The Spiro-*m*F-based device produced a somewhat higher FF (80.90%) than that of the other devices, ultimately resulting in the best PCE of 24.82%. The slightly lower performance in the forward scan is mainly due to the low FF. The small standard deviation of the PCEs among the tested devices points toward excellent reproducibility (Fig. 2D). PSC performance is highly sensitive to environmental conditions. Thus, to provide accuracy and reproducibility of the device performance metrics reported in Fig. 2D and table S2, we fabricated each device under the

same conditions: at 25°C and below 30% RH, with exclusion of strong light and oxygen. One of the best Spiro-*m*F-based devices was sent to an independent solar cell-accredited laboratory (Newport, Irvine, CA, USA) for certification, where a stabilized PCE of 24.64% (with $V_{OC} = 1.1814$ V, $J_{SC} = 26.1783$ mA cm^{-2} , and FF = 79.6%) was confirmed (fig. S16). On the basis of the bandgap of FAPbI₃ (1.48 eV), the obtained V_{OC} value quantifies the V_{OC} loss as 0.3 V, thus being close to the theoretical minimum value based on the radiative limit defined by the Shockley-Queisser theory (40, 41). Because the radiative limit is the near-maximum theoretical PCE of the solar cell, these results suggest that the non-radiative recombination of the device is largely suppressed in the Spiro-*m*F-based PSC, which is directly evidenced by external electroluminescence quantum efficiency (EL-EQE) measurement (fig. S17) (42). The reported 0.3-V V_{OC} loss is, to the best of our knowledge, the lowest

reported value to date for PSCs in any type of device. To demonstrate practical applicability and scalability of the Spiro-*m*F-based device, we also prepared a large-area cell with an area of 1 cm^2 , yielding the highest PCE of 22.31% with corresponding V_{OC} , J_{SC} , and FF of 1.178 V, 25.51 mA cm^{-2} , and 74.22%, as shown in Fig. 2E. By using space charge-limited current (SCLC) measurements, the hole mobility (μ) of the pristine HTMs is in order of Spiro-OMeTAD ($6.5904 \times 10^{-3} \text{ cm}^2 \text{ V}^{-1} \text{ s}^{-1}$) < Spiro-*o*F ($7.2902 \times 10^{-3} \text{ cm}^2 \text{ V}^{-1} \text{ s}^{-1}$) < Spiro-*m*F ($7.4748 \times 10^{-3} \text{ cm}^2 \text{ V}^{-1} \text{ s}^{-1}$) (fig. S18). The higher μ in Spiro-*m*F can be explained by denser solid-state packing through noncovalent inter- and intra-interactions induced by F atoms (43, 44), corresponding to the slightly enhanced J_{SC} and FF values of the Spiro-*m*F-based PSC. By contrast, in Spiro-*o*F, the outward appended F atoms of the central HTM unit may act as a steric hindrance such that intermolecular interaction is dampened, hence making it

Fig. 2. Photovoltaic performance. *J*-*V* curves of optimized devices based on (A) Spiro-OMeTAD, (B) Spiro-*m*F, and (C) Spiro-*o*F. (D) PCE distribution of each HTM. For each type of device, the solid transverse lines in the boxes are the average values obtained from 15 devices, and the error bars show the highest and lowest values at each point. (E) *J*-*V* curve of the Spiro-*m*F-based device with an area of 1 cm^2 (left); photograph of the device (right).



more difficult for the charge to hop between molecules (the more bent structure of Spiro-oF core relative to that of Spiro-mF is shown in the DFT study results).

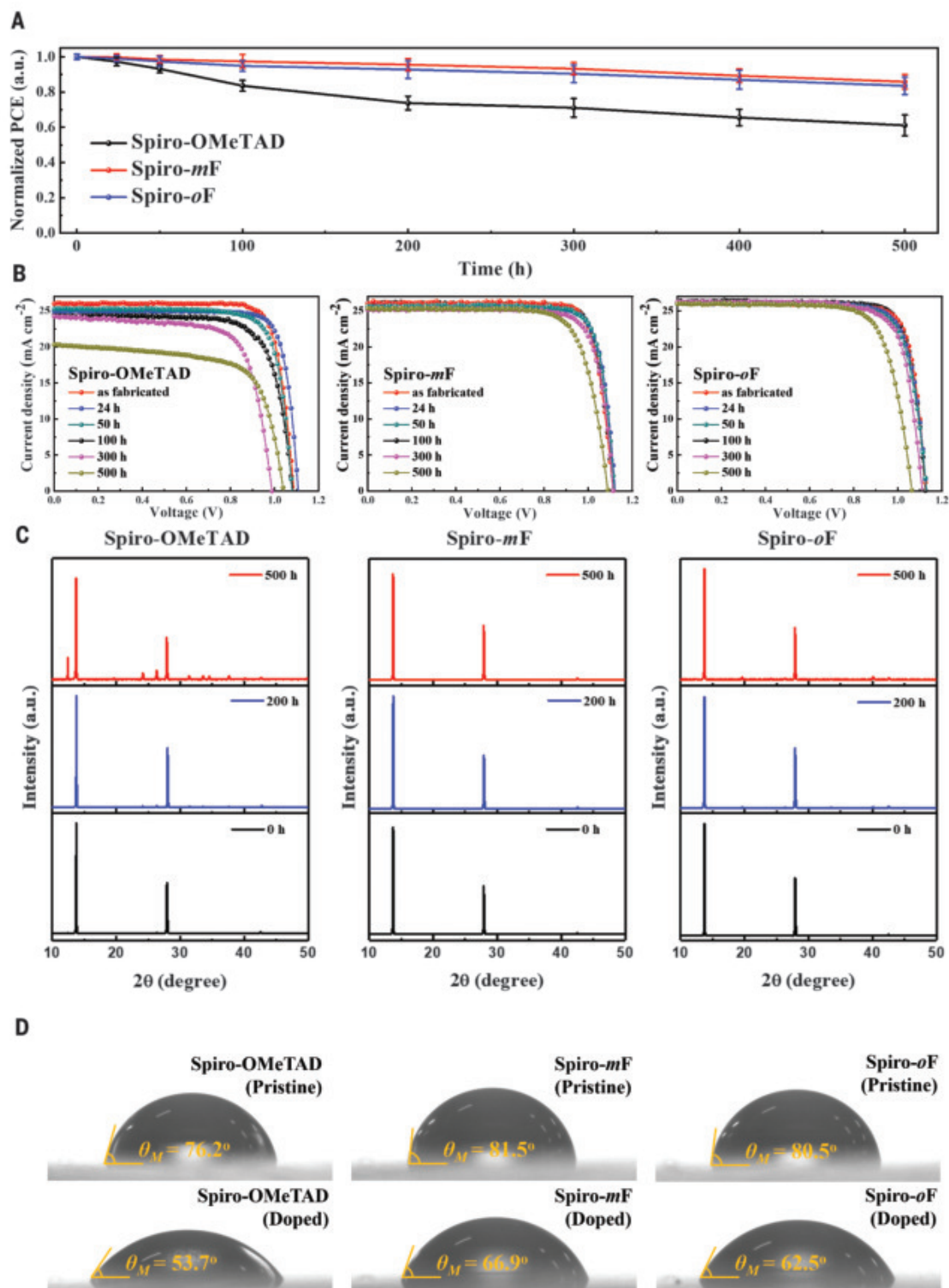
We also evaluated the charge dynamics occurring at the perovskite-HTM interface

using steady-state photoluminescence (PL) and time-resolved PL (TRPL) decay measurements. Figure S19A shows that upon depositing HTM on the perovskite film, the intensity of the steady-state PL spectrum was largely reduced, and the quenching efficacy followed Spiro-mF >

Spiro-oF > Spiro-OMeTAD, which is consistent with the hole mobility trend. Figure S19B shows the TRPL spectra of the devices based on the each HTM as recorded with the peak emission at 800 nm. The TRPL decay data were modeled by a bi-exponential formula

Fig. 3. Long-term stability and hydrophobicity.

(A) Long-term stability of Spiro-OMeTAD-, Spiro-mF-, and Spiro-oF-based devices in air (~50% RH) without encapsulation. (B) Evolution of *J*-*V* curves for the unencapsulated PSC devices, based on Spiro-OMeTAD, Spiro-mF, and Spiro-oF over a period of 500 hours. (C) Time evolution of XRD patterns of perovskite films with Spiro-OMeTAD, Spiro-mF, and Spiro-oF. (D) Contact-angle measurements of pristine and doped HTM films.



$[Y = A_1 \exp(-t/\tau_1) + A_2 \exp(-t/\tau_2)]$ (45–47), as listed in table S6, where fast (τ_1) and slow (τ_2) decay components are related to nonradiative and radiative recombination, respectively.

The fitted decay lifetimes (τ_1 , τ_2) are (1438 ns, 2923 ns), (119 ns, 2210 ns), (104 ns, 2299 ns), and (117 ns, 2305 ns) for perovskite without an HTM, with doped HTM Spiro-OMeTAD,

Spiro-mF, and Spiro-oF, respectively. Fast charge extraction and highly efficient charge-transfer processes are key factors for achieving the best PSC performance. Overall, on the basis of

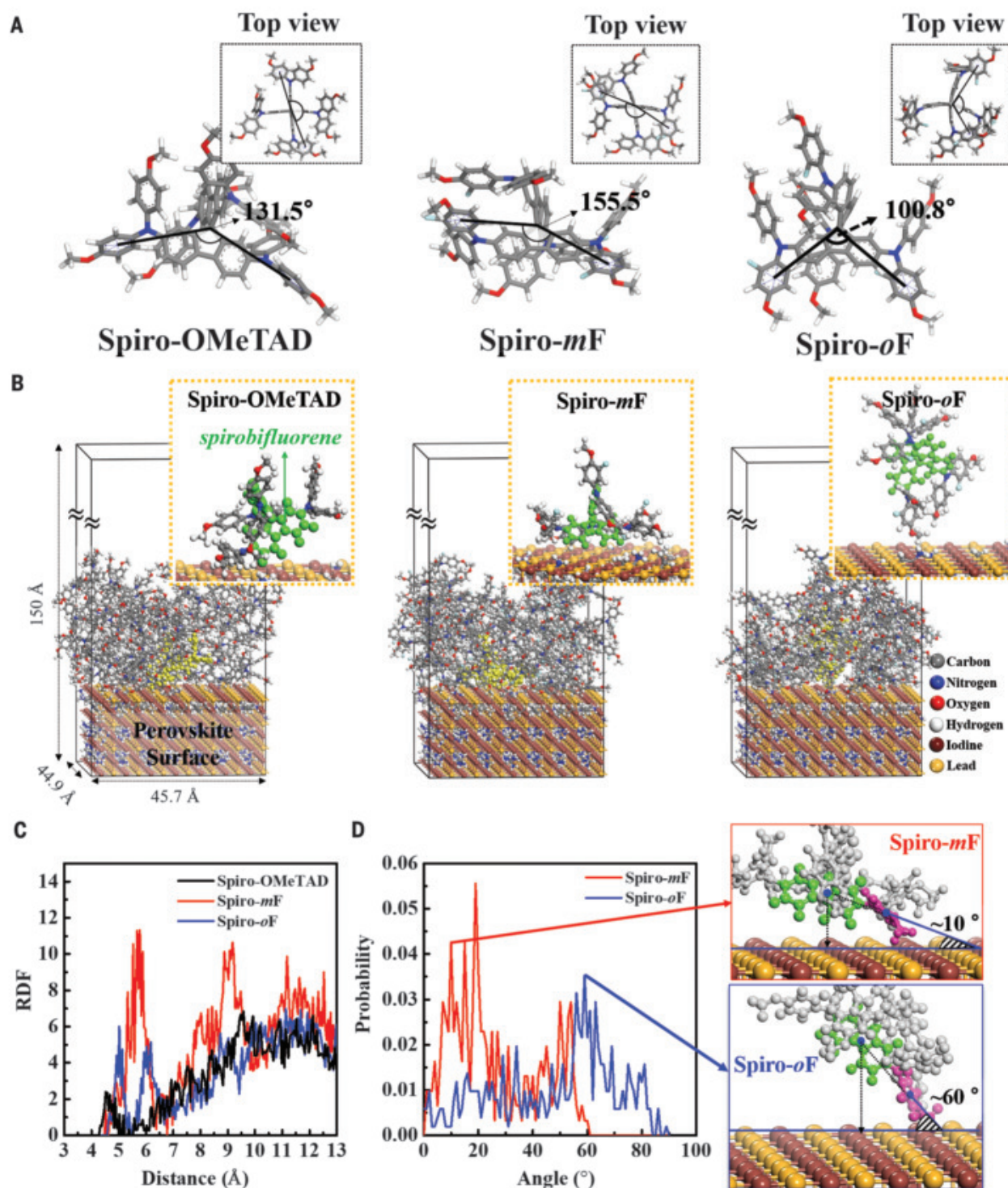


Fig. 4. Molecular simulations. (A) Optimized molecular structure of Spiro-OMeTAD, Spiro-mF, and Spiro-oF. Angles of fluorinated methoxyphenyl groups from the center of spirobifluorene are shown. (B) Adsorption structures of Spiro-OMeTAD, Spiro-mF, and Spiro-oF on the surface of perovskite. Enlarged adsorption states (yellow-colored atoms) are shown in yellow-dotted boxes. (C) RDF of fluorene groups and the surface of perovskite. (D) Probability distribution of angles of Spiro-mF and Spiro-oF from the perovskite surface. Red and blue insets show the angles measured with fluorene (green) and phenyl (pink) groups on the surface.

enhanced mobility and conductivity (the electrical conductivity data in fig. S20), the presented data demonstrate that the best parameters occur in the Spiro-*mF*-based device.

To directly ascertain the degradation processes occurring in perovskite films, we conducted long-term stability tests on the three devices without encapsulation under ~50% RH. The PCE of Spiro-OMeTAD-based control device dropped from 23.21 to 13.74%, corresponding to ~60% of its initial PCE after 500 hours; however, the PCE of both fluorinated HTM-based devices was quite stable, resulting in very high PCE retention (>87%) over the same measurement period. The PCE trends are presented in Fig. 3, and detailed photovoltaic parameters are found in tables S7 to S9. XRD patterns were tracked at regular intervals to estimate the morphological degradation of the device layers (Fig. 3C). The Spiro-OMeTAD-based device exhibited a clear deterioration of the typical perovskite XRD peaks after 500 hours, whereas no apparent impurity peaks were observed in the XRD patterns of devices fabricated with fluorinated HTMs. Moreover, after 3 weeks of storage, no deterioration was observed. From the electrochemical impedance spectroscopy (EIS) analysis with varying times (fig. S21), relative to Spiro-OMeTAD-based device, the fluorinated HTM-based devices, especially for Spiro-*mF*, one discloses smaller EIS resistance values, providing additional proof of their better morphological robustness and charge-transfer behavior. Contact-angle measurements were conducted to determine the surface water resistance of the neat and doped HTM layers on perovskite. As shown in Fig. 3D and table S10, the water droplet contact angle on fluorinated HTM films is larger than that on Spiro-OMeTAD film, indicating reduced hygroscopicity of the fluorine-doped Spiro-*mF* and Spiro-*oF* HTMs. The presence of fluorine atoms induces the creation of kinetic barriers that slow the intrusion of O₂ and H₂O. The increased hydrophobicity generated by using fluorinated Spiro-type HTMs is a key factor contributing to the enhanced stability of PSC devices.

We also conducted in-depth atomistic simulations of the DFT-optimized molecular structures of the three HTMs. When examining the free molecular structures, Spiro-*mF* exhibited a more unfolded structure regarding the angle between the centers of spirobifluorene and two fluorinated methoxyphenyl groups when compared with that of other HTMs (Fig. 4A). We also noticed that the fluorine atoms at the *ortho*-sites caused steric hindrance regarding the free movement of the methoxyphenyl groups. The adsorption state of each HTM on the perovskite surface was investigated by molecular dynamics (MD) simulations (see the “simulation details” section in the materials and methods, as well as Fig. 4B). Spiro-*mF*

and Spiro-*oF* adsorbed closer to the perovskite surface than Spiro-OMeTAD, as determined by observing the radial distribution function (RDF) of all phenyl groups on the perovskite surface (fig. S22). In particular, the fluorene units of Spiro-*mF* were found more on the perovskite surface than that of Spiro-*oF* (Fig. 4C), implying that the adsorbed structure of Spiro-*mF* and Spiro-*oF* could be different. We noticed that Spiro-*mF* featured a specific RDF peak from the perovskite surface due to the stretched structure of fluorene and phenyl groups on the surface; each peak represents the adsorbed components of Spiro-*mF* (phenyl and fluorene groups) (fig. S23). On the basis of the configurations sampled from the MD simulations, fluorene and phenyl groups of Spiro-*mF* adsorbed together on the perovskite surface, whereas those of Spiro-*oF* often did not adsorb on the perovskite surface together (Fig. 4D). The unfolded structure of Spiro-*mF* on perovskite is also described by the center-to-end distance (R_{cte}) of the molecule, where the R_{cte} of Spiro-*mF* and Spiro-*oF* was ~6.44 and ~5.99 Å, respectively (fig. S24A), indicating that the preservation of the free molecular structure of the HTMs occurred on the perovskite surface. The adsorbed Spiro-*mF* molecules were stacked in layers on the perovskite surface, which was revealed by the relative concentration of fluorene groups (fig. S24B). The stacked structure of Spiro-*mF* featured a higher hole-transfer integral (56 meV) than that of the randomly packed Spiro-*oF* (29 meV) and Spiro-OMeTAD (5 meV) on the surface (fig. S24, C and D, and supplementary text 3). The adsorbed Spiro-*mF*, therefore, is considered to be favorable for effective hole transport (17). Along with the detailed atomistic simulations, a comparative investigation of Spiro-OMeTAD versus its fluorinated analogs demonstrates that the fluorination of HTMs with controlled isomerism is a promising strategy to simultaneously achieve high performance and excellent device stability, thus advancing the realization of commercial PSCs.

REFERENCES AND NOTES

- National Renewable Energy Laboratory, Best research-cell efficiencies chart (2020); www.nrel.gov/pv/assets/pdfs/best-research-cell-efficiencies.20200218.pdf.
- M. Grätzel, *Acc. Chem. Res.* **50**, 487–491 (2017).
- N. J. Jeon et al., *Nature* **517**, 476–480 (2015).
- J.-W. Lee, D.-J. Seol, A.-N. Cho, N.-G. Park, *Adv. Mater.* **26**, 4991–4998 (2014).
- N. Pellet et al., *Angew. Chem. Int. Ed.* **53**, 3151–3157 (2014).
- E. A. Alharbi et al., *Nat. Commun.* **10**, 3008 (2019).
- J. H. Heo et al., *Nat. Photonics* **7**, 486–491 (2013).
- M. M. Lee, J. Teuscher, T. Miyasaka, T. N. Murakami, H. J. Snaith, *Science* **338**, 643–647 (2012).
- Y. Liu et al., *Sci. Adv.* **5**, eaaw2543 (2019).
- J. Burschka et al., *Nature* **499**, 316–319 (2013).
- N. J. Jeon et al., *Nat. Mater.* **13**, 897–903 (2014).
- M. Liu, M. B. Johnston, H. J. Snaith, *Nature* **501**, 395–398 (2013).
- H. J. Snaith, *J. Phys. Chem. Lett.* **4**, 3623–3630 (2013).
- S. D. Stranks et al., *Science* **342**, 341–344 (2013).
- N. J. Jeon et al., *J. Am. Chem. Soc.* **136**, 7837–7840 (2014).
- N. J. Jeon et al., *Nat. Energy* **3**, 682–689 (2018).
- M. Saliba et al., *Nat. Energy* **1**, 15017 (2016).
- U. Bach et al., *Nature* **395**, 583–585 (1998).
- Z. Li et al., *J. Am. Chem. Soc.* **138**, 11833–11839 (2016).
- J. Liu et al., *Energy Environ. Sci.* **7**, 2963–2967 (2014).
- F. Zhang et al., *Adv. Energy Mater.* **6**, 1600401 (2016).
- F. Bella, P. Renzi, C. Cavallo, C. Gerbaldi, *Chemistry* **24**, 12183–12205 (2018).
- M. Saliba et al., *Energy Environ. Sci.* **9**, 1989–1997 (2016).
- H. Chen, S. Yang, *J. Mater. Chem. A* **7**, 15476–15490 (2019).
- L. Fagioli, F. Bella, *Energy Environ. Sci.* **12**, 3437–3472 (2019).
- M. Wu, M. Sun, H. Zhou, J.-Y. Ma, T. Ma, *Adv. Funct. Mater.* **30**, 1906451 (2020).
- Y. Hou et al., *Science* **358**, 1192–1197 (2017).
- E. H. Jung et al., *Nature* **567**, 511–515 (2019).
- H. Bin et al., *Nat. Commun.* **7**, 13651 (2016).
- S. Holliday et al., *Nat. Commun.* **7**, 11585 (2016).
- Y. Sun et al., *Nat. Mater.* **11**, 44–48 (2012).
- F. Babudri, G. M. Farinola, F. Naso, R. Ragni, *Chem. Commun.* **2007**, 1003–1022 (2007).
- I. Benjamin, E. Z. Faraggi, Y. Avny, D. Davidov, R. Neumann, *Chem. Mater.* **8**, 352–355 (1996).
- H. Bronstein et al., *Chem. Mater.* **25**, 277–285 (2013).
- G. E. Eperon et al., *Energy Environ. Sci.* **7**, 982–988 (2014).
- H. Min et al., *Science* **366**, 749–753 (2019).
- Q. Jiang et al., *Nat. Photonics* **13**, 460–466 (2019).
- M. Kim et al., *Joule* **3**, 2179–2192 (2019).
- P. Wang et al., *Adv. Mater.* **32**, e1905766 (2020).
- S. M. Menke, N. A. Ran, G. C. Bazan, R. H. Friend, *Joule* **2**, 25–35 (2018).
- W. Shockley, H. J. Queisser, *J. Appl. Phys.* **32**, 510–519 (1961).
- T. Kirchartz, U. Rau, *Adv. Energy Mater.* **8**, 1703385 (2018).
- J.-F. Jheng et al., *Adv. Mater.* **25**, 2445–2451 (2013).
- K. Kawashima et al., *J. Am. Chem. Soc.* **138**, 10265–10275 (2016).
- Y. Iwata, R. G. Banal, S. Ichikawa, M. Funato, Y. Kawakami, *J. Appl. Phys.* **117**, 075701 (2015).
- D. Shi et al., *Science* **347**, 519–522 (2015).
- Y. Yang et al., *Nat. Commun.* **6**, 7961 (2015).

ACKNOWLEDGMENTS

Funding: This work was supported by the National Research Foundation of Korea (NRF) grant funded by the Korea government (MSIP) (2018R1A2A1A05077194 and 2014R1A5A1A009799); Center for Advanced Soft-Electronics funded by the Ministry of Science and ICT as Global Frontier Project (2012M3A6A5055225); Wearable platform Materials Technology Center (2016R1A5A1A009926) funded by the Korean Government (MSIT); the NRF funded by the Ministry of Science, ICT, and Future Planning (2020M1A2A2080746); Korea Institute of Energy Technology Evaluation and Planning (KETEP) grant funded by the Korea government (MOTIE) [20193091010460, Development of Super Solar cells for overcoming the theoretical limit of silicon solar cell efficiency (>30%); the Research Project Funded by Ulsan City (1.200042) of UNIST (Ulsan National Institute of Science and Technology); the Development Program of the Korea Institute of Energy Research (KIER) (CO-2401 and CO-2402); and computational resource from KISTI-HPC (KSC-2019-CRE-0056). **Author contributions:** C.Y., D.S.K., and S.K.K. conceptualized and supervised the project. J.-H.B. advised on the research. M.J. synthesized and characterized the HTM materials. I.W.C. fabricated and characterized the perovskite films and solar cells and did the stability test. E.M.G. and J.L. performed the molecular simulations. Y.C. performed CV and contact-angle measurements. M.K. performed the SCLC and XRD measurements. B.L. performed the EL-EQE measurements. S.J. conducted the UV and differential scanning calorimetry measurements. Y.J. and H.W.C. carried out PL and TRPL measurements. C.Y. and M.J. wrote the manuscript and all authors reviewed the manuscript. **Competing interests:** The authors declare no competing interests. **Data and materials availability:** All data are available in the manuscript or the supplementary materials.

SUPPLEMENTARY MATERIALS

science.sciencemag.org/content/369/6511/1615/suppl/DC1
Materials and Methods
Supplementary Text
Figs. S1 to S24
Tables S1 to S10
References (48–57)

13 March 2020; resubmitted 12 May 2020

Accepted 6 August 2020

10.1126/science.abb7167

OCEAN TEMPERATURE

High-impact marine heatwaves attributable to human-induced global warming

Charlotte Laufkötter^{1,2*}, Jakob Zscheischler^{1,2}, Thomas L. Frölicher^{1,2}

Marine heatwaves (MHWs)—periods of extremely high ocean temperatures in specific regions—have occurred in all of Earth's ocean basins over the past two decades, with severe negative impacts on marine organisms and ecosystems. However, for most individual MHWs, it is unclear to what extent they have been altered by human-induced climate change. We show that the occurrence probabilities of the duration, intensity, and cumulative intensity of most documented, large, and impactful MHWs have increased more than 20-fold as a result of anthropogenic climate change. MHWs that occurred only once every hundreds to thousands of years in the preindustrial climate are projected to become decadal to centennial events under 1.5°C warming conditions and annual to decadal events under 3°C warming conditions. Thus, ambitious climate targets are indispensable to reduce the risks of substantial MHW impacts.

A notable number of record-breaking marine heatwaves (MHWs) (1–3) have occurred in the past decades worldwide, including the Northeast Pacific 2013 to 2015 MHW (4); the Northwest Atlantic 2012 MHW (5); and extreme temperatures in the Tasman Sea (6), the Indonesian-Australian Basin (7), and the Southern Ocean (8) in 2015 and 2016. Recently, a large heatwave emerged in the Northeast Pacific, which raised concerns that an event similar to the Northeast Pacific 2013 to 2015 MHW will reappear (9).

The evolving literature on the impacts of MHWs (10) indicates serious consequences for marine life. Recent MHWs have caused entire ecosystems to restructure, have led to major socioeconomic impacts, and have disrupted ecosystem services (1, 10). As an example, the Northeast Pacific 2013 to 2015 MHW (often referred to as the blob) has caused increased mortality of sea birds, salmon, and marine mammals (11); very low ocean primary productivity (12); harmful algal blooms (13); and large alterations to open-ocean and coastal ecosystems (11, 14). Recent heatwaves in tropical and subtropical waters have caused substantial coral bleaching (15), defoliation of sea grass (16), and decreases in kelp biomass (1). Further impacts include alterations in biodiversity patterns of sessile invertebrates and demersal fish, shifts in community structure, and poleward shifts in tropical fish communities. Beyond their impacts on marine ecosystems, MHWs have led to the closure of fisheries (17) and have caused locally-large carbon outgassing events (16). Furthermore, substantial decreases in sea ice have been linked to individual MHWs (18).

Understanding whether and by how much anthropogenic climate change has contributed to the intensity and likelihood of extreme events is of substantial scientific and public interest—for example, to motivate efforts to limit global warming. Atmospheric heatwaves, droughts, and floods are routinely attributed to climate change (18, 19); however, there have been only a few attempts to attribute MHWs to climate change (6, 20–25). These publications have differed strongly in their methodologies, in their framings of the attribution question, and in their treatments of the uncertainties of the attribution process, which makes their results difficult to compare and interpret (18, 26). The link between anthropogenic climate change and the occurrence probability of individual MHWs is therefore currently not well understood.

Here, we first present an overview of all large MHWs that have occurred during the satellite era (September 1981 to December 2017). We then focus on all large, recent MHWs that have had a substantial, documented impact on marine ecosystems or ecosystem services. For each of those large MHWs, we quantify the contribution of anthropogenic climate change to their respective occurrence probability using a consistent attribution framework. To this end, we first compute the duration, intensity, and cumulative intensity (the area-weighted sum of all daily temperature exceedances) of each of these MHWs on the basis of satellite observations of sea surface temperature (SST). We have chosen these metrics because they are linked to the impact on marine organisms. Both the duration and the cumulative intensity of MHWs affect the ability of marine organisms to cope with heat stress (1, 15), and exceeding a certain temperature threshold—no matter for how long (27)—can be highly deleterious for some organisms.

For each MHW, we then separately estimate the probabilities that an MHW has occurred

that equals or exceeds the duration, intensity, and cumulative intensity of the observed MHW in preindustrial and present-day model simulations. These probabilities are denoted by $P_{\text{present-day}}^{\text{duration}}$, $P_{\text{present-day}}^{\text{intensity}}$, $P_{\text{present-day}}^{\text{cumulativeintensity}}$, $P_{\text{preindustrial}}^{\text{duration}}$, $P_{\text{preindustrial}}^{\text{intensity}}$, and $P_{\text{preindustrial}}^{\text{cumulativeintensity}}$, respectively.

Here, we explicitly take changes in the frequency of heatwaves as well as changes in the duration, intensity, or cumulative intensity of heatwaves into account (see materials and methods). Our approach builds on the work of Stott *et al.* (28) and Oliver *et al.* (6) but with several modifications. In contrast to most previous attribution studies, we specifically calculate the occurrence probabilities of heatwaves as opposed to the probabilities of extreme seasonal mean temperatures, which allows us to attribute heatwave duration, heatwave intensity, and cumulative intensity. Furthermore, building on recent methodological advances (25, 29), we use a rigorous model preselection, whereby we only allow models in the attribution analysis in which we find no statistical evidence that the simulated heatwave distributions are different from those in the observational record. Finally, we provide confidence intervals and quantify the uncertainty that stems from preindustrial temperature reconstructions to assess the robustness of our attribution statements.

Using the occurrence probabilities, we then calculate the fraction of attributable risk (FAR) (18, 28) for duration as

$$\text{FAR} = 1 - \frac{P_{\text{preindustrial}}^{\text{duration}}}{P_{\text{present-day}}^{\text{duration}}}$$

and analogously for intensity and cumulative intensity. Positive FAR values indicate a higher likelihood that the respective extreme event is the result of human influences. For example, at FAR > 0.5, the likelihood of an event occurring now is at least twice as that of its occurring under preindustrial conditions. At FAR > 0.8, it is at least five times likelier.

From September 1981 to December 2017, >30,000 distinct, spatiotemporally contiguous MHWs have occurred globally (with temperatures above the 99.5th percentile; see materials and methods for the MHW definition). The majority (90%) of these MHWs lasted <14 days and covered <0.2 million km². However, the 300 largest MHWs (with the highest cumulative intensities) covered, on average, 1.5 million km², lasted 40 days (Fig. 1A), had a peak temperature anomaly (Fig. 1C) of 5.0°C above climatology (see materials and methods), and had a cumulative intensity of 11,900°C days km² (Fig. 1E). The frequency, duration, intensity, and cumulative intensity of large MHWs increased during the observational period (Fig. 1, A, C, and E). In the first

¹Climate and Environmental Physics, Physics Institute, University of Bern, 3012 Bern, Switzerland. ²Oeschger Centre for Climate Change Research, University of Bern, 3012 Bern, Switzerland.

*Corresponding author. Email: laufkoetter@climate.unibe.ch

decade of the satellite record, 27 large MHWs occurred with an average duration of 32 days, an average peak temperature anomaly of 4.8°C, and an average cumulative intensity of 11,000°C days km². By contrast, 172 large MHWs occurred in the past decade, with an average duration of 48 days, an average peak temperature anomaly of 5.5°C, and an average cumulative intensity of 14,000°C days km².

For most of these large MHWs, little is known about their individual environmental consequences. In this study, we focus on all recent, large MHWs that have had a major documented impact in the region in which they occurred (10) and that have extended across at least 1 million km²—seven MHWs in total (Fig. 1, B, D, and F; and Table 1). These seven heatwaves (Table 1) include the North-

east Pacific 2013 to 2015 MHW, which is the largest and longest heatwave that occurred between 1981 to 2017 and had major ecological consequences (11, 12); the Northwest Atlantic 2012 heatwave that had substantial ramifications for fisheries (17); large heatwaves around Australia, which caused long-lasting, major losses in corals, kelp, and sea grass meadows (1, 30, 31); the Southwest

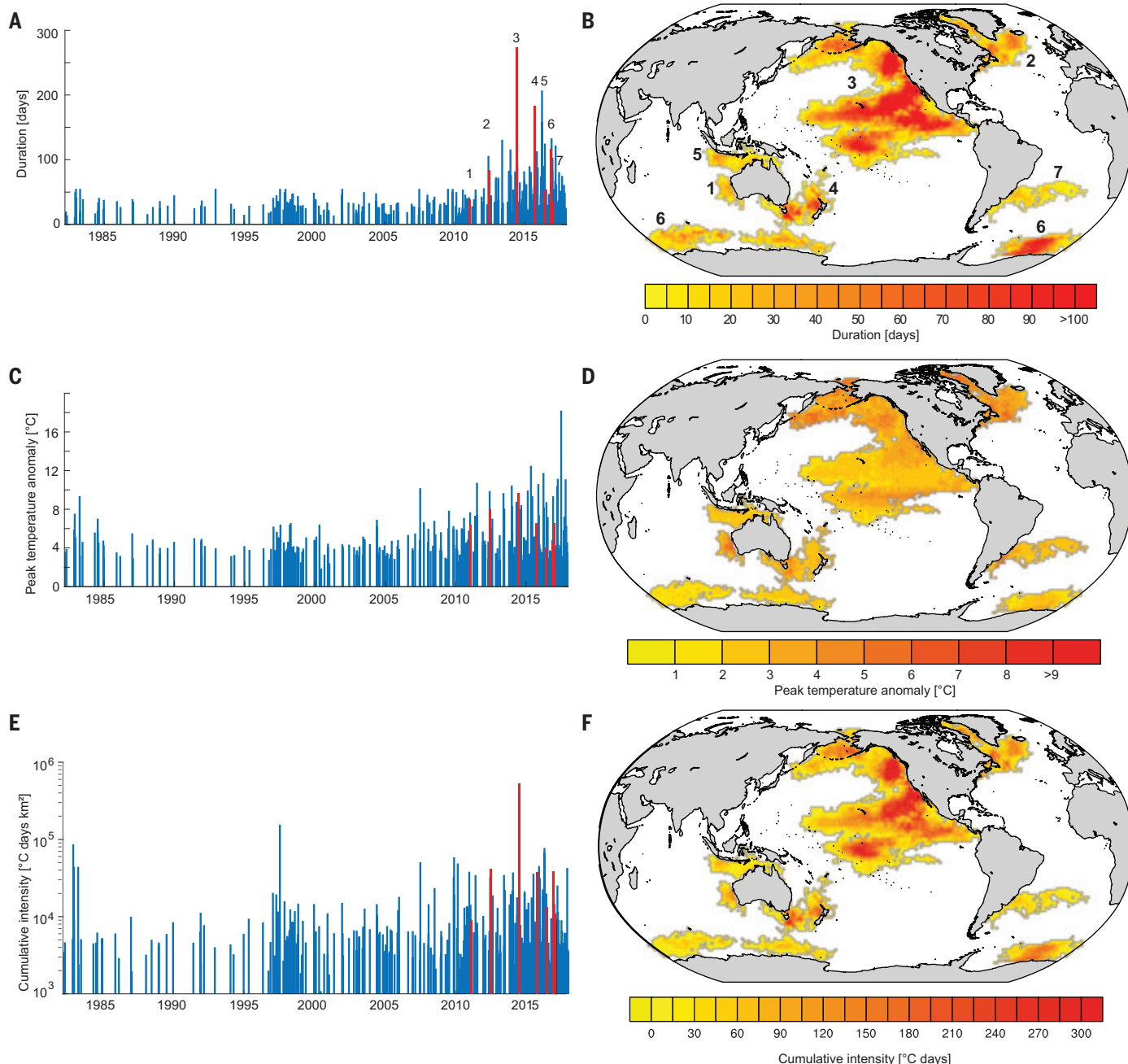
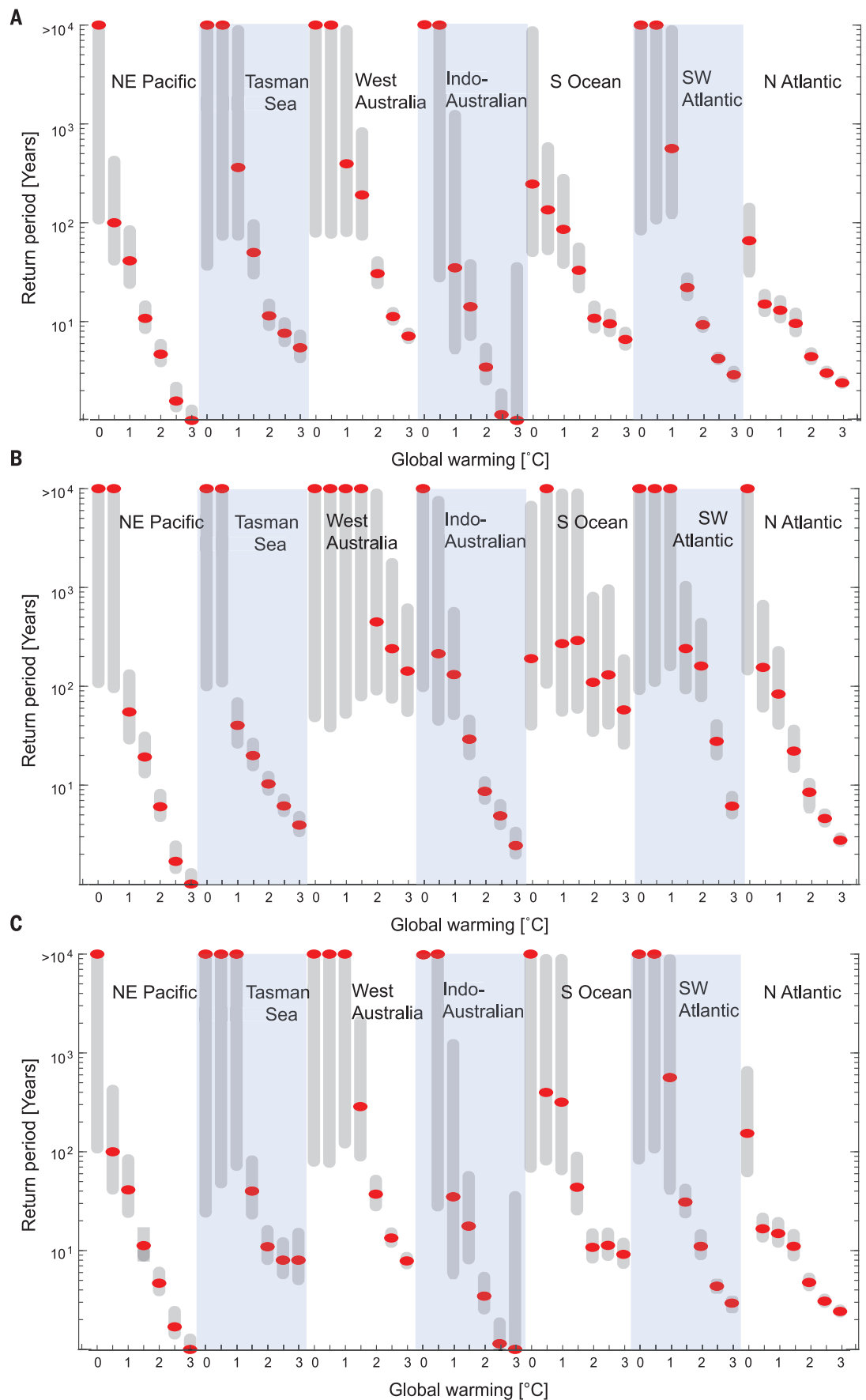


Fig. 1. Characteristics of MHWs during 1981 to 2017. (A, C, and E) Duration (A), peak temperature anomaly (C), and cumulative intensity (E) of the 300 largest heatwaves that occurred globally between September 1981 and December 2017. Each bar represents a spatiotemporal heatwave, which is defined as a spatiotemporally contiguous area where each grid cell exhibits daily temperature anomalies above the 99.5th percentile (materials and methods). The bars corresponding to the numbered heatwaves on the maps are marked in red. (B, D, and F) The maps show the duration (B), peak temperature anomaly (D), and the cumulative intensity (F) of the seven prominent recent heatwaves that are analyzed in this study.

Fig. 2. Projected changes in return periods of the seven attributed prominent MHWs under different global warming levels. (A to C) Point estimates (red dots) and 95% confidence intervals (gray bars) of the return periods of MHWs as long as observed (A), as intense as observed (B), or exhibiting as much cumulative intensity as observed (C) under different levels of global warming. The return periods are calculated by inverting the probability of heatwave occurrence (materials and methods).



Atlantic 2017 MHW, which caused fish mass mortalities (32); and the Southern Ocean 2016 MHW, which has been linked to strong decreases in sea ice (8).

With the exception of the Southwest Atlantic 2017 MHW, all analyzed MHWs have been the longest and most intense MHWs in their respective regions within satellite temperature recording (fig. S1). This raises the question of whether their occurrence has been influenced by anthropogenic climate change. By calculating the FAR, we determine to what extent the occurrence probability of heatwaves equaling or exceeding the observed duration, intensity, and cumulative intensity has already been affected by anthropogenic climate change.

The FAR of MHW intensity is generally very high, with point estimates between 0.97 and 1.0 for all but one of the MHWs that could be attributed and with narrow confidence intervals for most of the heatwaves (Table 1). These high FAR values indicate a more than 20-fold increase in occurrence probability of similarly warm MHWs caused by anthropogenic climate change. Additionally, according to our results, it is very unlikely that the MHWs could have reached the high temperatures that were measured without the influence of climate change. The only exceptions are the Western Australian 2011 MHW, which we could not attribute (materials and methods), and the Southern Ocean 2016, which has a FAR close to zero, indicating little change in occurrence probability as a result of climate change.

FAR values of heatwave duration are likewise very high. The point estimates are above 0.79 for five of the six heatwaves that could be attributed (Table 1). Exceptions are the Indo-Australian 2016 MHW, for which we could not

attribute the duration (materials and methods), and the Southern Ocean 2016 MHW, where we found a decreased occurrence probability in the present-day climate. In the Southern Ocean, several models simulate only a modest warming or even decreases in SST over the historical period. Additionally, many models show a reduction of interannual variability there (figs. S2 to S8). The lack of surface ocean warming in the Southern Ocean reflects large-scale, interhemispheric asymmetries in the mean ocean circulation. The Southern Ocean circulation is dominated by strong upwelling, which nearly anchors SST at preindustrial levels under transient global warming (33). However, simulating SST in the Southern Ocean is challenging for models, as the processes leading to the formation of sea ice and the formation of deep-water masses are currently not well represented, which decreases model fidelity in this highly dynamic region (34, 35).

FAR values of cumulative intensity are >0.96 for three of the four heatwaves that could be attributed (Table 1). Again, the only exception is the Southern Ocean, where we find a negative FAR value—that is, a lower occurrence probability in the present-day climate. Overall, our results clearly demonstrate that anthropogenic climate change has already had a substantial impact on the probability of individual MHW occurrences in terms of intensity, duration, and cumulative intensity.

To illustrate the effect of future climate change on the occurrence of the seven large MHWs, we calculated return periods for different levels of global warming (Fig. 2). For MHWs equaling or exceeding the duration, intensity, or cumulative intensity of the observed ones, return periods sharply decrease under global warming. MHWs were extremely

rare events during preindustrial times, with expected return periods of hundreds to thousands of years for North Atlantic MHWs and >10,000 years for all other MHWs in terms of their intensity, duration, and cumulative intensity.

Under the condition of 1.5°C of global warming, the return periods of all MHWs are reduced to ten to hundreds of years, with the exception of heatwaves that are as intense as the Western Australian MHW and the Southern Ocean MHW, which have slightly higher return periods. Under the condition of 3°C of warming, the return periods of all MHWs are only 1 to 10 years—again with the exception of the intensity of the Western Australian MHW and the Southern Ocean MHW, which have slightly higher return periods.

The intensity of the Southern Ocean MHW has a longer return period at 0.5°C of warming compared with preindustrial conditions. This is explained by high preindustrial temperature variability in many models and a modest warming in the present day (fig. S7). At higher levels of warming, the return periods shorten in the Southern Ocean as well, reaching return periods of <10 years for both heatwave duration and cumulative intensity at 3°C of warming. In a 3°C-warmer world, the regions in which the Northeast Pacific, the Southwest Atlantic, and the Indo-Australian Basin MHWs occurred all reach SSTs above the preindustrial 99th temperature percentile for >97% of the data, which means that they are essentially in a continuous, extreme heatwave state. Limiting global warming to 1.5° or 2°C will temporarily relieve these regions from heat pressure, such that expected return periods between 5 and 20 years (for heatwave duration, intensity, and cumulative intensity) might leave some limited time for recovery.

Table 1. Attribution of duration, intensity, and cumulative intensity of seven MHWs to anthropogenic climate change. In contrast to the three-dimensional heatwave definition used in Fig. 1, the heatwaves are defined here on one-dimensional time series, which represent regional averages across the areas where the respective heatwaves occurred (materials and methods). Duration denotes the number of consecutive

days above the 99th percentile, heatwave intensity is the average temperature anomaly above the baseline climatology in degrees Celsius, and cumulative intensity is the sum of all temperature anomalies over the duration of the heatwave. We present the point estimate for the attributable risk (FAR) and the 95% confidence interval in brackets. Heatwaves that we cannot attribute are denoted with a dash (materials and methods).

Heatwave number	Time and location	Intensity (°C)	FAR intensity	Duration (days)	FAR duration	Cumulative intensity (°C days 1000 km ²)	FAR cumulative intensity
1	Western Australian 2011	2.26	–	101	0.79 [–0.55, 0.97]	9	–
2	Northwest Atlantic 2012	2.15	0.97 [0.92, 0.99]	57	0.96 [0.94, 0.97]	41	0.96 [0.94, 0.98]
3	Northeast Pacific 2013 to 2015	1.56	1.0 [0.97, 1.0]	357	1.0 [0.99, 1.0]	530	1.0 [0.99, 1.0]
4	Tasman Sea 2015 and 2016	1.49	0.98 [0.92, 0.99]	175	1.0 [0.49, 1.0]	37	–
5	Indo-Australian Basin 2016	1.67	1.0 [0.77, 1.0]	90	–	13	–
6	Southern Ocean 2016*	1.0	0.03 [–2.71, 0.74]	183	–0.6 [–2.6, 0.26]	47	–6.5 [–42.26, –0.34]
7	Southwest Atlantic 2017	1.96	1.0 [0.74, 1.0]	82	1.0 [0.91, 1.0]	11	1.0 [0.87, 1.0]

*Represents two spatially distinct heatwaves that occurred simultaneously in different parts of the Southern Ocean.

The return periods calculated here are based on transient warming estimates under the Representative Concentration Pathway 8.5 (RCP8.5) high-emissions scenario. We obtain similar results when using the RCP2.6 scenario (fig. S10). However, we caution that the return periods for individual MHWs under stabilized 1.5° or 2°C warming levels might be different from those under transient warming levels because the climate system is closer to equilibrium and the ocean has had more time to take up heat and redistribute it within the ocean (36).

Both the FAR values and the estimated return periods are sensitive to several factors, including the framing of the attribution question, model evaluation and preselection, statistical uncertainties, uncertainties in the preindustrial SST reconstructions, and choice of the present-day time period (18, 37, 38). To increase robustness of our assessments, we performed several sensitivity tests to quantify these uncertainties.

First, we explicitly evaluate how well climate models reproduce the observed distributions of heatwave duration and intensity. We restrict our analysis to models that simulate statistically indistinguishable distributions of heatwave duration, intensity, and cumulative intensity when compared with observations. We also avoid bias adjustment to match the SST variance of the models with the variance of the satellite data (6, 24), as it is unclear whether this ensures a more realistic simulation of heatwave distribution. Notably, adjusting the variance does not necessarily improve the temporal and spatial variability in the simulated temperature data above a high percentile. However, even with our rigorous model evaluation and selection, the attribution statement depends inherently on the quality of the underlying model simulations.

Second, many studies do not quantify the goodness of the fit when estimating the occurrence probability of heatwaves. Particularly for rare, extreme events, which have very low occurrence probabilities, even small deviations in occurrence probability might strongly affect the FAR value. We address this issue by calculating 95% confidence intervals of the occurrence probability (materials and methods) to achieve more-robust attribution statements.

Third, regional disagreements between different pre-satellite era SST reconstructions might result in different MHW characteristics, which potentially might affect the FAR value. We therefore repeated our analysis using two additional SST reconstructions (tables S3 to S5) to show that, for the analyzed MHWs, the uncertainty introduced by the SST reconstruction is small for most heatwaves. The only exceptions are the duration of the NW Atlantic 2012 MHW, for which warming estimates between 0° and 0.74°C result in FAR values between 0.77 and 0.96, and the intensity of the Western Australian 2011 MHW, for which the

FAR varies between 0.47 and 0.73 under warming estimates between 0.51° and 0.77°C.

Finally, previous studies have defined different time periods as the present day, sometimes using data that reach up to 25 years into the future (22) when oceans are projected to be substantially warmer, thereby overestimating today's anthropogenic influence on heatwave occurrence risk. Here, we use the 1981 to 2017 period as the present day, which results in a conservative estimate of the present fraction of attributable risk.

Our study highlights the strong human influence on the occurrence probabilities of all recent large and severe MHWs, and it illustrates the substantially reduced return periods these extreme heat events will have under further global warming. Recent MHWs have had severe impacts on marine ecosystems, and these systems have required a long time to recover in the aftermath—if they have recovered at all (30, 31). Early warning systems such as seasonal to annual forecast systems of SST may help to reduce the risk of MHWs for ecosystems and human systems by enabling preventive measures, such as reducing fishing pressure (39). However, strongly reduced return periods of large MHWs will likely push marine organisms and ecosystems beyond their thermal limits and stress tolerance (3), potentially causing irreversible changes. Some of the most valuable and precious marine ecosystems, such as warm-water coral reefs, will likely be irretrievably lost. To maintain the existence of resilient and productive marine ecosystems and to prevent many oceanic regions from reaching a continuous, severe heatwave state, global warming needs to be severely limited.

REFERENCES AND NOTES

1. D. A. Smale et al., *Nat. Clim. Chang.* **9**, 306–312 (2019).
2. E. C. J. Oliver et al., *Nat. Commun.* **9**, 1324 (2018).
3. T. L. Frölicher, E. M. Fischer, N. Gruber, *Nature* **560**, 360–364 (2018).
4. E. Di Lorenzo, N. Mantua, *Nat. Clim. Chang.* **6**, 1042–1047 (2016).
5. K. Mills et al., *Oceanography* **26**, 191–195 (2013).
6. E. C. J. Oliver et al., *Nat. Commun.* **8**, 16101 (2017).
7. J. A. Benthuyssen, E. C. J. Oliver, M. Feng, A. G. Marshall, *J. Geophys. Res. Oceans* **123**, 1301–1326 (2018).
8. G. A. Meehl et al., *Nat. Commun.* **10**, 14 (2019).
9. D. J. Amaya, A. J. Miller, S.-P. Xie, Y. Kosaka, *Nat. Commun.* **11**, 1903 (2020).
10. M. Collins, M. Sutherland, L. Bouwer, S.-M. Cheong, T. Frölicher, H. Jacot Des Combes, M. Koll Roxy, I. Losada, K. McInnes, B. Ratter, E. Rivera-Arriaga, R. D. Susanto, D. Swingedouw, L. Tibig, in *IPCC Special Report on the Ocean and Cryosphere in a Changing Climate*, H.-O. Pörtner, D. C. Roberts, V. Masson-Delmotte, P. Zhai, M. Tignor, E. Poloczanska, K. Mintenbeck, A. Alegria, M. Nicolai, A. Okem, J. Petzold, B. Rama, N. M. Weyer, Eds. (Intergovernmental Panel on Climate Change, 2019).
11. L. Cavole et al., *Oceanography* **29**, 273–285 (2016).
12. F. A. Whitney, *Geophys. Res. Lett.* **42**, 428–431 (2015).
13. R. M. McCabe et al., *Geophys. Res. Lett.* **43**, 10366–10376 (2016).
14. W. W. L. Cheung, T. L. Frölicher, *Sci. Rep.* **10**, 6678 (2020).
15. T. P. Hughes et al., *Nature* **543**, 373–377 (2017).

16. A. Arias-Ortiz et al., *Nat. Clim. Chang.* **8**, 338–344 (2018).
17. A. J. Pershing et al., *Science* **350**, 809–812 (2015).
18. P. A. Stott et al., *WIREs Clim. Change* **7**, 23–41 (2016).
19. National Academies of Sciences, Engineering, and Medicine, *Attribution of Extreme Weather Events in the Context of Climate Change* (The National Academies Press, 2016).
20. I.-H. Park, S.-K. Min, S.-W. Yeh, E. Weller, S. T. Kim, *Environ. Res. Lett.* **12**, 044024 (2017).
21. A. D. King, D. J. Karoly, B. J. Henley, *Nat. Clim. Chang.* **7**, 412–416 (2017).
22. J. E. Walsh et al., *Bull. Am. Meteorol. Soc.* **99**, S39–S43 (2018).
23. E. Weller et al., *Bull. Am. Meteorol. Soc.* **96**, S100–S104 (2015).
24. E. C. J. Oliver, S. E. Perkins-Kirkpatrick, N. J. Holbrook, N. L. Bindoff, *Bull. Am. Meteorol. Soc.* **99**, S44–S48 (2018).
25. S. E. Perkins-Kirkpatrick et al., *Bull. Am. Meteorol. Soc.* **100**, S105–S110 (2019).
26. F. E. L. Otto, N. Massey, G. J. van Oldenborgh, R. G. Jones, M. R. Allen, *Geophys. Res. Lett.* **39**, L04702 (2012).
27. J. H. Stillman, *Physiology* **34**, 86–100 (2019).
28. P. A. Stott, D. A. Stone, M. R. Allen, *Nature* **432**, 610–614 (2004).
29. F. E. Otto et al., *Clim. Change* **149**, 399–412 (2018).
30. T. Wernberg et al., *Science* **353**, 169–172 (2016).
31. T. P. Hughes et al., *Science* **359**, 80–83 (2018).
32. G. Manta, S. de Mello, R. Trinchin, J. Badagian, M. Barreiro, *Geophys. Res. Lett.* **45**, 12,449–12,456 (2018).
33. J. Marshall, K. Speer, *Nat. Geosci.* **5**, 171–180 (2012).
34. J. Turner, T. J. Bracegirdle, T. Phillips, G. J. Marshall, J. S. Hosking, *J. Clim.* **26**, 1473–1484 (2013).
35. J. Sallée et al., *J. Geophys. Res.* **118**, 1830–1844 (2013).
36. A. D. King, T. P. Lane, B. J. Henley, J. R. Brown, *Nat. Clim. Chang.* **10**, 42–47 (2020).
37. A. Jézéquel et al., *Clim. Change* **149**, 367–383 (2018).
38. L. J. Harrington, F. E. Otto, *Environ. Res. Lett.* **13**, 123006 (2018).
39. N. Caputi et al., *Ecol. Evol.* **6**, 3583–3593 (2016).
40. C. Laufkötter, Attribution of Marine Heatwaves, OSF (2020); <http://doi.org/10.17605/OSF.IO/4HCDW>.

ACKNOWLEDGMENTS

We thank the World Climate Research Programme's Working Group on Coupled Modelling, which is responsible for the fifth phase of the Coupled Model Intercomparison Project (CMIP5), and the climate modeling groups for producing and making available their model output. COBE SST2, NOAA ERSST V5, and HadISST V1.1 data were provided by the NOAA/OAR/ESRL PSD, Boulder, Colorado, USA, from their website at www.esrl.noaa.gov/psd/. We also thank M. Schulte and P. Naveau for their very helpful advice on the theory of probabilities and general statistics and T. Stocker for feedback on the manuscript. **Funding:** C.L., T.L.F., and J.Z. acknowledge support from the Swiss National Science Foundation under grants 174124 (to C.L.), 170687 (to T.L.F.), and 179876 (to J.Z.). T.L.F. also received funding from the European Union's Horizon 2020 research and innovation program under grant agreement no. 820989 (project COMFORT, Our common future ocean in the Earth system – quantifying coupled cycles of carbon, oxygen, and nutrients for determining and achieving safe operating spaces with respect to tipping points) and computing resources from the CSCS Swiss National Supercomputing Center. **Author contributions:** C.L. and T.L.F. designed the study. All authors developed the statistical methods and analyzed the results. Calculations were made by C.L. The manuscript was written by C.L. with extensive input from T.L.F. and J.Z. **Competing interests:** The authors declare that they have no competing interests. **Data and materials availability:** The CMIP5 model data, SST satellite observations, and SST reconstructions are available online (see materials and methods for details). All other data are available in the main text or the supplementary materials. The code used to calculate the FAR values and the return periods can be found on OSF (40).

SUPPLEMENTARY MATERIALS

science.sciencemag.org/content/369/6511/1621/suppl/DC1
Materials and Methods
Supplementary Text
Figs. S1 to S11
Tables S1 to S8
References (41–51)

4 November 2019; accepted 4 August 2020
10.1126/science.aba0690

CONSCIOUSNESS

A neural correlate of sensory consciousness in a corvid bird

Andreas Nieder*, Lysann Wagener, Paul Rinnert

Subjective experiences that can be consciously accessed and reported are associated with the cerebral cortex. Whether sensory consciousness can also arise from differently organized brains that lack a layered cerebral cortex, such as the bird brain, remains unknown. We show that single-neuron responses in the pallial endbrain of crows performing a visual detection task correlate with the birds' perception about stimulus presence or absence and argue that this is an empirical marker of avian consciousness. Neuronal activity follows a temporal two-stage process in which the first activity component mainly reflects physical stimulus intensity, whereas the later component predicts the crows' perceptual reports. These results suggest that the neural foundations that allow sensory consciousness arose either before the emergence of mammals or independently in at least the avian lineage and do not necessarily require a cerebral cortex.

Sensory consciousness, the ability to have subjective experience that can be explicitly accessed and thus reported, arises from brain processes that emerged through evolutionary history (1, 2). Today, the neural correlates of consciousness are primarily associated with the workings of the primate cerebral cortex (3–6), a part of the telencephalic pallium that is laminar in organization

(7–9). Birds, by contrast, have evolved a different pallium since they diverged from the mammalian lineage 320 million years ago (10, 11). The bird pallium retains organizational principles reminiscent of the mammalian brain (12) but is distinctively nuclear and lacks a layered cerebral cortex (13–15). Despite this, birds demonstrate sophisticated perceptual and cognitive behaviors that suggest conscious experiences (16, 17).

The associative endbrain area called nidopallium caudolaterale (NCL) is linked to high-level cognition in birds (18, 19) and is considered a

putative avian analog of the mammalian prefrontal cortex (20), which plays a predominant role in sensory consciousness in primates (21–23). To signify a “neural correlate of consciousness” in primates, brain activity that systematically changes with the subject's report of whether or not it had perceived identical stimuli is identified (24, 25). We hypothesized that conscious experience originates from activity of the NCL in corvids and used a corresponding experimental protocol in which only the crows' internal state, not the physical stimulus properties, determined their subjective experience.

We trained two carrion crows (*Corvus corone*) to report the presence or absence of visual stimuli around perceptual threshold in a rule-based delayed detection task (Fig. 1A and supplementary materials and methods). At perceptual threshold, the internal state of the crows determined whether stimuli of identical intensity would be seen or not perceived. After a delay, a rule cue informed the crow about which motor action was required to report its percept. Thus, the crows could not prepare motor responses prior to the rule cues, which enabled the investigation of neuronal activity related to subjective sensory experience and its lasting accessibility.

The crows' proportion of “yes” responses in relation to increasing stimulus intensity gave rise to classical psychometric functions (Fig. 1,

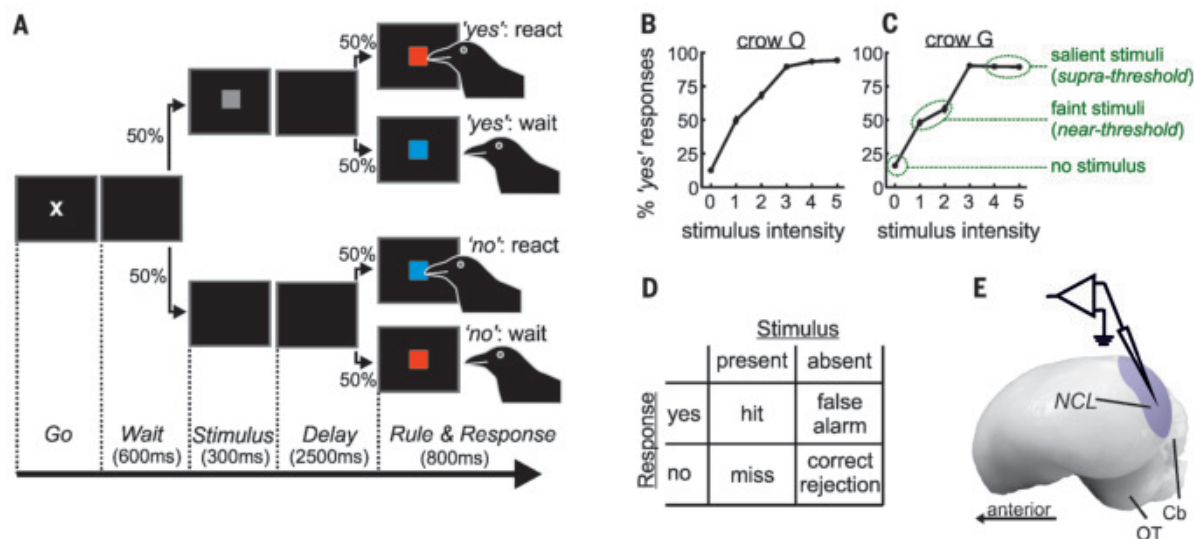


Fig. 1. Crows performed a delayed stimulus detection task. (A) Behavioral task. After the crow initiated a trial in the Go period, a brief visual stimulus of variable intensity appeared in 50% of the trials (stimulus trials), whereas no stimulus appeared in the other half of the trials (no stimulus trials). After a delay period, a rule cue informed the crow how to respond if it had seen or had not seen the stimulus. In stimulus trials (top), a red cue required a response for stimulus detection (“yes”), whereas a blue cue prohibited a response for stimulus detection. In no-stimulus trials (bottom), rule-response contingencies

were inverted. (B and C) Psychometric functions of crow O (B) and crow G (C). Grouping of trials into suprathreshold, near-threshold, and no-stimulus trials. Error bars (very small) indicate standard error of the mean. (D) Signal detection theory classifies an observer's behavior at detection threshold, given two stimulus conditions (stimulus present or absent) and two possible responses (“yes, stimulus present” and “no, stimulus absent”). (E) Lateral view of a crow brain depicting the nidopallium caudolaterale (NCL, shaded) in the telencephalon. Cb, cerebellum; OT, optic tectum.

B and C). Trials were classified into supra-threshold (the two highest stimulus intensities), near-threshold (the two lowest stimulus intensities at perceptual threshold), and no-stimulus categories (Fig. 1C). The crows' responses were classified according to signal detection theory into "hit" (correct "yes" response to a stimulus), "correct rejection" (correct "no" response for stimulus absence), "miss" (erroneous "no" response to stimulus presence), and "false alarm" (erroneous "yes" response for stimulus absence) (Fig. 1D).

While the crows performed the task, we recorded single-cell activity of 480 neurons ($n = 306$ for crow G; $n = 174$ for crow O) from the NCL (Fig. 1E and supplementary materials and methods). We first identified 262 task-selective neurons that showed differences in firing rates for suprathreshold trials versus no-stimulus trials (Mann-Whitney U test, $p < 0.01$). The selective time intervals of these neurons that together bridged the total trial period were classified into stimulus-related ($n = 155$) (Fig. 2A) and delay-related ($n = 165$) (Fig. 2B).

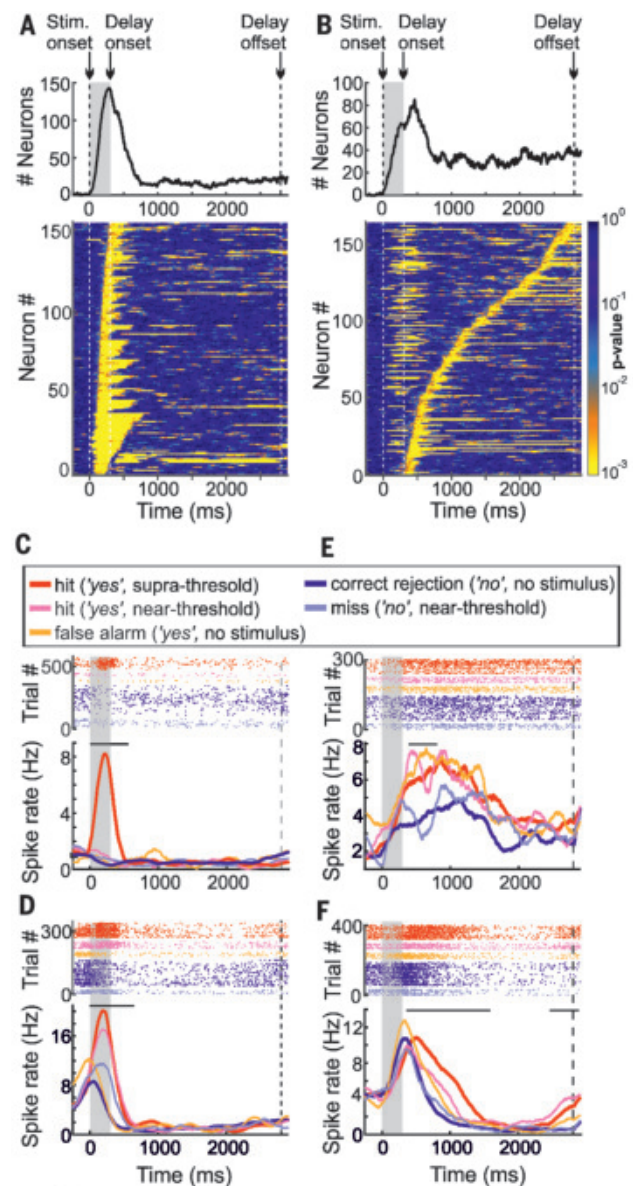
Next, we compared the discharges during the crows' "yes" versus "no" responses in the different trial categories (Fig. 1C and supplementary materials and methods). If neurons signal stimulus intensity, the responses to near-threshold stimuli should be indistinguishable irrespective of the crow's response. In addition, the responses during "false alarms" are expected to be similar to "correct rejections" in the no-stimulus condition. However, if neurons represent the crows' percept, they are expected to change activity as a function of the crows' later report. In this case, firing rates to near-threshold "no" responses should resemble those during "correct rejections" in no-stimulus trials. Likewise, discharges for near-threshold "yes" responses and "false alarms" should be more similar to those of supra-threshold "yes" responses.

During stimulus presentation, neurons responded mainly to stimulus intensity and only mildly to the crow's later reported conscious percept. The example neuron in Fig. 2C discharged exclusively to the presentation of a salient stimulus, without a correlation with the crow's "yes/no" responses. The neuron in Fig. 2D showed some correlation with the crow's later report because firing rates during near-threshold "yes" responses were similar to supra-threshold "yes" responses, whereas discharges during near-threshold "no" responses resembled "correct rejections."

During the subsequent delay period, however, many neurons responded according to the crows' impending report, rather than to stimulus intensity. The neuron in Fig. 2E showed categorically higher firing rates for all "yes" responses (suprathreshold and near-threshold "hits," as well as "false alarms" in the absence of stimuli) compared to all "no" responses ("no"

Fig. 2. Single-neuron responses in NCL. (A and B) Pattern of task selectivity for all stimulus-selective neurons during the stimulus (A) and delay period (B).

Bottom: Color-coded traces of significance values (every line represents a neuron); neurons sorted according to selectivity latency. Top: Cumulative time-resolved histogram of task-selective intervals. (C and D) Activity of two stimulus-period task-selective example neurons in relation to the crow's behavioral responses. Top panels depict dot raster histograms (every line is a trial, every dot is an action potential); bottom panels represent the corresponding averaged and smoothed spike density histograms. The vertical gray shading indicates the presentation of the stimulus (onset at 0 ms), the vertical dotted line signifies the end of the delay. The color code represents the five different trial categories, with red, orange, and pink colors representing "yes" response trials, and dark and light blue colors "no" response trials. The horizontal bars in each spike-density histogram signify the task-selective interval. (E and F) Activity of two delay-period task-selective example neurons in relation to the crow's behavioral responses. Same layout as in (C) and (D).



responses to near-threshold stimuli, "correct rejections" in the absence of stimuli) during the first half of the delay period. A similar effect can be witnessed for the neuron in Fig. 2F, which showed discharges that correlated with the report at the beginning and end of the delay period.

To find out whether the activity of the 262 task-selective neurons was related to the crows' report for the same near-threshold stimuli, we compared the firing rates in the neurons' respective selectivity intervals for different trial outcomes. We used receiver operating characteristic (ROC) analysis from signal detection theory (26) (supplementary materials and methods). We derived the area under the ROC curve (AUC), termed choice probability, as the

probability of predicting the subjective "yes/no" responses for identical stimuli for the stimulus and the delay phases separately (27).

We first compared the mean (rectified) activity during "hit" and "miss" trials for near-threshold stimuli in the stimulus presentation period. Choice probability was higher than the chance level of 0.5 (mean: 0.55; $p < 0.001$; one-sample Wilcoxon signed-rank test; $n = 155$ neurons; compared to a mean of 0.69 for supra-threshold "hits" and no-stimulus "correct rejections") (Fig. 3A). In addition, we compared the choice probability for "correct rejections" and "false alarms" during no-stimulus trials, which was comparable to chance (mean: 0.51; $p = 0.08$; one-sample Wilcoxon signed-rank test; $n = 155$ neurons) (Fig. 3B). Thus, during

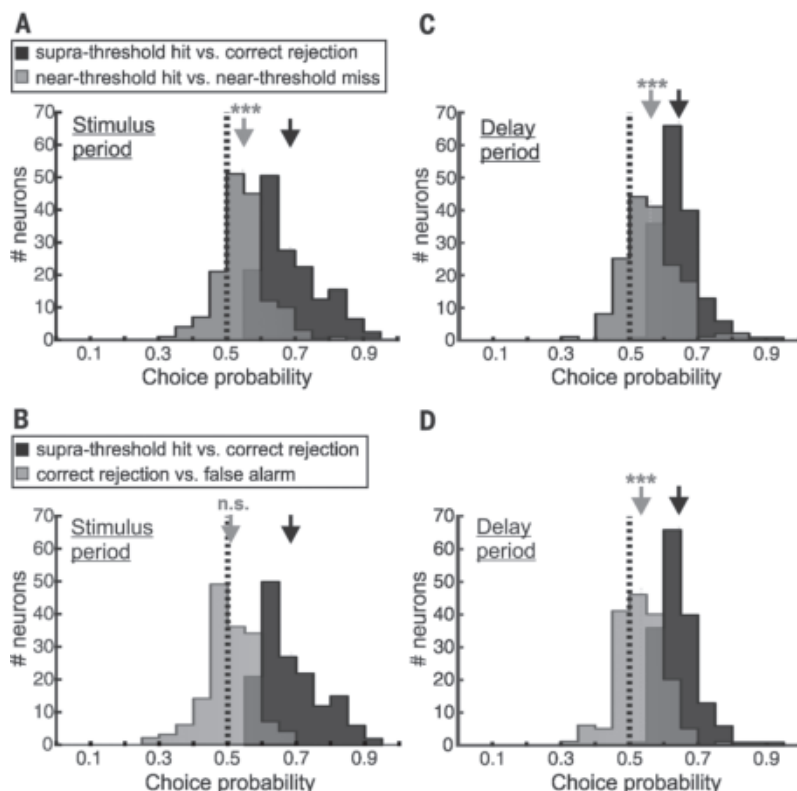


Fig. 3. Neuronal activity predicts “yes” versus “no” responses. Distribution of neuronal choice probabilities according to signal detection theory. (**A** and **B**) Choice probabilities during the stimulus period (155 neurons). (**C** and **D**) Choice probabilities during the delay period (165 neurons). Gray arrow indicates mean of choice probabilities for near-threshold hits versus near-threshold misses [(A) and (C)] and for correct rejections versus false alarms, respectively [(B) and (D)]. Choice probabilities in (A), (C), and (D) were significantly larger than chance level indicated by dotted vertical line ($***p < 0.001$; n.s., not significant). Black arrows indicate mean AUC values for suprathreshold hits versus correct rejections for comparison.

stimulus presentation, the neurons signaled the crows’ subsequent report only mildly.

However, the primarily stimulus-based activity changed to a predominantly report-driven representation during the delay. Both the choice probabilities for near-threshold “hit” and “miss” trials (mean: 0.56; Fig. 3C), as well as the choice probability for no-stimulus “correct rejections” and “false alarms” (mean: 0.53; Fig. 3D), were higher than expected by chance ($p < 0.001$ for both values; one-sample Wilcoxon signed-rank test; $n = 165$ neurons). On the background of a mean AUC of 0.64 for suprathreshold “hits” and no-stimulus “correct rejections,” both choice probabilities predicted the crows’ perceptual report rather than the physical stimulus. Notably, this effect was found not only for the very same faint stimuli, but also on “false alarm” trials, when the crows mistakenly reported perceiving a stimulus when in fact no stimulus was present. Thus, shortly after stimulus presentation, the neurons represented the crows’ later report.

To explore the time course of choice prediction from stimulus onset to delay offset irre-

spective of neuronal selectivity, we applied time-resolved population analyses based on the activity of all NCL neurons with sufficient trials per trial type ($n = 152$). We first trained a support vector machine (SVM) classifier to discriminate “yes” versus “no” responses on the basis of the spiking activity (28) (supplementary materials and methods). Cross-validation on “hits” in suprathreshold trials and “correct rejections” in no-stimulus trials indicated reliable information differentiating the crows’ alternative responses (fig. S1). To minimize the influence of stimulus intensity, we next trained the classifier with discharges exclusively from near-threshold trials in which crows subjectively made “yes” and “no” responses for identical stimulus intensities. After training, the classifier was tested with new data from the same neuronal population, but for suprathreshold “hits” versus “correct rejections” in the absence of stimuli. Indeed, the classifier was able to correctly assign the new trials into “yes” versus “no” responses, with particularly high accuracy at stimulus offset and toward the end of the delay (Fig. 4A). This indicates that

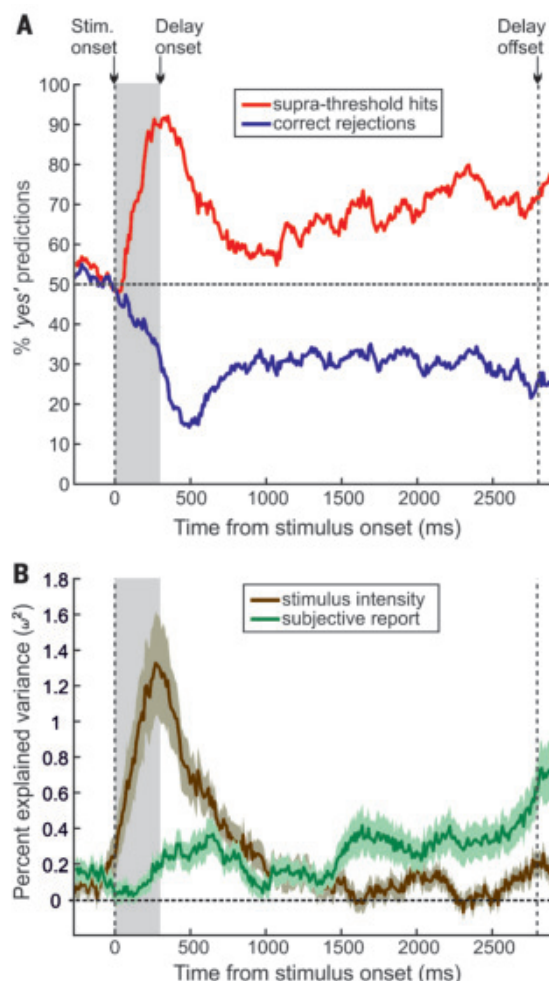
a population of neurons contained information about the crows’ subjective experience throughout the trial.

Finally, we quantified how much information about the physical stimulus and the later report was carried by the activity of the same population of NCL neurons across the trial. We calculated the percent explained variance (ω^2 , PEV) for stimulus intensity and “yes/no” response (29, 30) (supplementary materials and methods). We found that stimulus intensity information increased sharply after stimulus presentation, but then rapidly decayed and vanished during the following delay (Fig. 4B). Instead, the neurons increasingly encoded the crows’ perceptual report until it reached a peak level toward the end of the delay (Fig. 4B). A similar response pattern was found for predictions on near-threshold trials of a SVM-classifier trained on population responses of “yes” responses in suprathreshold trials (“hits”) and “no” responses in no-stimulus trials (“correct rejections”) (fig. S2). The neuronal population results suggest that NCL neurons switch from initially mainly representing stimulus intensity to predominantly encoding the crows’ subjective experience later in the trial and before a required behavioral report.

A difference between the neuronal activities of one reported perceptual state versus the other for equal visual stimuli is considered to be a “neural correlate of visual consciousness” (3, 5, 21–23). Our finding thus constitutes an empirical marker of avian sensory consciousness. As for any animal, the qualitative nature of this subjective experience—“what it is like” for a crow to be consciously aware of sensory data—remains hidden (31). Moreover, whether pure subjective experience itself (“phenomenal consciousness”) can and should be dissociated from its report (“access consciousness”) remains intensely debated (1, 32).

Our report of a two-stage process in awareness in the corvid NCL is markedly similar to findings in the primate cerebral cortex, where the initial sweep of activity is also mainly involved in unconscious vision, whereas activity correlating with consciousness is delayed relative to stimulus onset activity (21, 33–36). To explain these effects, the global neuronal workspace theory (25, 37) posits that only sensory activity that is strong enough can access awareness by causing a state termed “global ignition” in higher brain centers such as prefrontal cortex. “Ignition” causes information about a brief stimulus to become sustained and broadcasted back through recurrent interactions between many brain areas, thereby also characterizing the transition of a sensory representation into the explicit working memory state (1, 23). The NCL may very well constitute the avian brain site of an “all-or-none” ignition process that leads either to a high degree of activation causing and maintaining

Fig. 4. Time-resolved neuron population analyses. (A) A support vector machine (SVM) classifier trained on near-threshold trial activity predicts the crows' "yes" responses from suprathreshold "hit" trials and "no" responses from correct rejection no-stimulus trials. Chance level is 50%. (B) Sliding-window percent explained variance (ω^2) analysis quantifying the information about the stimulus intensity and report-associated subjective percept.



information about conscious experience across a temporal gap for a future goal, or to a vanishing response. Combining report-based behavioral protocols in crows with no-report protocols may help to disentangle the neural mechanisms involved in generating, maintaining, and reporting conscious experience (38, 39). This two-stage process in awareness could prove to be a general and evolutionarily stable principle of how sensory consciousness is achieved in vertebrates in general.

Our finding also provides evidence for the phylogenetic origins of consciousness (2). It excludes the proposition that only primates or other mammals possessing a layered cerebral cortex are endowed with sensory consciousness. To reconcile sensory consciousness in birds and mammals, one scenario would postulate that birds and mammals inherited the trait of consciousness from their last-common ancestor. If true, this would date the evolution of consciousness back to at least 320 million years when reptiles and birds on the one hand, and mammals on the other hand, evolved from the last common stem-amniotic ancestor (40).

Alternatively, consciousness emerged independently on the basis of convergent evolution on different branches of the vertebrate "tree of life." According to this hypothesis, consciousness was absent in the common stem-amniotic ancestor, but—comparable to homeothermy—evolved later and independently during the rise of, at least, birds and mammals. Yet another scenario would predict a gradual emergence of consciousness. Here, different degrees of conserved pallial connectivity patterns in vertebrates could give rise to aspects of sensory consciousness across phylogeny. Combining measurements of brain signals with controlled behavioral protocols will help to delineate the origins of conscious experience in the animal kingdom.

REFERENCES AND NOTES

- G. A. Mashour, P. Roelfsema, J. P. Changeux, S. Dehaene, *Neuron* **105**, 776–798 (2020).
- D. B. Edelman, A. K. Seth, *Trends Neurosci.* **32**, 476–484 (2009).
- D. A. Leopold, N. K. Logothetis, *Nature* **379**, 549–553 (1996).
- G. Kreiman, I. Fried, C. Koch, *Proc. Natl. Acad. Sci. U.S.A.* **99**, 8378–8383 (2002).

- V. de Lafuente, R. Romo, *Nat. Neurosci.* **8**, 1698–1703 (2005).
- C. Koch, M. Massimini, M. Boly, G. Tononi, *Nat. Rev. Neurosci.* **17**, 307–321 (2016).
- L. Puelles et al., *J. Comp. Neurol.* **424**, 409–438 (2000).
- E. D. Jarvis et al., *Nat. Rev. Neurosci.* **6**, 151–159 (2005).
- L. Puelles, *Int. J. Dev. Biol.* **62**, 207–224 (2018).
- S. Kumar, S. B. Hedges, *Nature* **392**, 917–920 (1998).
- S. B. Hedges, *Nat. Rev. Genet.* **3**, 838–849 (2002).
- M. Shanahan, V. P. Bingman, T. Shimizu, M. Wild, O. Güntürkün, *Front. Comput. Neurosci.* **7**, 89 (2013).
- H. J. Karten, *Philos. Trans. R. Soc. Lond. B Biol. Sci.* **370**, 20150060 (2015).
- J. Dugas-Ford, C. W. Ragsdale, *Annu. Rev. Neurosci.* **38**, 351–368 (2015).
- S. Olkowitz et al., *Proc. Natl. Acad. Sci. U.S.A.* **113**, 7255–7260 (2016).
- N. J. Emery, N. S. Clayton, *Science* **306**, 1903–1907 (2004).
- A. Nieder, *Curr. Opin. Behav. Sci.* **16**, 8–14 (2017).
- L. Veit, A. Nieder, *Nat. Commun.* **4**, 2878 (2013).
- H. M. Ditz, A. Nieder, *Nat. Commun.* **11**, 686 (2020).
- O. Güntürkün, *Curr. Opin. Neurobiol.* **15**, 686–693 (2005).
- V. de Lafuente, R. Romo, *Proc. Natl. Acad. Sci. U.S.A.* **103**, 14266–14271 (2006).
- T. I. Panagiotaropoulos, G. Deco, V. Kapoor, N. K. Logothetis, *Neuron* **74**, 924–935 (2012).
- B. van Vugt et al., *Science* **360**, 537–542 (2018).
- V. A. Lamme, *Trends Cogn. Sci.* **10**, 494–501 (2006).
- S. Dehaene, J. P. Changeux, *Neuron* **70**, 200–227 (2011).
- D. M. Green, J. A. Swets, *Signal Detection Theory and Psychophysics* (Wiley, 1966).
- K. H. Britten, W. T. Newsome, M. N. Shadlen, S. Celebrini, J. A. Movshon, *Vis. Neurosci.* **13**, 87–100 (1996).
- C.-C. Chang, C.-J. Lin, *ACM Trans. Intell. Syst. Technol.* **2**, 1–27 (2011).
- M. R. Warden, E. K. Miller, *Cereb. Cortex* **17** (suppl. 1), i41–i50 (2007).
- S. N. Jacob, A. Nieder, *Neuron* **83**, 226–237 (2014).
- T. Nagel, *Philos. Rev.* **83**, 435–456 (1974).
- N. Block, *Trends Cogn. Sci.* **9**, 46–52 (2005).
- H. Supér, H. Spekreijse, V. A. Lamme, *Nat. Neurosci.* **4**, 304–310 (2001).
- R. Q. Quiroga, R. Mukamel, E. A. Isham, R. Malach, I. Fried, *Proc. Natl. Acad. Sci. U.S.A.* **105**, 3599–3604 (2008).
- K. G. Thompson, J. D. Schall, *Nat. Neurosci.* **2**, 283–288 (1999).
- V. A. Lamme, P. R. Roelfsema, *Trends Neurosci.* **23**, 571–579 (2000).
- B. J. Baars, *Trends Cogn. Sci.* **6**, 47–52 (2002).
- N. Tsuchiya, S. Frässle, M. Wilke, V. Lamme, *Trends Cogn. Sci.* **20**, 242–243 (2016).
- N. Block, *Trends Cogn. Sci.* **23**, 1003–1013 (2019).
- P. Arhem, B. I. B. Lindahl, P. R. Manger, A. B. Butler, in *Consciousness Transitions: Phylogenetic, Ontogenetic, and Physiological Aspects*, H. Liljenstrom, P. Arhem, Eds. (Elsevier, 2008), pp. 77–96.

ACKNOWLEDGMENTS

We thank D. Liao for reading an earlier version of the manuscript.

Funding: This work was supported by a DFG grant NI 618/6-1 to A.N. **Author contributions:** A.N., L.W., and P.R. designed the experiment. A.N. and L.W. conducted the experiments. L.W., P.R., and A.N. analyzed the data. A.N., L.W., and P.R. wrote the paper. A.N. supervised the study. **Competing interests:** The authors declare no competing financial interests. **Data and materials availability:** All data necessary to assess the conclusions of this study are available in the main text or the supplementary materials. All behavioral and electrophysiological data are archived at the Institute of Neurobiology, University of Tübingen, Germany.

SUPPLEMENTARY MATERIALS

science.sciencemag.org/content/369/6511/1626/suppl/DC1
Materials and Methods
Figs. S1 and S2

3 February 2020; accepted 27 July 2020
10.1126/science.abb1447

SPECTROSCOPY

Photon-recoil imaging: Expanding the view of nonlinear x-ray physics

U. Eichmann^{1*}, H. Rottke¹, S. Meise¹, J.-E. Rubensson², J. Söderström², M. Agåker^{2,3}, C. Sätthé³, M. Meyer⁴, T. M. Baumann⁴, R. Boll⁴, A. De Fanis⁴, P. Grychtol⁴, M. Ilchen^{4,5}, T. Mazza⁴, J. Montano⁴, V. Music^{4,5}, Y. Ovcharenko⁴, D. E. Rivas⁴, S. Serkez⁴, R. Wagner⁴, S. Eisebitt^{1,6}

Addressing the ultrafast coherent evolution of electronic wave functions has long been a goal of nonlinear x-ray physics. A first step toward this goal is the investigation of stimulated x-ray Raman scattering (SXRS) using intense pulses from an x-ray free-electron laser. Earlier SXRS experiments relied on signal amplification during pulse propagation through dense resonant media. By contrast, our method reveals the fundamental process in which photons from the primary radiation source directly interact with a single atom. We introduce an experimental protocol in which scattered neutral atoms rather than scattered photons are detected. We present SXRS measurements at the neon K edge and a quantitative theoretical analysis. The method should become a powerful tool in the exploration of nonlinear x-ray physics.

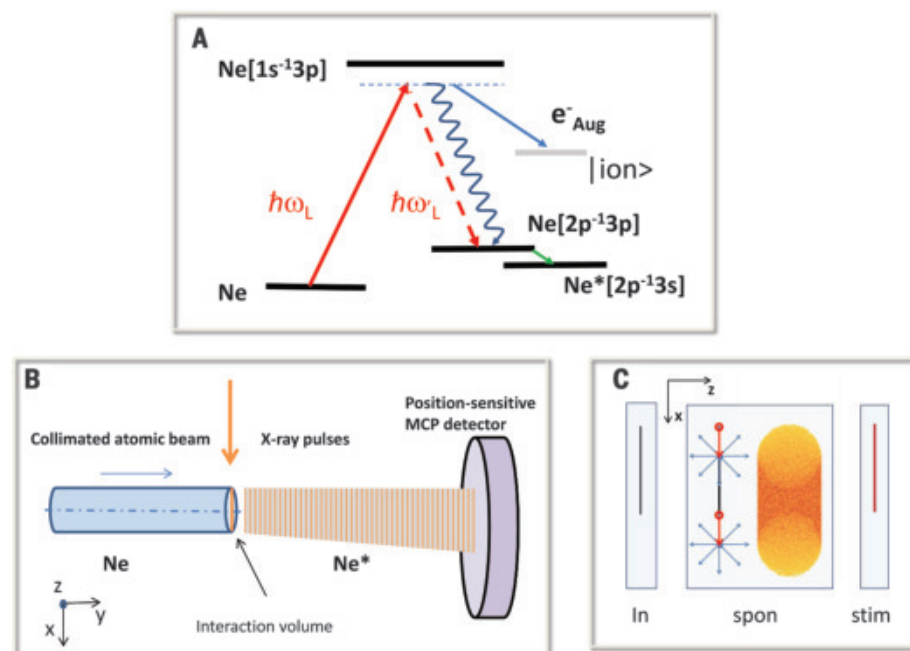
Our awareness of nonlinear processes has changed the way we think about the interaction between light and matter, and has inspired the development of numerous optical techniques (1–3). Among the most fundamental and practically important applications of these processes is the control and manipulation of quantum dynamics in atoms and molecules by short and intense laser pulses. Typically, such experiments involve a combination of light pulses that couple to the coherent wave function dynamics of the investigated system (e.g., in the stimulated Raman adiabatic passage technique) (4). This type of experiment has

been crucial in the progress of quantum engineering of chemistry and quantum matter (5). It has been a long-standing vision to extend the concepts from the optical into the x-ray regime; combining the merits of laser and x-ray spectroscopy would enable entry into the world of nonlinear x-ray physics (6), where local quasi-atomic core levels give access to interactions on atomic length and time scales. This goal has been one of the motivations for developing x-ray free-electron lasers (XFELs), and indeed these facilities now provide pulse intensities sufficient for investigation of nonlinear x-ray physics (6–11).

Stimulated x-ray emission has been observed in dense gases (12, 13), in liquids (14), and in solids (15, 16), and considerable effort has gone into the development of stimulated x-ray Raman scattering (SXRS), which is the basic building block of nonlinear x-ray spectroscopy (13, 17). SXRS was first observed (18) by direct analysis of the scattered photons in an x-ray spectrometer, exploiting the amplification of the XFEL pulses in a dense medium. Although such x-ray lasing effects highlight pulse propagation in media and are of great importance in nonlinear x-ray optics, their modeling introduces uncertainties that impede investigation of the quantum dynamics in single atoms or molecules.

For dilute samples, direct measurement of SXRS is hampered by a background attributable to the primary photons, which almost coincide with the scattered photons in momentum space. We introduce photon-recoil imaging (PRI), which monitors the momentum transfer from the photons to the atoms by the deflection of their path in a supersonic beam. The low momentum transfer in SXRS is used to discriminate against spontaneous x-ray Raman scattering, in which the momentum transfer is much larger. PRI also discriminates

Fig. 1. Scheme and experimental setup of the Ne* recoil measurement to detect stimulated x-ray Raman scattering. (A) Excitation and decay pathways in x-ray scattering in the vicinity of the inner-shell $1s \rightarrow 3p$ transition. $\text{Ne}[2p^{-1}3p]$ is populated by spontaneous Raman scattering (solid red arrow plus blue wiggly line) and by stimulated Raman scattering via two photons from the XFEL with photon energies $\hbar\omega_L$ and $\hbar\omega_L$ (solid and dashed red arrows). The transiently excited resonance decays predominantly nonradiatively by emitting an Auger electron e^-_{Aug} (solid blue arrow). Detectable long-lived metastable $\text{Ne}^*[2p^{-1}3s]$ atoms are formed by spontaneous decay of the $\text{Ne}[2p^{-1}3p]$ state on a nanosecond time scale (green arrow). (B) Experimental setup to detect metastable Ne^* atoms and their deflection with a position-sensitive MCP detector. (C) Possible projections of deflected atoms from the interaction volume on the detector. Left: Projection of the mere interaction volume (black line). Center: Ne^* pattern after spontaneous Raman scattering (right side). Scheme of Ne^* deflection: Absorption of an XFEL photon causes photon momentum in the forward direction (red arrows), followed by isotropic momentum transfer after spontaneous x-ray photon emission (blue arrows). Right: Ne^* pattern after stimulated Raman scattering is a mere projection of the interaction volume (red line).



¹Max Born Institute, 12489 Berlin, Germany. ²Department of Physics and Astronomy, Uppsala University, SE-751 20 Uppsala, Sweden. ³MAX IV Laboratory, Lund University, SE-221 00 Lund, Sweden. ⁴European XFEL, 22869 Schenefeld, Germany. ⁵Institut für Physik, University of Kassel, 34132 Kassel, Germany. ⁶Institut für Optik und Atomare Physik, Technische Universität Berlin, 10623 Berlin, Germany. *Corresponding author. Email: eichmann@mbi-berlin.de

against abundant charged particles, which is crucial because competing processes such as multiphoton ionization populate highly charged ions at these pulse energies. Whereas the well-established cold target recoil-ion momentum spectroscopy (COLTRIMS)/reaction microscope technique monitors recoil momentum of charged particles in photoionization or fragmentation processes (19–21), PRI focuses on neutral species.

The experiment was performed at the Small Quantum Systems (SQS) instrument at the SASE3 undulator beam line of the European XFEL (22, 23). We used the core resonances of neon as a showcase to demonstrate that PRI indeed can be used to monitor SXRS on the single-atom level and showed that the results are quantitatively described within the framework of the density matrix formalism using realistically simulated XFEL pulses. In PRI, a position-sensitive microchannel plate (MCP) detector is placed downstream of a collimated pulsed atomic beam (Fig. 1B). In an interaction region where a photon beam crosses this atomic beam, energy and momentum are transferred to the atoms in a scattering process. The detector is sensitive to atoms with internal energy only, and the momentum transfer is reflected in the deflection of the atomic path (24, 25).

In a simplifying two-step picture, an x-ray photon excited the Ne atom in the vicinity of the $1s \rightarrow 3p$ inner-shell resonance at a photon energy of $\hbar\omega_L = 867.3$ eV (26) (Fig. 1A). The lifetime of this state is ~ 2.5 fs (26), the decay being dominated by Auger transitions. About 2% of the excited atoms decayed radiatively, predominantly by the $2p \rightarrow 1s$ transition at ~ 849 eV (18, 27). This process left the Ne atom in bound $[2p^{-1}3p]_J$ states with excitation energies of ~ 18.5 eV (28). These states to a large extent decayed to metastable $\text{Ne}^* [2p^{-1}3s]_{J=2}$ on the nanosecond time scale, long after the interaction with the XFEL pulse. Although the latter step was irrelevant for the SXRS process, it was essential for the measurement method because metastable Ne^* atoms were detected in the downstream MCP detector (24, 29, 30).

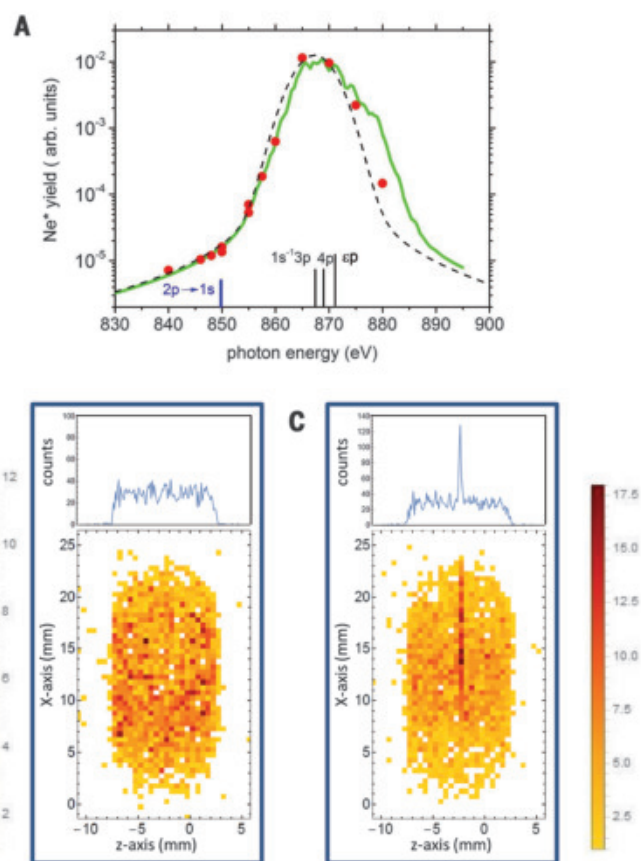
If atoms were excited without momentum transfer, they would continue toward the detector with their original velocity, and the interaction region where the atom and photon beams cross would be directly imaged on the detector. Because the photon beam was narrow relative to the atomic beam, it was expected that a line appeared, with length and thickness corresponding to the cross sections of the atom and photon beams, respectively (Fig. 1C). The atom did, however, acquire momentum in the scattering process. In the first absorption step, this momentum transfer corresponded to a recoil velocity of ~ 14 m s $^{-1}$ along the direction perpendicular to its original velocity. In our case, this fact led to a

Fig. 2. Total and position-resolved Ne^* yields after interaction of Ne atoms with XFEL radiation. (A) Scan of the incident XFEL photon energy in the vicinity of the Ne $1s \rightarrow 3p$ transition. Red points: Measured Ne^* yield produced via spontaneous Raman scattering; the statistical error bars of the data points are within the point size. Dashed black curve: Simulated Ne^* yield via spontaneous Raman scattering using a Gaussian XFEL pulse with a bandwidth of 8 eV full width half maximum (23) convolved with the natural Lorentzian line shape of the resonance. Green curve: Result of a density matrix calculation averaged over 30 theoretically derived chirped XFEL pulses. Blue bar: Energy of the $2p \rightarrow 1s$ transition used in the calculation; Black bars: $1s \rightarrow 3p$ and $4p$ transition energies and the ionization limit ϵ_p .

(B) Distribution of Ne^* atoms deflected as a result of momentum transfer in the spontaneous x-ray Raman scattering at an incident photon energy of 860 eV. The upper panel displays the projection of the Ne^* yield onto the z axis. (C) Same as (B), but recorded at 855 eV incident photon energy. Additionally, a narrow stripe of enhanced Ne^* yield appears, which has its origin in the recoilless stimulated Raman scattering as explained in the text and in Fig. 1. The projection in the upper panel clearly shows a peak due to the stimulated x-ray Raman scattering.

clearly visible displacement of ~ 5 mm on the detector. Because spontaneous emission in the second step of the process was quasi-isotropic, a randomly oriented recoil of similar magnitude as in the first step resulted in a large spread (Fig. 1C) of velocities, and consequently the momentum transfer in the spontaneous scattering process was expected to give a shifted and blurred image of the interaction region. Maintaining the simplifying two-step picture of the SXRS process, the second step of the scattering process was now due to stimulated emission. In this case the emitted photon had almost the same momentum as the photon absorbed in the first step, and a clear image of the interaction region was retrieved.

In Fig. 2A, the total number of detected metastable Ne^* atoms is plotted on a logarithmic scale over more than three orders of magnitude as a function of the photon energy. Note that metastable Ne^* atoms were observed at incident photon energies down



to 840 eV (i.e., as far as 28 eV below the $1s \rightarrow 3p$ resonance). In Fig. 2B, the detector image resulting from excitation at 860 eV is shown. A broad distribution, as expected from a spontaneous scattering process, is observed. When the incident energy was centered at 855 eV (Fig. 2C), close to the energy for $2p \rightarrow 1s$ transition, an additional sharp line appeared, which indeed corresponded to a sharp image of the interaction region. As described above, this observation is precisely what was expected for the SXRS process. The additional sharp line was visible for incident photon energies in the range between 845 and 857.5 eV (see also Fig. S3).

We carried out a rigorous theoretical treatment of the process within the density matrix formalism using simulated XFEL pulses (23). In Fig. 3A, we show the results for the yield of metastable Ne^* atoms produced by the spontaneous Raman scattering ($\text{Ne}^*_{\text{spont}}$) and by SXRS ($\text{Ne}^*_{\text{stim}}$). The $\text{Ne}^*_{\text{spont}}$ yield (black curve) displayed the resonance and compared well

Fig. 3. Comparison of calculated populations of excited Ne* atoms after spontaneous and stimulated Raman scattering with experimental results as a function of the incident x-ray photon energy.

(A) The calculated population of Ne* atoms by spontaneous (black curve) and stimulated (blue curve) Raman scattering. The curves have been multiplied by a single common factor to match (fit by eye) the experimental data for the yield of spontaneously populated Ne* atoms (red points). (B) The ratio $\text{Ne}^*_{\text{stim}}/\text{Ne}^*_{\text{spon}}$ from theoretical data (small red squares) compared with the ratio $\text{Ne}^*_{\text{spon}}/\text{Ne}^*_{\text{stim}}$ (blue points) determined from the experimental yields. Error bars denote SD.

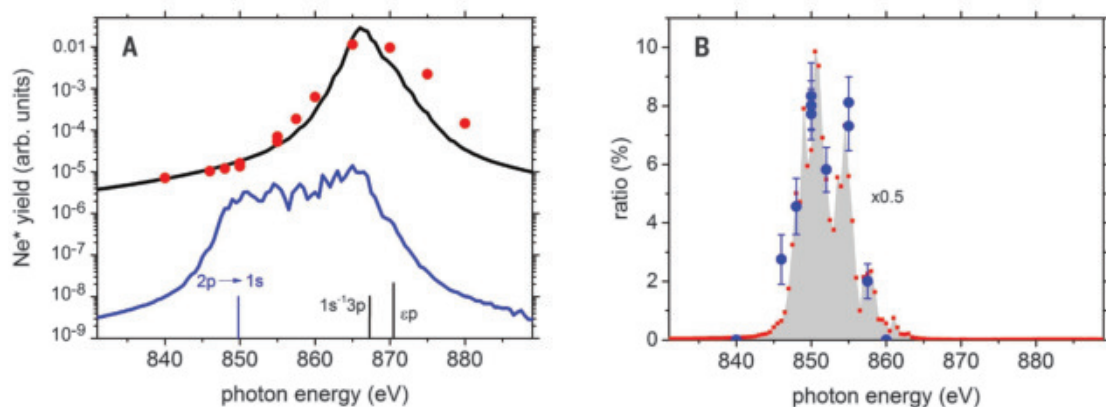
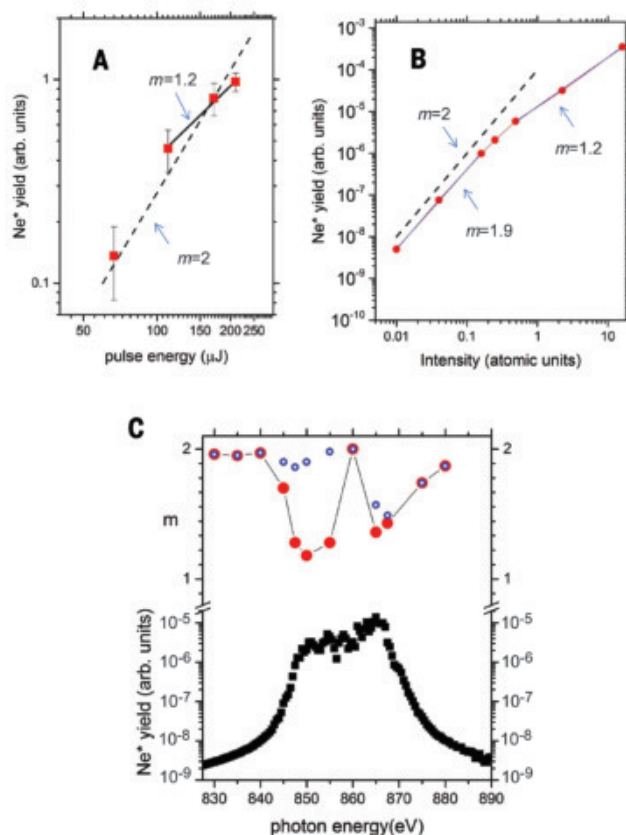


Fig. 4. Measured and calculated dependence of the $\text{Ne}^*_{\text{stim}}$ yield on the XFEL pulse energy.

(A) $\text{Ne}^*_{\text{stim}}$ yield (counts in the narrow stripe shown in Fig. 2C) as a function of the XFEL pulse energy (intensity) measured at an incident photon energy of 850 eV. The dashed curve represents a yield proportional to the square of the XFEL pulse energy, also displayed in (B). The solid black curve is a weighted fit to the upper three data points. Error bars denote SD. (B) Calculated $\text{Ne}^*_{\text{stim}}$ yield as a function of the XFEL intensity using unchirped pulses at an incident photon energy of 850 eV. (C) Calculated $\text{Ne}^*_{\text{stim}}$ (black squares) yield, displayed using unchirped XFEL pulses (same as shown in Fig. 3A) together with the exponent m of the power law I^m characterizing the intensity dependence of the $\text{Ne}^*_{\text{stim}}$ yield at intensities below $0.9 \times 10^{16} \text{ W cm}^{-2}$ (open blue circles) and above that intensity (red points).



with the experimental data of the metastable Ne^* yield. The theoretical result for the SRXS process (blue curve) shows that the yield rose sharply just below the inner-shell $2p \rightarrow 1s$ resonance at 849 eV toward higher photon energy and stayed relatively flat until it sharply declined beginning at the resonance photon energy of the $1s \rightarrow 3p$ transition. It is obvious from the data that both resonances enhanced the $\text{Ne}^*_{\text{stim}}$ yield. To see how the theoretical

SRXS data agree with the experimental data, in Fig. 3B we compare the measured $\text{Ne}^*_{\text{stim}}$ yield normalized to the $\text{Ne}^*_{\text{spon}}$ yield with the ratio determined using the data shown in Fig. 3A. We found a good overall agreement of the ratio as a function of the photon energy. With the XFEL pulse intensity used in the calculations, the deviation from the observed ratio was always smaller than a factor of 2. At photon energies below 852 eV, the $\text{Ne}^*_{\text{spon}}$ yield de-

creased slowly with lower incident photon energy so that the ratio almost directly reflected the decreasing $\text{Ne}^*_{\text{stim}}$ yield. On the other hand, when approaching the $1s \rightarrow 3p$ resonance, the $\text{Ne}^*_{\text{spon}}$ yield was orders of magnitude larger than the $\text{Ne}^*_{\text{stim}}$ yield, leaving the ratio close to zero.

We further explored the stimulated x-ray Raman scattering by investigating the $\text{Ne}^*_{\text{stim}}$ yield as a function of the intensity of the XFEL pulses. In Fig. 4A, we show a measurement of the $\text{Ne}^*_{\text{stim}}$ yield at an incident photon energy of 850 eV as a function of the XFEL pulse energy. The double logarithmic plot shows that the data points to a good approximation followed a quadratic power law I^m with $m = 2$ (dashed line). Theoretically, the $\text{Ne}^*_{\text{stim}}$ yield (Fig. 4B) followed a nearly quadratic power law at low intensities, and changed to a power law with a slope of $m = 1.2$ at higher XFEL intensities. Obviously, the inner electron transition is already close to saturation. We note that at this intensity, the Rabi oscillation frequency is on the order of the inverse lifetime of the core excited state. In Fig. 4C we show the power-law exponent across the resonance for two intensity regions. At pulse intensities well below $0.9 \times 10^{16} \text{ W cm}^{-2}$, we found an exponent of $m = 2$ over a wide range of incident photon energies, except at the $1s \rightarrow 3p$ resonance and toward higher energies. Off-resonance, we found a quadratic behavior, as expected for the SXRS process.

Our work establishes PRI as a tool for the study of nonlinear x-ray physics. In contrast to direct SXRS measurements, PRI is free from background noise caused by the primary radiation and undisturbed by modifications of the signal due to interactions and pulse propagation in dense media. In basic molecular physics, it has been a persistent objective to implement nonlinear x-ray methods (6, 7, 17) to investigate and control coherent wave function evolution and intramolecular

charge transfer. Information about the electronic-vibronic dynamics on the fastest relevant time scale is potentially of paramount importance for the fundamental understanding of chemical properties and reactions. Because PRI unambiguously monitors the dependence of SXRS on the properties of the incident radiation, the method will be particularly fruitful when intense, ultrashort, well-defined, multicolor XFEL pulses with controlled time delay (see discussion in supplementary text and figs. S7 and S8) (23) become available in the near future.

REFERENCES AND NOTES

1. R. Boyd, *Nonlinear Optics* (Elsevier, 2003).
2. S. W. Hell, J. Wichmann, *Opt. Lett.* **19**, 780–782 (1994).
3. K. Bergmann, H. Theuer, B. W. Shore, *Rev. Mod. Phys.* **70**, 1003–1025 (1998).
4. N. V. Vitanov, A. A. Rangelov, B. W. Shore, K. Bergmann, *Rev. Mod. Phys.* **89**, 015006 (2017).
5. J. L. Bohn, A. M. Rey, J. Ye, *Science* **357**, 1002–1010 (2017).
6. S. Mukamel, D. Healton, Y. Zhang, J. D. Biggs, *Annu. Rev. Phys. Chem.* **64**, 101–127 (2013).
7. S. Tanaka, S. Mukamel, *Phys. Rev. Lett.* **89**, 043001 (2002).
8. L. Young et al., *Nature* **466**, 56–61 (2010).
9. G. Doumy et al., *Phys. Rev. Lett.* **106**, 083002 (2011).
10. L. Young et al., *J. Phys. At. Mol. Opt. Phys.* **51**, 032003 (2018).
11. T. Mazza et al., *Nat. Commun.* **6**, 6799 (2015).
12. N. Rohringer et al., *Nature* **481**, 488–491 (2012).
13. V. Kimberg et al., *Faraday Discuss.* **194**, 305–324 (2016).
14. T. Kroll et al., *Phys. Rev. Lett.* **120**, 133203 (2018).
15. M. Beye et al., *Nature* **501**, 191–194 (2013).
16. H. Yoneda et al., *Nature* **524**, 446–449 (2015).
17. N. Rohringer, *Philos. Trans. R. Soc. A* **377**, 20170471 (2019).
18. C. Weninger et al., *Phys. Rev. Lett.* **111**, 233902 (2013).
19. J. Ullrich et al., *Rep. Prog. Phys.* **66**, 1463–1545 (2003).
20. A. Rudenko et al., *Phys. Rev. Lett.* **101**, 073003 (2008).
21. M. Kircher et al., *Nat. Phys.* **16**, 756–760 (2020).
22. T. Tschentscher et al., *Appl. Sci.* **7**, 592 (2017).
23. See supplementary materials.
24. U. Eichmann, T. Nubbemeyer, H. Rottke, W. Sandner, *Nature* **461**, 1261–1264 (2009).
25. U. Eichmann, A. Saenz, S. Eilzer, T. Nubbemeyer, W. Sandner, *Phys. Rev. Lett.* **110**, 203002 (2013).
26. A. Müller et al., *Astrophys. J.* **836**, 166 (2017).
27. J. Nilsen, *Matter Radiat. Extremes* **1**, 76–81 (2016).
28. A. Kramida, Yu. Ralchenko, J. Reader, NIST ASD Team, NIST Atomic Spectra Database (version 5.7.1) (NIST, 2019).
29. A. Robert et al., *Science* **292**, 461–464 (2001).
30. F. Penent et al., *Phys. Rev. Lett.* **86**, 2758–2761 (2001).
31. U. Eichmann et al., Zenodo DOI: 10.5281/zenodo.3901619 (2020).

ACKNOWLEDGMENTS

We thank European XFEL (Schenefeld, Germany) for providing x-ray free-electron laser beamtime at the SQS instrument, and we thank its staff for their assistance. **Funding:** Supported by the Volkswagen Foundation within a Peter Paul Ewald Fellowship (M.I. and V.M.) and the Swedish Science Council. **Author contributions:** U.E., S.E., H.R., and J.-E.R. proposed the study and wrote the manuscript with input from all authors. The experiment was carried out by U.E., H.R., S.M., J.-E.R., J.S., M.A., C.S., M.M., T.M.B., R.B., A.D.F., P.G., T.M., Y.O., D.E.R., and S.E. after adding the pulsed gas source and detection system by S.M., U.E., H.R., J.S., T.M., and Y.O. and additional help in preparation and commissioning of the instrument by M.I., J.M., V.M., and R.W. The data were analyzed by U.E. and H.R. with input on simulated XFEL pulses by S.S. **Competing interests:** None declared. **Data availability:** All data needed to evaluate the conclusions in the paper are in the paper or the supplementary materials, and all data underlying the figures are accessible online (31).

SUPPLEMENTARY MATERIALS

science.sciencemag.org/content/369/6511/1630/suppl/DC1
Supplementary Text
Figs. S1 to S8
References (32, 33)

15 April 2020; accepted 2 July 2020
10.1126/science.abc2622

IMMUNOMETABOLISM

Succination inactivates gasdermin D and blocks pyroptosis

Fiachra Humphries¹, Liraz Shmuel-Galia¹, Natalia Ketelut-Carneiro¹, Sheng Li², Bingwei Wang³, Venkatesh V. Nemmara⁴, Ruth Wilson¹, Zhaozhao Jiang¹, Farnaz Khalighinejad⁵, Khaja Muneeruddin^{6,7}, Scott A. Shaffer^{6,7}, Ranjan Dutta⁸, Carolina Ionete⁵, Scott Pesiridis⁹, Shuo Yang², Paul R. Thompson⁷, Katherine A. Fitzgerald^{1*}

Activated macrophages undergo a metabolic switch to aerobic glycolysis, accumulating Krebs' cycle intermediates that alter transcription of immune response genes. We extended these observations by defining fumarate as an inhibitor of pyroptotic cell death. We found that dimethyl fumarate (DMF) delivered to cells or endogenous fumarate reacts with gasdermin D (GSDMD) at critical cysteine residues to form S-(2-succinyl)-cysteine. GSDMD succination prevents its interaction with caspases, limiting its processing, oligomerization, and capacity to induce cell death. In mice, the administration of DMF protects against lipopolysaccharide shock and alleviates familial Mediterranean fever and experimental autoimmune encephalitis by targeting GSDMD. Collectively, these findings identify GSDMD as a target of fumarate and reveal a mechanism of action for fumarate-based therapeutics that include DMF, for the treatment of multiple sclerosis.

Cell death pathways are important for host defense. Necroptosis and pyroptosis also contribute to inflammatory disease through the release of danger-associated molecular patterns (DAMPs) (1). The pore-forming protein gasdermin D (GSDMD) is the executioner of pyroptosis. Caspase cleavage of GSDMD liberates an N-terminal p30 fragment (GSDMD-N), which oligomerizes and forms pores in the plasma membrane. These pores serve as a conduit for the release of interleukin-1 β (IL-1 β) and IL-18 and, ultimately, the demise of the cell (1, 2).

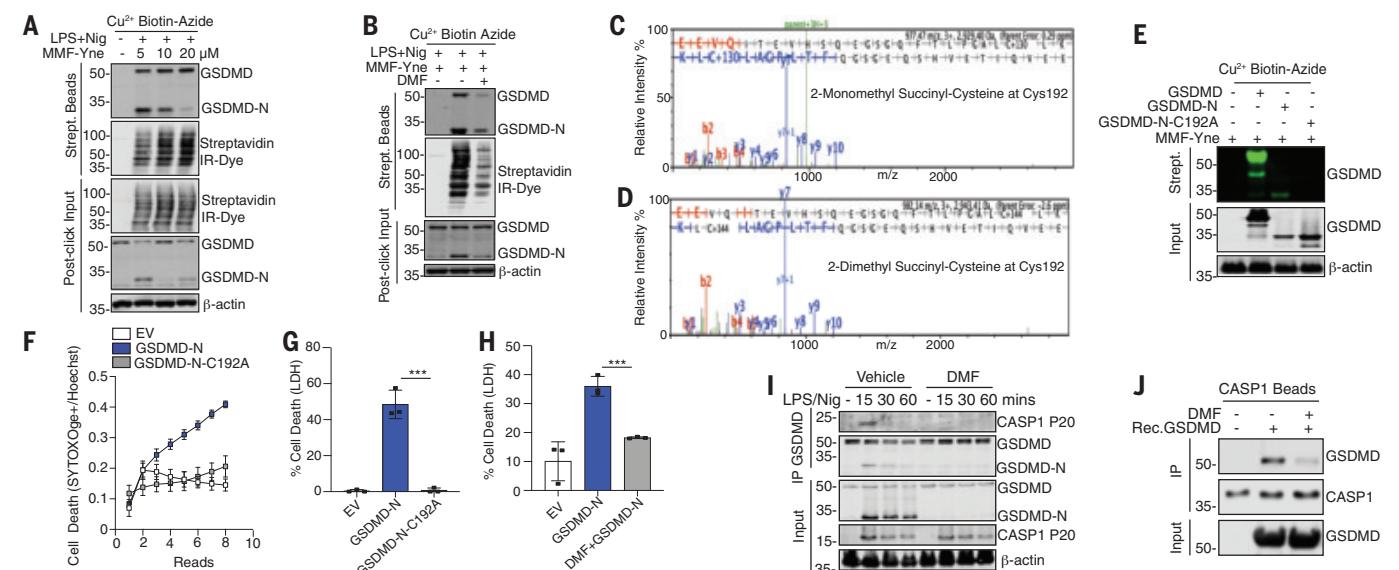
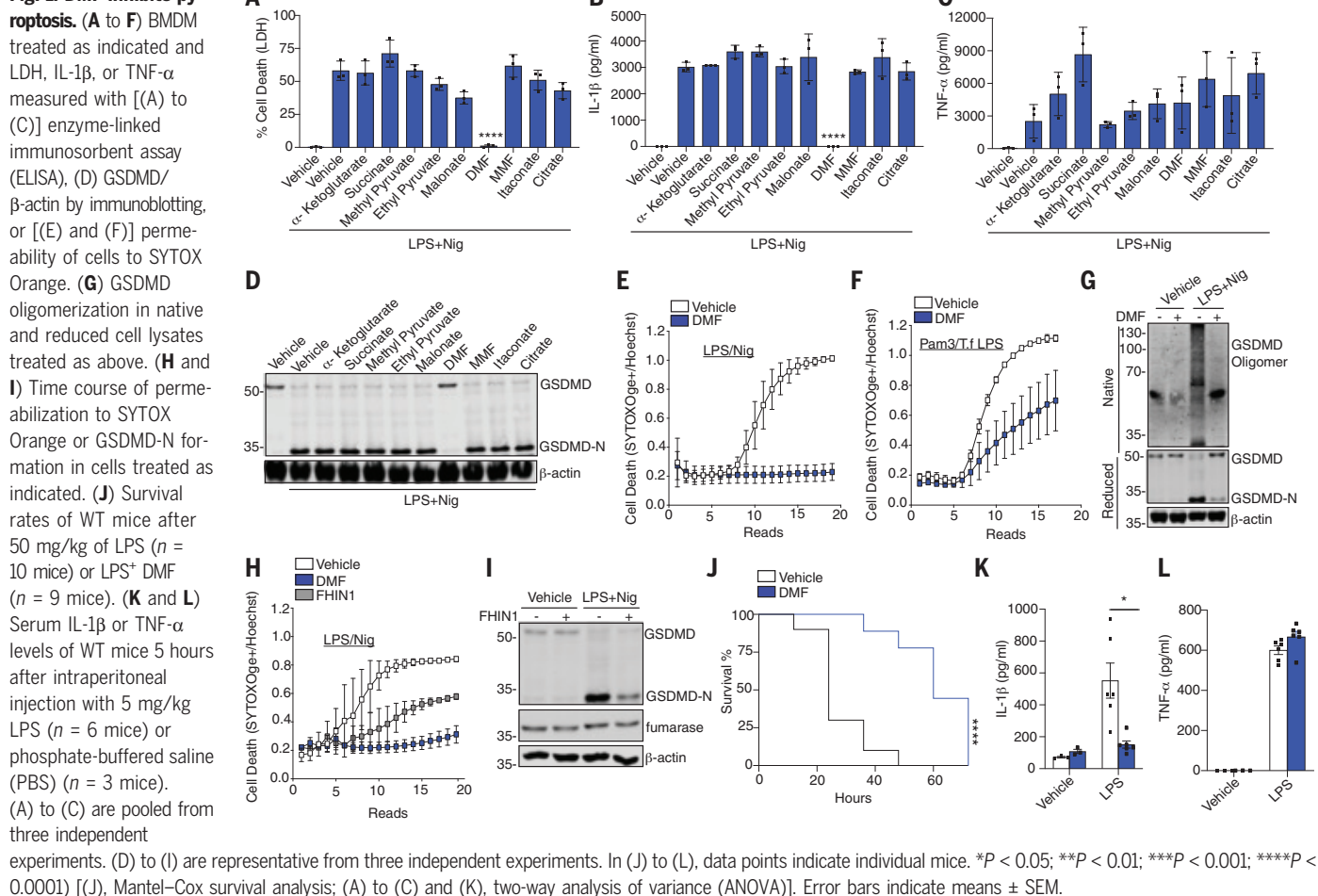
Numerous studies have shown that cell metabolism affects inflammatory responses. Lipopolysaccharide (LPS)-activated macrophages switch from oxidative phosphorylation to aerobic glycolysis. Krebs' cycle intermediates, such as succinate and itaconate, accumulate and moonlight as positive and negative regulators of inflammatory gene expression (3–8). To determine whether Krebs' cycle intermediates modulate pyroptosis, we tested their effect on inflammasome responses. Bone marrow-derived macrophages (BMDMs) were primed with LPS for 2 hours before being exposed to metabolites and then exposed to nigericin

(Nig). Inflammasome activation and pyroptosis were then measured. The metabolites were added after LPS to avoid any impact on transcription. Dimethyl fumarate (DMF) potentially blocked LPS-Nig-induced release of lactate dehydrogenase (LDH) (Fig. 1A) and IL-1 β (Fig. 1B) but not tumor necrosis factor- α (TNF- α) (Fig. 1C). DMF also blocked the formation of GSDMD-N (Fig. 1D). Monomethyl fumarate (MMF), a cell-impermeable derivative of fumarate, had no inhibitory effect. DMF impaired kinetic cell death over 6 hours (Fig. 1E and fig. S1A). DMF even impaired cell death when added after Nig treatment (fig. S1, B and C). The inhibitory effect of DMF was also observed in BMDMs after transfected LPS (Fig. 1F), Salmonella infection (fig. S1, D and E), or poly(deoxyadenylic-thymidylic) [poly(dA:dT)] (fig. S1, F and G). DMF also blocked LPS-Nig-induced cell death and LDH release in human THP1 (fig. S2, A to C) and CD14⁺ monocytes (fig. S2, D and E). BMDMs pretreated with DMF had decreased GSDMD oligomerization in response to LPS-Nig, indicating that DMF blocks pore formation (Fig. 1G).

Fumarate accumulated in LPS-activated macrophages (fig. S2F), similar to prior studies (5, 7). To assess the effect of endogenous fumarate, we induced its accumulation in cells by blocking fumarate hydratase with FH1N1 (Fig. S2F). FH1N1 impaired cell death (Fig. 1H and fig. S2G) and reduced the formation of GSDMD-N (Fig. 1I). DMF has previously been reported to exhibit antiinflammatory activity through nuclear respiratory factor 2 (NRF2) or glyceraldehyde-3-phosphate dehydrogenase (GAPDH) (9, 10). Cells treated with the GAPDH inhibitor heptilidic acid (HA) (11) or the NRF2 inhibitor ML385 (12) had no impact on cell death (fig. S3, A and B), LDH release (fig. S3C), IL-1 β release (fig. S3D), or GSDMD-N formation (fig. S3, E and F). HA and ML385 inhibited

¹Program in Innate Immunity, Department of Medicine, University of Massachusetts Medical School, Worcester, MA 01605, USA. ²Department of Immunology, Key Laboratory of Immunological Environment and Disease, State Key Laboratory of Reproductive Medicine, Nanjing Medical University, Nanjing, China. ³Department of Pharmacology, Nanjing University of Chinese Medicine, Nanjing, China. ⁴Department of Chemistry and Biochemistry, Rowan University, Glassboro, NJ 08028, USA. ⁵Department of Neurology, University of Massachusetts Medical School, Worcester, MA 01605, USA. ⁶Mass Spectrometry Facility, University of Massachusetts Medical School, Shrewsbury, MA 01545, USA. ⁷Department of Biochemistry and Molecular Pharmacology, University of Massachusetts Medical School, Worcester, MA 01605, USA. ⁸Department of Neurosciences, Lerner Research Institute, Cleveland Clinic, Case Western Reserve University, Cleveland, OH 44106, USA. ⁹Innate Immunity Research Unit, GlaxoSmithKline, Collegeville, PA 19426, USA.

*Corresponding author. Email: kate.fitzgerald@umassmed.edu

Fig. 1. DMF inhibits pyroptosis.

the GAPDH and NRF2 target genes *Nos2* and *Hmox1*, respectively (fig. S3, G to I). Suppression by means of small interfering RNA of the gene encoding NRF2 (*Nfe2l2*) also failed to affect pyroptosis (fig. S3, J and K). Thus, the regulatory effects of DMF are independent of NRF2 or GAPDH. Fumarate also suppressed pyroptosis in vivo. Wild-type (WT) mice receiving a lethal dose of LPS succumbed to LPS shock within 48 hours, whereas mice administered LPS and a single dose of DMF showed increased survival (fig. 1J). DMF reduced IL-1 β (fig. 1K) but not TNF- α levels (fig. 1L). An in vivo-compatible fumarate hydratase inhibitor, FHIN2, that elevated fumarate levels in vivo also reduced IL-1 β levels (fig. S4, A and B). Thus, fumarate inhibits pyroptosis in vivo.

We next used a chemoproteomic approach to identify targets of DMF. We synthesized monomethyl fumarate alkyne (MMF-Yne), a cell-permeable fumaric acid-alkyne (13) that mimics DMF but has an alkyne handle, for target identification (fig. S5, A and B). Like DMF, MMF-Yne inhibited LPS-Nig-induced LDH release (fig. S5C) and IL-1 β (fig. S5D). To identify MMF-Yne-bound targets, we used click chemistry (fig. S6). Immunoblotting revealed that the probe reacts with multiple proteins in pyroptotic lysates (fig. S7A). Treatment

with unlabeled DMF reduced the MMF-Yne signal (fig. S7A). Mass spectrometry identified GSDMD as a MMF-Yne target (fig. S7B). MMF-Yne dose-dependently labeled GSDMD (fig. 2A). Furthermore, DMF blocked MMF-Yne labeling of GSDMD (fig. 2B). Maximum occupancy of 1 μ M GSDMD was achieved at 25 μ M DMF (fig. S7, C to E). Thus, DMF can target GSDMD.

Fumarate derivatizes protein cysteines to generate 2-(succinyl)-cysteine, an irreversible posttranslational modification that affects protein function (9). Liquid chromatography–tandem mass spectrometry (LCMS/MS) peptide mapping experiments showed that treatment of recombinant human or mouse GSDMD with MMF led to abundant monomethyl succination (2-monomethyl succinyl-cysteine) at Cys¹⁹¹ in human and Cys¹⁹² in mouse GSDMD, respectively (fig. S8, A and C). DMF also modified (2-dimethyl succinyl-cysteine) GSDMD at the same cysteines (fig. S8, B and D). Neither of these were detected in vehicle controls. In addition to Cys¹⁹², mouse GSDMD was succinated on nine other cysteines (table S1). Human GSDMD was succinated on four additional cysteines (table S1). We also immunoprecipitated GSDMD from DMF-treated BMDMs and analyzed tryptic digests by means of MS/MS. This approach revealed a combination of 2-

monomethyl and 2-dimethyl succination of GSDMD on Cys¹⁹² (Fig. 2, C and D) as well as Cys⁵⁷ and Cys⁷⁷ (fig. S9). LPS-Nig treatment in the presence of FHIN1 also resulted in modification of GSDMD by endogenous fumarate (fig. S10, A and B). Thus, GSDMD is succinated by exogenous or endogenous fumarate.

Cys¹⁹² (Cys¹⁹¹ in humans) is critical for GSDMD-N oligomerization (14). MMF-Yne modifies full-length GSDMD and GSDMD-N but not GSDMD-N-C192A (Fig. 2E). Although GSDMD-N induced cell permeability and LDH release in human embryonic kidney (HEK) 293T cells, which is consistent with previous studies (14, 15), GSDMD-N-C192A did not (Fig. 2, F and G). DMF inhibited the GSDMD-N-induced release of LDH (Fig. 2H). Because DMF can impair both processing and activity of GSDMD, we hypothesized that succination may prevent caspase 1-GSDMD interactions. DMF completely blocked this (Fig. 2I). Processing of caspase 1 was not impaired by DMF. Succination of GSDMD in vitro also reduced its binding to caspase 1 that was immunoprecipitated from cells (Fig. 2J). Thus, DMF modifies GSDMD, blocking its processing, oligomerization, and cell death.

GSDMD is critical for pyroptosis. However, in its absence, cell death still occurs, albeit

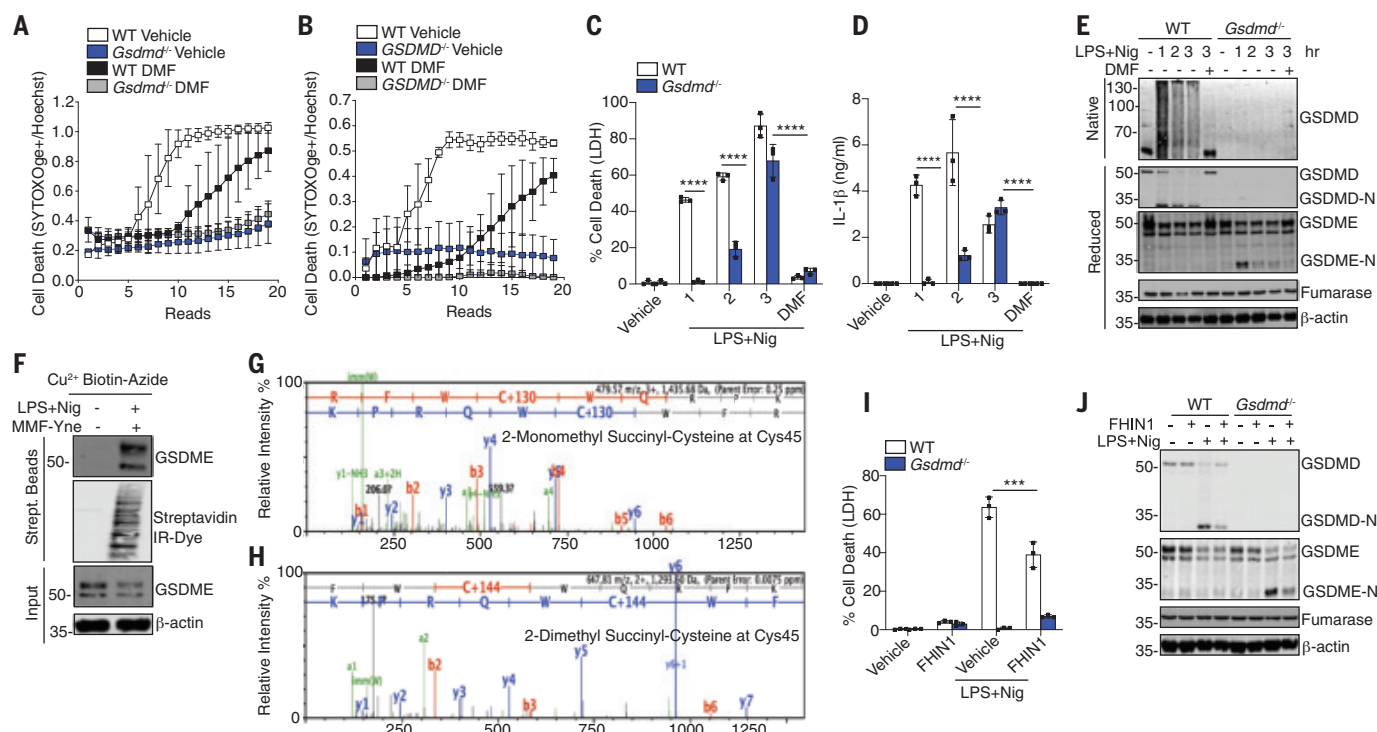


Fig. 3. DMF targets GSDMD and GSDME. (A and B) Kinetic cell death of (A) WT and *Gsdmd*^{-/-} BMDMs or (B) WT and *GSDMD*^{-/-} THP1 cells treated as indicated. (C and D) LDH and IL-1 β release from WT and *Gsdmd*^{-/-} BMDMs. (E) Immunoblot of GSDMD and GSDME in native and reduced cell lysates from BMDMs. (F) Immunoblot of GSDME in streptavidin pulldown from clicked lysates. (G and H) Representative mass spectrometry spectra of succinated

GSDME. (I) Immunoblot analysis of GSDMD and GSDME from WT and *Gsdmd*^{-/-} BMDMs. [(A) and (B)] Representative of three independent experiments. [(C), (D), and (I)] Pooled data from three independent experiments. [(E), (F), and (J)] Representative images from three independent experiments. ****P* < 0.0001, *****P* < 0.00001 (two-way ANOVA). Error bars indicate means \pm SEM.

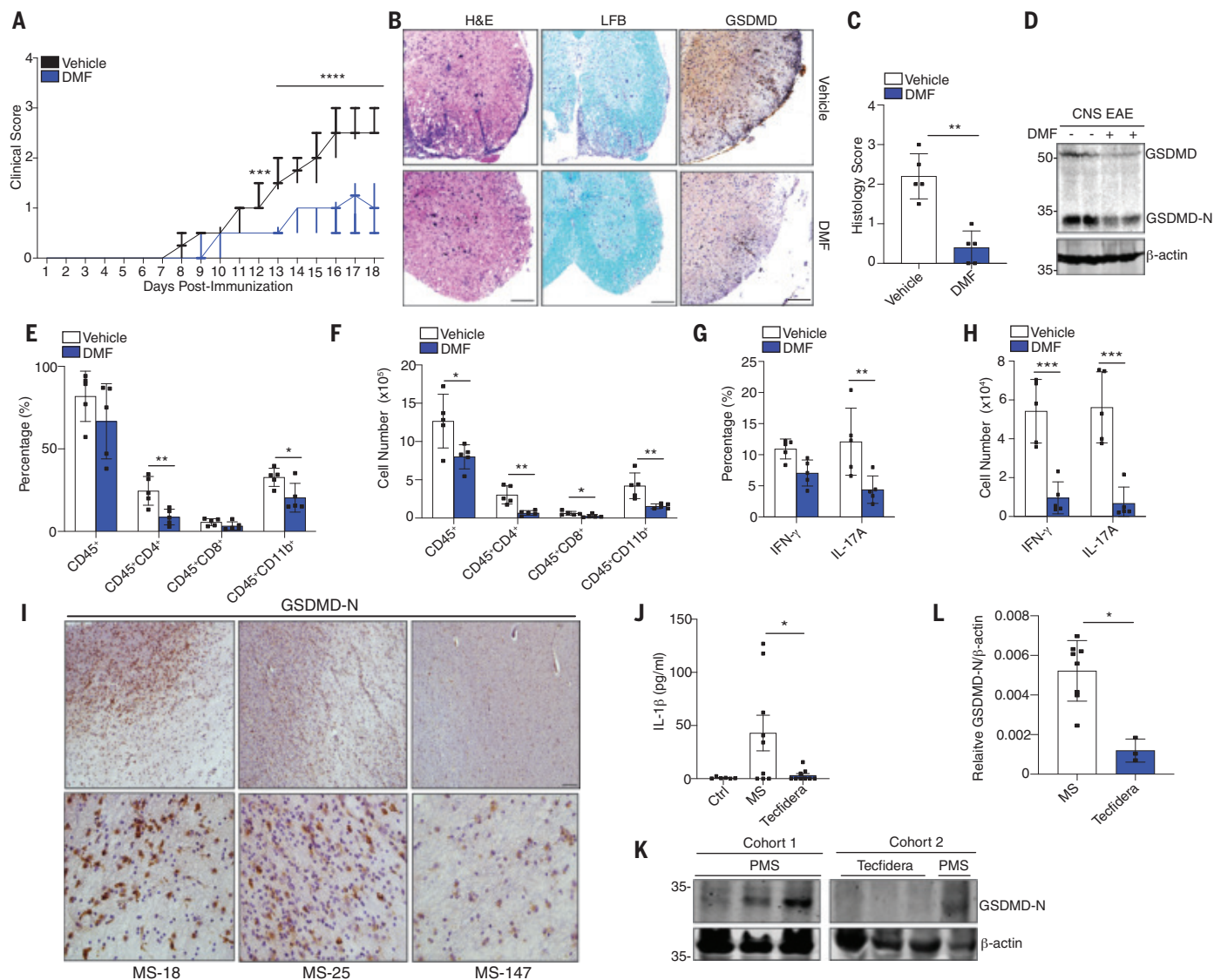


Fig. 4. Succination of GSDMD alleviates EAE and MS. (A) Clinical scores of WT mice administered vehicle or DMF daily after EAE induction, respectively ($n = 10$ mice). (B) Representative hematoxylin and eosin (H&E), Luxol fast blue (LFB), and anti-GSDMD staining and (C) pathology evaluation of spinal cord sections from mice, showing inflammatory cell infiltration and demyelination, respectively. Scale bar, 200 μ m. (D) Immunoblot of GSDMD in spinal cord tissue. (E and F) Flow cytometry analysis of CD45⁺ leukocytes, CD45⁺CD4⁺ T cells, CD45⁺CD8⁺ T cells, and CD45⁺CD11b⁺ monocytes that infiltrated the spinal cords and brains of the mice in (A) ($n = 5$ mice). (G and H) T_H1 (IFN- γ) and T_H17 (IL-17A⁺) cells from CD4⁺ T cells ($n = 5$ mice). (I) Immunohistochemistry

staining of GSDMD-N in post mortem lesions from MS patients. Scale bars, 100 μ m (top), 25 μ m (bottom). (J) IL-1 β levels in serum from healthy controls ($n = 6$ donors), MS patients (MS; $n = 9$ donors), and MS patients receiving Tecfidera delayed release capsules ($n = 9$ donors). (K) Immunoblot of GSDMD-N and (L) densitometry analysis of GSDMD-N in PBMCs from [(J) and (K)] MS ($n = 8$ donors) or PMS Tecfidera ($n = 3$ donors). [(A), (C), and (E) to (H)] Pooled data from two independent EAE experiments. * $P < 0.05$; ** $P < 0.01$; *** $P < 0.001$ [(A) and (C), Mann-Whitney U test; (E) to (H), multiple t test]. (A) Box and whisker plot. [(C), (E) to (H), (J), and (L)] Error bars indicate means \pm SEM.

with slower kinetics (2). Consistently, DMF inhibited cell death in both WT and *Gsdmd*-deficient BMDMs (Fig. 3A) and THP1 cells (Fig. 3B). DMF similarly suppressed LDH (Fig. 3C) and IL-1 β levels in both WT and *Gsdmd*-deficient BMDMs (Fig. 3D). Gasdermin E (GSDME) drives apoptosis in *Gsdmd*-deficient cells (16). GSDME processing in *Gsdmd*-deficient cells was also blocked by DMF (Fig. 3E). DMF inhibited GSDMD- and GSDME-driven cell death comparably (fig. S1L, A and B). MMF-Yne

also modifies GSDME (Fig. 3F). DMF and MMF succinated GSDME at Cys⁴⁵ (Fig. 3, G and H) and additional sites (table S1). Treatment of cells with FHIN1 attenuated GSDMD-independent (GSDME-dependent) cell death (Fig. 3I) and the generation of GSDME-N (Fig. 3J). Thus, fumarate modifies GSDMD and GSDME through succination.

GSDMD is an important driver of inflammatory diseases (17). *Gsdmd*-deficient mice are protected from experimental autoimmune en-

cephalitis (EAE) (18). Fumarate analogs such as DMF are approved by the U.S. Food and Drug Administration (FDA) for the treatment of multiple sclerosis (MS). Two newer MS drugs, diroximel fumarate and tepilamide fumarate, also blocked LPS-Nig-induced pyroptosis and GSDMD-N formation (fig. S12, A to C). DMF blocked the onset of EAE and reduced neuropathology and demyelination (Fig. 4, A to C). DMF also reduced GSDMD-N in central nervous system (CNS) tissue (Fig. 4, B and D).

GSDMD was essential for cell infiltration to the CNS during EAE. Mice receiving DMF demonstrated reduced infiltration of myeloid cells, CD4⁺ and CD8⁺ T cells (Fig. 4, E and F, and fig. S13A). DMF reduced T helper 1 (T_H1) [interferon- γ ⁺ (IFN- γ ⁺) and T_H17 (IL-17A⁺) cell numbers in the CNS (Fig. 4, G and H, and fig. S13B). Post mortem brain tissue from MS patients stained positive for GSDMD-N (Fig. 4I and table S4). Patients with MS had elevated levels of IL-1 β and GSDMD-N in peripheral blood mononuclear cells (PBMCs) (Fig. 4, J to L, and table S3). Both IL-1 β and GSDMD-N were reduced in patients taking DMF (Tecfidera) (Fig. 4, J to L, and table S3). Thus, DMF reduces GSDMD-driven responses in EAE, which supports a model in which elevated GSDMD contributes to MS. GSDMD has also been linked to familial Mediterranean fever (FMF). FMF results from constitutive activation of the pyrin inflammasome, and mice that harbor the *Mefv*^{V726/V726} allele exhibit features of the human disease. *Gsdmd*-deficient mice are rescued from disease in this model (19). Administration of DMF alleviated weight loss, splenomegaly, IL-1 β secretion, GSDMD-N formation, and liver pathology in the *Mefv*^{V726/V726} mouse model (fig. S14, A to E).

These data collectively indicate that fumara- tate mitigates pyroptosis. Succination of GSDMD on Cys¹⁹² prevents its processing and oligomerization, which limits pore formation, cytokine release, and cell death (fig. S15). Additional studies reinforce the importance of Cys¹⁹¹/Cys¹⁹² as a target of other GSDMD-targeting drugs (15, 20, 21). Our study provides mechanistic insight into the immunomodulatory activity of Tecfidera (DMF) used for MS and underscores the importance of GSDMD as a driver of chronic inflammation. This work also highlights the potential for the treatment of chronic inflammatory diseases with inhibitors of GSDMD.

REFERENCES AND NOTES

1. J. Shi et al., *Nature* **526**, 660–665 (2015).
2. N. Kayagaki et al., *Nature* **526**, 666–671 (2015).
3. E. L. Mills et al., *Nature* **556**, 113–117 (2018).
4. S.-T. Liao et al., *Nat. Commun.* **10**, 5091 (2019).
5. V. Lampropoulou et al., *Cell Metab.* **24**, 158–166 (2016).
6. M. Bambouskova et al., *Nature* **556**, 501–504 (2018).
7. G. M. Tannahill et al., *Nature* **496**, 238–242 (2013).
8. J. S. Muhammad et al., *Immunotargets Ther.* **8**, 29–41 (2019).
9. M. Blatnik, N. Frizzell, S. R. Thorpe, J. W. Baynes, *Diabetes* **57**, 41–49 (2008).
10. M. D. Kornberg et al., *Science* **360**, 449–453 (2018).
11. A. Singh et al., *ACS Chem. Biol.* **11**, 3214–3225 (2016).
12. M. Kato, K. Sakai, A. Endo, *Biochim. Biophys. Acta* **1120**, 113–116 (1992).
13. R. A. Kulkarni et al., *Nat. Chem. Biol.* **15**, 391–400 (2019).
14. X. Liu et al., *Nature* **535**, 153–158 (2016).
15. J. Hu et al., *Nat. Immunol.* **21**, 736–745 (2020).
16. C. Rogers et al., *Nat. Commun.* **10**, 1689 (2019).
17. B. A. McKenzie et al., *Proc. Natl. Acad. Sci. U.S.A.* **115**, E6065–E6074 (2018).
18. S. Li et al., *J. Exp. Med.* **216**, 2562–2581 (2019).
19. A. Kanneganti et al., *J. Exp. Med.* **215**, 1519–1529 (2018).
20. J. K. Rathkey et al., *Sci. Immunol.* **3**, eaat2738 (2018).
21. G. Sollberger et al., *Sci. Immunol.* **3**, eaar6689 (2018).

ACKNOWLEDGMENTS

Funding: This work is supported by pilot grants from the Worcester Foundation for Biomedical Research and the Dan and Diane Riccio Fund for Neuroscience from UMASS Medical School. F.H. is a GSK postdoctoral fellow. N.K.-C. is a Cancer Research Irvington Fellow, and L.S.-G. is an EMBO long-term fellow and a Crohn's and Colitis Foundation fellow. **Author contributions:** F.H. conceived the study, developed the concept, performed experiments, analyzed data, and wrote the manuscript. L.S.-G., N.K.-C., R.W., and Z.J. performed experiments and analyzed data. S.L., B.W., and S.Y. performed and analyzed EAE experiments. S.P. provided experimental advice. C.I., R.D., and F.K. provided clinical expertise and PBMCs from consenting MS patients through the University of Massachusetts MS Center biorepository. S.A.S. and K.M. designed and performed mass spectrometry experiments. V.V.M. and P.R.T. synthesized the MMF-Yne probe. K.A.F. conceived the study, developed the concept, supervised the research, and wrote the manuscript. **Competing interests:** K.A.F. serves on the scientific advisory board of Quench Bio and

NodThera. The University of Massachusetts Medical School have filed a provisional patent application on succination of GSDMD described in this study, listing F.H., P.T., and K.A.F. as inventors. **Data and materials availability:** All data in this paper are presented in the main text and supplementary materials.

SUPPLEMENTARY MATERIALS

science.sciencemag.org/content/369/6511/1633/suppl/DC1
Materials and Methods
Figs. S1 to S15
Tables S1 to S4
References (22–24)
MDAR Reproducibility Checklist
View/request a protocol for this paper from *Bio-protocol*.

31 March 2020; accepted 5 August 2020
Published online 20 August 2020
10.1126/science.abb9818

PROTEIN DESIGN

Designed protein logic to target cells with precise combinations of surface antigens

Marc J. Lajoie^{1,2,*}†, Scott E. Boyken^{1,2,*}†, Alexander I. Salter^{3,4,*}, Jilliane Bruffey^{1,2,5}, Anusha Rajan^{3,4}, Robert A. Langan^{1,2}†, Audrey Olshefsky^{1,6}, Vishaka Muhunthan^{3,4}, Matthew J. Bick^{1,2}†, Mesfin Gewe⁴, Alfredo Quijano-Rubio^{1,2,6}, JayLee Johnson¹, Garreck Lenz¹, Alisha Nguyen¹, Suzie Pun^{6,7}, Colin E. Correnti⁴, Stanley R. Riddell^{3,4,8}, David Baker^{1,2,9}†

Precise cell targeting is challenging because most mammalian cell types lack a single surface marker that distinguishes them from other cells. A solution would be to target cells using specific combinations of proteins present on their surfaces. In this study, we design colocalization-dependent protein switches (Co-LOCKR) that perform AND, OR, and NOT Boolean logic operations. These switches activate through a conformational change only when all conditions are met, generating rapid, transcription-independent responses at single-cell resolution within complex cell populations. We implement AND gates to redirect T cell specificity against tumor cells expressing two surface antigens while avoiding off-target recognition of single-antigen cells, and three-input switches that add NOT or OR logic to avoid or include cells expressing a third antigen. Thus, de novo designed proteins can perform computations on the surface of cells, integrating multiple distinct binding interactions into a single output.

Biological systems are complex; therefore, interventions that perturb these systems must achieve specific targeting in mixed populations of closely related cells. Cells displaying a specific surface marker can be targeted with antibodies, but a single marker is rarely sufficient

to identify specific cell types. Bispecific antibodies can achieve some selectivity by simultaneously engaging two targets (1, 2), but this strategy requires delicate tuning of the individual binding affinities to reduce interactions with cells expressing just one of the targets. A generalized approach for distinguishing cells using combinations of surface markers is needed. Toward this end, we sought to develop a modular protein system capable of taking multiple binding events as input, computing combinations of Boolean logic operations (AND, OR, and NOT) without requiring cellular machinery for signal integration, and producing a single output (Fig. 1A).

How does one design a system that activates only on the surface of a cell and not in solution? Given that antigen binding at the cell surface increases the local concentration of the bound protein, such a system potentially could be constructed from an actuator that

¹Institute for Protein Design, University of Washington, Seattle, WA, USA. ²Department of Biochemistry, University of Washington, Seattle, WA, USA. ³Immunotherapy Integrated Research Center, Fred Hutchinson Cancer Research Center, Seattle, WA, USA. ⁴Clinical Research Division, Fred Hutchinson Cancer Research Center, Seattle, WA, USA. ⁵Graduate Program in Molecular and Cellular Biology, University of Washington, Seattle, WA, USA. ⁶Department of Bioengineering, University of Washington, Seattle, WA, USA. ⁷Molecular Engineering and Sciences Institute, University of Washington, Seattle, WA, USA. ⁸Department of Medicine, University of Washington School of Medicine, Seattle, WA, USA. ⁹Howard Hughes Medical Institute, University of Washington, Seattle, WA, USA.

*These authors contributed equally to this work.

†Corresponding author. Email: mlajoie@lyell.com (M.J.L.); dabaker@uw.edu (D.B.) ‡Present address: Lyell Immunopharma, Inc., Seattle, WA, USA.

responds to proximity. To be generally useful, the actuation must be modular and independent of target antigen identity. We began from de novo designed protein switches that activate in solution: latching orthogonal cage-

key protein (LOCKR) (3) switches consist of a structural “cage” protein that uses a “latch” domain to sequester a functional peptide in an inactive conformation until binding of a separate “key” protein induces a conforma-

tional change that enables binding to an effector protein. Cage, key, and effector bind in a three-way equilibrium, and the sensitivity of the switch can be tuned by adjusting the relative cage-latch and cage-key affinities.

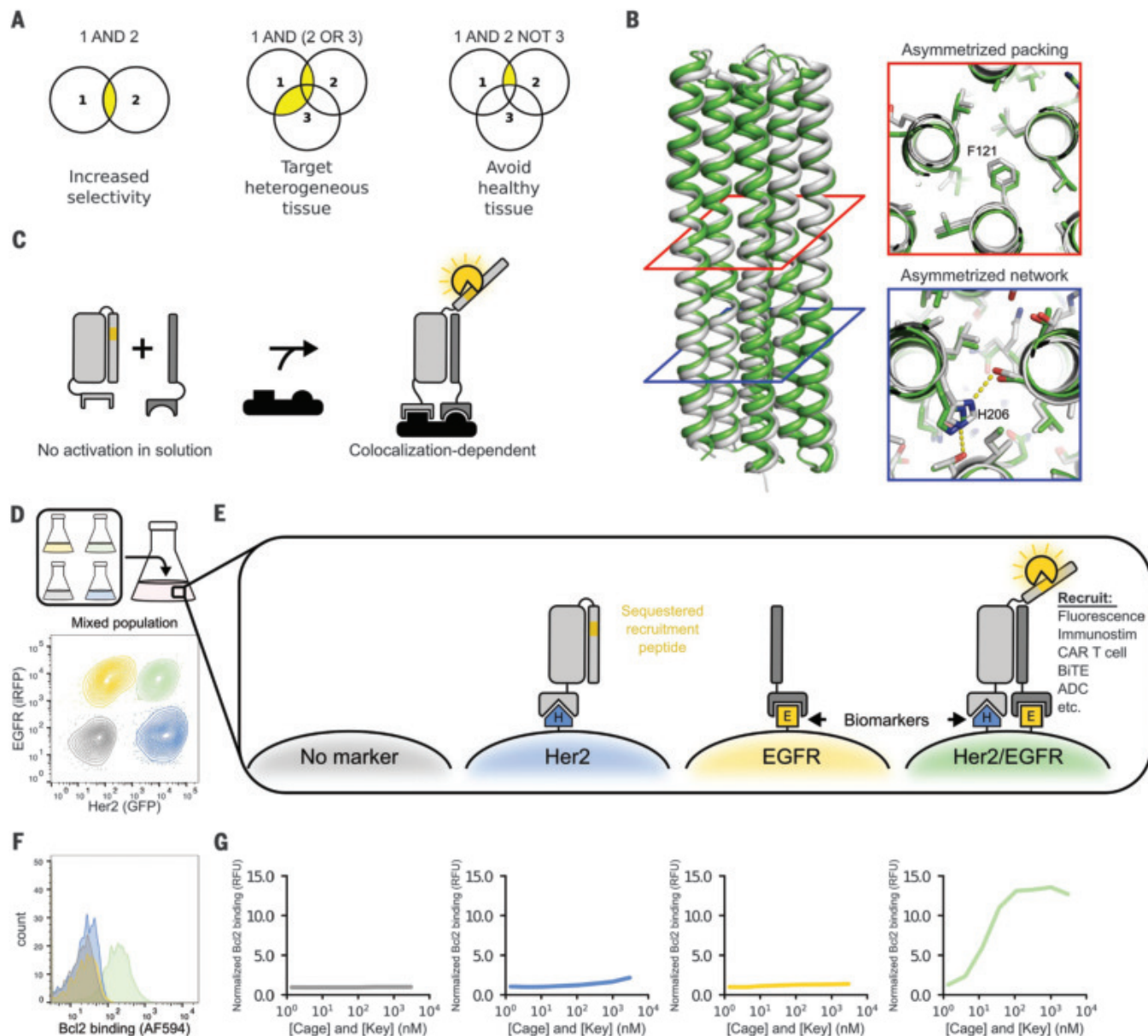


Fig. 1. A de novo designed protein switch performs AND logic on the cell surface. (A) The ability to compute logic operations on the surface of cells enables more precise targeting. (B) Structure of cage design used to create Co-LOCKR; the x-ray crystal structure (white, PDB ID 7JH5) matches the computational design model (green) with an RMSD of 1.1 Å across all backbone atoms. Cross sections illustrate asymmetric packing of hydrophobic residues (red square) and an asymmetric hydrogen bond network (blue square). F, Phe; H, His. (C) Colocalization-dependent protein switches are tuned so that cage and key do not interact in solution but strongly interact when colocalized on a surface by way of targeting domains. (D) Flow cytometry discriminates Her2⁺EGFR⁺ cells in a mixed population of K562 cells

expressing Her2-eGFP (blue), EGFR-iRFP (yellow), both (green), or neither (gray). (E) An effector protein is recruited only when cage and key are colocalized on the surface of the same cell (AND logic). (F) The mixed population of cells from (D) was incubated with 111 nM Her2-targeted cage, 111 nM EGFR-targeted key, and 50 nM Bcl2-AF594. Bcl2 binding was only observed for the Her2⁺EGFR⁺ cells. (G) The mixed population of cells from (D) was incubated with a dilution series of Her2-targeted cage and EGFR-targeted key, washed, and then incubated with 50 nM Bcl2-AF594. Bcl2 binding is reported relative to K562 cells incubated with 3000 nM Her2-targeted cage, 3000 nM EGFR-targeted key, and 50 nM Bcl2-AF594. RFU, relative fluorescence units.

Previous LOCKR switches functioned in the yeast cytoplasm (3) but were aggregation-prone once purified, likely because of domain swapping of symmetric repeats inherited from the parental α -helical homotrimer (4). To alleviate aggregation, we used Rosetta (5) to design a new LOCKR switch with shorter helices, improved hydrophobic packing, and an addi-

tional hydrogen bond network to promote interaction specificity among the helices (fig. S1, see the computational protein design section of the supplementary materials). The new design was nearly 100% monomeric (fig. S2, top), and a 2.1-Å x-ray crystal structure [Protein Data Bank (PDB) ID 7JH5] closely matched the design model (Fig. 1B and table S1) with a

root mean square deviation (RMSD) of 1.1 Å across all backbone atoms and an RMSD of 0.5 Å across all sidechain heavy atoms in the newly designed hydrogen bond network (Fig. 1B).

To install an output function into colocalization-dependent LOCKR (Co-LOCKR), we chose the Bim-Bcl2 pair as a model system (Bcl2, B cell

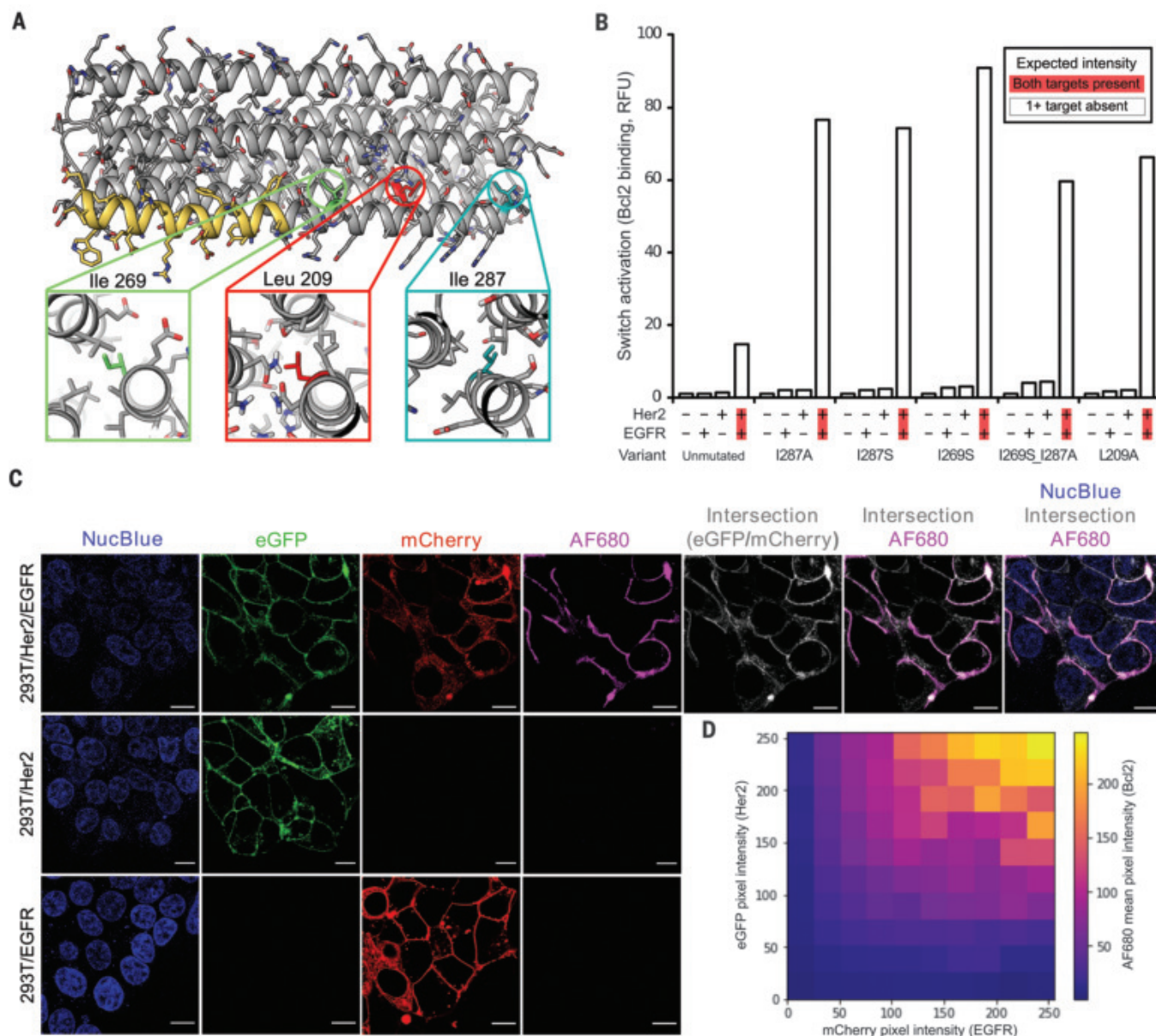


Fig. 2. Tuning Co-LOCKR sensitivity. (A) Design model of Co-LOCKR with the Bim functional peptide in yellow. Three buried hydrophobic amino acids were mutated to Ala or Ser to weaken the cage-latch affinity, thereby favoring cage-key binding. (B) Tuned Co-LOCKR variants exhibit greater colocalization-dependent activation than the unmutated parental variant. CL_{C_HK_E} variants recruiting Bcl2-AF594 were evaluated by flow cytometry using the mixed population of cells from Fig. 1D. The data shown represent 12.3 nM CL_{C_HK_E} ($n = 1$), and fig. S5C shows the complete dilution series for each variant. S, Ser; L, Leu. (C) Confocal microscopy of HEK293T cell lines shows that Co-LOCKR switches recruit Bcl2-

AF680 effector proteins only where Her2 and EGFR are colocalized. Each cell line was incubated with CL_{C_HK_E} (I269S cage) and Bcl2-AF680 before imaging. NucBlue is a nuclear stain, eGFP indicates Her2 localization, mCherry indicates EGFR localization, AF680 indicates Bcl2 binding in response to Co-LOCKR activation, and white indicates the intersection of Her2-eGFP and EGFR-mCherry signal. Scale bars, 10 μ m. See fig. S16, A to C, for uncropped versions of these images. (D) Heatmap showing the intensity of AF680 signal (Co-LOCKR activation) versus eGFP (Her2) and mCherry (EGFR) pixel intensity. Calculations were based on the uncropped 293T-Her2-EGFR image in fig. S16A.

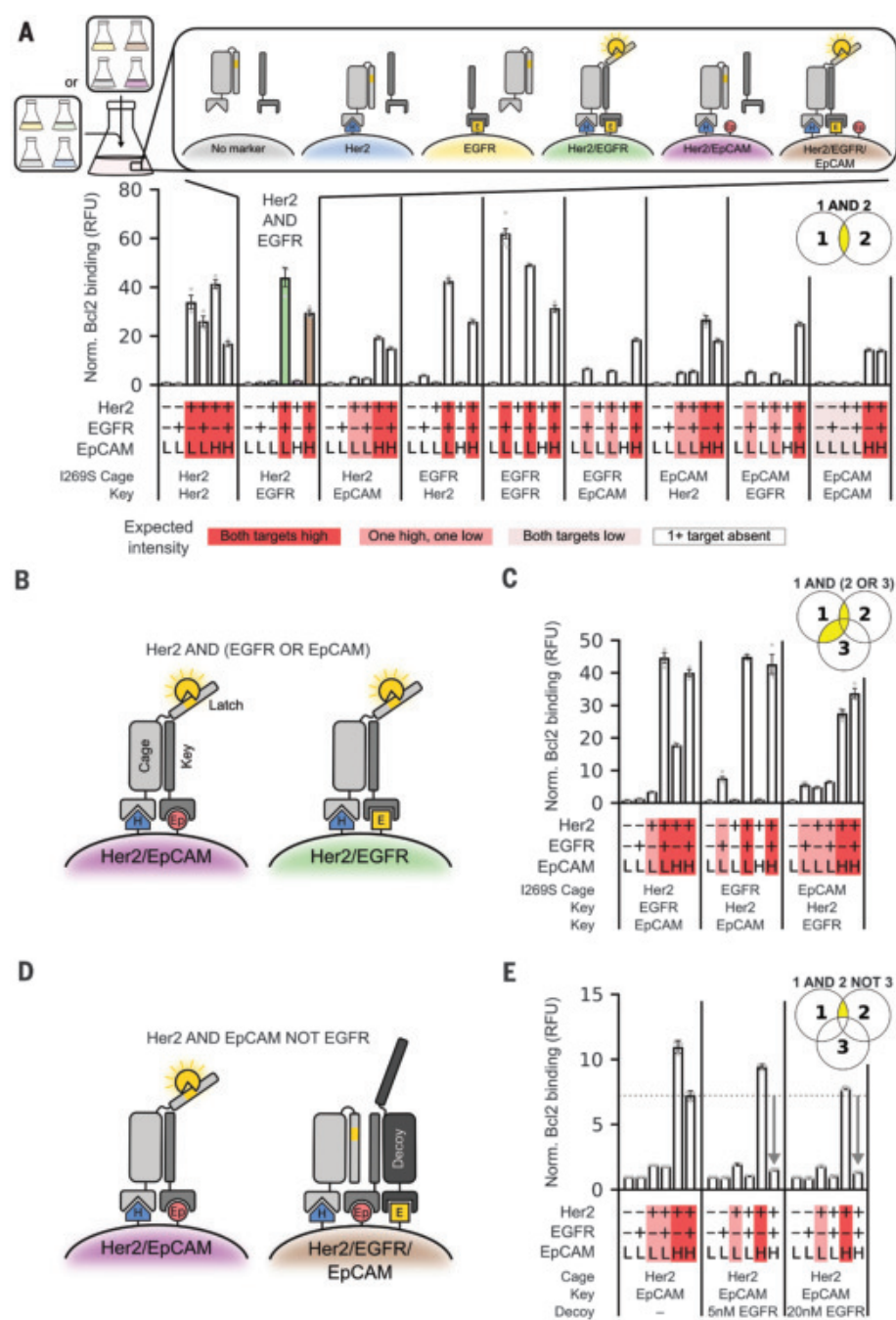


Fig. 3. Co-LOCKR performs two- and three-input logic operations in mixed cell populations.

(A) Co-LOCKR was used to recruit Bcl2-AF594 in mixed populations of K562 cells expressing different combinations of Her2, EGFR, and EpCAM. Marker expression for each cell line and identity of the cage and key targeting domains are indicated below each bar plot. Red highlighting indicates the expected magnitude of Bcl2-AF594 signal based on relative antigen expression. (B) Schematic of [Her2 AND either EGFR OR EpCAM] logic mechanism. (C) [Ag₁ AND either Ag₂ OR Ag₃] logic combinations were used to recruit Bcl2-AF594. (D) Schematic of [Her2 AND EpCAM NOT EGFR] logic mechanism. The decoy acts as a sponge to sequester the key, thereby preventing cage activation. (E) CL_{C_H}K_EDe was used to recruit Bcl2-AF594. Compared with the simple CL_{C_H}K_E AND gate (left), recruitment of decoy to EGFR-expressing cells reduced activation to near background levels. For all panels, population 1 was [K562-EpCAM^{hi}, K562-EGFR-EpCAM^{hi}, K562-Her2-EpCAM^{hi}, and K562-Her2-EGFR-EpCAM^{hi}], and population 2 was [K562-EpCAM^{lo}, K562-EGFR-EpCAM^{lo}, K562-Her2-EpCAM^{hi}, and K562-Her2-EGFR-EpCAM^{hi}]. Fluorescence intensities are normalized to the negative control. Error bars represent SEM of six independent replicates for K562 and K562-EGFR and three independent replicates for all others. Statistics are reported in table S4.

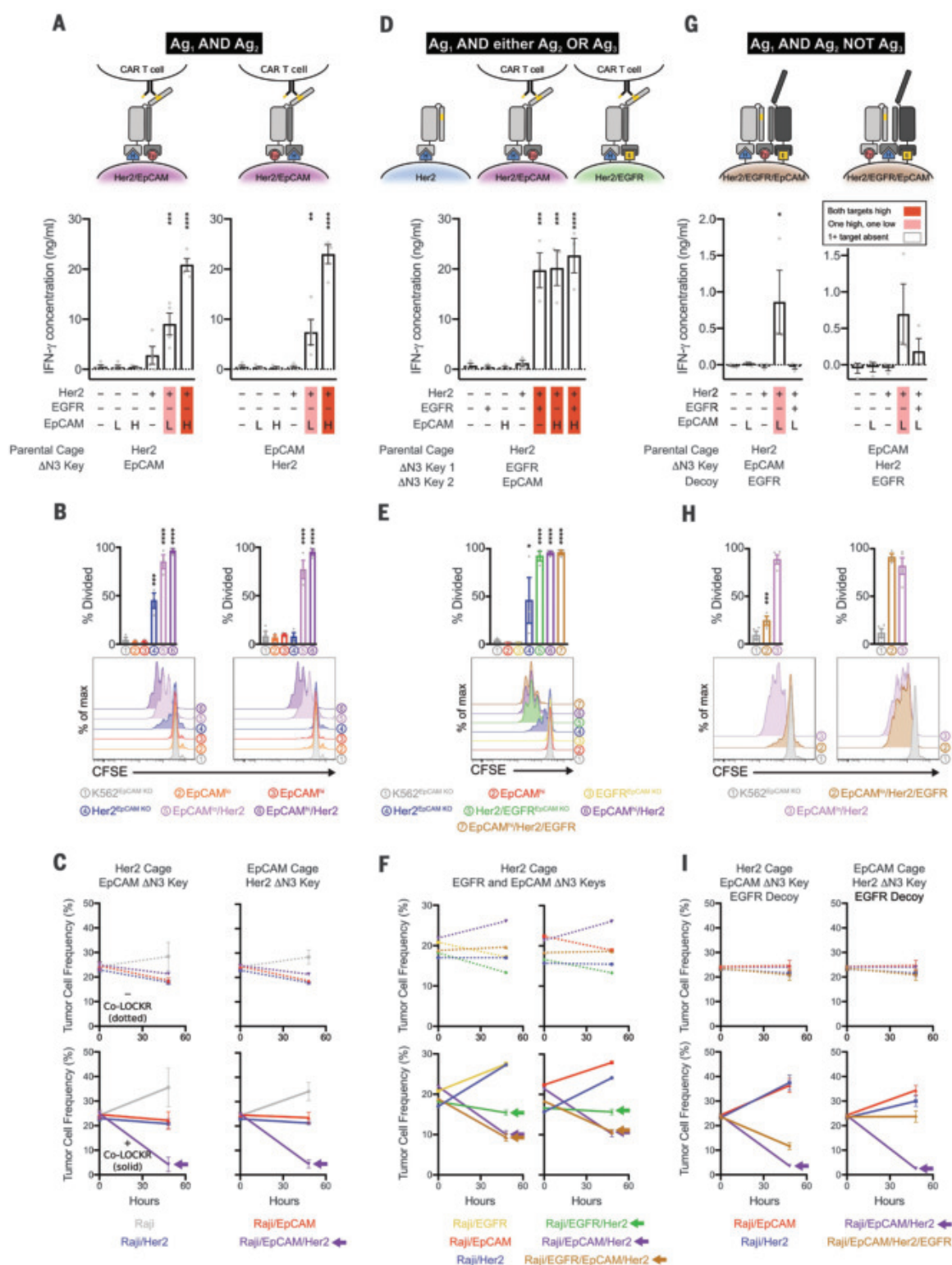
lymphoma 2; Bim, Bcl2-interacting mediator of cell death) (6). Bim was encoded into the latch as a sequestered peptide, and Bcl2 was used as the effector. We added targeting domains that recruit the Co-LOCKR cage and key to cells expressing target antigens. While the targeting domains should bind to any cell expressing their target antigens, only cells with both antigens should colocalize cage and key (Fig. 1C). Because Co-LOCKR is thermodynamically controlled, complex formation occurs at much lower solution concentrations when the components are bound to and colocalized on a surface than when they are unbound (fig. S3, A and B); colocalization shifts the binding equilibrium in favor of complex formation (fig. S3C).

To evaluate the ability of Co-LOCKR to target cells coexpressing a precise combination of surface antigens, we developed a mixed-population flow cytometry assay by combining four K562 cell lines expressing Her2-eGFP, EGFR-iRFP, both, or neither (eGFP, enhanced green fluorescent protein; EGFR, epidermal growth factor receptor; iRFP, near-infrared fluorescent protein) (Fig. 1D). We used designed ankyrin repeat protein (DARPin) domains (7, 8) to target the cage and key to Her2 and EGFR, respectively. If the system functions as designed, only cells coexpressing both Her2 and EGFR should activate Co-LOCKR and bind Bcl2 (Fig. 1E): The cage contains the sequestered Bim peptide, and the key is required for its exposure. We refer to this Co-LOCKR configuration as CL_{C_H}K_E; in this nomenclature, CL refers to Co-LOCKR, C_H indicates that the cage is targeted to Her2, and K_E indicates that the key is targeted to EGFR (table S2). When the mixed population of cells was coincubated with an equimolar dilution series of cage and key (3 μM to 1.4 nM) and washed before adding AlexaFluor594-labeled Bcl2 (Bcl2-AF594), the expected sigmoidal binding curve was observed for the Her2-EGFR cells but not for cells expressing either antigen alone (Fig. 1, F and G).

We next sought to tune the dynamic range of Co-LOCKR activation to increase colocalization-dependent activation sensitivity and responsiveness. The sensitivity of previous LOCKR switches was tuned by shortening the latch to produce a “toehold,” which allows the key to outcompete the latch (3), but this also promoted aggregation (fig. S2, bottom). We therefore focused on designing mutations rather than toeholds to tune the relative interaction affinities of the Co-LOCKR system to be colocalization dependent (fig. S4). We mutated large, hydrophobic residues in the latch [Ile²⁸⁷→Ala (I287A), I287S, I269S] or cage (I209A) to weaken cage-latch affinity (Fig. 2A). Biolayer interferometry indicated that increasingly disruptive mutations improved responsiveness (fig. S5, A and B), and flow cytometry showed

Fig. 4. Co-LOCKR directs CAR T cell specificity using two- and three-input logic operations. (A, D, and G) Mean IFN- γ concentration in cell supernatants 24 hours after coculture of cage, key, and K562 cells with CAR T cells. Marker expression for each cell line and identity of the cage and key targeting domains are indicated below each bar plot. Red highlighting indicates the expected magnitude of signal based on the target cell's relative antigen expression. Error bars represent SEM of $n = 4$ (A) or 3 [(D) and (G)] healthy T cell donors. AND/NOT logic is demonstrated with EpCAM^{lo} target K562 cells because T cell effector function was leaky for EpCAM^{hi} target cells (see fig. S15A).

(B, E, and H) CAR T cell proliferation in response to [Her2 AND EpCAM] (B), [Her2 AND EGFR OR EpCAM] (E), or [Her2 AND EpCAM NOT EGFR] (H) logic. Bar plots are the percent of T cells that have undergone at least one cell division by 72 hours after coculture of CAR T cells, cage, key, and target K562 cells. Histograms show flow cytometric analysis of CFSE (carboxyfluorescein succinimidyl ester) dye dilution gated on CD8⁺ lymphocytes. The data are representative of $n = 3$ biological replicates with healthy T cell donors. **(C, F, and I)** CAR T cell cytotoxicity against mixed populations of target Raji cells expressing combinations of Her2, EGFR, and EpCAM. Line graphs show mean frequency of Raji target cells after 0 or 48 hours of coculture with CAR T cells. $n = 4$ [(C) and (F)] or 3 (I) healthy donors. Arrows indicate cell lines targeted by Co-LOCKR.



that tuning the cage-latch interface enhanced colocalization-dependent signal without compromising specificity (Fig. 2B and fig. S5C). Colocalization-dependent activation occurred

even at low nanomolar concentrations of CL- $C_{H}K_E$ (fig. S5, D and E). Very little effector binding was observed for cells expressing Her2 or EGFR alone, confirming that Co-

LOCKR has single-cell targeting resolution in a mixed population. Of the switches tested, I269S exhibited the greatest activation (fig. S6A), the parental Co-LOCKR design exhibited

the lowest off-target activation (fig. S6B), and I287A exhibited the highest specificity (on-target signal divided by max off-target signal) (fig. S6C).

Colocalization-dependent activation was observed further at the subcellular level by confocal microscopy. CL_{C_HK_E} recruited Bcl2-AF680 to the plasma membrane of Her2⁺EGFR⁺, but not Her2⁺ or EGFR⁺ human embryonic kidney 293T (HEK293T) cells (Fig. 2C). Co-LOCKR activation levels correlated with the extent of Her2-eGFP and EGFR-iRFP colocalization on the plasma membrane (Fig. 2D).

To assess the flexibility of Co-LOCKR, we attempted to specifically target alternative pairwise combinations of three cancer-associated antigens [Her2, EGFR, and EpCAM (epithelial cell adhesion molecule)]. Each of these antigens are expressed at differing levels by engineered K562 cell lines or human cancer cell lines (figs. S7A and S8A and table S3). Using the I269S variant to maximize detection of low levels of antigen, (i) Co-LOCKR distinguished the correct pair of antigens in every case, and (ii) the magnitude of Bcl2 binding corresponded with the expression level of the less-expressed of the two target antigens (Fig. 3A and fig. S8, B and C), consistent with a stoichiometric binding mechanism for colocalization-dependent activation. Together, these results demonstrate the modularity of Co-LOCKR to target several antigens expressed at differing levels. Although we chose DARPins as targeting domains to allow facile expression of Co-LOCKR variants, single-chain variable fragments can also be used (fig. S9).

The colocalization-dependent activation mechanism of Co-LOCKR can in principle be extended to include OR logic by adding a second key fused to a targeting domain against an alternative surface marker (Fig. 3B) and NOT logic by adding a decoy protein fused to a targeting domain against a surface marker to be avoided; the decoy acts as a sponge to sequester the key, thereby preventing cage activation (Fig. 3D). Using Her2, EGFR, and EpCAM as model antigens (Ag), we first explored [Ag₁ AND either Ag₂ OR Ag₃] logic on the surface of cells (Fig. 3B). To assess the programmability of Co-LOCKR targeting, we tested all three combinations: [Her2 AND either EGFR OR EpCAM], [EGFR AND either Her2 OR EpCAM], and [EpCAM AND either Her2 OR EGFR]. In all cases, the correct cell subpopulation was targeted at levels consistent with the limiting target antigen (Fig. 3C). For example, CL_{C_EK_HK_{E_P}} targeted cells expressing EGFR-EpCAM^{lo} 10-fold over background, Her2-EGFR-EpCAM^{lo} 59-fold over background, and Her2-EGFR-EpCAM^{hi} 56-fold above background but did not target cells missing one or more of the antigens (Fig. 3C, middle panel).

We next explored [Ag₁ AND Ag₂ NOT Ag₃] logic using CL_{C_HK_{E_P}D_E} (D meaning decoy) and the same set of model antigens (Fig. 3D). We tuned the decoy-key affinity with designed point mutations to maximize the abrogation of activation when the decoy is targeted and to minimize the interference of the decoy with activation when it is not targeted (fig. S10). Recruitment of decoy reduced activation to near-background levels on cells with Ag₃ on their surface, while reducing activation on cells lacking Ag₃ by only 15% (Fig. 3E). Consistent with the stoichiometric sequestration mechanism, Ag₃ must be expressed at higher levels than Ag₂ so that the decoy can sequester all molecules of the key (Fig. 3D). While bispecific antibodies can be made to approximate [Ag₁ AND Ag₂] logic by tuning binding affinity, we are not aware of any current approach that can achieve the precise [Ag₁ AND Ag₂ NOT Ag₃] logic of Fig. 3E and fig. S11.

As a first step toward a real-world application, we explored the retargeting of primary human T cell effector function against tumor cells in vitro. We designed a Bcl2 chimeric antigen receptor (CAR) that targets Bim peptides displayed on the surface of a target cell; the CAR contains a stabilized variant of human Bcl2, a flexible extracellular spacer domain (9), CD28 and CD3ζ signaling domains, and a truncated EGFR (EGFRt) selection marker (10) linked by a T2A ribosomal skipping sequence (fig. S12A). The Bcl2 CAR functions as designed: Purified CD8⁺EGFRt⁺ Bcl2 CAR T cells efficiently recognized K562 cells stably expressing a surface-exposed Bim-GFP fusion protein (fig. S12, B and C).

With Bcl2 CAR T cells in hand, we investigated whether the Co-LOCKR proteins could mediate T cell activation by Raji and K562 cells expressing combinations of Her2, EGFR, and EpCAM. The Raji cells expressed lower levels of transduced antigens than did the K562 cell lines (fig. S7 and table S3) and hence more stringently test Co-LOCKR sensitivity, whereas the K562 cells better assess specificity. CL_{C_HK_{E_P}} and CL_{C_{E_P}K_H} (using the parental unmutated cage) promoted interferon-γ (IFN-γ) release only when cocultured with Raji-Her2-EpCAM cells and not Raji-EpCAM or Raji-Her2 cells (fig. S12D). Titration experiments showed that CAR T effector function could be specifically targeted using between 2.5 nM and 20 nM of Co-LOCKR without causing unintended activation by off-target cells (fig. S13); even lower concentrations would likely be effective using higher-affinity binding domains.

Next, we assessed the ability of Co-LOCKR to direct CAR T cell cytotoxicity against specific subsets of cells within a mixed population. Raji, Raji-EpCAM, Raji-Her2, and Raji-Her2-EpCAM were differentially labeled with fluorescent CellTrace dyes and mixed together with CAR

T cells and CL_{C_HK_{E_P}} (fig. S12F), and killing of each of the cell lines was assessed using flow cytometry. After 48 hours, Raji-Her2-EpCAM cells were preferentially killed, but a fraction of Raji-EpCAM cells were also targeted (fig. S12G), suggesting that even the parental cage and key were too leaky for CAR T cell recruitment. We overcame this basal activation by modifying the length of the key (fig. S12E): The combination of parental cage and ΔN3 key (three N-terminal amino acids deleted) selectively targeted Raji-EpCAM cells and mitigated unintended killing of Raji-EpCAM and Raji-Her2 cells (fig. S12, F and G). A chromium release assay showed that CL_{C_HK_{E_P}} targeted only Raji-Her2-EpCAM cells and initiated rapid cell killing within 4 hours (fig. S12H). Thus, Co-LOCKR can be used to restrict IFN-γ release and cell killing to only those tumor cells that express a specific pair of antigens.

We next evaluated Co-LOCKR AND logic for additional tumor antigen pairs ([Her2 AND EpCAM] and [Her2 AND EGFR]) and varying antigen density profiles using K562 cell lines (fig. S7A and table S3) and solid tumor lines (fig. S8A). Raji cells with low antigen density yielded modest IFN-γ (fig. S14A), K562-Her2-EpCAM^{lo} and SKBR3 breast cancer cells yielded intermediate IFN-γ (Fig. 4A and fig. S14B), and both K562-Her2-EpCAM^{hi} and K562-Her2-EGFR cells yielded high IFN-γ release for their respective Co-LOCKRs (Fig. 4A and fig. S14C). CL_{C_{E_P}K_H} induced IFN-γ release in response to Raji-Her2-EpCAM 3.9-fold above background; SKBR3, 4.8-fold above background; K562-Her2-EpCAM^{lo}, 16-fold above background; and K562-Her2-EpCAM^{hi}, 51-fold above background, with minimal off-target cytokine release. IFN-γ production did not increase appreciably when the target cells expressed high levels of a single antigen. CAR T cells proliferated only upon coculture with target cells coexpressing the correct pair of antigens, and the degree of proliferation positively correlated with antigen density (Fig. 4B and fig. S14D). The flow cytometry-based killing assay demonstrated AND gate selective cytotoxicity with both CL_{C_HK_{E_P}} and CL_{C_{E_P}K_H} against Raji-Her2-EpCAM without depleting single antigen-positive cells (Fig. 4C). A similar result was observed for both CL_{C_HK_E} and CL_{C_EK_H} against Raji-Her2-EGFR (fig. S14E), although killing was less effective, likely because of the lower expression levels of EGFR compared with EpCAM in Raji-Her2-EGFR and Raji-Her2-EpCAM, respectively. Additionally, we did not observe fratricide of the EGFRt⁺ CAR T cells used in the experiment, which could have been targeted by the anti-EGFR DARPin (fig. S14F).

Encouraged by robust AND logic, we evaluated more complex operations involving

combinations of AND and either OR or NOT logic. CAR T cells cocultured with AND/OR Co-LOCKRs (CL_{C_HK_ED_E}, CL_{C_EK_HK_ED_E}, and CL_{C_ED_HK_E}) each carried out [Ag₁ AND either Ag₂ OR Ag₃] logic with respect to IFN- γ production (Fig. 4D and fig. S14G) and proliferation (Fig. 4E) against K562 cell lines, as well as selective killing in a mixed population of Raji cell lines (Fig. 4F and fig. S14H). CAR T cells cocultured with an AND/NOT Co-LOCKR (CL_{C_HK_ED_E}) carried out [Her2 AND EpCAM NOT EGFR] logic: IFN- γ production and proliferation were induced in the presence of K562-Her2-EpCAM^{lo} but not K562-Her2-EGFR-EpCAM^{lo} cells (Fig. 4, G and H). Consistent with the observations above, Ag₃ in the NOT operation had to be expressed at higher levels than Ag₂ (Fig. 4, G to I, and fig. S15). While these data indicate that careful antigen selection and some tuning are necessary for robust control of logical operations, the ability of CL_{C_ED_HK_E} to direct CAR T cell mediated killing of Her2⁺EpCAM⁺ cells but not Her2⁺EGFR⁺EpCAM⁺ cells (Fig. 4I, right-hand panel) further highlights the power of Co-LOCKR to perform [Ag₁ AND Ag₂ NOT Ag₃] logic for specific cell targeting.

Two previous strategies improved the specificity of CAR T cells by approximating AND logic. First, Kloss *et al.* (11) directly modulated signaling from a suboptimally activating first generation CAR (CD3 ζ only) using a chimeric costimulatory receptor (CCR; costimulatory domain only) that recognizes a distinct second antigen. Although T cell activation is reduced in the absence of the second antigen, targeting remains leaky because the CAR T cells can lyse both tumor and normal cells expressing the antigen targeted by the CD3 ζ CAR, even when the CCR is not engaged. Second, Morsut *et al.* (12) developed synthetic Notch receptors that modularly induce expression of effector proteins in engineered cells. Roybal *et al.* (13) applied this technology to enhance CAR T cell specificity using a synthetic Notch receptor that upon engaging one antigen induces expression of a CAR recognizing a second antigen. Although this if-then logic strategy has shown promise in preclinical models in which the target antigens exist distally, the CAR will kill any nearby cell expressing the target antigen, so off-tumor toxicity can occur when the Notch receptor and CAR targets are expressed in neighboring healthy tissues (14). Co-LOCKR has potential advantages over these approaches, as activation requires binding in cis to a precise combination of target antigens before recruiting the cognate CAR T cells, and thus it can direct killing without harming neighboring off-target cells displaying single antigens (Fig. 4, C, F, and I). OR (15, 16) and NOT (15, 17) logic has also been described for CAR T cells, but not in combination with AND logic as described here.

Our CAR T cell experiments demonstrate the potential for Co-LOCKR to mediate targeting specificity in vitro; however, several additional challenges will have to be met for Co-LOCKR to be a clinically translatable therapeutic. In vivo studies will be needed to assess and improve the pharmacokinetics of the Co-LOCKR components. Immunogenicity of the designed proteins is also a potential concern, as with any other system comprising nonhuman proteins. As Co-LOCKR activation is thermodynamically controlled, the therapeutic index will depend on the affinity of the targeting domains used to direct the Co-LOCKR proteins to antigens on the target cells: If the affinities are subnanomolar, dosing can be far below the 40-nM level where activation starts to occur in solution (fig. S13). CAR T efficacy could also be improved by optimizing the CAR, for example, by using alternative signaling molecules (18–20).

The power of Co-LOCKR results from the integration of multiple coherent or competing inputs that determine the magnitude of a single response. The output signal—exposure of the functional peptide on the latch—is increased by key binding and countered by decoy competition. Thus, the proteins can intrinsically perform logic rather than relying on cellular machinery for signal integration. Although our present work has focused on development of the Co-LOCKR system and CAR T cell applications, the Co-LOCKR system should be powerful for engineering biology in any setting that requires proximity-based activation or targeting of specific subpopulations of cells.

REFERENCES AND NOTES

1. C. Sellmann *et al.*, *J. Biol. Chem.* **291**, 25106–25119 (2016).
2. Y. Mazor *et al.*, *Sci. Rep.* **7**, 40098 (2017).
3. R. A. Langan *et al.*, *Nature* **572**, 205–210 (2019).
4. S. E. Boyken *et al.*, *Science* **352**, 680–687 (2016).
5. A. Leaver-Fay *et al.*, *Methods Enzymol.* **487**, 545–574 (2011).
6. L. Delgado-Soler, M. Pinto, K. Tanaka-Gil, J. Rubio-Martinez, *J. Chem. Inf. Model.* **52**, 2107–2118 (2012).
7. C. Zahnd *et al.*, *J. Mol. Biol.* **369**, 1015–1028 (2007).
8. D. Steiner, P. Forrer, A. Plückthun, *J. Mol. Biol.* **382**, 1211–1227 (2008).
9. M. Hudecek *et al.*, *Cancer Immunol. Res.* **3**, 125–135 (2015).
10. X. Wang *et al.*, *Blood* **118**, 1255–1263 (2011).
11. C. C. Kloss, M. Condomines, M. Cartellieri, M. Bachmann, M. Sadelain, *Nat. Biotechnol.* **31**, 71–75 (2013).
12. L. Morsut *et al.*, *Cell* **164**, 780–791 (2016).
13. K. T. Roybal *et al.*, *Cell* **164**, 770–779 (2016).
14. S. Srivastava *et al.*, *Cancer Cell* **35**, 489–503.e8 (2019).
15. J. H. Cho, J. J. Collins, W. W. Wong, *Cell* **173**, 1426–1438.e11 (2018).
16. E. Zah, M.-Y. Lin, A. Silva-Benedict, M. C. Jensen, Y. Y. Chen, *Cancer Immunol. Res.* **4**, 498–508 (2016).
17. V. D. Fedorov, M. Themeli, M. Sadelain, *Sci. Transl. Med.* **5**, 215ra172 (2013).
18. S. Tammana *et al.*, *Hum. Gene Ther.* **21**, 75–86 (2010).

19. Y. Kagoya *et al.*, *Nat. Med.* **24**, 352–359 (2018).
20. C. Sun *et al.*, *Cancer Cell* **37**, 216–225.e6 (2020).

ACKNOWLEDGMENTS

We thank A. Scharenberg, W. Lim, R. Klausner, L. Stewart, A. Roy, Z. Chen, A. Briggs, E. Gray, D. Stetson, M. Pepper, L. Carter, B. Weitzner, J. Pearl, H. Moffett, I. Haydon, D. Campbell, S. Hauschka, N. King, and J. Zalatan for helpful advice; D. Prunkard and H. Nguyen for technical assistance with flow cytometry and cell sorting; A. Kang for setting up crystal trays and looping crystals; R. Ravichandran for protein purification; and S. Berger for sharing biotinylated Bcl2, D. Hockenbery for sharing SKBR3 cells, and D. Trono for sharing lentiviral packaging plasmids. We also thank the W. M. Keck Center for Advanced Studies in Neural Signaling (NIH grant S10 OD016240) and the helpful input of N. Peters and G. Liu for confocal microscopy experiments.

Funding: This work was supported by the HHMI (D.B.), the Open Philanthropy Project (D.B.), the NSF (D.B., CHE-1629214), the DTRA (D.B., HDTRA1-18-1-0001), the Nordstrom Barrier IPD Directors Fund (D.B.), the Washington Research Foundation and Translational Research Fund (D.B.), the Audacious Project organized by TED (D.B.), and the NIH (S.R.R., R01 CA114536; J.B., NIGMS T32GM008268). M.J.L. was supported by a Washington Research Foundation Innovation Postdoctoral Fellowship and a Cancer Research Institute Irvington Fellowship from the Cancer Research Institute. S.E.B. was supported by the Burroughs Wellcome Fund Career Award at the Scientific Interface. A.I.S. was supported by the FHCR interdisciplinary training grant in cancer research and Hearst Foundation. A.O. was supported by NIH NCI grants 1R21CA232430-01 and T32CA080416. **Author contributions:** M.J.L., S.E.B., A.I.S.: Conceptualization, Methodology, Investigation, Software, Data analysis, Writing – original draft, Writing – review and editing, Visualization, and Supervision. J.B.: Investigation, Data analysis, Writing – original draft, Writing – review and editing, and Visualization. A.R.: Investigation. R.A.L.: Investigation and Software. A.O.: Methodology, Investigation, Software, Data analysis, and Visualization. V.M.: Investigation. M.J.B.: Investigation, Software, and Data analysis. M.G., A.Q.-R., J.J., G.L., A.N.: Investigation. S.P., C.E.C., S.R.R.: Supervision. D.B.: Conceptualization, Writing – original draft, Writing – review and editing, Visualization, and Supervision. M.J.L., S.E.B., and D.B. conceived of the study. M.J.L., S.E.B., A.I.S., J.B., and A.O. designed the experiments. M.J.L., S.E.B., and R.A.L. designed the LOCKR proteins. M.J.L., A.I.S., A.R., and M.G. made the target cell lines. M.J.L., S.E.B., J.B., R.A.L., A.Q.-R., J.J., G.L., and A.N. performed cloning, protein expression, and biochemical characterization experiments. S.E.B. and M.J.B. solved the crystal structure. M.J.L., J.B., and A.O. quantified Co-LOCKR activation using flow cytometry. A.O. performed the microscopy experiment and data analysis. A.I.S., A.R., and V.M. performed the T cell experiments. M.J.L., S.E.B., A.I.S., J.B., R.A.L., A.O., and M.J.B. analyzed the data. M.J.L., S.E.B., A.I.S., S.P., C.E.C., S.R.R., and D.B. supervised the study. M.J.L., S.E.B., A.I.S., and D.B. wrote the manuscript. All authors reviewed the manuscript and provided feedback. **Competing interests:** M.J.L., S.E.B., A.I.S., J.B., R.A.L., M.G., C.E.C., S.R.R., and D.B. are inventors on patents related to this work. M.J.L., S.E.B., A.I.S., R.A.L., M.J.B., S.R.R., and D.B. hold equity in Lyell Immunopharma. D.B. holds equity in Sana Biotechnology. M.J.L., S.E.B., R.A.L., M.J.B., and S.R.R. are employees of Lyell Immunopharma. A.I.S. is a consultant of Lyell Immunopharma. **Data and materials availability:** Coordinates and structure files have been deposited to the Protein Data Bank (PDB) under ID 7JH5. The python script used to analyze confocal microscopy images is included in the supplemental material. Expression plasmids and cell lines are available upon request. Primary T cells are not available.

SUPPLEMENTARY MATERIALS

science.sciencemag.org/content/369/6511/1637/suppl/DC1
Materials and Methods
Figs. S1 to S21
Tables S1 to S5
Supplementary Scripts
References (21–33)
MDAR Reproducibility Checklist

20 December 2019; accepted 28 July 2020
Published online 20 August 2020
10.1126/science.aba6527

PARASITE GENETICS

A single-cell RNA-seq atlas of *Schistosoma mansoni* identifies a key regulator of blood feeding

George Wendt^{1*}, Lu Zhao^{1*}, Rui Chen¹, Chenxi Liu², Anthony J. O'Donoghue², Conor R. Caffrey², Michael L. Reese^{1,3}, James J. Collins III^{1†}

Schistosomiasis is a neglected tropical disease that infects 240 million people. With no vaccines and only one drug available, new therapeutic targets are needed. The causative agents, schistosomes, are intravascular flatworm parasites that feed on blood and lay eggs, resulting in pathology. The function of the parasite's various tissues in successful parasitism are poorly understood, hindering identification of therapeutic targets. Using single-cell RNA sequencing (RNA-seq), we characterize 43,642 cells from the adult schistosome and identify 68 distinct cell populations, including specialized stem cells that maintain the parasite's blood-digesting gut. These stem cells express the gene *hnf4*, which is required for gut maintenance, blood feeding, and pathology in vivo. Together, these data provide molecular insights into the organ systems of this important pathogen and identify potential therapeutic targets.

Schistosomes dwell inside the host's circulation, often for decades, where they feed on blood and lay eggs, which become trapped in host tissues and cause disease pathology. Because this parasite is a metazoan composed of multiple tissue types, understanding the schistosome's biology on a molecular level during parasitism could suggest therapeutic strategies. Single-cell RNA sequencing (scRNA-seq) has been used to comprehensively describe tissue types and physiology of diverse metazoans (1), including larval schistosomes (2), but we lack a comprehensive description of the cell types present in egg-laying adults because specific molecular markers are known for only a small number of cell types (3–8).

To define the molecular signature of adult schistosome cell types, we dissociated adult *Schistosoma mansoni*, isolated cells by fluorescence-activated cell sorting (FACS), and generated scRNA-seq libraries using a 10x genomics chromium controller (fig. S1A). Schistosomes are dioecious, and sexual maturation of the female worm's reproductive organs, including the ovary and vitellaria, requires sustained physical contact with the male worm (9). Accordingly, we generated scRNA-seq libraries from adult male parasites, adult sexually mature female parasites, and age-matched virgin female parasites. We then performed clustering, identifying 68 molecularly distinct clusters composed of 43,642 cells (Fig. 1A, fig. S1B, and table S1). These included three clusters of cells expressing somatic stem cell (i.e., neoblast) markers such as the RNA bind-

ing protein *nanos2*, the cell surface receptor *notch*, and the receptor tyrosine kinase *fgfra* (3) (Fig. 1B and fig. S2A); eight clusters expressing markers of tegument ("skin"-like surface) progenitors (4, 5) (fig. S2B); two clusters of parenchymal cells (Fig. 1C and fig. S2C); one cluster of ciliated flame cells that are part of the worm's protonephridial (excretory) system (Fig. 1D and fig. S2D); eight clusters of muscles (Fig. 1E); and a cluster of esophageal gland cells (Fig. 1F and fig. S2E). Despite being composed of thousands of nuclei, our analysis also identified clusters corresponding to syncytial tissues: the tegument (4) (Fig. 1G and fig. S2F) and gut (Fig. 1H and fig. S2G). We failed to identify cells from the female ootype (an organ involved in eggshell formation) (9) and the protonephridial ducts (10), possibly because of their multinucleate nature. Gene ontology analyses of these clusters (table S2) confirmed expected findings (enrichment of "DNA replication" in "neoblast 1") and revealed previously uncharacterized biology such as the enrichment of "extracellular matrix structural components" in muscle clusters, suggesting that muscles are the source of extracellular matrix in schistosomes, similar to planarians (11).

We uncovered unexpected molecular complexity within the schistosome nervous system, identifying 30 clusters expressing the neuroendocrine protein *7b2* (Fig. 1I) and one apparent neuronal cluster that did not express high levels of *7b2* but did express several synaptic molecules (e.g., *synapsin*) (fig. S3A and table S1). Examination of genes from these neuronal cell clusters uncovered distinct molecular fingerprints for several populations (figs. S3, A to E, and S4; and table S1) and highly ordered structural and regional specialization in the central and peripheral nervous systems, including left-right asymmetry (fig. S3B) and nine types of apparently ciliated neurons (fig. S3, C and D). This complexity is surprising, given the relatively "sedentary"

lifestyle of adult parasites in the portal vasculature (9).

Schistosome muscle is also very heterogeneous, with eight muscle clusters that possess distinctive expression patterns (fig. S5, A to C). Some populations occur diffusely throughout the animal (muscle 1 and muscle 2), whereas others are anatomically restricted, such as muscle 7 cells that reside next to the gut, suggesting that they are enteric muscles.

Similar to planarians (12), many morphogens that regulate Wnt (fig. S6, A to D) and TGF- β signaling (fig. S6, E to H) are expressed in muscle and neuronal cells of schistosomes. Homologs of many of these genes are expressed specifically in planarian muscles (1) and have been implicated in regeneration in planarians (12). Though schistosomes survive amputation (13), there is no evidence of whole-body regeneration. This expression pattern in a nonregenerative animal suggests that these genes may regulate schistosome neoblasts during homeostasis.

The pathology of schistosome infection is driven by the host's inflammatory responses to parasite eggs (14). Thus, we examined the differences between male, sexually mature female, and age-matched virgin females at the cellular level (Fig. 2A). All adult parasites have germline stem cells (GSCs) marked by expression of *nanos1* (6). Our scRNA-seq data revealed that GSCs have very similar gene expression regardless of sex or maturity (Fig. 2B and fig. S7A). Like GSCs, GSC progeny fall into the same clusters in both male and female parasites, suggesting no major sex- or maturation-dependent differences in early gametogenesis (Fig. 2C and fig. S7B). However, later germ cells cluster according to sex, with expression of late female germ cell markers found predominantly in mature females (Fig. 2D and fig. S7C) and late male germ cell markers found only in males (fig. S7D).

The sexually mature schistosome ovary is structured such that GSCs reside at the anterior end and mature oocytes at the posterior end (6, 15). The GSC marker *nanos1* is expressed in the proliferative anterior compartment (Fig. 2B, top, and fig. S8, A to D), whereas the late female germ cell marker *bmpg* is expressed most highly in the posterior ovary (Fig. 2D, top, and fig. S8C). Our scRNA-seq data show that the GSC progeny cluster sits between GSCs and late female germ cells on the uniform manifold approximation and projection (UMAP) plot (Fig. 2A), with the GSC progeny marker *meiob* expressed most highly between the anterior and posterior ovary (Fig. 2C and fig. S7B). Concurrent visualization of these clusters reveals an organized linear architecture (fig. S8E). Notably, both mature and virgin females express the marker *meiob* (Fig. 2C), suggesting that virgin female GSCs express differentiation markers without

¹Department of Pharmacology, UT Southwestern Medical Center, Dallas, TX 75390, USA. ²Center for Discovery and Innovation in Parasitic Diseases, Skaggs School of Pharmacy and Pharmaceutical Sciences, University of California, San Diego, 9500 Gilman Dr., La Jolla, CA 92093, USA. ³Department of Biochemistry, UT Southwestern Medical Center, Dallas, TX 75390, USA.

*These authors contributed equally to this work.
†Corresponding author. Email: jamesj.collins@utsouthwestern.edu

male stimulus. Thus, male parasites may regulate this developmental checkpoint by promoting survival of differentiating GSCs rather than by inducing commitment, consistent with studies suggesting that male-female pairing can suppress apoptosis in the vitellaria of virgin female worms (16).

We also examined the vitellaria, another male-sensitive, stem cell-dependent tissue that

produces the yolk cells of the parasite's eggs. Despite a different function and organization, we observed parallels between ovary and vitellaria maturation, such as an apparent lineage from stem cell to mature tissue (fig. S9, A to D). We also found a low frequency of vitellocyte-like cells in males (17) (fig. S9A). Finally, we identified pairing-independent sexual tissues such as the flatworm-specific Mehlis' gland,

which plays an enigmatic role in egg production (9) (fig. S9E).

In addition to sexual tissues, we observed sexual dimorphism in nonreproductive tissues, including three muscle clusters (muscles 5, 6, and 8) that appear to be largely restricted to female parasites (table S3), with muscle 8 representing muscle cells that surround the ovary (fig. S10). In some cases, we observed

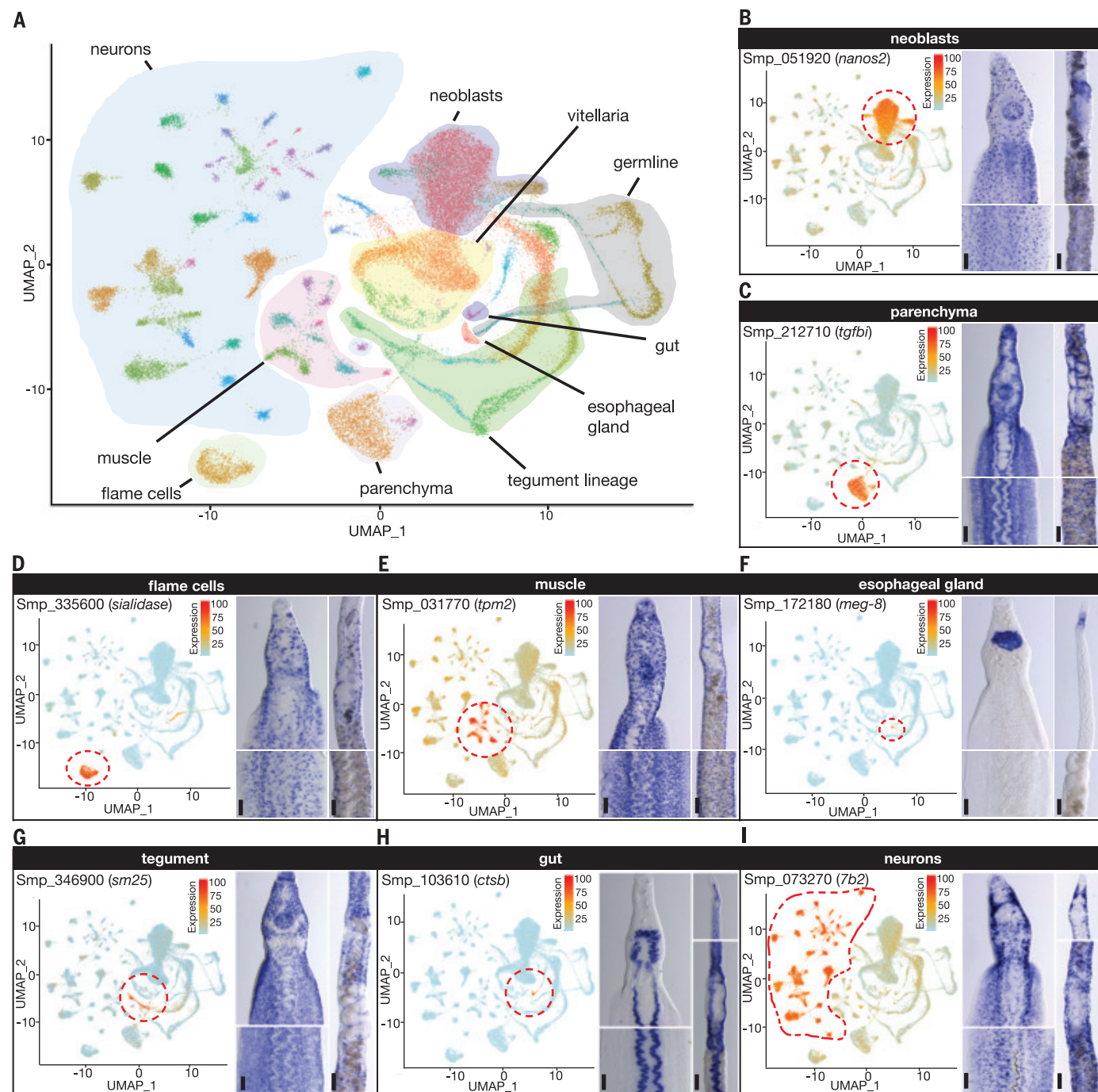


Fig. 1. *S. mansoni* single-cell atlas. (A) UMAP plot of the 68 scRNA-seq clusters. (B to I) UMAP plot (left) and whole-mount in situ hybridization (WISH) of the indicated gene and its expression in the noted tissue in the head (middle, top) and body (middle, bottom) of a male and the ovary (right, top) [(B) to (E) and (G)]

or the head (right, top) [(F), (H), and (I)] and vitellaria (right, bottom) of a mature female parasite. Scale bars are 100 μ m. UMAP plots are colored by gene expression (blue is low, and red is high). The regions enclosed by red dashed lines indicate the location of the relevant clusters on the UMAP plot.

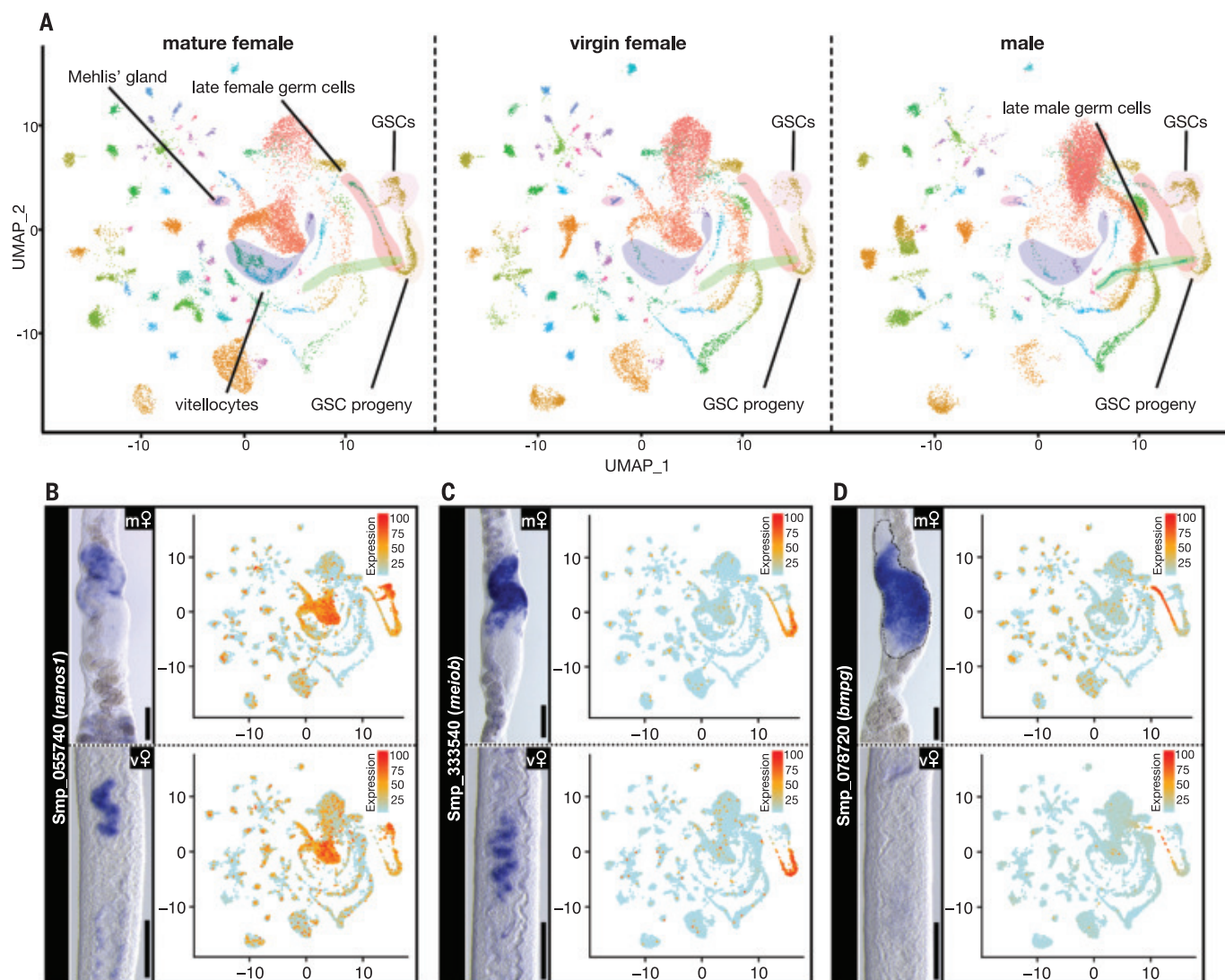


Fig. 2. The germ lineage in schistosome ovaries. (A) UMAP plots of all clusters split by parasite sex. Sexual tissues are labeled. (B to D) WISH (left) and UMAP plot (right) of gene expression of the indicated gene in sexually mature females (m♀) (top) and virgin females (v♀) (bottom) for the GSC marker *nanos1* (B), the GSC progeny marker *meiob* (C), and the late female germ cell marker *bmpg* (D). The dashed line in (D) indicates the boundary of the ovary. Scale bars are 100 μ m. UMAP plots are colored by gene expression (blue is low, and red is high).

unexpected numbers of male cells in clusters of female sexual tissues, which we attribute to neoblasts expressing low levels of differentiated tissue markers, similar to what has been observed in planarians (1) (fig. S11 and supplementary text).

Egg production is the primary driver of pathology, but this pathology is exacerbated by the parasite's stem cell-mediated longevity (3). Previous work suggests that adult neoblasts are molecularly homogeneous and predominantly give rise to cells involved in tegument production (4, 5), but free-living flatworms are known to possess functionally distinct neoblasts that produce specific tissues (18). We identified a subpopulation of neoblasts (*eled*⁺ neoblasts) that formed a putative nontegument lineage as suggested by a linear “path” of cells from *eled*⁺ neoblasts to the gut (Fig.

3A and fig. S12, A to F). These *eled*⁺ neoblasts expressed *hnf4* (Fig. 3A and fig. S12, B and C), a marker of gut neoblasts in planarians (18). Given the importance of gut-mediated blood digestion for egg production (19), we sought to perturb this lineage by RNA interference (RNAi) of genes expressed in this lineage (fig. S13, A and B). We found that knocking down *hnf4* resulted in a ~3.8-fold increase in *eled*⁺ neoblasts (Fig. 3B and fig. S13, C to F) and a concomitant decrease in the expression of several gut markers (fig. S14, A and B). Indeed, RNA-seq on *hnf4*(RNAi) animals demonstrated that more than 70% of transcripts expressed in the gut cluster were down-regulated (fig. S14, C and D; and table S4).

To understand whether stem cells functioned normally in *hnf4*(RNAi) animals, we first looked at apoptosis using terminal deoxy-

nucleotidyl transferase-mediated deoxyuridine triphosphate nick end labeling (TUNEL) and found no difference in *hnf4*(RNAi) animals, ruling out increased cell death (fig. S15A). Next, we looked at tegument production using 5-ethynyl-2'-deoxyuridine (EdU) pulse-chase approaches. We found a significant increase in tegument production in *hnf4*(RNAi) animals compared with controls (fig. S15, B and C), ruling out a broad stem cell-differentiation defect. Our ability to monitor new gut production by EdU pulse-chase approaches was complicated by the fact that gut marker expression was largely absent in most *hnf4*(RNAi) parasites (fig. S14, A and B). In cases where we could detect gut marker expression in EdU pulse-chase experiments, we found that gut-like tissue was being produced in *hnf4*(RNAi) parasites but was morphologically abnormal

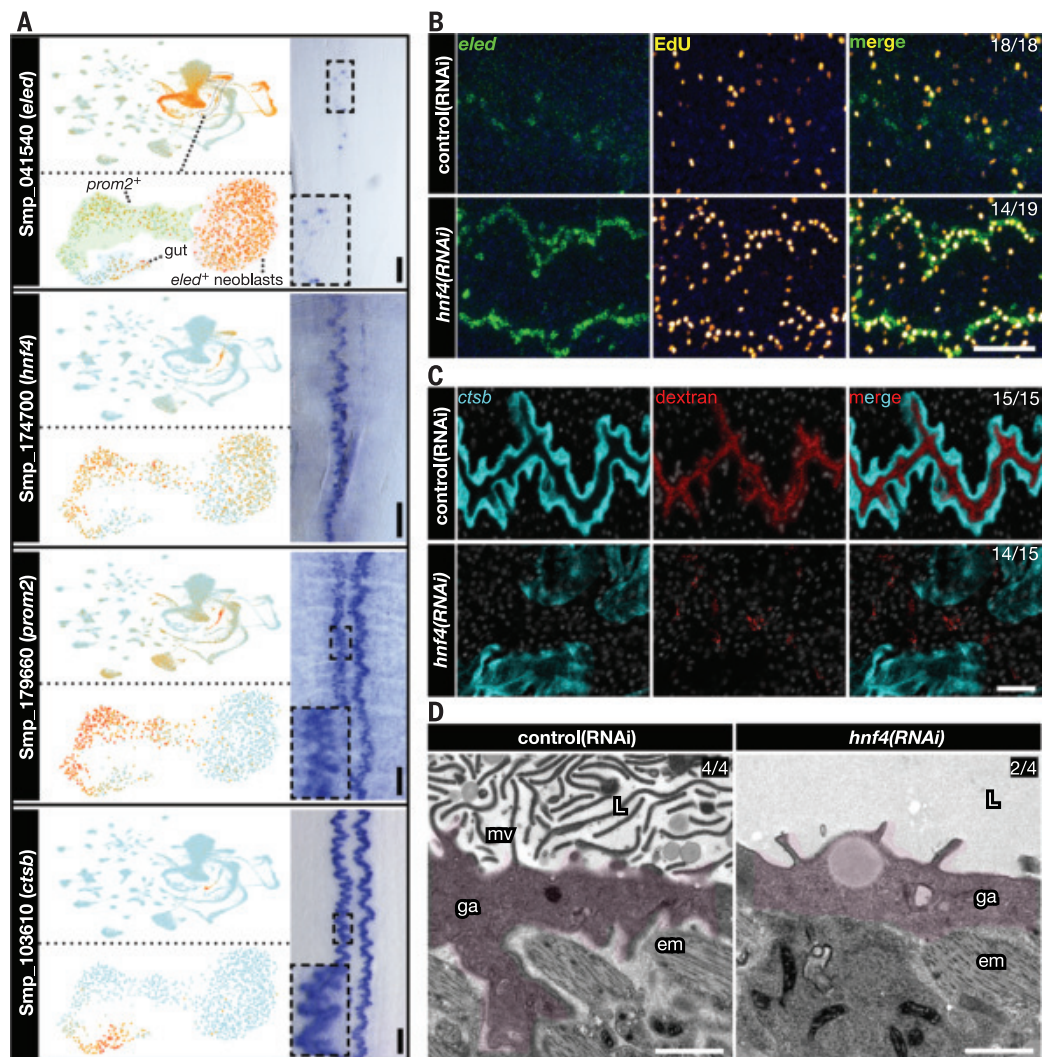


Fig. 3. An *hnf4* homolog regulates a previously uncharacterized gut lineage. (A) UMAP plots of the expression pattern of the indicated gene on the original dataset (left, top) or the reclustered dataset (left, bottom) and a colorimetric WISH (right) of a male parasite's trunk for *eled*, *hnf4*, *prom2*, and *ctsb*. The insets show magnifications of the regions enclosed by the dashed boxes. (B) FISH and EdU labeling showing the expression of *eled* (green) and EdU⁺ proliferative cells (yellow) in control(RNAi) or *hnf4*(RNAi) animals. *n* ≥ 18 parasites, two biological replicates. (C) FISH of *ctsb* (cyan) and fluorescent

dextran (red) in the gut lumen in control(RNAi) and *hnf4*(RNAi) animals. *n* = 15 parasites, three biological replicates. (D) TEM micrographs, showing the gut of control(RNAi) and *hnf4*(RNAi) animals. mv, microvilli; ga, gastrodermis; L, lumen; em, enteric muscle. *n* = 4 parasites, two biological replicates. Nuclei are blue or gray in (B) and (C), respectively. The number of parasites similar to the representative image is in the upper-right corner of each panel. Scale bars are 100 μm in (A), 50 μm in (B), 20 μm in (C), and 1 μm in (D). UMAP plots are colored by gene expression (blue is low, and red is high).

(fig. S15D). Examination of the expression of *eled* and the gut marker *ctsb* revealed that locations where *eled*⁺ neoblasts were abundant lacked normal gut tissue (fig. S15E). This suggests that the impairment of gut production is at least partially responsible for the gut defects after *hnf4* RNAi.

To assess gut structure, we next supplemented the culture media of *hnf4*(RNAi) parasites with fluorescently labeled dextran [which labels the gut lumen (20)]. After 12 hours of culture, all control(RNAi) parasites, but only 1 out of 15 *hnf4*(RNAi) parasites, had dextran in the lumen (Fig. 3C). The dextran failed to enter the digestive tract of the *hnf4*(RNAi) parasites (fig. S16A), suggesting either a com-

plete loss of patency or a defect in the parasite's ability to coordinate dextran ingestion. We then examined *hnf4*(RNAi) animals by transmission electron microscopy (TEM). The schistosome gut is a syncytial blind tube-like structure with a microvilli-filled lumen (21). Though gut tissue was still present, we found a significant decrease in luminal microvilli (Fig. 3D and fig. S16B) and two out of four *hnf4*(RNAi) animals had dilated lumens compared with controls (fig. S16C).

To assess the digestive capability of *hnf4*(RNAi) parasites, we added red blood cells (RBCs) to the media and observed the parasites' ability to uptake and digest the cells. *hnf4*(RNAi) parasites failed to either ingest (15/69) or digest

RBCs (54/69) (Fig. 4A and fig. S17A). Because we observed a decrease in the expression of proteolytic enzymes by RNA-seq (table S4), we studied whether *hnf4* RNAi resulted in loss of cysteine (cathepsin) protease activity [which contributes to hemoglobin digestion (22, 23)]. By measuring cathepsin activity of lysates in *hnf4*(RNAi) parasites using a fluorogenic peptidyl substrate, we found that cathepsin B activity was decreased 8.2-fold relative to that in control parasites (Fig. 4B), consistent with gene expression analyses (table S4). By contrast, aspartyl protease activity was similar in control and *hnf4*(RNAi) parasites (fig. S17B), which could reflect expression of aspartic proteases in nongut tissues that were unaffected after

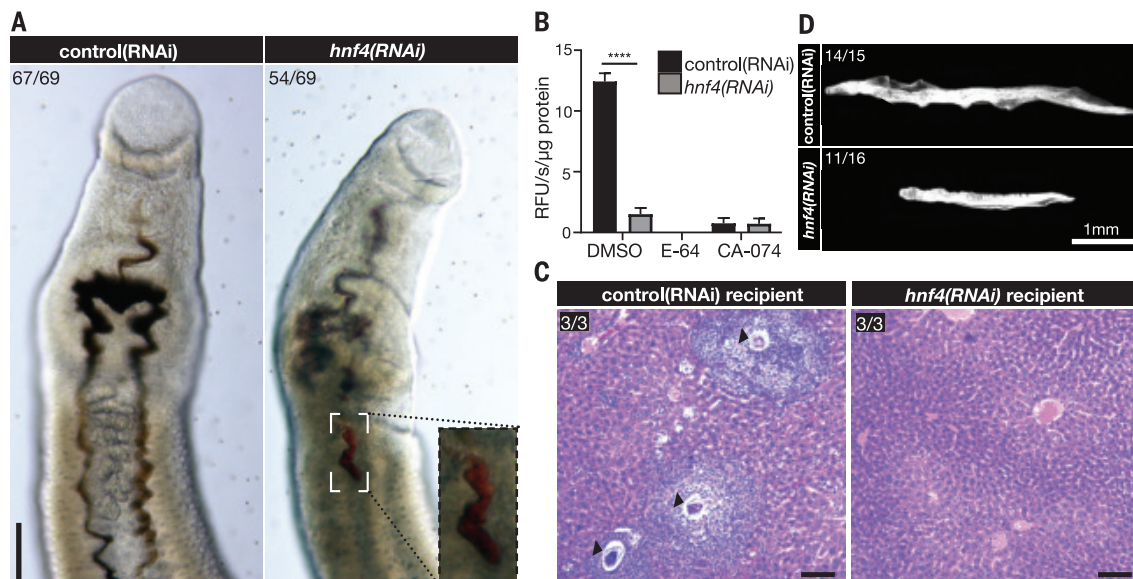


Fig. 4. *hnf4* is required for blood feeding and pathology. (A) Brightfield microscopy images of control(RNAi) or *hnf4*(RNAi) animals cultured with RBCs. The inset shows a magnification of the boxed area. (B) Cathepsin activity of lysates from control(RNAi) or *hnf4*(RNAi) animals, as determined by cleavage of Z-FR-AMC peptide substrate with no inhibitor [dimethyl sulfoxide (DMSO)], a broad cysteine protease inhibitor (E-64), or a cathepsin B-selective inhibitor (CA-074). $n = 3$ biological replicates of assays carried out in technical triplicates. Error bars indicate

95% confidence interval. **** $p < 0.0001$ (Welch's t test). RFU, relative fluorescence units. (C) Hematoxylin and eosin (H&E)-stained mouse liver sections 22 days after transplant with RNAi-treated parasites. Arrowheads show granulomata. Sections are from $n = 3$ recipients. (D) Parasites recovered from transplant recipients. $n > 15$ parasites from three recipients. Nuclei are white. The number of parasites or sections similar to the representative micrograph is in the upper-left corner of each panel. Scale bars are 100 μm in (A) and (C) and 1 mm in (D).

hnf4 RNAi (tables S1 and S4). Together, these data suggest that *hnf4* is at least indirectly required for the digestion of hemoglobin, in part by regulating the expression of cathepsin B, which is a key contributor to the digestion of blood proteins, including hemoglobin (22, 23), in *S. mansoni*.

We examined whether *hnf4* was required to cause disease in the host by transplanting control and *hnf4*(RNAi) parasites into uninfected mice and then perfusing the mice 22 to 30 days after transplant. Worm recovery was statistically indistinguishable [control(RNAi) = 72% versus *hnf4*(RNAi) = 49%, $p = 0.136$, Welch's t test] (fig. S17C). This observation is not entirely unexpected because schistosomes can acquire nutrients through their tegument (19). Nonetheless, mice receiving *hnf4*(RNAi) parasites had morphologically normal livers in contrast to abundant egg-induced granulomata in livers of control parasite recipients (Fig. 4C and fig. S17D). Additionally, recovered male *hnf4*(RNAi) parasites were significantly shorter than controls (2.87 versus 5.21 mm, respectively; $p < 0.0001$; Welch's t test) (Fig. 4D and fig. S17E). These results show that *hnf4* is at least indirectly required for parasite growth and egg-induced pathology in vivo. Together, these data suggest that *hnf4*, specifically, and gut homeostasis, generally, are potential therapeutic targets to blunt the pathology caused by adult parasites.

Here, we describe a comprehensive single-cell atlas of the adult schistosome, identify

regulators of gut biology, and leverage this knowledge to experimentally block schistosome-induced pathology in the host. We envision these data serving as a catalyst toward understanding other aspects of schistosome biology (e.g., reproductive biology) and serving as a foundation for understanding the development of various cellular lineages during the parasite life cycle. Indeed, our approach serves as a template for the investigation of other understudied and experimentally challenging parasitic metazoans, improving our understanding of their biology and enabling the discovery of therapies for these pathogens.

REFERENCES AND NOTES

- C. T. Fincher, O. Wurtzel, T. de Hoog, K. M. Kravarik, P. W. Reddien, *Science* **360**, eaaq1736 (2018).
- B. Wang et al., *eLife* **7**, e35449 (2018).
- J. J. Collins III et al., *Nature* **494**, 476–479 (2013).
- G. R. Wendt et al., *eLife* **7**, e33221 (2018).
- J. J. Collins III, G. R. Wendt, H. Iyer, P. A. Newmark, *eLife* **5**, e12473 (2016).
- J. Wang, J. J. Collins III, *Int. J. Parasitol.* **46**, 405–410 (2016).
- G. P. Dillon, J. C. Illes, H. V. Isaacs, R. A. Wilson, *Parasitology* **134**, 1589–1597 (2007).
- Z. Lu et al., *Sci. Rep.* **6**, 31150 (2016).
- P. F. Basch, *Schistosomes: Development, Reproduction, and Host Relations* (Oxford Univ. Press, 1991).
- R. A. Wilson, L. A. Webster, *Biol. Rev. Camb. Philos. Soc.* **49**, 127–160 (1974).
- L. E. Cote, E. Simental, P. W. Reddien, *Nat. Commun.* **10**, 1592 (2019).
- J. N. Witley, M. Mayer, D. E. Wagner, J. H. Owen, P. W. Reddien, *Cell Rep.* **4**, 633–641 (2013).
- I. Popiel, D. L. Irving, P. F. Basch, *Tissue Cell* **17**, 69–77 (1985).
- E. J. Pearce, A. S. MacDonald, *Nat. Rev. Immunol.* **2**, 499–511 (2002).

- P. M. Nollen, R. D. Floyd, R. G. Kolzow, D. L. Deters, *J. Parasitol.* **62**, 227–231 (1976).
- S. E. Galanti, S. C. Huang, E. J. Pearce, *PLOS Negl. Trop. Dis.* **6**, e1509 (2012).
- M. K. Shaw, D. A. Erasmus, *J. Helminthol.* **56**, 51–54 (1982).
- J. C. van Wolfswinkel, D. E. Wagner, P. W. Reddien, *Cell Stem Cell* **15**, 326–339 (2014).
- P. J. Skelly, A. A. Da'dara, X. H. Li, W. Castro-Borges, R. A. Wilson, *PLOS Pathog.* **10**, e1004246 (2014).
- S. L. Hall et al., *Mol. Biochem. Parasitol.* **179**, 18–29 (2011).
- G. P. Morris, *Experientia* **24**, 480–482 (1968).
- C. R. Caffrey, L. Goupil, K. M. Rebello, J. P. Dalton, D. Smith, *PLOS Negl. Trop. Dis.* **12**, e0005840 (2018).
- M. Sajid et al., *Mol. Biochem. Parasitol.* **131**, 65–75 (2003).
- J. Collins, A single-cell RNAseq atlas of *Schistosoma mansoni* identifies a key regulator of blood feeding, v2, dataset. Dryad (2020); <https://doi.org/10.5061/dryad.0k6dj9h9xk>.

ACKNOWLEDGMENTS

We thank C. Paz for technical assistance and G. Hon for expertise in scRNA-seq library preparation. Schistosome-infected mice and *Biomphalaria glabrata* snails were provided by the National Institute of Allergy and Infectious Diseases (NIAID) Schistosomiasis Resource Center of the Biomedical Research Institute (Rockville, MD, USA) through National Institutes of Health (NIH)-NIAID contract HHSN2722017000141 for distribution through BEI Resources. FACS was performed with the aid of the Moody Foundation Flow Cytometry Facility at the University of Texas Southwestern Medical Center (UTSW). TEM imaging and sample preparation was performed with the aid of the Electron Microscopy Core at UTSW. RNA-seq was performed with the aid of the McDermott Center Next Generations Sequencing Core at UTSW. **Funding:** This work was supported by NIH grants R01 R01A121037 (J.J.C.), R01 R01A150715 (M.L.R.), R21 R21A133393 (A.J.O.D.), and F30 F30A131509-01A1 (G.W.); Welch Foundation grants I-1948-20180324 (J.J.C.) and I-1936-20170325 (M.L.R.); National Science Foundation grant MCB1553334 (M.L.R.); the Burroughs Wellcome Fund (J.J.C.); Wellcome Trust grant 107475/Z/15/Z (J.J.C.); and Bill and Melinda Gates Foundation grant OPP1171488 (C.R.C.). **Author contributions:** Conceptualization: G.W., L.Z., R.C., C.L., A.J.O.D., C.R.C., J.J.C.; Investigation: G.W., L.Z., R.C., C.L., J.J.C.; Designing web-based resources: M.L.R.; Writing – original draft: G.W., L.Z., J.J.C.; Writing – review and editing: all authors. **Competing interests:** The authors declare no competing interests.

Data and materials availability: A searchable database of scRNA-seq data can be accessed at www.collinslab.org/schistocyte; raw scRNA-seq plots can be accessed at Dryad (24). Raw and some processed data from scRNA-seq and *hnf4* RNAi RNA-seq experiments have been deposited in the NCBI Gene Expression Omnibus under accession number GSE146737.

SUPPLEMENTARY MATERIALS

science.sciencemag.org/content/369/6511/1644/suppl/DC1
Materials and Methods
Supplementary Text
Figs. S1 to S18
Tables S1 to S7

References (25–34)
MDAR Reproducibility Checklist

17 March 2020; accepted 31 July 2020
10.1126/science.abb7709

PARASITE GENETICS

Large-scale RNAi screening uncovers therapeutic targets in the parasite *Schistosoma mansoni*

Jipeng Wang^{1*}, Carlos Paz^{1*}, Gilda Padalino², Avril Coghlan³, Zhigang Lu³, Irina Gradinaru¹, Julie N. R. Collins¹, Matthew Berriman³, Karl F. Hoffmann², James J. Collins III^{1†}

Schistosome parasites kill 250,000 people every year. Treatment of schistosomiasis relies on the drug praziquantel. Unfortunately, a scarcity of molecular tools has hindered the discovery of new drug targets. Here, we describe a large-scale RNA interference (RNAi) screen in adult *Schistosoma mansoni* that examined the function of 2216 genes. We identified 261 genes with phenotypes affecting neuromuscular function, tissue integrity, stem cell maintenance, and parasite survival. Leveraging these data, we prioritized compounds with activity against the parasites and uncovered a pair of protein kinases (TAO and STK25) that cooperate to maintain muscle-specific messenger RNA transcription. Loss of either of these kinases results in paralysis and worm death in a mammalian host. These studies may help expedite therapeutic development and invigorate studies of these neglected parasites.

Studies of gene function in intramammalian schistosome parasites have been limited to relatively small numbers of genes (1). Therefore, we developed a large-scale RNA interference (RNAi) screening platform on adult schistosomes that prioritized a list of 2320 of the worm's ~10,000 protein-coding genes (fig. S1A and table S1). We generated double-stranded RNAs (dsRNAs) and treated adult male and female pairs with dsRNA over the course of a 30-day experiment (Fig. 1A). After filtering genes that either did not amplify by polymerase chain reaction or failed to generate sufficient concentrations of dsRNA, a total of 2216 genes were screened (table S1).

Schistosomes live in the veins surrounding the host intestines and attach to the vascular endothelium to avoid being swept away in the blood and trapped in host organs. Under in vitro culture conditions, healthy parasites attach to the substrate with a combination of their oral and ventral suckers (movie S1). We thus reasoned that substrate attachment would be a useful quantitative metric to define RNAi treatments that affect parasite vitality and to predict in vivo survival. Therefore, we monitored parasites for 30 days to identify substrate attachment and other visible defects.

Schistosomes possess adult somatic stem cells (neoblasts) that rejuvenate parasite tissues, including the intestine and tegument (skin) (2, 3). The parasites also contain large numbers of proliferative germline stem cells (GSCs) in their reproductive organs (2) that are essential for producing eggs, the central drivers of parasite-induced pathology in vivo (4). Therefore, we monitored the maintenance of neoblasts and GSCs by labeling parasites with the thymidine analog ethynyl deoxyuridine (EdU) before the conclusion of the experiment (Fig. 1A). Because of the variable rate at which the reproductive organs of female worms degenerate during in vitro culture (5), stem cell proliferation was only monitored in male worms. For genes with RNAi phenotypes uncovered during our screen, we confirmed gene identity by sequencing and mitigated potential off-target effects by designing an additional dsRNA targeting a nonoverlapping gene region or by examining sequence identity of hits with other *Schistosoma mansoni* genes (fig. S1). These studies identified 195 genes with fully penetrant attachment phenotypes, of which 121 possessed phenotypes in addition to attachment, including tissue and intestinal edema (36 genes), head (26) and/or tegument (78) degeneration, muscular hypercontraction (6), and death (36) (Fig. 1B and table S2). RNAi of an additional 66 genes resulted in stem cell maintenance defects but caused no other visible phenotypes (e.g., attachment), suggesting an essential role for stem cell maintenance (fig. S2 and table S3). We cannot rule

out the possibility of false negatives among the genes with no phenotype and encourage greater scrutiny of such genes by alternate knockdown approaches or analysis of different phenotypic readouts.

Of the 66 genes required for stem cell survival, RNAi of over 90% (60 of 66) led to defects in the maintenance of both proliferative cells in the male testes and neoblasts (fig. S2). However, for a minority of genes, this maintenance defect appeared to be specific to either proliferative cells in the testes or neoblasts (fig. S2). Gene Ontology enrichment analysis identified genes important for protein translation, including gene products involved in ribosomal structure, tRNA aminoacylation, and ribosomal RNA (rRNA) processing as putative regulators of proliferative cell maintenance (fig. S3A). Although this could reflect an enhanced sensitivity of actively proliferating cells to alterations in protein translation, studies have highlighted “non-housekeeping” roles for translational regulators in controlling stem cell function (6).

Of the 195 genes essential for parasite attachment, a large fraction share sequence similarity with other organisms, including other medically relevant schistosome species (table S4). Additionally, most genes with an attachment phenotype (172 of 195 genes; 88%) possess a close homolog from *Caenorhabditis elegans* or *Drosophila melanogaster* that likewise has a loss-of-function phenotype (table S5). Gene Ontology analyses of genes with attachment phenotypes further revealed that the dominant group of enriched genes were those encoding components necessary for protein turnover via the ubiquitin-proteasome system (UPS) (fig. S3B). Proteolysis is important for larval and adult viability in vitro (7, 8), and our data identified that key components from virtually every arm of the UPS were required for adult parasite vitality during in vitro culture (fig. S4A). Indeed, RNAi of nearly all UPS components resulted in extensive tissue degeneration and in some cases adult parasite death (fig. S4, B and C).

To determine if any genes associated with attachment phenotypes encoded proteins targeted by existing pharmacological agents, we searched the literature and the ChEMBL database (table S6) (9). This analysis uncovered 205 compounds potentially targeting 49 *S. mansoni* proteins. We selected 14 of these compounds (table S7) and examined the activities of these compounds on worms cultured

¹Department of Pharmacology, UT Southwestern Medical Center, Dallas, TX 75390, USA. ²Institute of Biological, Environmental and Rural Sciences (IBERS), Aberystwyth University, Aberystwyth, Wales, UK. ³Wellcome Sanger Institute, Wellcome Genome Campus, Hinxton, Cambridge CB10 1SA, UK.

*These authors contributed equally to this work.

†Corresponding author. Email: jamesj.collins@utsouthwestern.edu

in vitro either by automated worm movement tracking or on the basis of parasite attachment. More than half of the compounds tested (8 of 14) on worms at 10 μ M reduced parasite movement by >75%, and half of the compounds (7 of 14) caused fully penetrant substrate attachment defects by day 7 posttreatment (Fig. 2, A and B, and movie S2). Similarly, seven of these compounds affected the movement of post-infective larvae (schistosomula), suggesting activity against multiple life cycle stages (table S8).

Among the compounds that emerged from these studies was simvastatin, a 3-hydroxy-3-methylglutaryl coenzyme A reductase inhibitor with known effects on parasites both in vitro and in vivo (10). The proteasome inhibitor ixazomib affected both schistosome movement (Fig. 2A) and attachment (Fig. 2B), mirroring results in a recent report of the proteasome inhibitor bortezomib (7). However, the most potent effects on adult parasites were observed with CB-5083 and NMS-873, which inhibit the UPS component p97 by either competing with adenosine triphosphate (ATP) (11) or binding to an allosteric site (12), respectively (fig. S5A). Similar to the death observed after long-term p97 RNAi treatment (Fig. 1B), both p97 inhibitors led to death in vitro (movie S3). Despite their distinct biochemical mechanisms of action, we noted similar deformations in the structure of the parasite tegument after treatment with either

CB-5083 or NMS-873, suggesting that these compounds have similar pharmacological effects on the parasite (Fig. 2C).

We then assessed if NMS-873 and CB-5083 affected UPS function by measuring the accumulation of ubiquitinated proteins using an antibody that recognizes Lys⁴⁸ (K48) polyubiquitinated proteins marked for proteasome-mediated destruction (13). We observed the accumulation of polyubiquitinated proteins after RNAi of p97 and after treatment of schistosomes with either CB-5083 or NMS-873 (fig. S5B). Consistent with CB-5083 or NMS-873 acting via p97 inhibition to blunt protein degradation, we found that p97 RNAi treatment together with low concentrations of either drug led to additive increases in polyubiquitinated protein accumulation (fig. S5C). We also observed accumulation of polyubiquitinated proteins after either RNAi of *proteasome subunit beta type-2* or treatment with ixazomib (fig. S5D). These effects on the degradation of ubiquitinated proteins appeared to be specific to inhibition of UPS function rather than a nonspecific effect due to reduced worm vitality (fig. S5D).

We then depleted UPS components using RNAi and surgically transplanted these worms into the mesenteric veins of recipient mice (fig. S6A), and we measured parasite egg deposition in host tissues and parasite survival. After hepatic portal perfusion, we recovered

about 55% of transplanted control RNAi-treated worms (Fig. 2D and fig. S6B), and these parasites established patent infections, depositing large number of eggs into the livers of recipient mice (Fig. 2E and fig. S6, C and D). By contrast, we failed to recover parasites after hepatic portal perfusion of mice receiving p97 (Fig. 2D) or *proteasome subunit beta type-2* (fig. S6B). As a consequence, the livers in these mice were devoid of eggs, and we observed no signs of egg-induced granulomata (Fig. 2E and fig. S6, C and D). We also observed RNAi-treated parasites at various stages of infiltration by host immune cells (fig. S6, E and F). This suggests that these parasites are unable to remain in the portal vasculature and are cleared via the liver by the immune system. Taken together, these data highlight the essentiality and druggability of the schistosome UPS.

Another group of potentially druggable targets to emerge from our RNAi screen were protein kinases, 19 of which led to defects in either parasite attachment or stem cell maintenance. RNAi of two STE20 serine-threonine kinases, *tao* and *stk25*, which are homologs of the human TAO1/2/3 and STK25/YSK1 protein kinases, respectively, led to rapid detachment from the substrate (fig. S7A) and a concomitant posterior paralysis and hypercontraction of the body, such that the parasites took on a distinctive “banana”-shaped morphology (Fig. 3A, fig. S7B, and movie S4).



Fig. 1. Summary of RNAi phenotypes. (A) RNAi treatment regimen. Parasites were monitored for visible abnormalities, and at day 29 EdU was added to medium to label proliferative cells. (B) Categories of RNAi phenotypes observed. *kin-17* (Smp_023250), *cog1* (Smp_132980), *p97* (Smp_018240), *c44* (Smp_136260), *prpf4b* (Smp_068960), *gtf2f1* (Smp_088460), *stk25* (Smp_096640). Scale bar, 100 μ m.

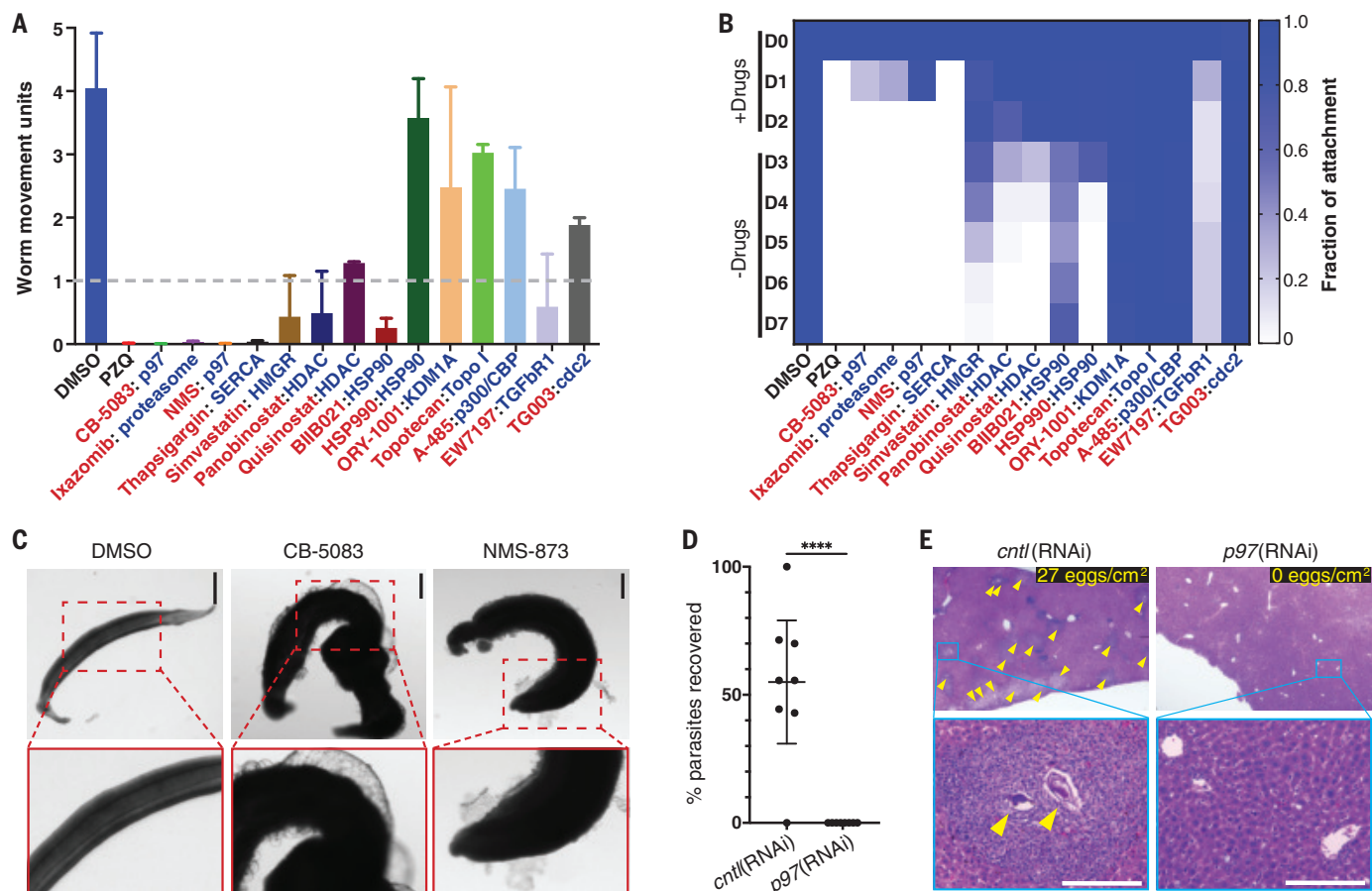


Fig. 2. Compounds prioritized from RNAi studies have effects on schistosomes in vitro. (A) Effects on worm motility of compounds (red text) at 10 μ M for 72 hours predicted to target schistosome proteins (blue text) essential for parasite attachment. $n = 12$ worm pairs, evaluated in three biological replicates. Data are means \pm SD. Dashed line, threshold for 75% reduction in motility. DMSO, dimethyl sulfoxide (control). (B) Heat map showing time course for the fraction of male worms attached to the substrate after treatment with compounds for 72 hours as in (A). Three biological replicates were

performed. (C) Effects of CB-5083 or NMS-873 (10 μ M, 72 hours) treatment on male parasites. (D) Percent recovery of *p97(RNAi)* or control RNAi [*cntl(RNAi)*] male parasites surgically transplanted into mice. $n = 8$ transplants for each group. **** $P < 0.0001$, t test. Data are means \pm 95% confidence intervals (CIs). (E) Hematoxylin and eosin staining of livers from mice receiving control or *p97(RNAi)* parasites. Yellow arrowheads indicate egg-induced granulomata. (Top right) Counts of eggs per square centimeter of liver section are shown ($n = 3$ livers). Scale bars, 100 μ m [(C) and (E)].

Aside from RNAi of *stk25* and *tao*, this banana-shaped phenotype of worms was distinctive, as it was only observed after RNAi of a CCM3/PDCD10 homolog (*Smp_031950*), a known heterodimerization partner with the mammalian STK25 kinase (14). We failed to observe death of either *stk25*- or *tao*-depleted parasites during in vitro culture. However, after surgical transplantation, we noted a reduction in the recovery of *tao* or *stk25* RNAi-treated parasites from recipient mice, and these recipient mice displayed few signs of egg-induced granulomata formation (Fig. 3, B and C, and fig. S7, C and D). Thus, both *tao* and *stk25* appear to be essential for schistosome survival in vivo.

Given the distinct and specific nature of the *stk25*- and *tao*-associated banana phenotype, we reasoned that these kinases may act in concert to mediate signaling processes in the worm. The *Drosophila* STK25 ortholog (GCK3) is a substrate of TAO, and these proteins function in a signaling cascade essential for

tracheal development (15). Likewise, we observed that recombinant *S. mansoni* STK25 (SmSTK25) could serve as a substrate for the *S. mansoni* TAO (SmTAO) in an in vitro kinase assay (fig. S8, A and B). The human STK25 is activated by phosphorylation of a conserved threonine residue within its activation loop (16). By mass spectrometry, we observed that this conserved threonine (T) within the predicted SmSTK25 activation loop (T173) was phosphorylated after incubation of recombinant SmTAO with catalytically inactive SmSTK25 (fig. S8, C and D). Using an antibody that recognizes activation loop phosphorylation in STK25 orthologs (16), Western blotting revealed SmSTK25 T173 autophosphorylation after an in vitro kinase reaction; this signal was abrogated in controls lacking ATP and when the SmSTK25 catalytic K48 residue was mutated to arginine (R) (Fig. 3D and fig. S8E). Consistent with our mass spectrometry results, we detected robust phos-

phorylation of T173 when recombinant SmTAO was incubated with kinase-dead SmSTK25 (kdSmSTK25) (Fig. 3D), suggesting that SmTAO can phosphorylate a key residue for the activation of the mammalian STK25.

We reasoned that the schistosome TAO and STK25 might be acting in a signaling module to mediate critical processes in the parasite. To define these processes, we performed transcriptional profiling on RNAi-treated parasites just before observing detachment and hypercontraction (day 6 and day 9 for *tao* and *stk25* RNAi treatments, respectively) (fig. S9, A and B). We found that expression levels of differentially regulated genes after RNAi with either *tao* or *stk25* were correlated (Fig. 3E) and that more than half of these differentially regulated genes were common in both datasets (fig. S9C and table S9). Notably, RNAi of either *tao* or *stk25* was specific and did not affect expression of the other kinase gene of this pair (Fig. 3, E and F).

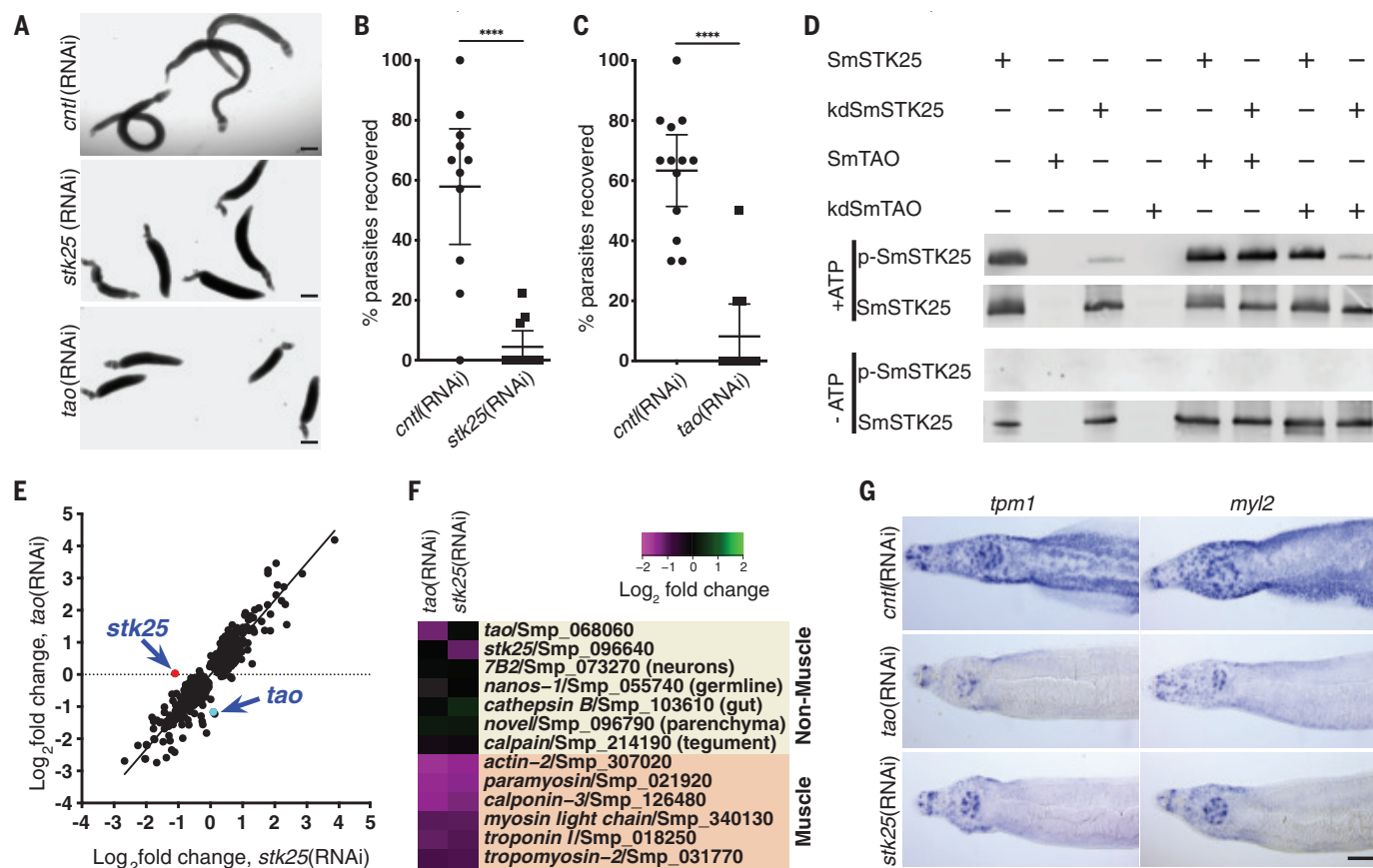


Fig. 3. The protein kinases SmSTK25 and SmTAO are essential to maintain muscular function. (A) RNAi of *stk25* or *tao* causes parasite hypercontraction. (B and C) Percent recovery of *stk25*(RNAi), *tao*(RNAi), or control(RNAi) male parasites surgically transplanted into mice. $n \geq 11$ transplants for each group. **** $P < 0.0001$, t test. Data are means \pm 95% CIs. (D) Western blot to detect phospho-T173 (p-SmSTK25) or total SmSTK25 after an in vitro kinase reaction with or without ATP. Data represent results

of two experiments. (E) Scatter plot showing the relationship between the differentially expressed genes [$P(\text{adjusted}) < 0.001$; Benjamini-Hochberg-corrected Wald test] after *stk25* or *tao* RNAi treatment ($r = 0.9$, $P < 0.0001$; Pearson correlation). (F) Heat map showing expression of tissue-specific transcripts after RNAi of *tao* or *stk25*. (G) In situ hybridization for *tropomyosin 1* (*tpn1*; Smp_340760) and a myosin light chain (*myl2*; Smp_132670) after RNAi at day 13. Scale bars, 500 μm (A) or 100 μm (G).

By examining the tissue-specific expression of differentially regulated genes on an adult schistosome single-cell expression atlas using cells from schistosome somatic tissues (17), we found that roughly 40% (51 of 129) of the most-down-regulated genes after *tao* and *stk25* RNAi were specific markers of parasite muscle cells (fig. S10, A to C, and table S9). Indeed, nearly half of all mRNAs specifically enriched in muscle cells (60 of 135) from this single-cell atlas, including key muscle contractile proteins, were down-regulated after RNAi of *tao* and *stk25* (Fig. 3F; fig. S10, B and D; and table S10). These transcriptional effects appeared to be largely specific to parasite muscles (Fig. 3F, fig. S10B, and table S10).

In principle, loss of muscle-specific mRNAs could be due to either loss of muscle cells or down-regulation of muscle-specific mRNAs. We therefore labeled F-actin in schistosome muscle fibers with phalloidin and performed in situ hybridization to detect muscle-specific mRNAs. RNAi-treated parasites exhibited a reduction in the expression of mRNAs encod-

ing the contractile proteins tropomyosin 1 and myosin light chain by in situ hybridization (Fig. 3G) but no qualitative defects in phalloidin staining of body wall muscles (fig. S11). Thus, it appears that these kinases are required to maintain the transcription of many muscle-specific mRNAs in intact muscle cells. The heads of *tao* and *stk25* RNAi parasites retained their capacity for movement (movie S4) and partially maintained the expression of muscle-specific mRNAs (Fig. 3G). Thus, there appears to be a relationship between the maintenance of muscle-specific mRNA expression and locomotion.

Taken in their entirety, our data suggest that STK25 and TAO kinases cooperate in the schistosome to mediate signaling essential for sustaining the transcription of muscle-specific mRNAs. As a consequence, loss of either SmSTK25 or SmTAO activity results in muscular function defects compromising parasite survival in vivo. As whole-body knockouts of mouse STK25 are homozygous viable and display no obvious deleterious phenotypes (18), SmSTK25

represents an attractive target for therapeutic intervention. Similar cross-examination of genes associated with other phenotypic classes (e.g., tissue edema) may provide insights into the specificity of the various phenotypes observed in this work.

Technological advances have paved the way for large-scale analyses of gene function in protozoan parasites (19–21), but such analyses have been lacking for helminth parasites. Our systematic analysis of gene function in schistosomes allowed us to effectively prioritize targets and potential specific inhibitors with activities on worms. Future efforts should further explore the potency and selectivity of not only the compounds our studies have uncovered (Fig. 2, A and B, and table S6) but also larger libraries of compounds with known molecular targets (22). However, to mitigate potential issues with host toxicity, it is also worth exploring whether parasite-selective inhibitors of validated target proteins can be uncovered. Not only does this study enhance our understanding of schistosome biology, but also it

provides a new lens to prioritize genes of interest in other medically and agriculturally important parasitic flatworms. Collectively, we anticipate such studies will expedite the discovery of new antihelminthics.

REFERENCES AND NOTES

1. A. Guidi *et al.*, *PLOS Negl. Trop. Dis.* **9**, e0003801 (2015).
2. J. J. Collins 3rd *et al.*, *Nature* **494**, 476–479 (2013).
3. J. J. Collins 3rd, G. R. Wendt, H. Iyer, P. A. Newmark, *eLife* **5**, e12473 (2016).
4. E. J. Pearce, A. S. MacDonald, *Nat. Rev. Immunol.* **2**, 499–511 (2002).
5. J. Wang, R. Chen, J. J. Collins 3rd, *PLOS Biol.* **17**, e3000254 (2019).
6. M. Buszczyk, R. A. Signer, S. J. Morrison, *Cell* **159**, 242–251 (2014).
7. B. Bibo-Verdugo *et al.*, *ACS Infect. Dis.* **5**, 1802–1812 (2019).
8. J. F. Nabhan, F. El-Shehaby, N. Patocka, P. Ribeiro, *Exp. Parasitol.* **117**, 337–347 (2007).
9. D. Mendez *et al.*, *Nucleic Acids Res.* **47** (D1), D930–D940 (2019).
10. L. Rojo-Arreola *et al.*, *PLOS ONE* **9**, e87594 (2014).
11. D. J. Anderson *et al.*, *Cancer Cell* **28**, 653–665 (2015).
12. P. Magnaghi *et al.*, *Nat. Chem. Biol.* **9**, 548–556 (2013).
13. K. Newton *et al.*, *Cell* **134**, 668–678 (2008).
14. D. F. Ceccarelli *et al.*, *J. Biol. Chem.* **286**, 25056–25064 (2011).
15. C. L. C. Poon *et al.*, *Dev. Cell* **47**, 564–575.e5 (2018).
16. C. Preisinger *et al.*, *J. Cell Biol.* **164**, 1009–1020 (2004).
17. G. Wendt *et al.*, *Science* **369**, 1644–1649 (2020).
18. M. Amrutkar *et al.*, *Diabetes* **64**, 2791–2804 (2015).
19. S. Alsfjord *et al.*, *Genome Res.* **21**, 915–924 (2011).
20. E. Bushell *et al.*, *Cell* **170**, 260–272.e8 (2017).
21. S. M. Sidik *et al.*, *Cell* **166**, 1423–1435.e12 (2016).
22. J. Jones *et al.*, *Proc. Natl. Acad. Sci. U.S.A.* **115**, 10750–10755 (2018).
23. J. Collins, Large-scale RNAi screening uncovers new therapeutic targets in the human parasite *Schistosoma mansoni*. Dryad (2020); doi:10.5061/dryad.zs7h44j4v.

ACKNOWLEDGMENTS

We thank M. McConathy, C. Furrh, and G. Pagliuca for technical assistance; F. Hunter and N. Bosc for advice about retrieving data from ChEMBL; and M. Cobb and E. Ross for suggestions regarding kinase studies. Infected mice and *Biomphalaria glabrata* snails were provided by the National Institute of Allergy and Infectious Diseases (NIAID) Schistosomiasis Resource Center of the Biomedical Research Institute (Rockville, MD, USA) through National Institutes of Health (NIH)-NIAID Contract HHSN2722017000141 for distribution through BEI Resources. **Funding:** The work was supported by the National Institutes of Health R01AI121037 (J.J.C.), the Welch Foundation I-1948-20180324 (J.J.C.), the Burroughs Wellcome Fund (J.J.C.), and the Wellcome Trust 107475/Z/15/Z (J.J.C., K.F.H., M.B.) and 206194 (M.B.). C.P. was supported by a Howard Hughes Medical Institute Gilliam Fellowship and National Science Foundation Graduate Research Fellowship SPA0001848. **Author contributions:** Conceptualization, J.W., C.P., M.B., K.F.H., J.J.C.; investigation, J.W., C.P., G.P., A.C., Z.L., I.G., J.N.R.C.; writing of original draft, J.W., C.P., J.J.C.; writing, review, and editing, all authors. **Competing interests:** The authors declare no competing interest. **Data and materials availability:** Videos of RNAi attachment phenotypes can be accessed at www.collinslab.org/schistocyte or in (23). RNA sequencing analyses have been deposited in the NCBI Gene Expression Omnibus (GSE146720).

SUPPLEMENTARY MATERIALS

science.sciencemag.org/content/369/6511/1649/suppl/DC1
Materials and Methods
Figs. S1 to S11
Tables S1 to S10
References (24–60)
Movies S1 to S4
MDAR Reproducibility Checklist

17 March 2020; accepted 31 July 2020
10.1126/science.abb7699

Y EVOLUTION

The evolutionary history of Neanderthal and Denisovan Y chromosomes

Martin Petr^{1*}, Mateja Hajdinjak^{1,2}, Qiaomei Fu^{3,4,5}, Elena Essel¹, Hélène Rougier⁶, Isabelle Crevecoeur⁷, Patrick Semal⁸, Liubov V. Golovanova⁹, Vladimir B. Doronichev⁹, Carles Laluzza-Fox¹⁰, Marco de la Rasilla¹¹, Antonio Rosas¹², Michael V. Shunkov¹³, Maxim B. Kozlikin¹³, Anatoli P. Derevianko¹³, Benjamin Vernot¹, Matthias Meyer¹, Janet Kelso^{1*}

Ancient DNA has provided new insights into many aspects of human history. However, we lack comprehensive studies of the Y chromosomes of Denisovans and Neanderthals because the majority of specimens that have been sequenced to sufficient coverage are female. Sequencing Y chromosomes from two Denisovans and three Neanderthals shows that the Y chromosomes of Denisovans split around 700 thousand years ago from a lineage shared by Neanderthals and modern human Y chromosomes, which diverged from each other around 370 thousand years ago. The phylogenetic relationships of archaic and modern human Y chromosomes differ from the population relationships inferred from the autosomal genomes and mirror mitochondrial DNA phylogenies, indicating replacement of both the mitochondrial and Y chromosomal gene pools in late Neanderthals. This replacement is plausible if the low effective population size of Neanderthals resulted in an increased genetic load in Neanderthals relative to modern humans.

Ancient DNA (aDNA) has transformed our understanding of human evolutionary history, revealing complex patterns of population migration and gene flow, including admixture from archaic humans into modern humans. Particularly important have been analyses of autosomal sequences (1, 2), which represent a composite of genealogies of any individual's ancestors. Although mitochondrial DNA (mtDNA) and Y chromosomes only provide information about single maternal and paternal lineages, they offer a distinctive perspective on various aspects of population history such as sex-specific migration, matrilocality and patrilocality, and variance in reproductive success between individuals (3–5). Furthermore, because of their lower effective population size (N_e) compared with that of autosomal loci, coalescent times of mtDNA and Y chromosomes sampled from two populations provide an upper bound for the last time they experienced gene flow.

The mtDNA and autosomal sequences of Neanderthals, Denisovans, and modern humans have revealed puzzling phylogenetic discrepancies. Autosomal genomes show that Neanderthals and Denisovans are sister groups that split from modern humans between 550 thousand and 765 thousand years (ka) ago (6). By contrast, the mtDNAs of Neanderthals and modern humans are more similar to one another [time to the most recent common ancestor (TMRCA) of 360 to 468 ka ago] than to the mtDNAs of Denisovans (7). Notably, ~400-ka-old early Neanderthals from Sima de los Huesos were shown to carry mitochondrial genomes related to Denisovan mtDNAs (8, 9). This suggests that Neanderthals originally carried a Denisovan-like mtDNA, which was later completely replaced through ancient gene flow from an early lineage related to modern humans (7, 9).

The Y chromosomes of Neanderthals and Denisovans should provide an additional source of information about population splits and gene flow events between archaic and modern humans or populations related to them. However, with the exception of a small amount of Neanderthal Y chromosome coding sequence (118 kb) (10), none of the male Neanderthals or Denisovans studied to date have yielded sufficient amounts of endogenous DNA to allow comprehensive studies of archaic human Y chromosomes.

Previous genetic studies identified two male Denisovans, Denisova 4 (55 to 84 ka old) and Denisova 8 (106 to 136 ka old) (11, 12), and two male late Neanderthals, Spy 94a (38 to 39 ka old) and Mezmaiskaya 2 (43 to 45 ka old) (13) (Fig. 1A). To enrich for Y chromosome DNA from these individuals, we performed hybridization capture using probes we designed to target ~6.9 Mb of the nonrecombining portion

¹Department of Evolutionary Genetics, Max Planck Institute for Evolutionary Anthropology, D-04103 Leipzig, Germany. ²The Francis Crick Institute, NW1 1AT London, UK. ³Key Laboratory of Vertebrate Evolution and Human Origins of Chinese Academy of Sciences, IVPP, CAS, Beijing 100044, China. ⁴CAS Center for Excellence in Life and Paleoenvironment, Beijing 100044, China. ⁵University of Chinese Academy of Sciences, Beijing 100049, China. ⁶Department of Anthropology, California State University, Northridge, Northridge, CA 91330-8244, USA. ⁷Université de Bordeaux, CNRS, UMR 5199-PACEA, 33615 Pessac Cedex, France. ⁸Royal Belgian Institute of Natural Sciences, 1000 Brussels, Belgium. ⁹ANO Laboratory of Prehistory 14 Linia 3-11, St. Petersburg 1990 34, Russia. ¹⁰Institute of Evolutionary Biology, Consejo Superior de Investigaciones Científicas, Universitat Pompeu Fabra, 08003 Barcelona, Spain. ¹¹Área de Prehistoria, Departamento de Historia, Universidad de Oviedo, 33011 Oviedo, Spain. ¹²Departamento de Paleobiología, Museo Nacional de Ciencias Naturales, Consejo Superior de Investigaciones Científicas, 28006 Madrid, Spain. ¹³Institute of Archaeology and Ethnography, Siberian Branch, Russian Academy of Sciences, Novosibirsk, Russia.

*Corresponding author. Email: mp@bodkan.net (M.P.); kelso@eva.mpg.de (J.K.)

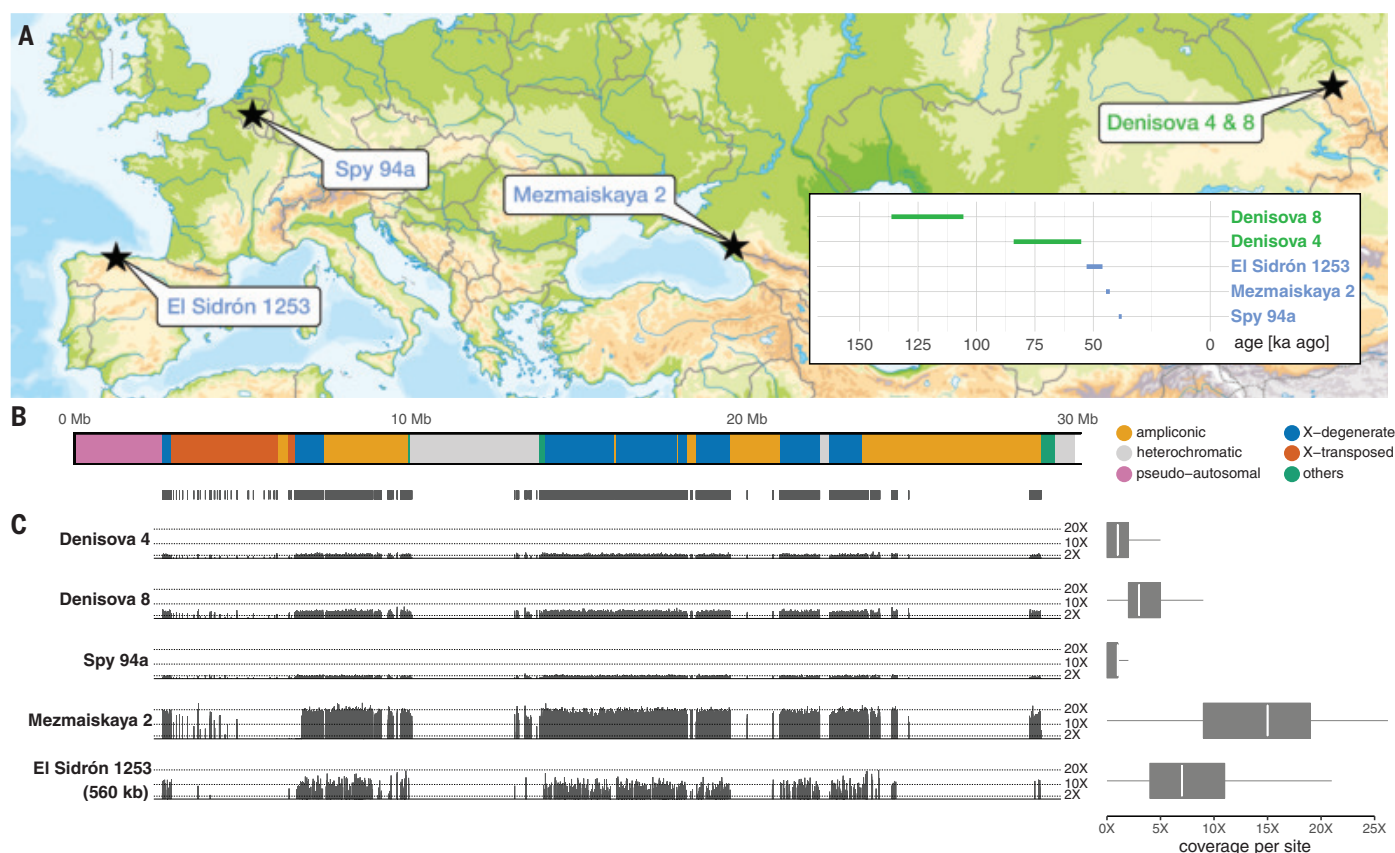


Fig. 1. Overview of male archaic humans in our study. (A) Archaeological site locations. Ages of specimens are shown as an inset (12, 13, 15). (B) Portion of the human Y chromosome targeted for capture [legend on right, coordinates of genomic regions are from (30)]. Thin black vertical lines show individual target capture regions.

(C) (Left) Spatial distribution of sequencing coverage along the ~6.9 Mb of capture target regions. The heights of the thin vertical bars represent average coverage in each target region. Coordinates are aligned to match the chromosome shown in (B). (Right) Coverage across all target sites for each individual to the left.

of the human Y chromosome (Fig. 1B) (14). This yielded sequence coverage of 1.4 \times for Denisova 4, 3.5 \times for Denisova 8, 0.8 \times for Spy 94a, and 14.3 \times for Mezmaiskaya 2 (Fig. 1C and table S2). In addition, we used a capture array designed for modern human Y chromosomes (3) to obtain 7.9 \times coverage of ~560 kb of the Y chromosome from the ~46- to 53-ka-old El Sidrón 1253 Neanderthal (Fig. 1C and table S2), which has been analyzed previously (15, 16).

To call genotypes of the captured archaic human and previously published modern human Y chromosomes (4, 17, 18), we leveraged the haploid nature of the human Y chromosome and implemented a consensus approach that requires at least 90% of the reads observed at each site covered by at least three reads to agree on a single allele (14). This minimizes the impact of aDNA damage on genotyping accuracy while allowing for a small amount of sequencing error or contamination (fig. S8) (14).

To determine the relationships between Denisovan, Neanderthal, and modern human Y chromosomes, we constructed a neighbor-joining tree from the Y chromosome genotype calls (14). Unlike the rest of the nuclear genome, which puts Denisovans and Nean-

derthals as sister groups to modern humans (2), the Denisovan Y chromosomes form a separate lineage that split before Neanderthal and modern human Y chromosomes diverged from each other (Fig. 2A). Notably, all three late Neanderthal Y chromosomes cluster together and fall outside of the variation of present-day human Y chromosomes (Fig. 2A).

To estimate the TMRCA of archaic and modern human Y chromosomes, we adapted a previously published method that calculates the archaic-modern human TMRCA as a proportion of the deepest known split in present-day human Y variation (4, 10, 14) and is therefore robust to low coverage and aDNA damage (10) (fig. S8 and table S2). We first calculated the mutation rate in the 6.9-Mb target region to be 7.34×10^{-10} per base pair per year [bootstrap confidence interval (CI) 6.27×10^{-10} to 8.46×10^{-10}] (fig. S11 and table S11) (14) and used it to estimate a TMRCA of ~249 ka ago (bootstrap CI 213 to 293 ka ago) (fig. S11 and table S11) (14) for the African A00 lineage and a set of non-African Y chromosomes (4, 18). This is consistent with other studies of present-day human Y chromosomes (4, 17), suggesting that the Y chromosomal regions we sequenced are

not unusual in terms of their mutation rate. We then used this A00 divergence time of 249 ka ago to infer TMRCA between archaic Y chromosomes and present-day non-African Y chromosomes for each archaic individual (fig. S14 and table S12) (14). The two Denisovan Y chromosomes split from the modern human lineage around 700 ka ago (Denisova 8: 707 ka ago, CI 607 to 835 ka ago; Denisova 4: 708 ka ago, CI 550 to 932 ka ago) (Fig. 2B and table S12). By contrast, the three Neanderthal Y chromosomes split from the modern human lineage about 370 ka ago: 353 ka ago for Spy 94a (CI 287 to 450 ka ago), 370 ka ago for Mezmaiskaya 2 (CI 326 to 420 ka ago), and 339 ka ago for El Sidrón 1253 (CI 275 to 408 ka ago) (Fig. 2B and table S12). Additionally, we used the proportion of sharing of derived alleles with the high-coverage Mezmaiskaya 2 to estimate the TMRCA of the three Neanderthal Y chromosomes to around 100 ka ago (figs. S25 and S26). We validated the robustness of all TMRCA estimates using filters of varying levels of stringency and different genotype calling methods and also by comparing capture and shotgun sequence results (figs. S19, S21, and S23). Although there was some evidence of capture

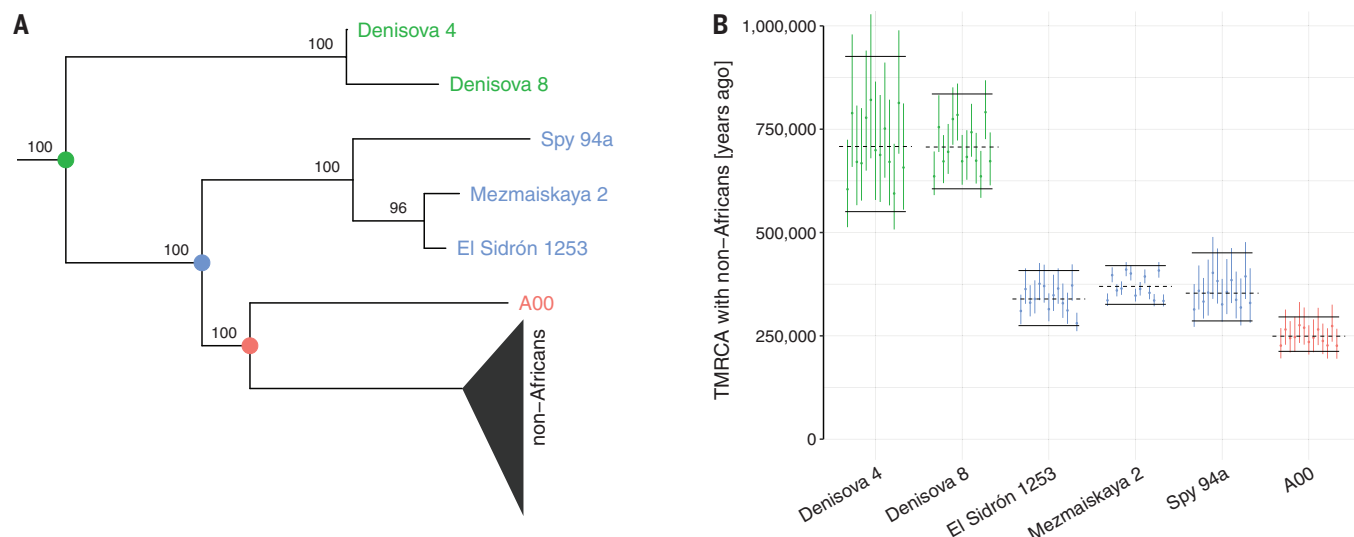


Fig. 2. Phylogenetic relationships between archaic and modern human Y chromosomes. (A) Neighbor-joining tree estimated from the Y chromosome genotype calls, excluding C-to-T and G-to-A polymorphisms, rooted with a chimpanzee as the outgroup (14). Numbers show bootstrap support out of 100 bootstrap replicates. Terminal branch lengths are not informative about the ages of specimens (Fig. 1A), owing to differences in sequence quality.

(B) Estimates of TMRCA between Y chromosomes along the x axis and a panel of 13 non-African Y chromosomes. Each dot represents the TMRCA with a single non-African Y chromosome, with error bars showing 95% CI from a resampling of branch counts (14). Black horizontal lines show the mean TMRCA calculated across the full non-African panel (dashed lines) with resampling-based 95% CI (solid lines) (14).

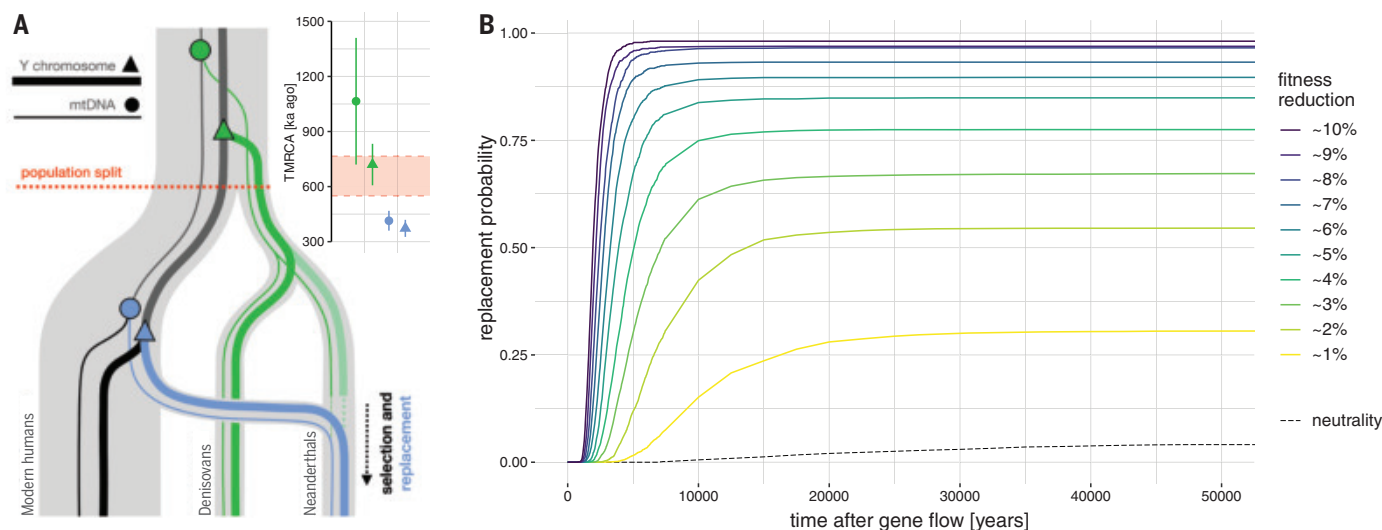


Fig. 3. Proposed model for the replacement of Neanderthal Y chromosomes and mtDNA. (A) Relationships between archaic and modern human mtDNA and Y chromosomes. The semitransparent Neanderthal lineage indicates a (as yet unsampled) hypothetical Y chromosome replaced by an early lineage related to modern human Y chromosomes. Most recent common ancestors with modern human lineages are shown for mtDNA (circles) and Y chromosomes (triangles). The inset shows TMRCA estimates for the four nodes in the diagram: Y chromosome TMRCA as estimated by our study and mtDNA TMRCA estimates from the literature (7, 8). The red shaded area highlights the 95% CI for the

population split time between archaic and modern humans, shown as the dotted red horizontal line (6). (B) Probability of replacement of a non-recombining, uniparental Neanderthal locus over time, assuming a given level of fitness burden relative to its modern human counterpart. Trajectories are based on forward simulations across a grid of parameters (figs. S27 to S29) (14), with N_e of modern humans and Neanderthals fixed at 10,000 and 1000, respectively. Modern human introgression was simulated in a single pulse at 5%. Replacement probabilities from a wider range of model parameters are shown in fig. S31.

bias in the data (fig. S7), we observed no consistent differences between capture data and shotgun sequences or between individuals showing different read length distributions, indicating that technical biases do not affect our inferences (fig. S21).

Our estimates of the Neanderthal-modern human TMRCA (Fig. 2B) are younger than the previous estimate of ~588 ka ago from the El Sidrón 1253 individual (10). This older estimate was calculated from ~3× coverage of 118 kb of nuclear exome capture sequence and,

because of the limited amount of data, used single-nucleotide polymorphisms supported even by single reads (10, 16). However, this is problematic because it can result in an increased rate of erroneously called genotypes, leading to some derived alleles that El Sidrón

1253 shares with both Neanderthals and modern humans being converted to the ancestral state, increasing the apparent TMRCA. When we applied filtering designed to mitigate errors (14) to the original El Sidrón 1253 data, we arrived at TMRCA estimates for El Sidrón 1253 consistent with all other Neanderthals in our study (fig. S22).

The Denisovan-modern human Y chromosome TMRCA estimates agree with population split times inferred from autosomal sequences, suggesting that the differentiation of Denisovan Y chromosomes from modern humans occurred through a simple population split (19). By contrast, the young TMRCA of Neanderthal and modern human Y chromosomes and mtDNAs suggest that these loci have been replaced in Neanderthals through gene flow from an early lineage closely related to modern humans (Fig. 3A) (7). Previous work indicates that the rate of gene flow from modern humans into Neanderthals was on the order of only a few percent (20, 21). Because the fixation probability of a locus is equal to its initial frequency in a population (22), the joint probability of both Neanderthal mtDNA and Y chromosomes being replaced by their introgressed modern human counterparts starting from a low initial frequency is even lower. However, owing to their low N_e and reduced efficacy of purifying selection, Neanderthals have been shown to have accumulated an excess of deleterious variation compared with modern humans (16), and it has been suggested that introgressed DNA was not neutral (23, 24).

To explore the dynamics of modern human Y chromosomes introgressed into Neanderthals, we simulated introgression of a nonrecombining, uniparental locus under purifying selection (14, 25). We considered a range of values for the following parameters: Neanderthal and modern human N_e , the time that both populations evolved independently after their split, and the amount of sequence under selection, all of which affect the amount of deleterious variation that accumulated in Neanderthal and modern human populations before introgression (14). We simulated introgression of modern human Y chromosomes into the Neanderthal population in a single pulse and varied the contribution between 1 and 10%. We then traced the frequency of the introgressed modern human Y chromosomes in Neanderthals over 100 ka. For each combination of parameters, we calculated how much lower the fitness of an average Neanderthal Y chromosome is compared with an average modern human Y chromosome using all linked deleterious mutations on each simulated chromosome (14). This allows us to make a general statement about the probability of replacement in terms of the difference in fitness between Neanderthal and modern human Y chromosomes while abstracting

over other factors that affect reproductive fitness but are currently impossible to simulate accurately (26).

For example, assuming 5% gene flow from modern humans, we found that even a 1% reduction in Neanderthal Y chromosome fitness increases the probability of replacement after 50 ka to ~25%, and a 2% reduction in fitness increases this probability to ~50% (Fig. 3B). However, the rate of gene flow as well as any factor that contributes to the difference in fitness between Neanderthal and modern human Y chromosomes will have a pronounced effect on the replacement probability (figs. S27 to S32). Given the crucial role of the Y chromosome in reproduction and fertility and its haploid nature, it is possible that deleterious mutations or structural variants on the Y chromosome have a larger impact on fitness than considered in our simulations. We therefore refrain from making predictions about the specific process of replacement, because we lack information about the frequencies of introgressed Y chromosomes in older Neanderthals, potential sex bias in the gene flow, and the fitness effects of single-nucleotide and structural variants on the Y chromosome (26). Nevertheless, our models are a proof-of-principle demonstration that even a simple difference in the efficacy of purifying selection between two lineages can markedly affect introgression dynamics of nonrecombining, uniparental DNA.

We conclude that the Y chromosomes of late Neanderthals represent an extinct lineage closely related to modern human Y chromosomes that introgressed into Neanderthals between ~370 and ~100 ka ago. The presence of this Y chromosome lineage in all late Neanderthals makes it unlikely that genetic changes that accumulated in Neanderthal and modern human Y chromosomes before the introgression led to incompatibilities between these groups (10). Furthermore, we predict that the ~400-ka-old Sima de los Huesos Neanderthals should carry a Y chromosome lineage more similar to that of Denisovans than to that of later Neanderthals (8, 9). Although the amount of modern human gene flow into Neanderthals appears to have been limited (13, 20, 21), we demonstrate that the replacement of mtDNA and Y chromosomes in Neanderthals is highly plausible, given the higher genetic load in Neanderthals compared with that in modern humans. Our results imply that differences in genetic load in uniparental loci between two hybridizing populations is a plausible driver for the replacements observed in other hybridization events (27–29).

REFERENCES AND NOTES

1. R. E. Green *et al.*, *Science* **328**, 710–722 (2010).
2. M. Meyer *et al.*, *Science* **338**, 222–226 (2012).
3. S. Lippold *et al.*, *Investig. Genet.* **5**, 13 (2014).
4. M. Karmin *et al.*, *Genome Res.* **25**, 459–466 (2015).

5. I. Olalde *et al.*, *Science* **363**, 1230–1234 (2019).
6. K. Prüfer *et al.*, *Nature* **505**, 43–49 (2014).
7. C. Posth *et al.*, *Nat. Commun.* **8**, 16046 (2017).
8. M. Meyer *et al.*, *Nature* **505**, 403–406 (2014).
9. M. Meyer *et al.*, *Nature* **531**, 504–507 (2016).
10. F. L. Mendez, G. D. Poznik, S. Castellano, C. D. Bustamante, *Am. J. Hum. Genet.* **98**, 728–734 (2016).
11. S. Sawyer *et al.*, *Proc. Natl. Acad. Sci. U.S.A.* **112**, 15696–15700 (2015).
12. K. Douka *et al.*, *Nature* **565**, 640–644 (2019).
13. M. Hajdinjak *et al.*, *Nature* **555**, 652–656 (2018).
14. See supplementary materials.
15. R. E. Wood *et al.*, *Archaeometry* **55**, 148–158 (2013).
16. S. Castellano *et al.*, *Proc. Natl. Acad. Sci. U.S.A.* **111**, 6666–6671 (2014).
17. Q. Fu *et al.*, *Nature* **514**, 445–449 (2014).
18. S. Mallick *et al.*, *Nature* **538**, 201–206 (2016).
19. K. Prüfer *et al.*, *Science* **358**, 655–658 (2017).
20. M. Kuhlwilm *et al.*, *Nature* **530**, 429–433 (2016).
21. M. J. Hubisz, A. L. Williams, A. Siepel, *PLOS Genet.* **16**, e1008895 (2020).
22. J. F. Crow, M. Kimura, *An Introduction to Population Genetics Theory* (The Blackburn Press, 1970).
23. K. Harris, R. Nielsen, *Genetics* **203**, 881–891 (2016).
24. I. Juric, S. Aeschbacher, G. Coop, *PLOS Genet.* **12**, e1006340 (2016).
25. B. C. Haller, P. W. Messer, *Mol. Biol. Evol.* **36**, 632–637 (2019).
26. S. Colaco, D. Modi, *Reprod. Biol. Endocrinol.* **16**, 14 (2018).
27. J. W. Ballard, M. C. Whitlock, *Mol. Ecol.* **13**, 729–744 (2004).
28. T. Bonnet, R. Leblois, F. Rousset, P.-A. Crochet, *Evolution* **71**, 2140–2158 (2017).
29. F. A. Seixas, P. Boursot, J. Melo-Ferreira, *Genome Biol.* **19**, 91 (2018).
30. L. Skov, M. H. Schierup; Danish Pan Genome Consortium, *PLOS Genet.* **13**, e1006834 (2017).
31. M. Petr, “The evolutionary history of Neanderthal and Denisovan Y chromosomes” - code and Jupyter notebooks. Zenodo (2020); doi:10.5281/zenodo.3941654.
32. M. Petr, “The evolutionary history of Neanderthal and Denisovan Y chromosomes” - Y chromosome capture designs. Zenodo (2020); doi: 10.5281/zenodo.3940568.

ACKNOWLEDGMENTS

We thank S. Pääbo, M. Stoneking, B. Peter, M. Slatkin, L. Skov, and E. Zavala for helpful discussions and comments on the manuscript. **Funding:** Q.F. was supported by funding from the Chinese Academy of Sciences (XDB26000000) and the National Natural Science Foundation of China (91731303, 41925009, 41630102). A.R. was funded by Spanish government (MICINN/FEDER) (grant number CGL2016-75109-P). The reassessment of the Spy collection by H.R., I.C., and P.S. was supported by the Belgian Science Policy Office (BELSPO 2004-2007, MO/36/0112). M.V.S., M.B.K., and A.P.D. were supported by the Russian Foundation for Basic Research (RFBR 17-29-04206). This study was funded by the Max Planck Society and the European Research Council (grant agreement number 694707). **Author contributions:** M.P. and J.K. analyzed data. M.H., Q.F., and E.E. performed laboratory experiments. H.R., I.C., P.S., L.V.G., V.B.D., C.L.-F., M.d.I.R., A.R., M.V.S., M.B.K., and A.P.D. provided samples. B.V., M.M., and J.K. supervised the project. M.P. and J.K. wrote and edited the manuscript with input from all co-authors.

Competing interests: The authors declare no competing interests. **Data and materials availability:** Complete source code for data processing and simulations, as well as Jupyter notebooks with all analyses and results, can be found at Zenodo (31). Coordinates of the capture target regions and sequences of the capture probes are available at Zenodo (32). All sequence data are available from the European Nucleotide Archive under the accession number PRJEB39390.

SUPPLEMENTARY MATERIALS

science.sciencemag.org/content/369/6511/1653/suppl/DC1
Materials and Methods
Figs. S1 to S32
Tables S1 to S14
References (33–67)
MDAR Reproducibility Checklist

9 March 2020; accepted 6 August 2020
10.1126/science.abb6460



Faculty Position in Computational Materials Science

at the Ecole polytechnique fédérale de Lausanne (EPFL)

The Institute of Materials in the School of Engineering invites applications for a **tenure track Assistant Professor** position in **Computational Materials Science**. We seek exceptional individuals who will develop and drive a research program at the forefront of the field, who have strong dedication to teaching at the undergraduate and graduate levels, and who will be proactive members of their professional and university communities.

Applications are invited covering research in any area of computational materials science, with a particular focus on computational and data-driven materials discovery. This is of special relevance to the Swiss research landscape as EPFL is the leading house of the National Centre for Competence in Research MARVEL (nccr-marvel.ch), dedicated to the computational design and discovery of novel materials. Examples of topics of interests include, but are not limited to, the development of theoretical and computational methods for materials modeling, and/or their application to understand, predict, design, and discover novel materials.

As a faculty member of the School of Engineering the successful candidate will be expected to initiate an independent and creative research program and participate in undergraduate and graduate teaching. Internationally competitive salaries and start-up resources, together with sustained internal funding and benefits are offered.

Applications should include 1) a cover letter with a statement of motivation (one to two pages), 2) curriculum vitae, 3) research plans (up to five pages), 4) teaching interests and plans (up to two pages), 5) publications list (including - if possible - links to your up-to-date research profile on e.g. ResearcherID or Google Scholar), 6) names and contact information for three (min) to five (max) referees. Applications must be uploaded in PDF format to the recruitment web site:

<https://facultyrecruiting.epfl.ch/position/23691277>

Formal evaluation of candidates will begin on **15 December 2020**.

Enquires may be addressed to:

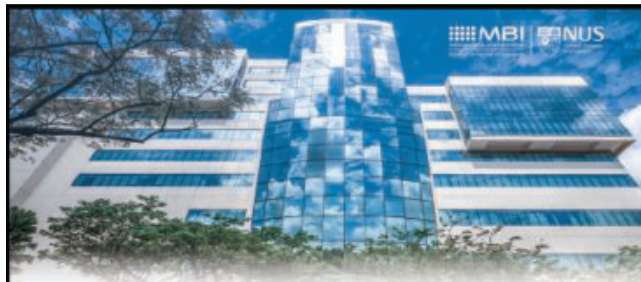
Prof. Nicola Marzari

Search Committee Chair

e-mail: cms-search@epfl.ch

For additional information on EPFL, please consult the websites: www.epfl.ch, sti.epfl.ch, imx.epfl.ch

EPFL is an equal opportunity employer and family friendly university. It is committed to increasing the diversity of its faculty. It strongly encourages women to apply.



MECHANOBIOLOGY INSTITUTE, NATIONAL UNIVERSITY OF SINGAPORE FACULTY POSITIONS AT ALL LEVELS

The Mechanobiology Institute (MBI) at the National University of Singapore (NUS) invites applications from outstanding candidates for multiple tenure-track faculty positions at all levels: Assistant Professor, Associate Professor, and Full Professor.

MBI is seeking candidates with a commitment to both independent and collaborative interdisciplinary research in a broad area of mechanical and dynamical processes in cell, tissue and organ development, aging, repair and regeneration.

Consideration will be given to candidates with a strong track record in incorporating single-cell analysis, omics and bioinformatics, high-throughput screens, and/or computation and modeling.

Compelling research programs in other areas, such as advanced methodology development in imaging and image analysis using artificial intelligence, nano-biotechnology, and diagnostics, will also be considered.

Candidates should have a Ph.D. degree and post-doctoral training in relevant fields, along with demonstrated excellence in research and interest in teaching. A junior faculty candidate is expected to demonstrate significant creativity and independence in research, and participate in teaching at the graduate and undergraduate levels. A senior faculty candidate is expected to have an outstanding track record in research, teaching and mentoring, and exhibit leadership and vision.

TO APPLY

Send the following materials to the MBI Faculty Recruitment Committee at mbihr@nus.edu.sg

Cover letter, Curriculum Vitae with bibliography, Statement of research interest and plan, Teaching statement, Contact details of at least 4 referees (Assistant Professor) or 6 referees (Associate and Full Professor)

Successful applicants will hold joint appointments as Principal Investigators at MBI and tenure-track faculty members in an appropriate NUS department, and can expect internationally competitive salary and benefits, core support, as well as generous start-up packages.

Shortlisted candidates will be invited for a campus visit interview. For accelerated consideration, please apply by **November 15, 2020**; however, applications will be accepted until all positions are filled.



MBI is a leading multi-disciplinary institute devoted to developing new paradigms for understanding biological functions in health and diseases from the perspective of cell, tissue and organ mechanics/dynamics and mechano-signal transduction. The institute operates on a fully integrated open-lab philosophy, with extensive infrastructure support by core facilities dedicated to technologies such as state-of-the-art light microscopy, nano- and micro- fabrication, and computing.

mbi.nus.edu.sg/recruitment



ASSISTANT/ASSOCIATE/FULL PROFESSOR - FACULTY POSITION IN CELL BIOLOGY

The Department of Cell Biology at The University of Oklahoma Health Sciences Center (OUHSC) invites exceptional scientists to apply for **tenured/tenure-track eligible faculty positions**. Successful candidates are expected to develop/maintain a fully independent and dynamic research program. All candidates with research interests addressing fundamental questions relevant to Cell Biology will be considered. Candidates with expertise in cilia/centrosomes/microtubules, adult stem cells/tissue regeneration, and neurobiology are of special interest. A Ph.D., M.D., or equivalent is required.

The Department of Cell Biology is one of five basic science departments within the College of Medicine at OUHSC, providing a highly interactive cohort of scientists with interests in cardiovascular biology, vision, cancer, stem cells, neuroscience, cilia, calcium signaling, ion channels and basic cell biology. The department has its own imaging core with a wide variety of imaging equipment including a live cell imaging system, a standard confocal system, and a two-photon confocal microscope. The department is ranked 12th nationally in NIH funding among Cell Biology departments.

OUHSC is a comprehensive health center that includes Colleges of Pharmacy, Dentistry, Nursing, Allied Health, Public Health, Medicine, and the Graduate College. It is home to two hospitals and an NCI-designated Cancer Center. OUHSC has multiple NIH-sponsored Centers that provide infrastructure and support in the areas of Aging/Geroscience, Diabetes, Cancer, Vision, and Immunology/Microbiology. Local funding is available on a competitive basis. Total sponsored awards at OUHSC for FY20 are \$190 million, an increase of almost 30% over FY19. NIH awards for FY20 are over \$86 million, an increase of 40% over FY19.

OUHSC Core Facilities include the state-of-the-art Laboratory for Molecular Biology and Cytometry Research, which provides services specializing in genomics, proteomics, bioinformatics, cytometry, and imaging. The Division of Comparative Medicine manages facilities for rodent (barrier & conventional), aquatics, and larger species. There are currently approximately 300 IACUC-approved active animal use protocols. The Oklahoma Medical Research Foundation (OMRF) is adjacent to OUHSC and maintains a collaborative partnership with OUHSC. All OMRF core facilities are available to OUHSC investigators.

Successful applicants will receive a competitive salary, generous, multi-year start-up package, and be assigned newly renovated laboratory space. Appointment to **Assistant Professor** will require evidence of outstanding research accomplishments. Appointment to **Associate** or **Full Professor** will require an established research program funded by a national agency. All members of the department participate in the teaching mission of the College of Medicine and the Graduate College. For further information about the department go to <https://basicsciences.ouhsc.edu/cb/>.

Candidates should submit a curriculum vitae, a description of current research interests and future research plans as one pdf file. Letters of recommendation will be requested at a later stage. Please send the application packet to Paula Slaughter at paula-slaughter@ouhsc.edu. Confidential inquiries may be addressed to Eric Howard, Ph.D. at eric-howard@ouhsc.edu.

The University has a commitment to diversity, equality and inclusion. All qualified applicants will receive consideration. The University of Oklahoma Health Sciences Center is an equal employment opportunity and affirmative action institution <http://www.ou.edu/eoo>! Individuals with disabilities and protected veterans are encouraged to apply.

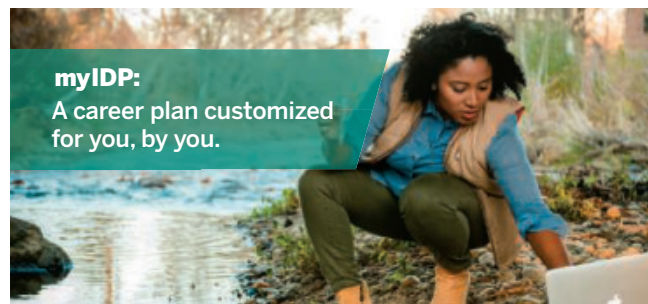


POSTDOCTORAL FELLOWS IN -OMICS RESEARCH

Postdoctoral fellowships are available to pursue research supported by NIH grants and other funds to assess the epigenomic, genomic and transcriptomic effects, and microbiome following environmental pollutant and dietary supplement exposure on inflammation and cancer. Research also involves COVID-19 and PTSD patients. Ph.D. in any biomedical sciences is required. Preference given to expertise in Immunology. Experience in -omics technology not required.

Send c.v. and 3 references to Dr. Mitzi Nagarkatti, Chair of Department of Pathology, Microbiology and Immunology, University of South Carolina School of Medicine, Columbia, SC 29208 by applying to: <http://uscjobs.sc.edu/postings/86441>.

UofSC does not discriminate in educational or employment opportunities on the basis of race, sex, gender, gender identity, transgender status, age, color, religion, national origin, disability, sexual orientation, genetics, protected veteran status, pregnancy, childbirth or related medical conditions.



For your career in science, there's only one **Science**

Features in myIDP include:

- Exercises to help you examine your skills, interests, and values.
- A list of 20 scientific career paths with a prediction of which ones best fit your skills and interests.



Visit the website and start planning today!
myIDP.sciencecareers.org

Science Careers
NIAAAS

In partnership with:





FACULTY POSITION

Biochemistry and Structural Biology
UT Health San Antonio (UTHSA)
Joe R. and Teresa Lozano Long School of Medicine

We are seeking outstanding candidates for a tenured **Associate Professor** or **Full Professor** position. We are particularly interested in candidates with expertise in biochemistry and cancer biology. The Department houses University-supported core facilities in macromolecular structure and interactions [NMR spectroscopy, X-ray crystallography, mass spectrometry (proteomics and metabolomics), and the Center for Innovative Drug Discovery (high throughput screening and medicinal chemistry). (<https://wp.uthscsa.edu/biochemistry/core-facilities/>).

UT Health San Antonio comprises Medical, Graduate, Dental, Nursing and Health Profession schools. It is also home to the Nathan Shock Center for Aging, the NCI-designated Mays Cancer Center, the Greehey Children's Cancer Research Institute, the Glenn Biggs Institute for Alzheimer's and Neurodegenerative Diseases, the Center for Neuroscience, and a NIH Clinical Translational Science Award. San Antonio is the seventh largest city in the U.S., with a historical downtown, a vibrant economy, affordable housing, and ample recreational opportunities.

Applicants must have a strong record of publishing in peer-reviewed journals and obtaining federal funding. Candidates who are committed to the development of new cancer therapeutics are particularly encouraged to apply. The position offers a generous startup package, superior scientific sources, and the potential for substantial recruitment funds from the UT STARs Program and the Cancer Prevention and Research Institute of Texas (CPRIT). Successful applicants will join a multidisciplinary team of 12 primary and 10 adjunct/cross appointed faculty in Biochemistry and Structural Biology (<https://wp.uthscsa.edu/biochemistry/team-members/faculty/>), and will serve as a mentor for students and research fellows, and contribute to teaching in our graduate and professional programs. UTHSA is committed to a culturally and gender diverse faculty and has been designated a Hispanic Serving Institution.

Interested candidates should visit <https://uthscsa.referrals.selectminds.com/faculty> to apply online. Select the Faculty tab and enter job number **20000963** on the keyword box. Please upload a curriculum vitae, a two-page description of research interests, a list of three to four referees and a cover letter addressed to Dr. Jean Jiang, Chair of the Faculty Search Committee. Review of applications will begin immediately upon receipt and will continue until the position is filled. For any questions in regard to this position, please email: BSB-Search@uthscsa.edu.

UT Health San Antonio is an Equal Employment Opportunity/Affirmative Action Employer including protected veterans and persons with disabilities. All faculty appointments are designated as security sensitive positions.



Center for Molecular Medicine
UNIVERSITY OF GEORGIA

ASSISTANT/ASSOCIATE PROFESSOR TENURE-TRACK FACULTY POSITION

The University of Georgia announces a tenure-track faculty position at the level of **Assistant** or **Associate Professor** with teaching and research responsibilities in the Center for Molecular Medicine (CMM) (<http://cmm.uga.edu>). The CMM is dedicated to better understanding the molecular and cellular basis of human disease and where possible, to use basic discovery for the advancement of therapeutic development. To advance this mission, we are seeking applications from outstanding investigators.

Candidates with interests in the following areas are encouraged to apply:

- regenerative medicine and tissue repair
- stem cells and organoid models for human disease and development
- molecular and cellular basis of cancer, including cancer stem cells
- metabolic disease and metabolic regulation in human disease

All applicants must have a Ph.D. degree in a relevant discipline. Applicants at the **Assistant** level must have at least two years relevant postdoctoral research experience as well as a publication record and a research plan commensurate with rank.

Applicants at the **Associate** level should provide documentation of an established, well-funded and impactful research program.

An attractive start-up package with highly competitive conditions of employment will be offered. Laboratory space will be located in the new Center for Molecular Medicine Building on Riverbend Road, adjacent to the Center for Complex Carbohydrate Research. The Center benefits from strong interactions with UGA researchers at the Center for Drug Discovery, Developmental Biology Alliance, CCRC as well as academic departments on campus.

The University of Georgia (www.uga.edu) is a land grant/sea institution located ninety miles northeast of Atlanta (www.visitathensga.com) and offers an outstanding quality of life in the Athens region (www.georgia.gov).

Applications should include a cover letter, research statement and CV. Three confidential letters from referees should be submitted separately. All materials should be submitted at <http://www.ugajobsearch.com/postings/168562>. Completed applications received by **October 31, 2020** are assured full consideration.

The University of Georgia is an Equal Opportunity/Affirmative Action employer. All qualified applicants will receive consideration for employment without regard to race, color, religion, sex, national origin, ethnicity, age, genetic information, disability, gender identity, sexual orientation or protected veteran status. Persons needing accommodations or assistance with the accessibility of materials related to this search are encouraged to contact Central HR (hrweb@uga.edu). Please do not contact the department or search committee with such requests.



**Science 2019
TOP EMPLOYERS**

Who's the Top Employer for 2019?

Science Careers' annual survey reveals the top companies in biotech & pharma voted on by Science readers.

Read the article and employer profiles and listen to podcasts at sciencecareers.org/topemployers



FACULTY POSITION

Biochemistry and Structural Biology
UT Health San Antonio
Joe R. and Teresa Lozano Long School of Medicine

We are seeking faculty candidates at the rank of **Assistant Professor** on the tenure-track. We are particularly interested in candidates with expertise in structural biology (X-ray crystallography, NMR, or cryoEM) and research interests in cancer development and progression. The Department houses University-supported core facilities in macromolecular structure and interactions [NMR spectroscopy, X-ray crystallography, surface plasmon resonance, calorimetry (ITC, DSC)], mass spectrometry (proteomics and metabolomics), and the Center for Innovative Drug Discovery (high throughput screening and medicinal chemistry). (<https://wp.uthscsa.edu/biochemistry/core-facilities/>).

UT Health San Antonio comprises of Medical, Graduate, Dental, Nursing and Health Profession schools. It is also home to the Nathan Shock Center for Aging, the NCI-designated Mays Cancer Center, the Greehey Children's Cancer Research Institute, the Glenn Biggs Institute for Alzheimer's and Neurodegenerative Diseases, the Center for Neuroscience, and a NIH Clinical Translational Science Award. San Antonio is the seventh largest city in the U.S., with a historical downtown, a vibrant economy, affordable housing, and ample recreational opportunities.

Applicants must have a strong publication record and are expected to secure extramural funding. Preference will be accorded to candidates who have been successful in obtaining K99/R00 funding from the NIH. The position offers a generous startup package, superior scientific sources, and the potential for substantial recruitment funds from the UT STARs Program and the Cancer Prevention and Research Institute of Texas (CPRIT). Successful applicants will join a multidisciplinary team of 12 primary and 10 adjunct/cross appointed faculty in Biochemistry and Structural Biology (<https://wp.uthscsa.edu/biochemistry/team-members/faculty/>), and will develop a productive research program, serve as a mentor for students and research fellows, and contribute to teaching in our graduate and professional programs. UTHSA is committed to a culturally and gender diverse faculty and has been designated a Hispanic Serving Institution.

Interested candidates should visit <https://uthscsa.referrals.selectminds.com/faculty> to apply online. Select the Faculty tab and enter job number **20000993** on the Keyword box. Please upload a curriculum vitae, a two-page description of research interests, a list of three to four referees and a cover letter addressed to Dr. Sandeep Burma, Chair of the Faculty Search Committee. Review of applications will begin immediately upon receipt and will continue until the position is filled. For any questions in regards to this position, please email: BSB-Search@uthscsa.edu.

UT Health San Antonio is an Equal Employment Opportunity/Affirmative Action Employer including protected veterans and persons with disabilities. All faculty appointments are designated as security sensitive positions.

By Emily Ashkin and Michelle Atallah

Full disclosure

“I stood in front of my entire lab and told them I had made zero progress in the last year,” Michelle declared. At the graduate program’s annual retreat, presentation after presentation had highlighted students’ successes. But Michelle, Emily, and two other Ph.D. students were taking a different approach, sharing our most painful failures—disappointed principal investigators, rejected fellowship applications, being one signature away from dropping out of grad school, you name it. The audience of Ph.D. students sat in silence, apparently shocked. But we weren’t ashamed. Quite the opposite—we were proud to be sharing our full selves and building a foundation for authentic relationships.

It began a few months earlier, when Emily was applying for graduate fellowships. Michelle, a previous National Science Foundation (NSF) fellowship winner, was tapped to help her through the process and was floored by how good Emily’s essays were—beautifully written, and describing achievements and experiences that made Michelle feel inadequate. So Michelle was surprised when Emily said that she felt applying wasn’t worth it because she was certain her poor undergrad grades were going to send her straight to the rejection pile. Michelle took a deep breath, smiled, and said, “I won the NSF with a GPA just like yours.” For both of us, this was our first time openly confessing our shortcomings to a colleague.

Setbacks are an inevitable part of grad school, but too often we try to hide them. By sharing our whole selves, including our failures, the two of us went on to build a deep, meaningful relationship. And we wanted others to experience that openness, camaraderie, and support.

We thought our program’s annual retreat would be a good opportunity to help set our peers on that path. We weren’t sure the organizers would be interested in a nonscientific session, but they were encouraging. So with excitement—and some nerves—we got to work preparing, joined by two classmates who also wanted to share their experiences.

The four of us began the workshop by presenting our stories onstage. Then we invited the audience members to turn to one another and share their own significant failures. An awkward silence followed—as we had expected—but it only lasted a few seconds. Soon the students jumped into engaged and enthusiastic conversation. Two first-year students began to cry when they discovered they both felt overwhelmed by impostor syndrome. Older students opened up about switching labs halfway through their



“By sharing our whole selves, including our failures, [we built] a deep, meaningful relationship.”

Ph.D.s. Students merged into larger groups as they realized how many of their colleagues shared the exact struggles they did. Even after the session ended, whispered conversations continued until the next speaker took the stage.

From that point forward, every presentation at the retreat incorporated some mention of the failures that led to the results. Students shared that their most significant data slides took more than a year to get right, or that the presented project was simply the first one that hadn’t failed. It reminded us that behind every impressive result is a person who is just trying their best.

Since the workshop, we have noticed a sustained change in our classmates. The answers to questions like, “How are you doing?” are

more honest and less perfunctory, and several students have mentioned they feel closer to their classmates. Students are asking one another for help not just on technical challenges, such as where to find a reagent or how to do a protocol, but also about how to handle the personal challenges that are part of grad school. When one student felt unprepared to give an important presentation, for example, they messaged the program-wide Slack channel for help. Several students replied, sharing advice, stories of similar experiences, or simply words of affirmation and encouragement.

It’s hard to relate to someone when all you know about them is their accomplishments. Talking about failure normalizes it and proves it’s nothing to be ashamed of. To lead by example, Emily notes that she did not win an NSF fellowship. It’s a disappointment, but she is proud to share it. ■

Emily Ashkin and Michelle Atallah are Ph.D. candidates at Stanford University in Palo Alto, California. Send your career story to SciCareerEditor@aaas.org.



Energy Material Advances

Energy Material Advances is an online-only, Open Access journal published in affiliation with **Beijing Institute of Technology (BIT)** and distributed by the **American Association for the Advancement of Science (AAAS)**. The journal publishes, research articles, review articles, short communications, perspectives, and editorials. *Energy Material Advances* covers multiple fields from cutting-edge material to energy science, investigating theoretical, technological as well as engineering aspects.

Submit your research to *Energy Material Advances* today!

Learn more at spj.sciencemag.org/energymatadv

The Science Partner Journal (SPJ) program was established by the American Association for the Advancement of Science (AAAS), the nonprofit publisher of the *Science* family of journals. The SPJ program features high-quality, online-only, Open Access publications produced in collaboration with international research institutions, foundations, funders and societies. Through these collaborations, AAAS furthers its mission to communicate science broadly and for the benefit of all people by providing top-tier international research organizations with the technology, visibility, and publishing expertise that AAAS is uniquely positioned to offer as the world's largest general science membership society. Visit us at: spj.sciencemag.org



@SPJournals



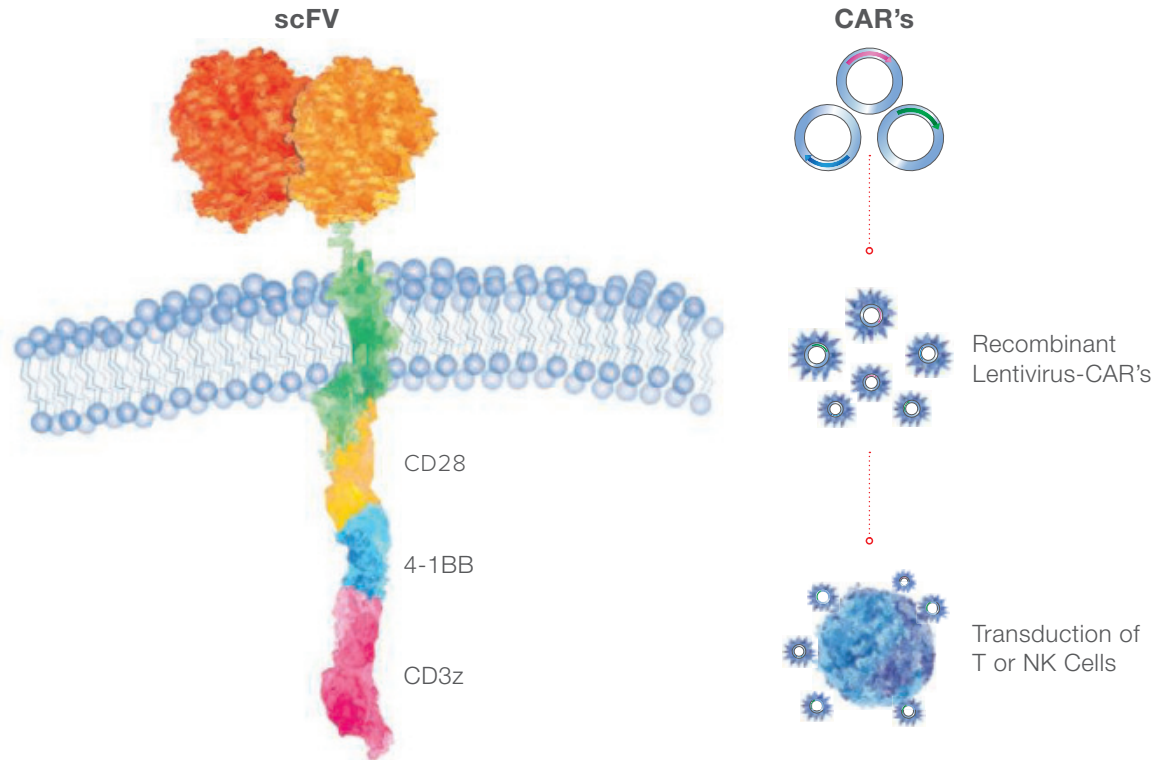
@SPJournals



OPEN ACCESS

Custom Lentivirus Generation

One-Stop-CRO for CAR-T Research



ProMab Biotechnologies commits to stay at the forefront of CAR-T technologies by providing an all-inclusive pre-clinical research program for CAR-T development. Our CAR-T platform utilizes lentivirus as it has become widely used as a vector to deliver specific genes of interest and to complement gene and cell therapy applications.

Our standardized and highly optimized platform enables ProMab to produce recombinant lentivirus with many benefits:

- Custom vector engineering from gene synthesis to plasmid production
- High titer: 10^8 to 10^{10} particles/ml
- Fast turnaround time: 2 to 3 weeks
- Variety of analytical options
- Ready to use CAR-T lentivirus
- Downstream to CAR-T or stable cell line development services

All products are for research only

Discover more | www.promab.com



2600 Hilltop Dr, Building B, Richmond, CA 94806

1.866.339.0871 | info@promab.com